MODELLING OF DEFECT STATES IN COVALENT AMORPHOUS SOLIDS

ANIEKAN MAGNUS UKPONG

A Thesis Presented for the Degree of

DOCTOR OF PHILOSOPHY

In the Department of Physics

Faculty of Science

UNIVERSITY OF CAPE TOWN

28 May 2008

‘The irreversibility of time is the mechanism that brings order out of chaos.’

Ilya Prigogine, 1984.

Dedication

This thesis is dedicated to my family, in particular to my son, Kingsley, who had to suffer the unfortunate consequences of my absence from home throughout the duration of this study, and to all scientists who are interested in the theoretical and computational study of condensed matter systems.

Acknowledgements

A research programme of this nature can hardly be successful without the contribution of numerous people, groups of people and organizations, and this research study is no exception. I am indebted to all the people who contributed directly or indirectly towards the success of this study. I am profoundly grateful to my supervisors, Professor David T. Britton and Professor Magit Härting, whose constant expert advice, countless suggestions, reviews, guidance and leadership gave enthusiasms to this research work.

I am also grateful to Professor Luciano Colombo, Department of Physics, University of Cagliari, Italy, for providing me with the original TBMD code on request. This served as the springboard for this study, and for very useful comments on the simulated incorporation of hydrogen to pure amorphous silicon structures. I also acknowledge with very sincere thanks, the assistance of Professor Risto M. Nieminen, Department of Physics, Helsinki University of Technology, Espoo, Finland, for providing the DOPPLER code and Dr. Ilja Mäkonnen for assistance with the technicalities involved in running the DOPPLER code and the interpretation of the high momentum distribution curves. I am also grateful to Dr. Leif Laaksonen, Centre for Scientific Computing, Espoo, Finland, for providing me with the gOpenMol-3.00 visualization package and for very helpful discussions.

In addition, I acknowledge with thanks, the technical support from Dr. Bruce Becker and Gareth de Vaux during the defect structure calculations on the UCT/CERN cluster of the Department of Physics, University of Cape Town. I have also benefited immensely from the numerous questions and observations of Alfred Yenwong-Fai during the programming stages for the atomic-level stress calculations. This work has also benefited substantially from fruitful discussions with other members of the Amorphous Silicon and Stress-Induced Diffusion Research Groups of the Department of Physics, University of Cape Town, and to whom I owe sincere gratitude.

I am particularly grateful to the Department of Physics, Faculty of Science, University of Cape Town, Republic of South Africa for providing me with a wonderful study environment for postgraduate research, and for financial support during the course of the programme. Finally, I owe very sincere gratitude to the University of Cape Town, for supporting my doctoral degree programme through the Research Council Scholarship, and to the Deutscher Akademischer Austausch Dienst (DAAD), Bonn, Germany for accepting responsibility for my doctoral training, and providing me with financial support throughout the duration of my doctoral research through scholarship No. SDV/A/04/29923.

Abstract

This study consists of the tight binding molecular dynamics simulations, of the bulk and defect structures, in hydrogenated amorphous silicon. Emphasis is given to the systematic analysis of the changes in the network structures, which occur due to the incorporation of hydrogen, at different levels of concentration. The atomic-level stress in the simulated structures is defined, in a manner that is consistent with the local structure. The concept of configurational landscapes is introduced, as a new analysis framework for the correlations between the stress fluctuations and the modifications of the local structure. In particular, for the analysis of stress variations within the domain of the order parameter field, two different categories of structural configurations are obtained. These are observed as a rugged region and a smooth region of the stress landscape, which are characterized by hydrogen concentrations of below 15%, and above 15%, respectively. For these two regions, it is found, that, a single scalar parameter is sufficient to characterize the structural order in the networks.

Positron annihilation characteristics obtained for structures within the two identified regions of the stress landscapes show that hydrogen causes the delocalization of the positron wave function. The observed hydrogen-induced delocalization, in combination with the improvement in structural order, at higher concentrations suggest, that the phenomenon of hydrogen induced relaxation of the silicon networks is universal, and not dependent on the procedures followed in obtaining the networks.

Table of Contents

Chapter One

Chapter Two

Chapter Three

Chapter Four

Chapter Five

Chapter Six

Chapter Seven

Chapter Eight

Chapter Nine

Chapter Ten

Chapter One

Introduction

An amorphous material is a topologically disordered material whose local structure has no translational symmetry in atomic positions. Amorphous materials can be classified broadly into tetrahedrally-bonded covalent solids, pnictides, chalcogenides, oxides and liquids. Since the first systematic study of an amorphous solid as a functional material was reported about six decades ago [1], the study of amorphous materials, in particular, tetrahedrally-bonded covalent solids, has developed considerably, both from the experimental and theoretical perspectives. This development arises primarily because of the need for new, robust and relatively inexpensive thin film materials suitable for a wide variety of technological applications. Over the last three decades, hydrogenated amorphous silicon (*a*-Si:H) has proved itself as an important prototype of tetrahedrally-bonded covalent amorphous solids [2-4]. This thesis will focus more on amorphous silicon (*a*-Si) and hydrogenated amorphous silicon as models of tetrahedrally-bonded covalent solids because of a number of reasons.

Firstly, *a*-Si is of immense technological importance, especially in its hydrogenated and doped forms. In microelectronics for instance, field effect transistors made from *a*-Si:H films are used as pixel switches in digital displays of mobile phones and modern laptop computers among many other applications [2-4]. Secondly, from an experimental point of view, the microstructure, structural order, macroscopic morphology, bond strain, macroscopic density, dominant type of structural defects, total hydrogen content and its spatial distribution, and the presence of other impurity atoms depend mainly on the method and physical conditions of growth of the thin film. Thirdly, and most relevant to this thesis, from a theoretical viewpoint, *a*-Si is *one of the simplest* tetrahedrally-bonded amorphous systems readily available for testing new theoretical concepts and simulation techniques that may be developed for disordered systems.

Some of the major advantages of studying *a*-Si as a model of tetrahedrally-bonded covalent solids include the following:

(i) *a*-Si is an elemental semiconductor material, making it a simple system to study compared to binary compounds or alloys, like hydrogenated amorphous silicon carbide or hydrogenated amorphous silicon nitride *etc*;

(ii) the success of the quantum mechanical description of covalent bonding in *a*-Si exclusively in terms of sp^3 hybridization is an advantage over other systems, such as amorphous carbon, where bonding also has to be described in terms of other types of hybridization [5];

(iii) the availability of numerous classes of interatomic potentials makes the dynamics of *a*-Si somewhat easier to describe. Hence, the properties of binary systems arising from the controlled doping of *a*-Si can be studied;

(iv) the availability of numerous experimental studies of the physical properties of *a*-Si in literature permits a comparative analysis of the results obtained from computer simulations;

(v) since the seminal work of Bernal [6], many good quality models of *a*-Si have been created, which serve as suitable starting points in many theoretical or computational studies involving *a*-Si:H;

(vi) it is possible to create supercell models which contain defects that are similar to native defects found in experimentally grown *a*-Si films using a suitable algorithm.

All these reasons make *a*-Si a good test material for the study of the properties of amorphous and glassy materials.

The use of the continuous random network (CRN) model [7], to describe the local network structure of *a*-Si was originally proposed by Polk [8, 9]. This approximation is based on strained Si-Si bonds, all of which are four-fold coordinated. However, unlike the CRN approximation, the actual *a*-Si:H structure contains a significant fraction of broken or dangling bonds, most of which are stabilized by hydrogen termination [10]. The breaking of overstrained bonds can be seen as allowing the structure to relax, therefore improving the short range order of the structure, whereas their termination with hydrogen prevents the formation of a perfectly ordered crystalline structure. There should therefore be a correlation, if not an interdependence, between the order in the structure, the stress in the network, and the concentration of hydrogen in the material. However, it is still not clear how the structural network modifications and the resulting structural order evolves under the influence of stress in *a*-Si:H. In this study, the concept of configurational landscapes [11] is therefore used to investigate these relationships at a fundamental level by investigating simulated structures.

One of the aims of this work is to investigate the properties of the thermalized positron state in bulk *a*-Si:H, in order to unravel the structural origin of the dominant positron annihilation signals in *a*-Si:H. This type of study is helpful in clarifying the microscopic mechanisms involved in the disorder-to-order transition observed in *a*-Si:H by investigating the delocalised state, which is associated with different characteristic regions of the stress landscape. Further information, more applicable to real materials, is gained by manual insertion of typical defects, into the simulated network, and determining the associated positron properties.

This thesis is structured as follows: chapters two to chapter five present the theoretical formulations, and computational modelling methodologies used. Chapter six presents the analysis of the thermodynamic stability, and the dynamical response of the simulated hydrogen-free structures. Also, the analysis of the structural modifications, which arise from the incorporation of variable concentrations of hydrogen, is also presented. Chapter seven presents the analysis of the fluctuations in atomic stresses. It also presents the analysis of the correlations between local stress fluctuations and the structural order, within the domain of the stress landscape. Chapter eight presents the analysis of the positron annihilation characteristic in the simulated bulk and defect structures in hydrogenated amorphous silicon. Chapter nine presents the discussion, and finally, chapter ten presents the conclusions.

Chapter Two

Structural Modelling

This chapter presents the details of the theoretical formulations and computational methodologies used in the simulations reported in this thesis. Where necessary, efforts are made to present as concisely as possible, the algorithms adopted in the numerical implementation schemes. The chapter starts with a general overview of the methods of simulating amorphous solids, and progressively specializes on the methods adopted in this study to simulate *a*-Si and *a*-Si:H, based on the tight binding framework. A justification of the choice of the tight binding method over other methods is also presented. Furthermore, this chapter presents a detailed quantum mechanical description of the interactions between the different species of atoms in a given model system. Throughout the chapter, several tests are carried out to ensure that the resulting network structures give reasonable physical properties.

The criteria for computing the electronic structure of amorphous materials within the tight binding scheme are also presented. A physical model of the bulk and local structures of tetrahedrally-bonded amorphous solids is also presented, in terms of parameters derivable from the pair correlation function. The details of the computer simulation scheme for obtaining superecll models of hydrogen-free and hydrogenated amorphous silicon are then presented.

2.1 Modelling Hydrogenated Amorphous Silicon

There are numerous approaches of obtaining computer-generated models of amorphous solids, and in all cases, the resulting topological properties depend mainly on the processes followed in the computer generation of the structures. These approaches range from models based on the dense random packing of hard spheres [12] for simple liquids and metallic glass, to models based on the continuous random network (CRN) approximation for modelling tetrahedrally-bonded covalent amorphous semiconductors. For instance, in modelling amorphous silicon, Wooten, Winer and Weaire [13] (WWW) introduced positional disorder into an ordered diamond structure by means of a Monte Carlo (MC) bond switching scheme, so that distorted tetrahedral coordination is always preserved for all atoms, but instead, five-fold and seven-fold rings are introduced.

Although the reliability of the full quantum mechanical description of bonding in *a*-Si:H is undisputed, it is still useful to provide an approximate quantum-mechanical scheme for identifying and characterizing the Si-Si and Si-H bonds in bulk models of *a*-Si:H. Even with the present state of development of sophisticated algorithms and computer speed, full *ab initio* calculations are still computationally expensive and the system size is usually small. In Refs. [14-16] for example, the *ab initio* simulations of *a*-Si are restricted to systems containing less than 100 atoms. Since simulated structures are known to be sensitive to the choice of interatomic potentials, it is one of the aims of this study to find a computationally efficient semi-empirical many-body potential suitable for the study of hydrogen in *a*-Si:H. The potential should further yield network disorder that is consistent with experimentally obtained *a*-Si:H structures.

In Ref. [17] Biswas, Grest and Soukoulis (BGS) introduced an alternative method of modelling *a*-Si, based on the principle of freezing liquid silicon (*l*-Si). In the BGS model, a hot melt of *l*-Si is quenched to a low temperature at a very fast rate using molecular dynamics (MD) methods, and the structure is relaxed with the *cluster potential* of Biswas and Haman [18,19]. In principle, any other cluster potential such as the Stillinger-Weber potential [20], or that of Pearson *et al.* [21], or even *cluster functionals*, such as those of Bolding and Anderson [22], or Baskes [23] could equally be used within the BGS approach to simulate *a*-Si with variable degree of success. The main difference between the methods of simulating *a*-Si based on the BGS scheme, and those based on Monte Carlo bond switching schemes [24,25] based on the CRN model is the unavoidable presence of coordination defects in the former. These generic defects are mainly three-fold and five-fold coordinated silicon atoms, which are present in the simulated structures as a direct consequence of the simulation process.

In computer simulations of bulk phases of silicon, it is usual to relax the structure with an interatomic potential. However, several forms of interatomic potentials have been proposed for silicon. These range from the simple Keating-type pair potentials [26,27], in which the orientation dependence of the tetrahedral network bonding is ignored, to empirical interatomic potentials in which the dependence of the bond order or bond strength on the local environment of the covalent bond is explicitly incorporated [28-36]. For the covalent structures considered in this study, it suffices to utilize a semi-empirical interatomic potential to account for the local environment of the covalent bond.

In this work, the method of simulating *a*-Si and *a*-Si:H is based on the principles of the BGS model. However, unlike the original BGS model, the method used is based on the implementation of the tight binding method of total energy calculations within the molecular dynamics simulation scheme [37]. This method utilizes parameterized interatomic potentials [38, 39] to account for near-neighbour interactions, and gives results that are accurate enough for direct comparison with results of first principles calculations in smaller systems [40-42]. The use of this computational model is motivated mainly by its successes in numerous computational studies of hydrogen-free *a*-Si [43, 44], and its hydrogenated forms [45, 46], generated within the quench from the melt technique. The simulated structural properties are directly comparable with experimentally determined properties of *a*-Si:H structures obtained by plasma enhanced chemical vapour deposition (PECVD) method [47] and hot wire chemical vapour deposition (HWCVD) methods [10, 48, and 49].

2.1.1 Tight Binding Hamiltonian

It is assumed that the behaviour of electrons in a covalent solid can be modelled in terms of the frozen core approximation [50] so that:

(i) the lowest-lying molecular orbitals are always occupied by the inner-shell (or core) electrons, and;

(ii) these core electrons are constrained to always remain doubly-occupied in all ground state configurations of a solid.

The Hamiltonian of a system of many ion cores and valence electrons can be expressed, within the adiabatic approximation, of the Born-Oppenheimer theory [51] as:

$$H_{total} = K_i + K_e + V_{ee} + V_{ei} + V_{ii} \,. \tag{2.1}$$

In this case, K_i and K_e represent the kinetic energy operator of the ions and electrons. The electron-electron, electron-ion and ion-ion interaction operators are represented by V_{ee}, V_{ei}, and V_{ii} respectively. The physical justification of this approximation is that almost all chemical properties of a solid are mainly related to the outermost (valence) electrons of an atom.

In the Born-Oppenheimer theory, the changes in the electronic orbitals, associated with the core electrons when an atom is moved from one environment to another, are assumed to be very small, and can therefore be neglected. In Eqn. (2.1), the many-body Hamiltonian can be expressed, in terms of the one-electron model, as the Hamiltonian of a single electron moving in the mean field potential $V(\boldsymbol{r})$, due to all other particles in the system, as well as due to any external potential acting on it. For a system of many electrons, under an external potential, V_{ext}, the Hohenberg-Kohn theorem [52] shows that:

(i) The external potential V_{ext} and total energy of the system E_{total} are unique functionals of the electron density $\rho(\boldsymbol{r})$, and

(ii) there exists a unique universal functional of the electron density $F[\rho(r)]$, which is independent of the external potential V_{ext}, such that the total energy $E[\rho(r)] = F[\rho(r)] + \int V_{ext}(r)\rho(r)dr$, has its minimum value at the correct ground state energy, where $F[\rho(r)] = \langle \psi_n | H | \psi_n \rangle$ is the ground state density functional of the one-electron Hamiltonian.

For a system under no external potential, let the electron Hamiltonian be expressed as

$$H = K + V_{ee} + V_{ei} \,, \tag{2.2}$$

so that it's n-th eigenfunction $|\psi_n\rangle$, corresponding to the eigenvalue of one electron energy level ε_n satisfies the relation

$$H|\psi_n\rangle = \varepsilon_n|\psi_n\rangle, \tag{2.3}$$

the basic idea of the tight binding (TB) model is to write the electron wave function $|\psi_n\rangle$, as a linear combination of atomic orbitals $|\phi_{ij}\rangle$, so that

$$|\psi_n\rangle = \sum_{ij} a_{ij}^{n}|\phi_{ij}\rangle . \tag{2.4}$$

In this case, l is an index that labels the quantum number and j labels the ions. The sum is over all occupied quantum states in a free atom or over all atoms in a solid in its ground state. The coefficients a_{lj}^{n} represent the eigenfunction of the n-th orbital, located at the j-th ion. In equation (2.4), the basis set of the atomic orbital $|\phi_{ij}\rangle$ does not always have to be orthogonal. Non-orthogonal basis sets can also be used, mainly to improve the transferability of the TB model. The use of non-orthogonal basis set leads to an improved and simplified parameterization of the tight binding Hamiltonian [53,54]. The transferability of the parameterization is ensured by incorporating the effects of the overlap between the different basis functions, and also by retaining the empirical nature of the TB model [55, 56].

In order to evaluate the energy band structure for a crystal, it is necessary to evaluate the diagonal matrix elements of the TB Hamiltonian, and the resulting overlap integrals [57], using the Bloch sum;

$$\langle\psi_n|H|\psi_n\rangle = N^{-1}\sum_{ij}\sum_{lm} a_{ij}^{n}\langle\phi_{lm}|H|\phi_{ij}\rangle , \tag{2.5}$$

where $\phi_{lm} = \phi_l(\boldsymbol{r} - \boldsymbol{r_m})$. The interatomic separation vectors can be denoted by $\boldsymbol{\rho_m} = \boldsymbol{r_m} - \boldsymbol{r_j}$, so that

$$\langle\psi_n|H|\psi_n\rangle = N^{-1}\sum_{n} exp(-i\boldsymbol{k}\cdot\boldsymbol{\rho_m})\int \phi^*(\boldsymbol{r} - \rho_m)H\phi(\boldsymbol{r})dV , \tag{2.6}$$

where $\boldsymbol{k}$ is an arbitrary wave vector, which does not necessarily imply that we are considering a periodic structure. In the two-centre approximation, all the integrals in Eqn. (2.6) are neglected, except those acting on the same atom and those acting between nearest-neighbour atoms with a separation ρ. In order to obtain the first-order energy, the evaluation of the integrals

$$\int \phi^{*}(\boldsymbol{r}) H \phi(\boldsymbol{r}) dV = -\beta \,; \tag{2.7}$$

and

$$\int \phi^{*}(\boldsymbol{r}-\boldsymbol{\rho}) H \phi(\boldsymbol{r}) dV = -\gamma \,, \tag{2.8}$$

is required in every step of the simulation, provided that $\langle \psi_n | \psi_n \rangle = 1$, where β gives the self energy, and γ gives the interaction energy. This increases the computational workload considerably. However, it is possible to orthogonalize the atomic orbitals $|\phi_{ij}\rangle$ in a way that the new basis set does not break the symmetry of their properties by using a new basis set $\{\phi_{ij}\}$, called the Löwdin orbitals [58]. The one-electron energy is given by

$$\varepsilon_n = \langle \psi_n | H | \psi_n \rangle = -\beta - \gamma \sum_{m} exp(i\boldsymbol{k} \cdot \boldsymbol{\rho}_m). \tag{2.9}$$

In a solid, the Schrödinger equation for the one-electron energy satisfies the secular equation

$$\sum \left(\langle \phi_{lm} | H | \phi_{l\alpha} \rangle - \varepsilon_n \delta_{ll'} \delta_{\alpha m} \right) a^{n}_{l'm'} = 0. \tag{2.10}$$

The matrix elements of the Hamiltonian entering the secular equation must be evaluated before the electronic structure problem can be solved satisfactorily.

The detailed justifications for using the TB approach in the simulation of covalent amorphous solids are presented Refs. [59-61]. In Ref. [62, 63], Weaire and Thorpe showed, that the electronic properties of tetrahedrally-bonded amorphous solids can be adequately described using the TB model. This model [64] correctly describes the existence of a gap [65], in the electronic density of states in elemental amorphous solids, which is also observed in *ab initio* studies [66, 67]. Subsequent studies [68, 69] of systems with compositional and topological disorder, using the TB model, also showed the preservation of this energy band gap. Furthermore, in Ref. [63], the TB model has been used to demonstrate that short-range topological disorder influences the electronic density of states. More recently, the TB model has been used to correctly account for the existence of mid-gap electronic states due to coordination defects, in tetrahedrally-bonded covalent semiconductors. In this formalism, the total energy is given by:

$$E^{total} = \sum_n \varepsilon + E_{rep} . \tag{2.11}$$

The first term describes the band structure energy, which is the quantum-mechanical bonding energy arising from the overlap of atomic orbitals. The band structure energy is evaluated as the sum of the approximate energies of all occupied electronic states. For the purposes of structural calculations, the band structure energy is the attractive part of the empirical potential. The second term is a two-body potential, which accounts for all other contributions to the total energy. This essentially represents the repulsive ion-ion interactions.

The calculation of the electronic structure becomes simplified if it is assumed that only a minimal basis set of atomic states is required, and these are states obtained from electronic shells which are partially occupied in free atoms. In most solids, these consist of the valence *s*- and *p*- states. The occupied electronic eigenstates and eigenvalues ε_n are obtained by minimizing the expectation value of the Hamiltonian for the state $|\psi_n\rangle$ with respect to the coefficients a_i. If the atoms remain neutral, when these electronic states are occupied by all the electrons present in the solid, the sum of the eigenvalues of the occupied states can be regarded as the total energy of the system. Physically, this means that the changes in the total energy of the system, as the atoms are rearranged or separated to form free atoms, is equal to the changes in the sum of occupied energy eigenvalues.

2.1.2 Band Structure Calculation

Within the semi-empirical TB model, the matrix elements entering the secular equation are obtained by fitting the atomic term values and hopping parameters to a database of experimental or first principles calculations of energy bands. A number of approximations are required to simplify the calculations. These are:

(i) a minimal basis set is used to describe bonding in Si due to sp^3 hybridization of atomic orbitals;

(ii) interactions between nearest neighbours are always short-ranged;

In order to proceed with the calculation of the occupied energy eigenvalues for the different bonding geometries in *a*-Si, it is necessary to obtain approximate values for the elements of the Hamiltonian matrix in the chosen basis of the atomic states.

These parameters include the Herman-Skillman atomic term values describing the Si self-energies, ε_s and ε_p for the *s* and *p* states [70]. These represent the diagonal elements of the TB Hamiltonian matrix, and are taken to be the same as the Hartree-Fock free-atom term values. When hydrogen is incorporated into the *a*-Si system, the atomic-term values for the hydrogen self-energy ε_s are also specified. The TB parameters also include an energy term $H_{ll'm}$, which accounts for the overlap interaction or coupling between electronic states on neighbouring atoms. These interatomic matrix elements are represented by the off-diagonal elements of the TB matrix.

In *a*-Si, because the bonding geometry in Si does not involve second neighbour bonds, these couplings can be neglected except for nearest-neighbour atoms. In the two-centre approximation [71,72], the nearest-neighbour couplings in solids have been shown to have the universal form [73-75]:

$$H_{ll'm} = \eta_{ll'm} \frac{\hbar^2}{md^2}, \qquad (2.\ 12)$$

where η is an energy term that describes the strength of the covalent bond between interacting neighbours, and *d* is the distance between any two interacting atoms. The first two subscripts indicate the angular-momentum quantum number of the atomic state, and the third indicates the angular momentum component *m* of the two states around the inter-nuclear axis. The parameter *m* is denoted by either σ if the magnitude of the angular momentum of the two states around the inter-nuclear axis is zero, or by π if it is equal to one. Eqn (2.12) is the hopping or bond integral. It is an empirical parameter, and should not be confused with $\langle \psi_n | H | \psi_n \rangle$, which gives the Hamiltonian matrix elements.

The exact forms of the nearest neighbour couplings are obtained by fitting an analytic form to values obtained from band structure calculations on semiconductors. It has been realized [76] that the form of the coupling in Eqn. (2.12) arises from the fact that semiconductor band structures could be well described using the tight-binding theory, but yet they are also very similar to free-electron band structures. The set of four interatomic coupling parameters, and the atomic term values, are all the parameters needed for the electronic structure calculation, and therefore to compute the properties of systems like *a*-Si and *a*-Si:H.

The use of the tight-binding formalism to parameterize electron band structures in covalent solids originated from the work of Slater and Koster [71]. This approach has been successfully applied to silicon in different states in several studies [77-83]. When this parameterization is supplemented with information on how the associated hopping parameters vary with interatomic separation, it becomes possible to construct total-energy functionals of the atomic positions [37]. The evaluation of the total-energy in a molecular dynamics simulation requires explicit interatomic potential functionals [84-96]. In this study, we are interested in the use of such a total-energy representation to account for the interatomic forces that give rise to structural relaxation during the tight-binding molecular dynamics simulation [97,98]. This provides the theoretical basis for the description of the bulk and electronic properties of different structural models of amorphous silicon.

The analytic bond order potential (BOP) for Si [34-36] is in principle, a better option for modelling the interatomic potential in *a*-Si. However, its use in modelling ionic interactions in a binary system is relatively new, and has only been reported for GaAs [36]. Furthermore, the full analytic BOP model requires 22 fitting parameters, and the determination of such parameters for *a*-Si:H is beyond the scope of the present study. Moreover, even for the simple case of elemental silicon, the full analytic BOP requires 19 fitting parameters [99], in contrast to the GSP model [38] which requires only 13 for the same system. The

GSP model suffices for the simulations reported in this thesis because it is computationally efficient and predicts physical properties which agree with *a priori* expectations, for tetrahedrally-bonded systems.

In order to model the interatomic interactions in *a*-Si, we start from the interatomic potential model developed in Refs. [93-96]. Here, the tight binding parameters, taken from Refs. [75-80], are combined with the short-range scaling function modification of the distance dependence of TB parameters proposed in the GSP model [38], to determine the TB Hamiltonian matrix elements. These matrix elements are determined in terms of the two-centre hopping parameters [100] as

$$H_\alpha\left(r_{ij}\right) = H_\alpha(1)\left(\frac{r_0}{r_{ij}}\right)^n \exp\left\{n\left[-\left(\frac{r_{ij}}{r_c}\right)^{n_c} + \left(\frac{r_0}{r_c}\right)^{n_c}\right]\right\}. \tag{2.13}$$

The hopping coefficients, $H_\alpha\left(\frac{r_0}{r_{ij}}\right)$ are the distance-dependent tight binding matrix elements, and $H_\alpha(1)$ are constant energy terms that prescribe the covalent bonding energy at equilibrium interatomic separation. r_0 and α represents the four possible types of interatomic hopping: *ssσ*, *spσ*, *ppσ*, and *ppπ*. The dimensionless parameter *n*, describes the hopping exponent. In Ref. [101] it was shown, that the total energy obtained from this model is accurate in reproducing the universal binding energy curves of different phases of bulk silicon, which agree with results obtained from first principles studies.

2.1.3 Si-Si Repulsive Interaction

There are no elemental impurities in hydrogen-free *a*-Si, and hence, there is no compositional disorder. The only interacting species of atoms is Si, and only Si-Si interactions have to be taken into account. In this study, the GSP model is adopted for modelling Si-Si interactions because it has been shown in numerous studies [101-108] that it correctly describes the local bonding environment in many forms of bulk silicon. The main idea of the GSP model is to improve the transferability [38] of the fitted TB parameters of Chadi [75-78] by introducing an exponential scaling function into the Harrison's universal r^{-2}

scaling [58] of the TB hopping parameters and the repulsive pairwise interaction. In the GSP model, the scaling function describing the dependence of the repulsive interaction, on interatomic separation r_{ij}, is similar in form to that of the hopping parameters of the TB Hamiltonian matrix elements. Hence the Si-Si pair potential is given by:

$$\phi^{\text{Si-Si}}\left(r_{ij}\right) = \phi^{\text{Si-Si}}(1)\left(\frac{r_0}{r_{ij}}\right)^{\mathrm{m}} exp\left\{m\left[-\left(\frac{r_{ij}}{r_c}\right)^{\mathrm{m_c}} + \left(\frac{r_0}{r_c}\right)^{\mathrm{m_c}}\right]\right\}. \tag{2.14}$$

The pair potential exponent m, and other fitting parameters m_c and r_c are adjusted to obtain the Si-Si binding energy of 2.5 eV at the equilibrium interatomic separation of 2.35 Å. This model of the interatomic potential retains the GSP form, and is useful for the present purpose to simulate the *a*-Si structure from a starting structure of crystalline silicon. An important feature of the GSP model is, that the total repulsive energy for a system of interacting atoms is a nonlinear functional of the sum of the repulsive pair potentials between the reference atom and its neighbours:

$$E_{rep} = \sum_i F\left(\sum_{i,j\neq i}\phi(\mathbf{r}_{ij})\right), \tag{2.15}$$

where $\mathbf{r_{ij}} = \mathbf{r_j} - \mathbf{r_i}$ is the separation vector between atoms *i* and *j*, and $\phi(\mathbf{r_{ij}})$ is the repulsive pair potential between atoms *i* and *j*. *F* is a polynomial used in fitting the hopping coefficients to ensure that the interatomic interactions are short-ranged and therefore preserve the Si-Si bond length.

2.1.4 Si-H Repulsive Interaction

In order to model bulk *a*-Si:H, it is important to note that there are three types of ionic interactions, Si-Si, Si-H and H-H, because of the introduction of hydrogen to the structure. In modelling the interaction of silicon atoms with hydrogen, we retain the GSP form such that

$$\phi^{\text{Si-H}}\left(r_{ij}\right) = \phi^{\text{Si-H}}(1)\left(\frac{r_0}{r_{ij}}\right)^{\mathrm{m}} exp\left\{m\left[-\left(\frac{r_{ij}}{r_c}\right)^{\mathrm{m_c}} + \left(\frac{r_0}{r_c}\right)^{\mathrm{m_c}}\right]\right\}, \tag{2.16}$$

and the hopping parameters for Si-H TB Hamiltonian matrix retain the same scaling form of the GSP model as in Si-Si interactions. However, Li and Biswas have shown [39], that when hydrogen is introduced into *a*-Si, the total repulsive energy is no longer a nonlinear functional of the sum of pair potentials. In fact, it is no longer clear what percentage of the Si-H and H-H interatomic potentials are to be included in the operand of Eqn. (2.15). The fractions to be used depend largely on the partitioning of the pair potentials between individual atomic species. In this study, it will be demonstrated that this partitioning is highly dependent on the concentration of hydrogen C_H.

It has been shown in Ref. [39], that the total repulsive energy for a system of interacting Si-H atoms can be partitioned into two parts:

(i) a fraction of the Si-H repulsive potential *c*, is included in the Si-Si repulsive energy functional, and

(ii) the remaining fraction (1-*c*), which is treated independently, so that the total repulsive energy is

$$E_{rep} = \sum_i F\left[\left(\sum_{i,j\neq i}\phi^{\text{Si-Si}}(r_j - r_{\text{i}})\right) + \text{c}\sum_{i,k\neq i}\phi^{\text{Si-H}}(r_k - r_i)\right] + (1-c)\sum_k^{\text{H}}\sum_i^{\text{Si}}\phi^{\text{Si-H}}(r_k - r_i)\,. \qquad (2.17)$$

The first term in Eqn. (2.18) is the modified Si-Si repulsive interaction. In this case, i and j represent near neighbour silicon atoms, and k denotes hydrogen atoms. The GSP model defines only the difference between the Si self energies, E_{s} and E_{p}, and not their absolute values. This important feature of the GSP model allows for the systematic partitioning of contributions to the total repulsive potential, since it is no longer a linear function of the Si-Si interaction.

In order to introduce the hydrogen TB parameters, some energy reference has to be chosen to preserve some well-known properties of the Si-H system. This reference is chosen in this work such that:

(i) if $c = 0$, the difference in Si self energy ΔE_{sp} is 8.30 eV, and;

(ii) if $c > 0$, the equilibrium Si-H bond length is 1.475 Å with a Si-H binding energy of 3.53 eV.

This value of the binding energy agrees very well with the experimental binding energy of ~3 eV reported in Refs. [109,110]. Since the H atom has only one *s* orbital, only three TB parameters are required for the electronic structure calculation. These three parameters are the orbital energy ε_s, and the magnitudes of the two overlap integrals $H_{ss\sigma}^{SiH}$ and $H_{sp\sigma}^{SiH}$, between Si and H.

These overlap integrals were determined at the equilibrium Si-H bond length, by adjusting the *c* parameter of the LB functional to preserve the energies of the two occupied molecular orbitals $a_1^+ = -18.20$ eV and $t_2^+ = -12.70$ eV, and the symmetric bond bending vibrational wave number of 976 cm^{-1} of the silane molecule [111]. The resulting TB parameters for the Si-H interactions are consistent with those of Kim *et al.* [109], with the exception of $\phi^{\mathrm{Si-Si}}(\mathrm{l})$ obtained as 3.4581 eV in agreement with the TB parameters of the original GSP model. The cutoff distances for the Si-Si interaction and Si-H interaction are set to 3.50 Å and 2.00 Å respectively, to ensure that the matrix elements of the TB Hamiltonian are not truncated too quickly. This allows for structural relaxations and changes in the local bonding environment to be preserved, even for high concentrations of hydrogen in amorphous silicon.

2.1.5 H-H Repulsive Interaction

The contributions of H-H interactions to the total repulsive energy can be ignored without violating energy requirements in an MD simulation of hydrogen in amorphous silicon if the concentration of hydrogen C_H, is very low. In this work, H-H interactions have been ignored at low C_H mainly because H-H interactions would yield molecular hydrogen, which is not part of the structural network of *a*-Si:H. This approximation holds also for Si-H systems where the H-H distance is large, for example in monohydride phase on the Si(111) surface, where the H-H distance is 3.84 Å [96,112]. This situation would be consistent with the fact that most of the hydrogen atoms found in typical *a*-Si:H networks exist only in bonded configurations, and not in molecular form. However, when C_H is permitted to be as high as 25% in *a*-Si, as will be simulated in this study, this situation is complicated due to energy requirements.

In Si-H systems, where models of H-H interactions are required, such as in the case where either the dihydride or trihydride phase exists on the Si(111) surface, it is necessary to minimize the H-H distance to either 2.20 Å or 2.40 Å [112], to enhance the H-H binding. On the other hand, in cases where metastable (bistable) diatomic hydrogen $\left(\mathrm{H}_2^*\right)$ are permissible [113], such as in the microscopic model of describing the Staebler-Wronski effect, the H-H distance must be minimized to permit the formation of molecular hydrogen. The H-H binding is achieved by minimizing the total repulsive energy in each case, by adjusting the c - parameter of the LB functional for the total repulsive energy. The GSP form is retained for the H-H interatomic potential as follows,

$$\phi^{\mathrm{H-H}}\left(r_{ij}\right) = \phi^{\mathrm{H-H}}(1)\left(\frac{r_0}{r_{ij}}\right)^{\mathrm{m}} exp\left\{m\left[-\left(\frac{r_{ij}}{r_c}\right)^{\mathrm{m_c}} + \left(\frac{r_0}{r_c}\right)^{\mathrm{m_c}}\right]\right\}. \tag{2.18}$$

In this case, the constant energy term, $\phi^{\mathrm{H-H}}(1) = 3.50$ eV, was obtained by fitting the hydrogen TB hopping parameters to the energy of the stretching mode of molecular hydrogen at the equilibrium H-H bond length. In this work, the vibrational energy measured for the stretch-mode of molecular hydrogen in the tetrahedral interstitial site in Si [114] was used, instead of the value in the gas. The above fitting procedure explicitly incorporates the physics of the interaction of H_2 with Si by including the influence of anharmonic effects on the vibrational frequency of free H_2 molecule [115]. The TB parameters used for the Si-H systems considered in this study are presented in Table 2.1

Table 2.1: The TB parameters of the Si-H system used in the simulations

TB parameters	**H-H**	**Si-Si**	**Si-H**
$H_{ss\sigma}(1)$	-7.59	-1.82	-3.54
$H_{sp\sigma}(1)$		1.96	5.09
$H_{pp\sigma}(1)$		3.06	
$H_{pp\pi}(1)$		-0.87	
r_0	0.74	2.35	1.48
r_c	1.60	3.67	2.19
n	2.18	2.00	1.97
n_c	14.00	6.48	13.27
m	4.22	4.54	2.26
m_c	14.00	6.48	13.27
$\phi(1)$	3.50	3.46	3.01
ε_s		-13.10	-8.34
ε_p		-4.80	
c	0.27	0.00	0.12

2.1.6 Simulation Parameters for the C-H System

The local structure of hydrogenated tetrahedral amorphous carbon (*ta*-C:H) was also modelled, using a similar tight binding formulation for the Hamiltonian matrix elements and interatomic interactions. The TB parameters for C-C interaction were taken directly from Xu *et al.* [116]. The distance-dependent two-centre hopping parameters between the *s* orbital of hydrogen and the *s* and *p* orbitals of carbon, denoted by $H_{ss\sigma}$ and $H_{ss\pi}$, were obtained by fitting the carbon TB hopping parameters to the electronic energy levels of the occupied molecular orbitals of methane for different interatomic distances, $r_{\text{H-C}}$. At low hydrogen concentration, the on-site energy, and TB parameters for C and H are unchanged from those of Refs. [117,118], but the *c*-parameter was set to 0.12, so that the H-H interaction was ignored. However, at high hydrogen concentrations, where the H-H interaction is nontrivial, the TB parameters for H-C interaction were determined by adjusting the *c*-parameter of the LB functional for total repulsive energy to preserve:

(i) the cohesive energy of 17.6 eV [118,119];

(ii) the energies of 0.190 eV and 0.1625 eV, corresponding to the symmetric and antisymmetric bond bending vibrational modes in methane [120].

In this case, the cohesive energy is defined as the increase in energy per mole of the material if all intermolecular forces are eliminated [121]. A similar approach has been successful in modelling the interaction of hydrogen with carbon surfaces [122], and with bulk tetrahedral amorphous carbon [123].

The main difference in the work presented here is that the c - parameter of the LB functional is adjusted, to preserve the cohesive energy of methane before fitting to vibrational and electronic energy levels, instead of fitting only the two-centre electronic parameters and scaling functions to the occupied eigenvalues of methane over a range of distances. The resulting parameters are listed in Table 2.2. It should be noted that structural adjustments and supercell energy requirements significantly limit the number of molecular hydrogen in the structure at high hydrogen concentration. The choice of the LB functional for the total repulsive energy conveniently allows for a scaling of the total energy to satisfy bonding requirements in *a*-Si:H and *ta*-C:H through the adjustable parameter c. In modelling C-H systems, the choice $c = 0$ leads to results of the original calculation of Ref. [116], where only C-C interactions are allowed. Bonded hydrogen

able 2.2: The TB parameters of the C-H system used in the simulations.

TB parameters	**H-H**	**C-C**	**C-H**
$H_{ss\sigma}(1)$	-0.44	-5.00	-6.54
$H_{sp\sigma}(1)$		4.70	6.81
$H_{pp\sigma}(1)$		5.50	
$H_{pp\pi}(1)$		-1.55	
r_0	2.14	1.54	1.09
r_c	0.71	2.18	1.19
n	0.45	2.00	0.59
n_c	1.57	6.50	3.20
m	1.02	3.30	2.26
m_c	0.85	8.67	13.27
$\phi(1)$	0.06	8.19	11.50
ε_s	-4.75	-2.99	-8.34
ε_p		3.71	
c	0.27	0.00	0.12

geometries are only obtainable at low and moderate concentrations of hydrogen, C_H, where c = 0.12. At very high C_H (18-25%), where molecular hydrogen is permissible, the c parameter is 0.27.

2.2 Tight Binding Molecular Dynamics Simulations

Molecular dynamics (MD) simulation is a statistical mechanics method in which the computer is used to generate atomic trajectories of a system of N atoms by numerical integration of Newton's equation of motion for a given interatomic potential, with specified initial conditions and boundary conditions [124]. The atomic trajectories are computed in a $6N$ dimensional phase space, which consists of $3N$ positions and $3N$ momenta. In MD simulations, the set of configurations of the system of atoms are distributed according to a prescribed statistical distribution function of initial condition, so that at sufficiently long simulation times, the phase space is fully sampled, and the averaging procedure yields the thermodynamic limit of the material property, provided the interatomic potential correctly describes the local structure in the material. The physical quantities are therefore obtained as averages over configurations which are distributed according to a given statistical ensemble.

In a conventional MD simulation, the time evolution of a system of atoms is usually followed by solving the classical equations of Newtonian mechanics for the trajectory of the atoms. This is usually achieved by integrating the equations of motion using a suitable time-integration algorithm. The algorithm for time integration is based on the finite difference method, where the simulation time is partitioned into discrete time steps on a time grid. The duration of one MD step, Δt is the basic distance between two consecutive points on the time grid. If the positions of atoms and the time derivatives of these positions, *i.e.* the velocities and accelerations are determined at time t, using a given time integrator algorithm, the integration scheme will give the same set of quantities at a later time $t+\Delta t$. The time evolution of the system can then be followed for a long time interval by iterating the procedure over a large number of time steps.

In Refs. [125,126], a few numerical methods of integrating the Newton's equations of motion, such as the leapfrog algorithm, the Gear's predictor-corrector algorithm, and the Verlet algorithm have been discussed. In this work, the Verlet algorithm is used, because of its computational efficiency and stability at very short time steps. Nonetheless, these schemes are only approximate methods of time integration, and are susceptible to statistical errors. These statistical errors include, firstly, truncation errors which are related to the accuracy of the finite difference method relative to the true solution. Truncation errors arise because finite difference calculations are based on a Taylor series expansion, which must be truncated at an arbitrary chosen term. Therefore truncation errors do not depend on the computer implementation, but are intrinsic to the time integrator algorithm used. Secondly, MD schemes are susceptible to round-off errors, which are associated with the finite number of digits used in the computer arithmetic in a particular implementation of any given time integrator algorithm.

In a tight binding molecular dynamics (TBMD) simulation, the matrix elements of the Hamiltonian matrix entering Eqn. (2.10) are evaluated, at every time step, in order to provide the forces required to displace atoms from their equilibrium position. These forces are evaluated in terms of the expectation values of the TB Hamiltonian as

$$F_\alpha = -\sum_{\mathrm{n}} f(\varepsilon_n, T)\langle\psi_n|\frac{\partial H}{\partial r_\alpha}|\psi_n\rangle - \frac{\partial E_{rep}}{\partial r_\alpha}, \tag{2.19}$$

where the function $f(\varepsilon_n, T)$ is the Fermi-Dirac distribution function for occupied electron states. The first term gives the attractive forces, which are defined to be equivalent to the Hellman-Feynman forces, discussed later, in section 4.3. These are calculated [127] as

$$-\sum_n f(\varepsilon_n, T)\langle\psi_n|\frac{\partial H}{\partial r_a}|\psi_n\rangle = -2\sum_n f(\varepsilon_n, T)\sum_{l\gamma}\sum_{l'\beta} c^n_{l'\beta} c^n_{l\beta}\,\frac{\partial H_{l'\beta l\gamma}(r_{l\beta})}{\partial r_a}. \tag{2.20}$$

In Eqn. (2.20), the second term represents the repulsive forces, and is obtained by differentiating the repulsive energy with respect to the interaction distances. The repulsive forces are determined in a computationally efficient manner by differentiating the repulsive energy, since the interatomic potentials for Si-Si; Si-H and H-H interactions are known short-ranged functions of position.

The full TBMD Hamiltonian, for the hydrogenated system, was obtained as the sum of the classical kinetic energy of the ions, the quantum mechanical electronic energy, and the classical short range repulsive energy as,

$$H = \frac{1}{2} m_i \sum_i v_i^2 + \sum_i f(\varepsilon_i, T)\langle\psi_i|H|\psi_i\rangle + \sum_i F\left[\left(\sum_{i,j\neq i}\phi^{Si-Si}(r_j - r_i)\right) + c\sum_{i,k\neq i}\phi^{Si-H}(r_k - r_i)\right] + (1-c)\sum_k^{H}\sum_i^{Si}\phi^{Si-H}(r_k - r_i). \qquad (2.21)$$

Hence, when the structure contains no hydrogen, c = 0, and the above expression simplifies to

$$H = \frac{1}{2} m_i \sum_i v_i^2 + \sum_i f(\varepsilon_i, T)\langle\psi_i|H|\psi_i\rangle + \sum_i F\left[\left(\sum_{i,j\neq i}\phi^{Si-Si}(r_j - r_i)\right)\right], \qquad (2.22)$$

where $f(\varepsilon_i, T)$ denotes the Fermi-Dirac distribution function, for the occupied energy states at a temperature T.

To solve the classical equations of motion, the two, third-order Taylor series expansion of the displacement vector $\boldsymbol{r}$(t), were evaluated with respect to time. For the forward shift in time $+\Delta t$,

$$\mathbf{r}(t+\Delta t) = \mathbf{r}(t) + \frac{d}{dt}\mathbf{r}(t)\Delta t + \frac{1}{2}\frac{d^2}{dt^2}\mathbf{r}(t)(\Delta t)^2 + \frac{1}{6}\frac{d^3}{dt^3}\mathbf{r}(t)(\Delta t)^3 + \frac{1}{4!}\frac{d^4}{dt^4}\mathbf{r}(t)(\Delta t)^4 + \dots . \qquad (2.23)$$

Similarly, for the backward shift in time $-\Delta t$,

$$\mathbf{r}(t-\Delta t) = \mathbf{r}(t) - \frac{d}{dt}\mathbf{r}(t)\Delta t + \frac{1}{2}\frac{d^2}{dt^2}\mathbf{r}(t)(\Delta t)^2 - \frac{1}{6}\frac{d^3}{dt^3}\mathbf{r}(t)(\Delta t)^3 + \frac{1}{4!}\frac{d^4}{dt^4}\mathbf{r}(t)(\Delta t)^4 + \dots \qquad (2.24)$$

The velocity form of the Verlet's algorithm was obtained from Eqns. (2.23) and (2.25) as:

$$\mathbf{r}(t+\Delta t) = 2\mathbf{r}(t) - \mathbf{r}(t-\Delta t) + \frac{d^2}{dt^2}\mathbf{r}(t)(\Delta t)^2 + \frac{1}{4!}\frac{d^4}{dt^4}\mathbf{r}(t)(\Delta t)^4 + \dots, \qquad (2.25)$$

where $\mathbf{a}(t) = \frac{d^2}{dt^2}\mathbf{r}(t)$ is the acceleration. Newton's equation of motion, $\mathbf{a}(t) = \frac{1}{m}(\mathbf{F}(t))$, was integrated numerically, using the resultant forces obtained from Eqn. (2.19).

The above simulation scheme, leads to the conservation of total energy and momentum of particles in the simulation box. These simulations were performed in the *microcanonical* (or NVE) ensemble, since the number of atoms, the volume of the simulation box and the total energy are constant. It was also possible to perform simulated annealing or quenching, where the temperature, and kinetic energy of ionic motion, was constantly re-scaled to the simulation time. This was done, in the *canonical* (or NVT) ensemble, by introducing a time-dependent frictional term, whose time evolution is driven by the imbalance between the instantaneous kinetic energy, and the average kinetic energy, given by $\frac{1}{2}\sum_i m_i v_i^2 = \frac{3}{2}KT$. The algorithm adopted for the implementation of the tight binding molecular dynamics simulations is presented in Fig. 2.1 as a flow chart.

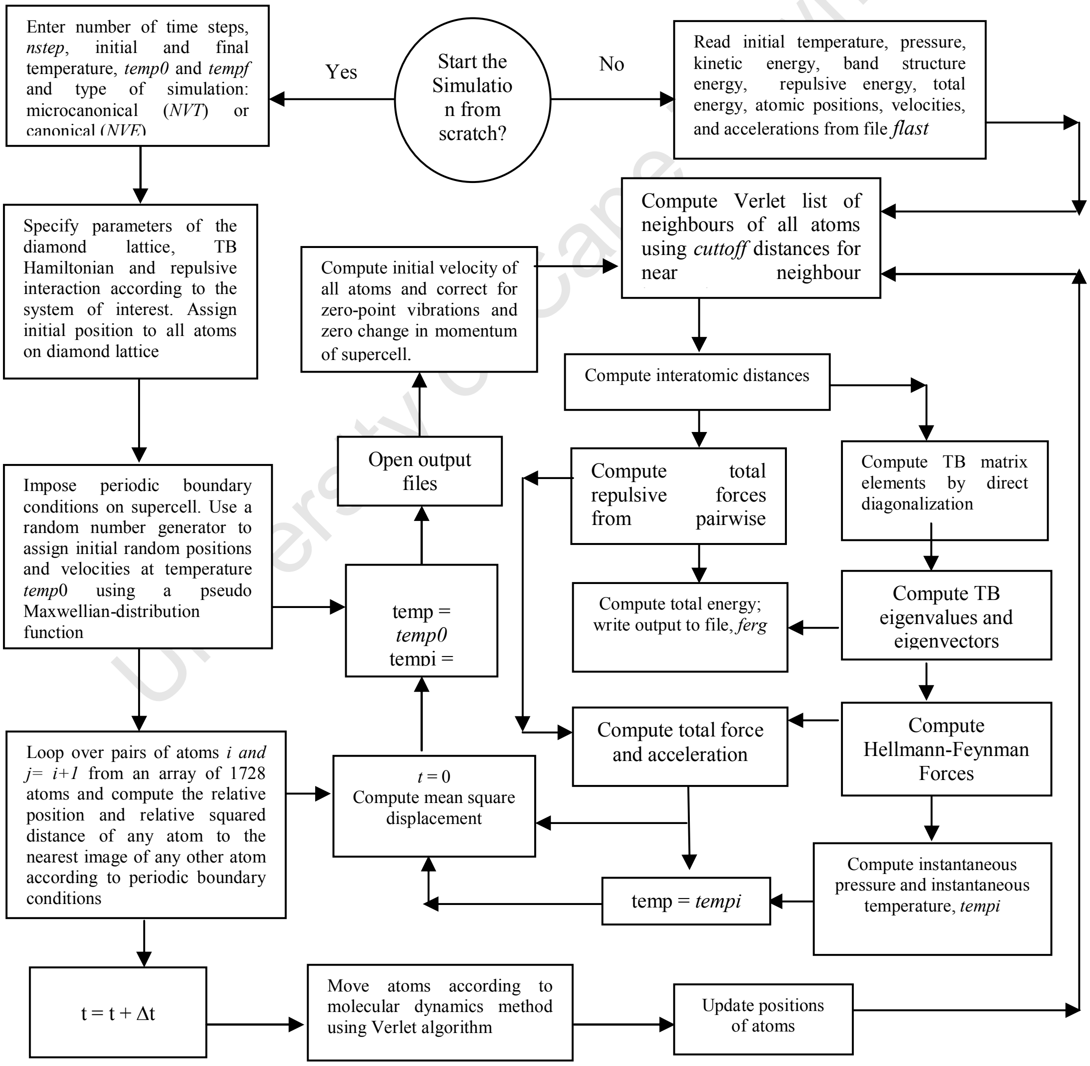

Figure 2.1 Block diagram showing the transfer of controls and data flow in the computer implementation algorithm of the tight binding molecular dynamics simulations.

2.2.1 Variable Supercell Method

The number of atoms in a real solid is typically in the order of 10^{23} atoms. The supercell method allows us to model such a large system successfully, by reducing it to a system of manageable size, which can be handled effectively by the available computing resources. In this method, a cluster of atoms is defined in an appropriate lattice, such that it is equivalent to the unit cell in the real solid, and then repeated in real space, without gaps and overlaps, by imposing periodic boundary conditions [128]. The imposition of periodic boundary conditions to the supercell does not automatically result in a translational symmetry of atomic positions, within the supercell, when this method is used to model amorphous structures. This is achieved by randomizing the initial positions of all the atoms in the supercell using a random number generator.

The use of the supercell method in structural studies was first employed in the investigation of structural defects in crystalline materials [129-131], and later extended to disordered materials [132]. In this study, the simulation box contains a total of (N_{Si} + N_H) atoms, N_{Si} silicon and N_H hydrogen atoms at constant volume, subject to periodic boundary conditions. The simulation starts with an initial supercell containing N_{Si} silicon atoms, placed in a perfectly ordered diamond structure at 300 K, with N_{H} set to zero. For the pure *a*-Si structure, this large supercell is obtained by repeating the conventional diamond cell, which contains eight Si atoms per cell, in all three directions. In order to hydrogenate the *a*-Si structure to produce *a*-Si:H, with variable concentrations of hydrogen in the supercell, the number of atomic species N_{Si} and N_H is varied using the scheme of Ref. [133].

The variable-atom supercell technique is a numerical method to obtain a simulation box with variable number of atoms in it, to achieve bulk structures with variable mass density. This method is adapted within the TBMD simulations scheme to account for the variable number of valence electrons in the simulated systems, by adjusting the total number of valence electrons. In terms of the hopping parameters of the TB Hamiltonian matrix, the total number of valence electrons is correspondingly set to ($4\times N_{Si}$ + $1\times N_H$), and the occupied eigenstates, and the corresponding eigenvectors are obtained by direct diagonalization of the tight binding (TB) Hamiltonian matrix using the standard eigensolvers from the open-source mathematical routines of the LAPACK library. The total energy is evaluated during the MD cycle as the sum of the band structure energy and the total repulsive energy. The forces are evaluated at every step of the MD simulation to search for a suitable global energy minimum, before properties of the system are computed.

Apart from the incorporation of hydrogen, the variable-atom supercell approach is also adapted for creating vacancy-like defects of variable sizes. This approach is also modified to simulate hydrogen-decorated defect complexes. Large-sized open volume defects were also created, and treated as a coalescence of vacancies. This is achieved by randomly deleting one silicon atom from a tetrahedral site, or by deleting a cluster of silicon atoms from the supercell.

2.2.2 Simulation of Hydrogen-Free Amorphous Silicon

All the silicon atoms in the supercell were initially placed on tetrahedral sites of the diamond structure in *c*-Si. Denoting the number of silicon and hydrogen atoms in the supercell with N_{Si} and N_H respectively, the number of hydrogen atoms was initially set to zero. The dimensions of the supercell was set to $10a_o$, where a_o = 5.43Å, the equilibrium lattice parameter of *c*-Si. This lattice parameter was chosen for the starting configuration in order to set the density to 2.33 gcm^{-3} [134]. Assuming a pseudo-Maxwellian distribution of speeds as a function of temperature, a random number generator was used to assign initial random positions and random speeds to the Si atoms in the supercell, subject to a maximum displacement from their equilibrium positions of 0.02 Å.

The initial supercell was heated to 3000 K in the canonical ensemble scheme, where the velocity and kinetic energy of ionic motion are constantly rescaled to the simulation temperature [135]. In the *NVT* simulation, the volume of the supercell $(10a_o)^3$, is chosen at the start of the simulation, by fixing the length of the cubic simulation box *l*, which remains unchanged throughout the simulation. It is clear from this, that a wide range of thermal energies was allowed during the initial process of heating. As the simulation time increases, the temperature of the supercell also increases, until the structure melts, without a change in volume of the simulation box. The resulting Newton's equations of motion were integrated using the velocity form of the Verlet algorithm with a time step Δt = 1fs. All interactions for separations beyond 3.50 Å were cutoff.

In order to test the suitability of the TB model used in the simulations, the mean square displacement (MSD) has been computed to predict the melting temperature of *c*-Si. The MSD of Si atoms from their initial equilibrium positions are shown in Fig. 2.2 as a function of instantaneous temperatures between the time the simulation started (T = 300 K), and the time the resulting liquid silicon (*l*-Si) was equilibrated (T = 3000 K). This is to demonstrate how high (or low) the *l*-Si temperature of 3000 K is, relative to the projected melting point of *c*-Si in the TB model proposed in this thesis. It is reckoned that, because the atoms are confined to a finite simulation box of fixed size, the plateau in the MSD shows the region of phase transition, which occurs between 1650 K and 1800 K. On this basis, it was deduced that the average melting point of the starting *c*-Si structure predicted, using the present TB formalism, is 1725 K. Taking pressure variations into consideration, since the simulations are done at constant volume, this melting point is in qualitative agreement with the experimental melting point of *c*-Si, which is typically 1687 K [136].

Furthermore, for comparison with other well-established models, the distribution of triplet correlation angles in the disordered *l*-Si structure was computed. Fig. 2.3 shows the distribution of the triplet correlation angle $g(\theta)$ at 3000 K, as a function of $\cos\theta$. A comparison of our *l*-Si properties with the properties of *l*-Si obtained in the TB model of Virkkunen *et al.* [136] shows, that the present formulation yields *l*-Si structures which show better agreement with first principles calculations presented in Ref. [137]. The triplet correlation function of the structure, melted at 3000 K, is also in good agreement with the results of the bond angle distribution in Ref. [100] for *l*-Si, and indicates a preferential correlation angle of slightly under 60°. The liquid silicon structure is equilibrated for 2 ps over 2000 MD time steps, over which a structure with minimum total energy is obtained, before it is finally quenched dynamically from 3000 K to 300 K, at the rate of 2.7×10^{17} K/sec over a duration of 10 ps.

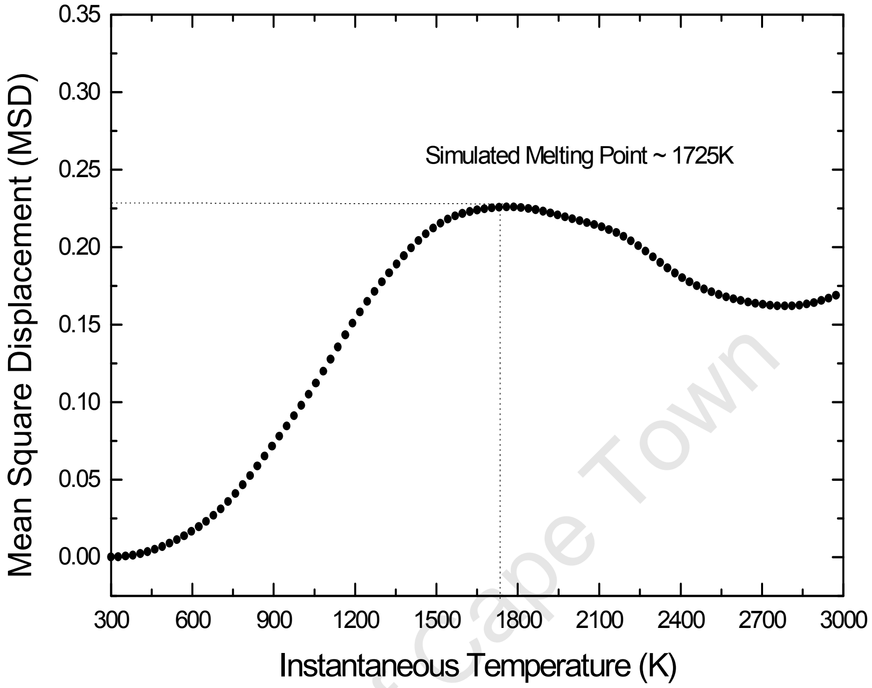

Figure 2.2 Mean square displacements of Si atoms from their equilibrium position, showing a projected melting point of 1725 K in qualitative agreement with the experimental melting point of *c*-Si.

The resulting structure inherently contains a very high number of three-fold (17%) coordinated sites and some five-fold (3.2 %) sites. In order to further reduce the number of these native defects, and to ensure that the resulting *a*-Si structure loses all memory of the crystallinity of the starting structure, it is further annealed to a temperature of 1500 K over a time of 1ps, before finally cooling down to 300 K. The resulting structure constitutes the hydrogen-free *a*-Si structure, used as the starting point for the selective hydrogen incorporation [138]. The average coordination number increases from 4.0, for the starting *c*-Si, to 4.16 for the hydrogen-free *a*-Si network. The total energy of the resulting *a*-Si is minimized over 5000 MD time steps, leading to a structure which is stable at 300 K, with changes in total energy less than 6.21×10^{-5} eV.

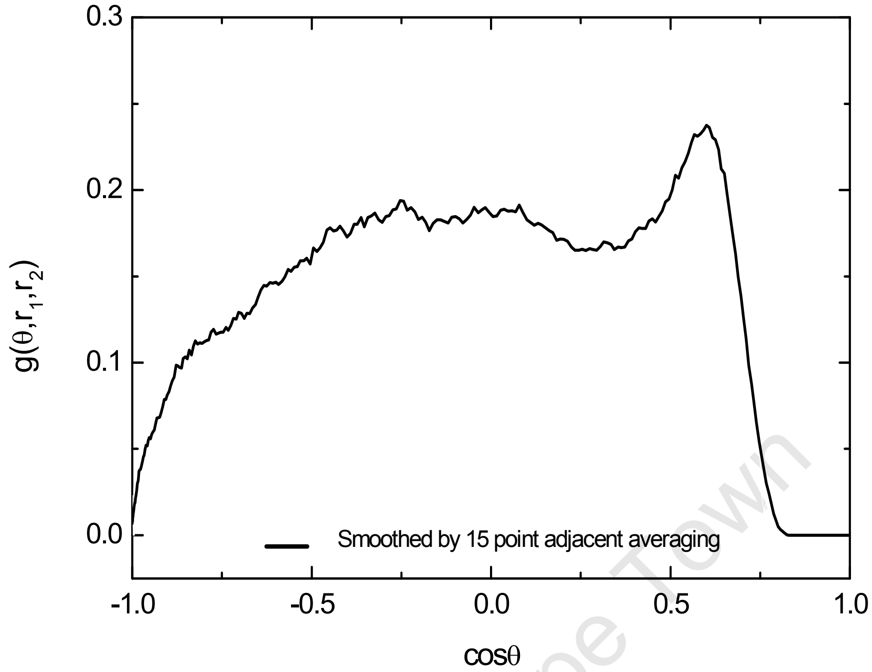

Figure 2.3 Liquid silicon (*l*-Si) triplet correlation angle $g(\theta)$ at 3000 K plotted as a function of the cosine of the correlation angle θ.

2.2.3 Incorporation of Hydrogen

The methods of producing computer models of *a*-Si:H fall into two broad categories [139]. These are:

(i) "dynamic" methods, where an initial cell of atoms (*typically c-Si*) is annealed and then quenched; and
(ii) "static" methods, where atoms are initially arranged in a cell via a predetermined geometric algorithm and then relaxed.

The present scheme of generating *a*-Si:H combines these two methods. This approach is motivated by three well-known facts. Firstly, in a liquid-quench simulation to produce pure *a*-Si, calculations usually start with a given 'sample' of liquid silicon, which is inherently highly disordered. A rapid simulated-quench of such a structure, to obtain a local minimum in the total energy, yields a disordered structure with a relatively large number of coordination defects, just as obtained in this work. Secondly, if a simulation starts with a lesser disorder relative to *c*-Si, a quench, to find total energy minimum, will yield crystalline silicon, with no coordination defects. Thirdly, hydrogen can be incorporated into *a*-Si networks using a static method. In such cases an incompletely melted structure of *c*-Si is chosen as a suitable starting point for simulating *a*-Si, to ensure that there are few coordination defects in the resulting amorphous silicon network.

Using the resulting atomic coordinates of the simulated pure structure, hydrogen is selectively incorporated into the network at 3-fold and 5-fold sites using the static algorithm of Ref. [138]. For the simulations reported here, the number of hydrogen atoms N_H, was set to 52, 86, 138, 173, 225, 259, 311, 346, 397 and 432 in each case, and the corresponding number of silicon atoms N_{Si} was reduced to 1676, 1642, 1590, 1555, 1503, 1469, 1417, 1382, 1331 and 1296 respectively. These ensure that the resulting structure corresponds to *a*-Si:H with percentages of atomic hydrogen concentration of three, five, eight, ten, 13, 15, 18, 20, 23, and 25 atomic percent respectively. The mass of H is lower than that of Si, therefore the resulting mass density of the hydrogenated structures is correspondingly lower as hydrogen concentration increases, just as in real *a*-Si:H.

This criterion ensures that for all hydrogen levels, the mass density of the *a*-Si:H is progressively lower than that of pure *a*-Si just as observed in typical *a*-Si:H networks. Because of the low activation energy of hydrogen migration in *a*-Si, relative to the strength of the Si-H bond [140,141], the hydrogenated structures are neither heated nor cooled. Instead, a static algorithm is used to relax the hydrogenated structure at 300 K in a constant energy MD simulation. Thermodynamic averages of total energy, pressure, and forces on the atoms in the simulation box are evaluated at constant energy within the microcanonical ensemble. In this particular microcanonical ensemble, only one energy value, corresponding to the simulation temperature of 300 K, is accessible to the system.

This scheme is used to minimize the total energy of the hydrogenated structures over 5000 time steps, in a search for the global minimum. The structures at 300 K yield a minimum total energy of -25.814 eV, -19.634 eV, and -19.601 eV for networks with 13%, 20%, and 25% hydrogen concentration respectively. After equilibration at each level of hydrogen, the change in total energy per step is less than 2.42 x10^{-3} meV. On this basis, the structures are considered stable. The hydrogenated networks were then allowed to equilibrate at constant energy for 1ps at 300 K. The networks were assumed to be fully relaxed when the resultant force on any atom was less than 0.003 eV$Å^{-1}$. To test, whether the simulated structure satisfies physically reasonable expectations, the structural properties of the resulting structures were computed. Statistical functions and parameters, which provide useful physical and structural information on the simulated structures, were also computed in terms of the pair correlation function, the bond angle distribution, and the total bulk stress for possible comparison with results obtained from experimental analysis.

2.3 Modelling the Local Structure of Hydrogenated Amorphous Silicon

So far, the local structure of *a*-Si:H has been modelled in terms of the possible geometries of the local bonding environment, and the resolution of the inter-atomic distances are typically of the order of the mean nearest neighbour distances or bond lengths of the interacting species. In describing the microstructure on the atomic scale, it is important to note that amorphous solids are generally in a thermodynamically non-equilibrium state, and in principle can assume many thermodynamic states depending on their preparation conditions. On a microscopic scale, the arrangement of atoms in *a*-Si is no longer unique as in *c*-Si. This non-uniqueness arises because a considerable amount of positional disorder relative to *c*-Si exists. However, in *a*-Si:H, the non-uniqueness is compounded by the addition of compositional and positional disorder. As a result, a unique and consistent criterion of describing the local structure of an amorphous solid is necessary.

Since the translational symmetry, that gives rise to long-range order in crystalline materials, is completely lost in amorphous solids, a description of the local structure in terms of the reciprocal lattice is of little value [4]. A physically meaningful way to describe the local structure of tetrahedrally-bonded amorphous solids is, to consider the structural order in real space from a statistical point of view. In the concept of a statistical distribution of atomic species, the statistical variables are the geometrical parameters. This allows the description of the local structure in terms of the distribution of interacting species of atoms, as a function of their spatial distance from a chosen reference atom.

On this basis, it was assumed that bulk *a*-Si, and *a*-Si:H can be described geometrically in terms of a continuous random network of Si atoms, as shown in Fig. 2.4. Macroscopically, the different structures are only distinguishable from one another in terms of their total hydrogen content. However, the above discussion implies that, if the basic building block of the bulk structure can be represented by a distorted Si-Si_4 tetrahedron, as shown in Fig. 2.5, then the bulk structure could be considered as a continuous random packing of distorted Si-Si_4 tetrahedra as shown in Fig. 2.6. Fig. 2.5 also illustrates the geometrical parameters that play important roles in the description of structural order in tetrahedrally-bonded amorphous solids. From Fig. 2.5, six parameters can be identified which characterize the structure of *a*-Si:H:

(i) the interatomic distance for first nearest neighbours r_1;
(ii) the angle θ between a central Si atom and any two of its nearest neighbours;
(iii) the interatomic distance for second nearest neighbours r_2;
(iv) the dihedral angle ϕ, which describes the angle between any two intersecting surfaces of the tetrahedron;
(v) the height d_1, of the Si-Si_4 tetrahedron; and
(vi) the edge d_2 of the distorted Si-Si_4 tetrahedron.

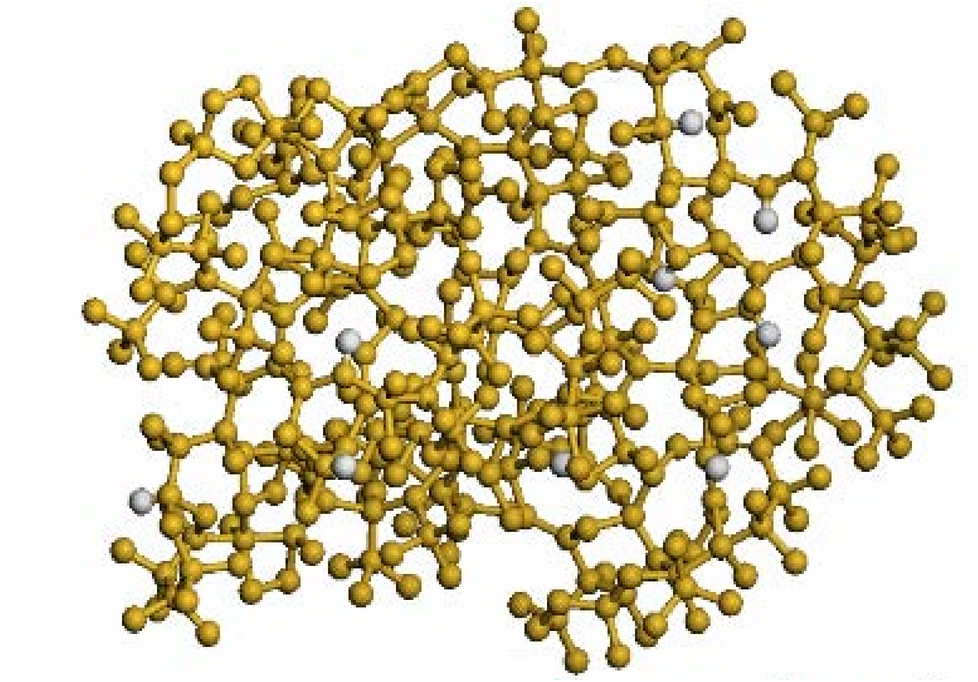

Figure 2.4 Ball and stick model of bulk tetrahedrally-bonded covalent amorphous solids in terms of a continuous random network of Si-Si bonds, where yellow balls denote Si atoms while white balls denote hydrogen atoms. Bulk structures are characterized in terms of the percentage hydrogen concentration, C_H.

This proposition is also suitable for describing the ordered local structure in *c*-Si in a consistent manner. In the case of a perfect, defect-free *c*-Si structure, the tetrahedron shown in Fig. 2.5 would be a regular tetrahedron with the length of edges d_2 constant, and equal to r_2, and a constant dihedral angle ϕ. The inherent order in *c*-Si implies therefore, that there are no fluctuations in any of these geometrical parameters. In tetrahedrally-bonded amorphous solids, the situation is different, because the Si-Si$_4$ tetrahedra are distorted, causing the tetrahedra to be irregular, and the distances for near neighbour separations are not constant.

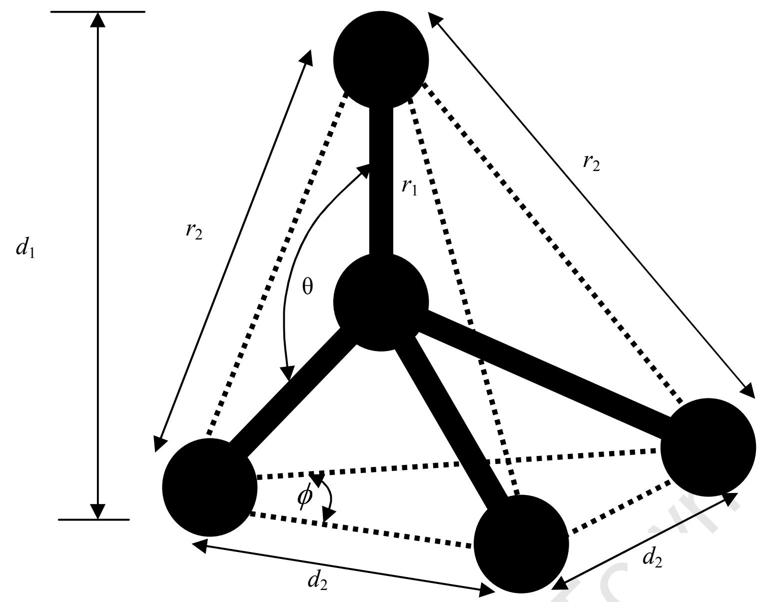

Figure 2.5 Representation of the basic building block of normal structural bonding (NSB) [4] geometry in tetrahedrally-bonded covalent amorphous solids in terms of a distorted Si-Si_4 tetrahedron, showing the geometrical parameters used in describing structural order in *a*-Si:H. The dotted lines define the edges of the distorted tetrahedron, and the bold lines represent the Si-Si bonds, where black balls denote the Si atoms.

Consideration of Fig. 2.5 suggests that the statistical distribution of r_1, r_2, and θ, and by implication, the statistical distribution of first and second nearest neighbours Z_1 and Z_2, are best used to describe the short-range order. On the other hand, the statistical distribution of ϕ and r_3 are better used to describe intermediate or medium-range order. Similarly, the statistical distribution functions of these parameters can be used as the basis for extracting variables which could be used to characterize order (or disorder) in amorphous solids. In this thesis, the pair correlation function $g(r)$, and triplet correlation function $g(\theta)$, where θ is the angle between a central silicon atom and any two of its nearest neighbours, are defined and computed as a function of hydrogen in the simulated structures.

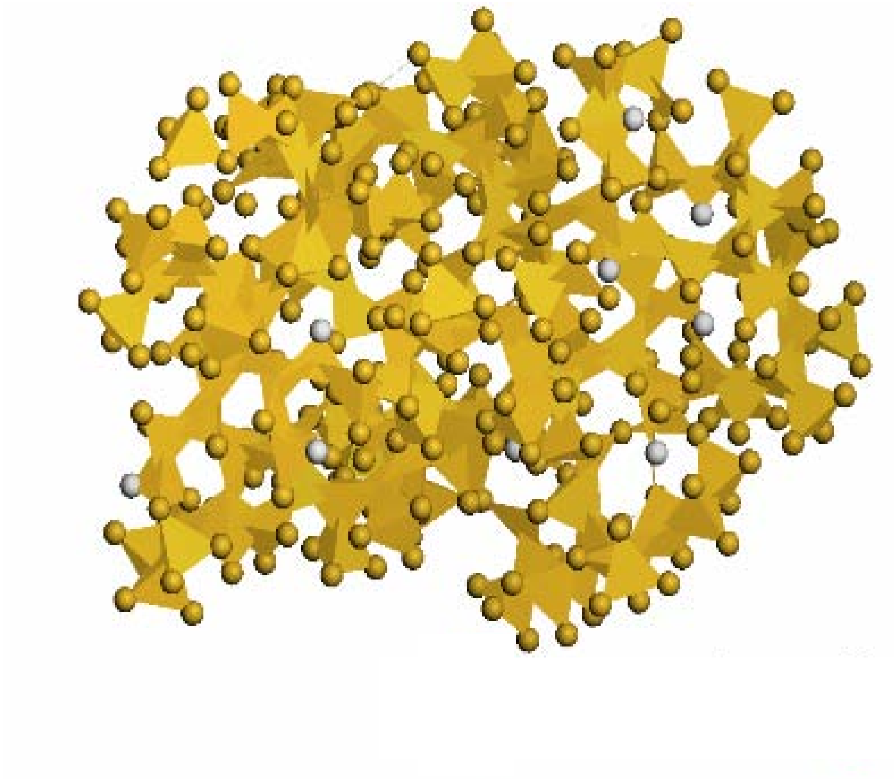

Figure 2.6 Geometrical model of the bulk structure of tetrahedrally-bonded covalent amorphous solids in terms of a random packing of distorted Si-Si_4 tetrahedra. Yellow balls denote Si atoms, and white balls denote hydrogen atoms.

Additional geometrical parameters have also been proposed for characterizing the mesoscopic order on a different length scale. The ring structure parameter [12,13] describes the number of atoms in a closed path that are linked to a fixed bond. In good quality a-Si models, it is usual to have five, six, seven or even eight membered-rings. Structures that contain three and four member rings are highly strained, defective, and are generally considered to be physically unrealistic, whereas structures with six- or seven-membered rings are comparatively more relaxed and stable. However, as the focus of this work is on short range order, ring statistics, and other description of medium range order are not explicitly considered.

2.3.1 Pair Correlation Function

The structure of materials can be characterized using a set of distribution functions for atomic positions [142]. The simplest of these distribution functions is the pair distribution function $g(r)$, also known as the pair correlation function. This distribution function gives a numerical estimate of the probability of finding a pair of atoms a distance r apart, relative to the probability expected for a completely random distribution of atoms at the same density. In most physical and computer generated models of *a*-Si, the local structure is analyzed in terms of the pair correlation function. This is mainly because the pair correlation function can be determined experimentally for direct comparison with results of computer simulations and theoretical predictions. In defining the pair correlation function, it is shown in Refs. [142,143] that the configurational distribution function must be integrated over the positions of all but two atoms, and that the appropriate normalization factors must be incorporated, so that

$$g(r) = \frac{N(N-1)}{\rho^2 Z}\int dr_3 dr_4 \ldots exp\left(-\beta U\left(r_1, r_2, \ldots, r_N\right)\right), \tag{2.26}$$

where Z represents the cluster integral and U denotes the configurational inter-atomic potential. In a system of identical atoms, the choice $i = 1$, $j = 2$ is arbitrary. An equivalent definition of the pair correlation function $g(r)$ in terms of the ensemble average of the product of delta-functions over all near neighbour pairs gives the expression:

$$g(\boldsymbol{r}) = \rho^{-2}\left\langle \sum_{i}\sum_{j\neq i}\delta(\boldsymbol{r}_i)\delta(\boldsymbol{r}_j - \boldsymbol{r})\right\rangle, \tag{2.27}$$

for a distance r, given that there is an atom at the coordinate origin. It is simply the ratio of the average number density $\rho(r)$ at a distance r from a given atom, to the density at a distance r from an atom in an ideal gas at the same macroscopic density.

In order to compute the pair correlation function $g(r)$, the following algorithm was followed:

(i) the range of data for computing $g(r)$ was chosen as $[0,{}^{L}/_{2}]$, where L is the length of the simulation box. This range was divided into 300 equal intervals, in small steps *dr*.

(ii) for a given structural configuration of atoms, the spatial coordinates of the atoms located at cordinates (r_1, r_2, r_3,…,r_N) were scanned.

(iii) an arbitrary atom *i*, located at point r_i from the origin of the simulation box was chosen as the reference from the configuration of atoms *i* (1, 2,…, *N*) in turn, until all atoms have been considered.

(iv) once the step above has been initiated, all other atoms *j* (1, 2,…, *N*-1) in the simulation box, that are located at a distance between *r* and *r* + *dr* away from the reference atom *i*, were counted. The total number of atoms counted was divided by the total number of reference atoms *N* that must be considered.

(v) the resulting number was divided by $4\pi r^2 dr$, the volume of the spherical shell. This account for the fact that as *r* gets larger, more particles are found with the separation *dr*.

(vi) this result is further divided by the particle number density so that *g*(*r*) = 1, for a uniform distribution. The interpretation is that if a spherical shell of inner radius *r* and outer radius *r* + *dr* is arbitrarily placed such that its centre coincides with the centre of a given reference atom, then a total of $N = \rho V$ atoms would be found inside the spherical shell, where ρ is the number density and *V* is the volume of that shell.

The pair correlation function is important for three main reasons. First, assuming that the interaction between atoms can be modelled in terms of the pair potential approximation, *g*(*r*) can be used to determine thermodynamic quantities such as pressure, excess entropy, chemical potential and the Helmholtz free energy [144,145]. Secondly, information about the pair correlation function *g*(*r*), can be obtained from neutron and X-ray diffraction experiments [146]. Finally, numerically determined pair correlation functions can be directly compared with results obtained from experiments or theoretical predictions [147-149].

In the ordered structure of a crystalline solid, the translational symmetry gives rise to long-range order, which makes the local environment of all atoms similar. The pair correlation will contain a set of δ-function-like peaks located at positions corresponding to the distance between any central atom and a certain shell of its neighbours. A zero background in the pair correlation function implies a zero probability of finding a near neighbour atom at distances other than the near neighbour distances in the crystalline solid. For the *c*-Si starting structure of our simulations, Fig. 2.7 shows sharp peaks corresponding to cordination shells at distances equal to the known lattice spacings of Si [150]. A disordered structure is characterized by broad peaks, with an unequal and non-zero background. The interatomic distances fluctuate around the value of *r* in the corresponding crystalline structure. In Fig. 2.8, a plot of *g*(*r*) for *a*-Si shows that the first peak is well-defined at 2.35 Å, just as in *c*-Si, but with a considerably broader width. When compared with Fig. 2.7, this broad, second peak corresponds to the merging of the second, third and fourth coordination peaks in *c*-Si.

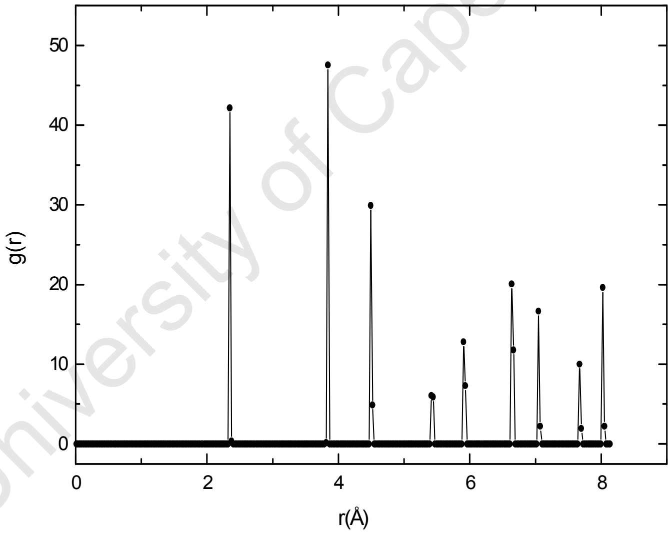

Figure 2.7 The pair correlation function *g*(*r*) of *c*-Si computed for a supercell containing 1728 Si atoms placed on the tetrahedral sites of a diamond lattice at 300 K.

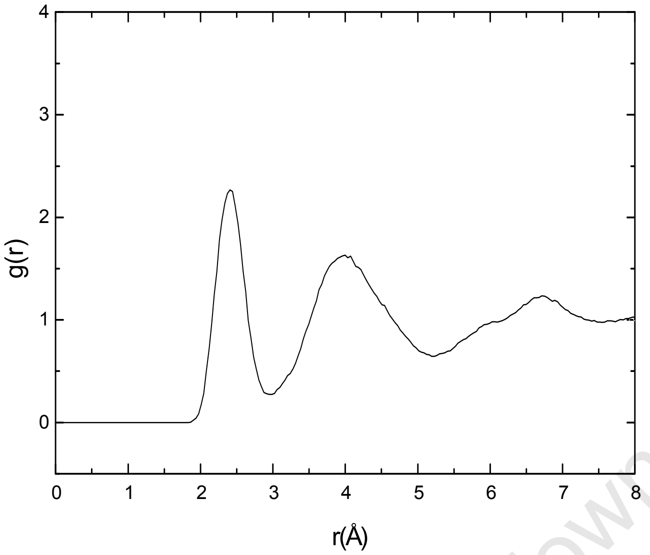

Figure 2.8 The pair correlation function $g(r)$ of hydrogen-free a-Si at 300 K computed from TBMD simulation of 1728 Si atoms.

2.3.2 Short Range Order

In ideal crystalline solids, there is neither compositional nor positional disorder. The entire crystal structure is completely determined by specifying the translational symmetry of the appropriate unit cell. Any deviations from this perfectly ordered structure constitutes a defect [4,56]. The situation is completely different in amorphous solids, because the basis consists of all the atoms in the solid, such that there is an absence of any regular repetitive pattern, and, therefore, there is no translational symmetry. However, what remains is not a complete disorder because a certain limited order still exists [151], described by the interatomic correlations in the first coordination shells.

The definition of the structure in amorphous materials can therefore only be meaningful, if the exact positions of the entire constituent atoms are known. Thus, a complete determination of the positions of all atoms in a given a-Si or a-Si:H structure would be necessary to describe the global structure. It is therefore necessary to characterize the local structure of amorphous solids in terms of parameters that retain unique information about the local structure, instead of simply prescribing the atomic positions only. Although the pair correlation function $g(r)$, is a one-dimensional measure of the mean probability distribution of near-neighbour distances, and does not give exact atomic positions, useful parametric information, that can be used to characterize the local structure modifications, can be obtained from it [152-154].

In terms of the 3D network model of the local structure of tetrahedrally bonded covalent amorphous solids, the factors utilized in determining short range order are the fluctuations in the mean first nearest neighbour distances δ_1, the fluctuations in the mean second nearest neighbour distances δ_2, and the fluctuations in the mean triplet correlation angle, or bond angle $\delta\theta$. In terms of these parameters, perfect order is characterized by zero fluctuations. For silicon, the first and second neighbour distances are exactly 2.35 Å and 3.85 Å, with corresponding coordination numbers of 4.0 and 12.0, respectively and the triplet atom correlation angle θ corresponds to the sp^3 tetrahedral angle of 109.47°. The fluctuations can be calculated, from the computed pair correlation function $g(r)$ of the simulated structures, by assuming a suitable statistical model for the distribution of interatomic distances within a given coordination shell, and then estimating the fitting parameters, for the chosen model.

The use of scalar parameters to characterize the degree of order (or disorder) in matter originated from Landau's theory of phase transitions [155,156]. In Refs. [157,158] for instance, a translational order parameter is defined in terms of the degree of similarity of a given amorphous structure to the corresponding ordered crystalline structure. In this case, this translational order is used to measure the tendency for atoms in the structure to assume the preferential spatial separation of the perfectly ordered structure, at the same density. Recently, an equivalent definition [159] has been given for the translational order parameter T in terms of a reduced pair correlation function $g(\xi)$. In this study of water, T has been defined as,

$$T = \frac{\int_0^{\xi_c} \left| g(\xi) - 1 \right| d\xi}{\xi_c}, \tag{2.28}$$

where $\left(\xi = r\rho^{\frac{1}{3}}\right)$ is the reduced distance between equivalent oxygen atoms in two different water molecules. ρ is the mass density and ξ_c is a cut-off distance, which specifies the preferred spatial separation in the reference structure.

The reduced distribution function $g(\xi)$, gives an estimate of the average probability density for inter-particle correlation in terms of the reduced distance, and is otherwise the same as the pair correlation function $g(r)$. The physical implication is that the limiting case $g(\xi) = 1$ corresponds to $T = 0$. This limit ensures a vanishing translational order in the structure, when the local structure is characterized by complete disorder, as in an ideal gas. On the other hand, the limiting case $g(\xi) \rightarrow \infty$ yields a large, positive value for T, showing the prevalence of translational order. The use of the translational order parameter T, as a measure of short range order, is qualitatively similar, to the use of the widths of the peaks in the pair correlation function, δ_1 and δ_2.

For structures with directional bonds, an orientational order parameter [160] has been defined, in terms of the extent to which the arrangement of any central atom, and its four nearest neighbours, conform to the tetrahedral symmetry imposed by sp^3 hybridization. This tetrahedral order parameter Q, is given by

$$Q = 1 - \frac{3}{8}\sum_{j=1}^{3}\sum_{\substack{k=j+1 \\ \langle i \rangle}}^{4}\left[cos\left(\theta_{ijk} + \tfrac{1}{3}\right)\right]^2 \quad , \tag{2.29}$$

where the index <i> indicates a sum over pairs of bonds connecting atom j and atom k with a central atom i, such that the indices j and k run over the four nearest neighbours of the reference atom i. The value of the orientational order parameter Q varies between 0 for an ideal gas, and 1 for an ideal tetrahedrally bonded network. If a silicon atom is placed at the centre of a regular tetrahedron, so that its nearest neighbours occupy the four vertices, then $\cos\theta_{jk} \equiv -\frac{1}{3}$, and θ_{jk} corresponds to the bond angle of 109.47° in silicon. The extent to which a given structure deviates from, or conforms to, the tetrahedral symmetry of sp^3 hybridization can therefore be studied in terms of the distribution of cosines of the triplet correlation angle [161,162]. An alternative formalism has been introduced in Ref. [163], where the orientational order parameter has the form $Q = \left\langle \cos\left(\theta_{jk} + \frac{1}{3}\right)^2 \right\rangle$. This form has been used successfully, to monitor the loss of local tetrahedral symmetry, during the dissolution and growth of small silicon clusters [163].

In this study, it is also assumed that the distribution of interatomic distances can be approximately represented by a normal distribution. This allows Gaussian peaks to be fitted to the first and second coordination peaks in the pair correlation function. The fitting parameters used include the Gaussian widths, and area of the first and second coordination peaks. The former provides a measure of the fluctuation in the interatomic separation, and the latter provides information on the mean number of first and second nearest-neighbours. In order to investigate the evolving structural order in the topologies of the simulated networks, the pair correlation function is computed for the simulated *a*-Si:H structures, containing hydrogen concentrations ranging from 0% to 25%. In each case, Gaussian peaks are fitted to the first and second peaks in *g*(*r*) and the fitted parameters are investigated as function of changing hydrogen level.

2.3.3 Medium Range Order

From the discussions, so far, it is clear that the prevalent topological disorder in *a*-Si:H does not completely destroy the short range order. It is also clear from chapter 2.3.1 that information about the correlations of atomic position can be obtained either experimentally or theoretically from the pair correlation function *g*(*r*). In either of these cases, the pair correlation function, only gives information for distances within the limit of 8.0 Å for which it is calculated. On length scales greater than the average distances over which inter-atomic forces act, it is no longer clear how to describe the mesoscopic structure. Medum range order denotes the physical correlations observable over distances beyond the length scales that produce peaks in the pair correlation function *g*(*r*), but shorter than the length scales which produce Bragg peaks [164]. It is intuitive however, to suggest that in terms of the CRN model, medium range order could be characterized by the distribution of dihedral angles, ϕ [165].

Studies of ordering in the mesoscopic structure of amorphous solids require techniques that are able to determine the position correlations of higher order such as triplet $g_3(r_1,r_2,r_3)$ and quadruplet $g_4(r_1,r_2,r_3,r_4)$ [142]. These multiple correlation functions should contain more information on the mesoscopic structure than the single pair correlation function $g(r)$. An alternative method of describing the medium range order involves the description of the bonding topology using ring statistics [166]. This approach involves counting the number of closed paths of bonds as a function of the number of bonds in that path.

Fluctuation electron microscopy (FEM) has been introduced recently [167,168], as an experimental method of measuring MRO in amorphous materials. In principle, the ring statistics and higher-order position correlation functions can equally be computed for any computational model of *a*-Si:H. However, in this thesis, emphasis will not be placed on the ordering of the mesoscopic structure, but on ordering at length scales predictable by the pair correlation function $g(r)$. It is therefore not immediately useful for our present purpose to undertake a computation of the ring structure or dihedral angle distribution.

2.3.4 Order Parameter

The use of order parameters to characterize the physical and chemical changes in matter is well documented [169,170]. Two examples T and Q, describing translational and orientational order respectively, have already been discussed in section 2.3.2. In a perfectly disordered system, all interatomic separations are equally possible. The pair correlation function for such a structure will therefore have a constant non-zero value. On the other hand, in a perfectly ordered system, the pair correlation function $g(r)$ is a set of δ-functions, centred at particular distances. At all other distances, the pair correlation function is zero. For a disordered topology on the other hand, the widths of the coordination peaks will be broad, because the positional disorder gives rise to a large fluctuation in interatomic distances. This means that the peaks showing the distribution of distances where near neighbour atoms exist can no longer be represented as δ-functions. In such structures, the pair correlation function $g(r)$ is zero only for distances significantly less than the equilibrium first neighbour separation r_0. At distances other than the minimum first near-neighbour distance, a non-zero pair correlation is obtained.

The incorporation of hydrogen into *a*-Si to form *a*-Si:H also introduces compositional disorder. Since the interatomic potentials between interacting species of atoms are short-ranged, and both positional and compositional disorders are present, an order parameter is required to study the evolution of structural order in the simulated topologies. Moreover, an order parameter is necessary for the investigation of the correlations between:

(i) structural order and hydrogen concentration,
(ii) order and stress, and
(iii) order and average coordination number.

It is therefore necessary to define an order parameter, such that the degree of order, or disorder, in the simulated structures can be characterized in terms of the above analysis. Recently, the variations in the full width at half maximum (FWHM), of the first and second coordination peaks, have been used to estimate the structural changes, and to show the evolving topological order in models of *a*-Si:H [171].

It is clear from the tetrahedral symmetry of the silicon structure that any measure of order (or disorder), using either the translational order parameter T, or any of the two variants of the orientational order parameter Q, will give similar results as measurements of short range order (or disorder) using deviations in first and second nearest neighbour distances, δ_1 and δ_2. This is because information about the bond angle deviations $\delta\theta$, is coupled into the distribution of these deviations. Therefore, in order to describe short range order in tetrahedrally-bonded solids, any pair of parameters extracted from the three coupled parameters, r_1, r_2, and θ can be used. It is therefore necessary to stipulate the ordering rule for each of the three degrees of freedom, denoted by the above pairs of parameters. In this study, we only investigate the ordering rule for deviations in r_1 and r_2, using the simulated structures, because of the observed coupling of the translational and orientational order, in the tetrahedrally bonded structures as described above.

It is therefore proposed in this thesis, that the standard deviation of the first and second nearest neighbour distances δ_1 and δ_2, are good scalar parameters to estimate the degree of positional disorder. Physically, as $\delta_1 \rightarrow 0$ and as $\delta_2 \rightarrow 0$, the pair correlation function tends to a set of δ-functions, and the structure becomes more ordered. On the other hand, as $\delta_1 \rightarrow \infty$ and $\delta_2 \rightarrow \infty$, the widths of the coordination peaks become very large, and the structure becomes more disordered.

The idea of using both δ_1 and δ_2 to characterize the structural order is non-trivial, because one first neighbour atom is always a second-nearest neighbour to another atom. The limits as $\delta_1 \rightarrow 0$ and $\delta_2 \rightarrow 0$, also implies that $\delta\theta \rightarrow 0$. In terms of the translational order parameter T, and orientational order parameters Q, these limits correspond to both $T \rightarrow 1$ and $Q \rightarrow 1$, for an ordered structure. On the other hand, a disordered structure is characterized by both $T \rightarrow 0$ and $Q \rightarrow 0$, which correspond to the limiting case where $\delta_1 \rightarrow \infty$, and $\delta_2 \rightarrow \infty$. In a-Si:H, this implies that $\delta\theta$ becomes very large for the most disordered structure. The order parameter field (δ_1, δ_2), has also been investigated in this study, for deviations from the ordering rule prescribed by $r_2 \approx 2r_1 \sin(\theta/2)$, in tetrahedrally-bonded structures. The results are tested for Si-H and C-H systems, and the implication of the main findings on structural order is discussed.

Chapter Three

Modelling Structural Defects

This chapter presents the methods used, in simulating structural defects in amorphous silicon, and also the complexes formed from the interaction of these defects with hydrogen. The methods of modelling the positron state in these defects are also presented.

3.1 Modelling Defects in Hydrogenated Amorphous Silicon

The simulated bulk structures of *a*-Si obtained by quenching a hot Si melt, within the TBMD scheme, inherently contains coordination defects. These native defects are also observed in other *a*-Si structures, simulated within the BGS model [172-175]. Although, two-fold coordinated Si sites, denoted as T_2 defects, have been proposed to explain the localized deep level states in *a*-Si [176], this defect geometry has yet to be observed experimentally, and the *a*-Si simulations in this study exclude T_2 defects. The predominant types of defects observed in simulated *a*-Si are: three-fold coordinated Si sites, denoted as T_3 or dangling bonds (DB); and five-fold coordinated Si sites, denoted as T_5 or floating bonds (FB).

A wide range of possible defect complexes will be explored in this thesis, without restricting their geometry to those found in *a*-Si:H thin films, which can be produced by applying specific growth techniques. One such important defect is the $4T_3$- complex, a combination of two T_3 pairs [177], to form a larger-sized defect complex made up of four dangling bonds. Experimentally, single T_3 pairs have only been detected on crystalline Si(100) surfaces [178]. However, in bulk material, the $4T_3$-complex is analogous to a Si monovacancy (V_1) in *c*-Si. In Ref. [179], the possibilities of *n*- vacancy clusters of various sizes V_n, where $n \leq 35$ have been investigated in *c*-Si. It must be noted that vacancy-type defects do not exist intrinsically in *a*-Si structures simulated by BGS based techniques [17]. As a result, these defects have to be created in an *ad hoc* manner. Apart from dangling bond clusters of various sizes, it is also possible to have an open-volume in *a*-Si structure formed, whenever bonds break and re-form during network rearrangement. In this case, the open volume is simply an empty space within the network, and constitutes a density defect. This supposition is conceptually consistent with the experimentally observed microvoids, of sizes between 10-100 Å, in *a*-Si prepared by evaporation or sputtering [180].

This work considers vacancy-type open volume defects V_n, for cases where $1 \leq n \leq 5$, although larger-sized vacancies are, in principle, possible. The reason for this choice is primarily to reduce computational cost and supercell energy restrictions, as will be discussed in chapter six. Several derivatives of the V_n defect, obtained from the incorporation of a variable number of H atoms in the defect model, to form H-decorated complexes, are also investigated. Structural defects in *a*-Si:H are described from two perspectives. Firstly, the structural geometries of generic defects are modelled computationally to study their structural stability. Secondly, their electronic signatures are investigated from quantum mechanical considerations, to study their electronic and vibrational density of states, activation energy, and dynamics.

3.1.1 Dangling Bonds and Floating Bonds

Fig. 3.1 shows the deviant bonding geometries in *a*-Si:H studied in this work. The defect geometry shown in Fig. 3.1(a), is known as a dangling bond defect. This is equivalent to a deviant bonding geometry obtained by breaking a covalent bond. In *a*-Si, all such deviations from normal structural bonding (NSB) constitute a deviant electronic configuration or defect, where an unpaired electron in the sp^3 hybridized orbital of Si is left unsatisfied. In terms of the convention of Kastener *et al.* [177], the ground state of the NSB geometry in Si, where one Si atom is bonded to four first nearest neighbours, as shown in Fig 3.1(b), is denoted as T_4^0 where the subscript denotes the number of first nearest neighbours, and the superscript denotes the charge state. Dangling bonds can be observed in three charged configurations, *i.e.* the neutral T_3^0, the positively charged T_3^+, and the negatively charged T_3^- states.

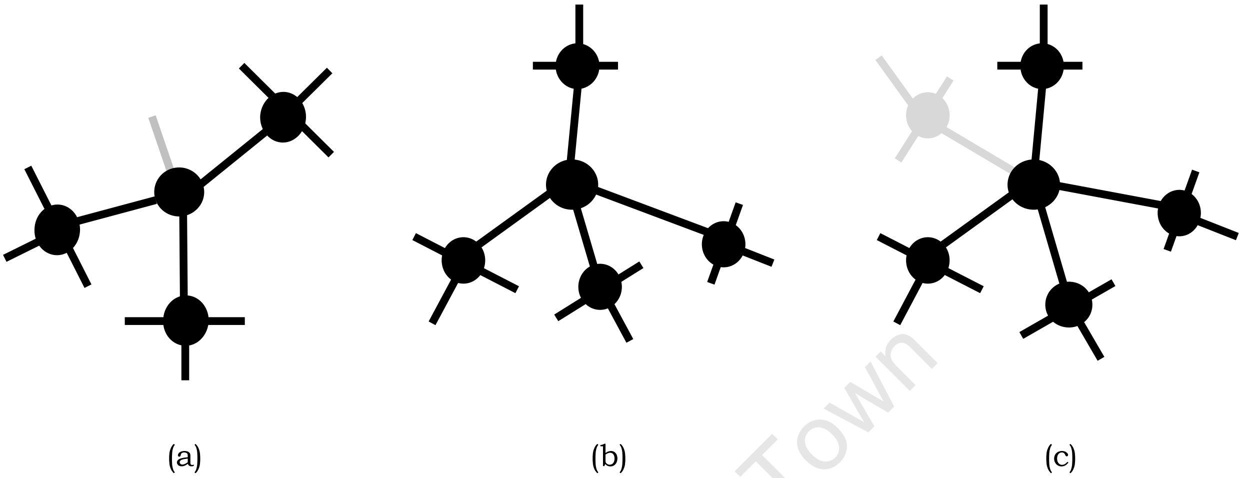

Figure 3.1 Two-dimensional structural models of native deviant bonding geometries showing (a) a dangling bond, (b) a distorted Si-Si$_4$ NSB, and (c) a floating bond defect.

Experimentally, dangling bonds can be detected using electron spin resonance (ESR) spectroscopy. ESR does not detect covalent bonds with pairs of electrons having opposite spins, but will detect, with high sensitivity, defects resulting from unpaired electrons which exhibit marked spin effects. Several ESR studies in undoped *a*-Si:H [181-184], and other phases of bulk Si [185] show, that the electronic signature of the T_3^0 defect is highly localized in the band gap. It is now a common belief, that the origin of the defect states in the energy band gap of *a*-Si is primarily due to dangling bonds. Similarly, it is believed, that the observed reduction of the density of these midgap states upon hydrogenation is due to the mechanism of dangling bond passivation by hydrogen [186-190].

The floating bond hypothesis of Pantelides [191-193], in which T_5 sites (see Fig. 3.1(c)) are considered as the dominant source of the ESR signal in *a*-Si, has not been proved wrong [194-197]. However, the controversy over the actual existence, or otherwise, of the T_5 defects is still a subject of discussion. Recent tight binding calculations [198] of local magnetic moments suggest, however, that the ESR signal of such a state is weak. This leads to the conclusion, that if the T_5 defect actually exists in *a*-Si, it must be a highly delocalized defect state. On this basis, it can be argued, that the contributions to the total electronic density of states, in the case of floating bond defects must be shifted towards the conduction band edge. This implies that floating bond defect states are resonant with the tail states, and are therefore, not as localized in the band gap as dangling bonds [199]. Hence, even if floating bond defects exist in *a*-Si, they must form resonance states with the conduction band tail states, and as such have little influence on either the optical band gap or the electronic quality of the material.

In the simulation of the H-free structure, T_3 and T_5 sites arise as intrinsic defects, but other coordination defects are explicitly excluded. However, as seen in other computational studies [200,201], the density of the T_5 sites is far lower than the density of T_3 sites. In order to prevent the formation of other cordination defects in the simulation, a sort of *book-keeping* is used, at the last step of the equilibration process, to check the contents of the Verlet list of neighbours of atom i (where $i = 1,2,3,\ldots,1728$). This allows for a counting of the number Z_1 of nearest neighbours of a given atom, to ensure that the number of nearest neighbours within a distance of 4.18 Å, lies within the limit $3 \leq Z_1 \leq 5$. This upper limit on the distance is chosen to include the first coordination shell, but not extend into the second. If $Z_1 < 3$ or $Z_1 > 5$, a logical statement is used to continue the structural rearrangement until the network relaxes to a lower energy with coordination numbers within the preferred range. This condition ensures that:

(i) no T_2 defects exist in the bulk of the simulated hydrogen-free structure; and

(ii) no T_6 or higher coordinated Si sites exist in the hydrogen-free structure.

Although, charged dangling bonds have been suggested in Ref. [177], all the T_3 sites obtained in this study are considered to be neutral dangling bond hybrids. It is not part of the aims of the present study to attempt a simulation of charged dangling bonds (T_3^+ and T_3^- sites) in the bulk structures of *a*-Si, and properties of the charged dangling bond hybrids will not be discussed further in this dissertation. This restriction is primarily due to the facts that:

(i) these charged dangling bond hybrids are observable in *a*-Si:H only after photo-excitation [4], and the present simulation does not involve light soaking; and

(ii) we are not aware as yet, of any experimental observation of charged dangling bond hybrids in undoped forms of *a*-Si:H, prior to light soaking. This implies that there is no experimental evidence to support the simulation of such structures in hydrogen-free *a*-Si.

3.1.2 Open Volume or Vacancy-like Defects

As shown in Fig. 3.2 and mentioned above, an open-volume defect can be created in *a*-Si by either deleting a Si atom, or a group of Si atoms, from the bulk structure. In addition, open volume defects could also form as empty regions in the structure whenever weak Si-Si bonds break and new bonds re-form. In all such cases, the open volume regions emerge as regions with low ionic density due to the missing ion core. Furthermore, such regions can also be created by the re-bonding of Si atoms, after a vacancy has migrated from its original site. Computationally, these open volume defects are considered to be analogous to voids in the real material. These defects can be formed in the real material from either:

(i) missing atoms or groups of atoms in bulk *a*-Si:H; or

(ii) the agglomeration of vacancy-like defects.

In *c*-Si, a monovacancy defect (V_1) is a localized defect, formed whenever a Si atom is missing from its tetrahedral site in the diamond lattice. This missing Si atom inadvertently leads to a situation where four dangling bonds ($4T_3$ sites) are created in very close proximity. In *a*-Si, if a silicon atom is missing from a four-fold coordinated site, the situation leads to a cluster of four dangling bonds, if all other sites are four-fold coordinated. If other defect types exist in the structure, in particular, floating bonds, in addition to the missing atom, the analysis in Ref. [202] suggests that, to minimize the total energy, a large structural relaxation is required for bonds to re-arrange and re-form.

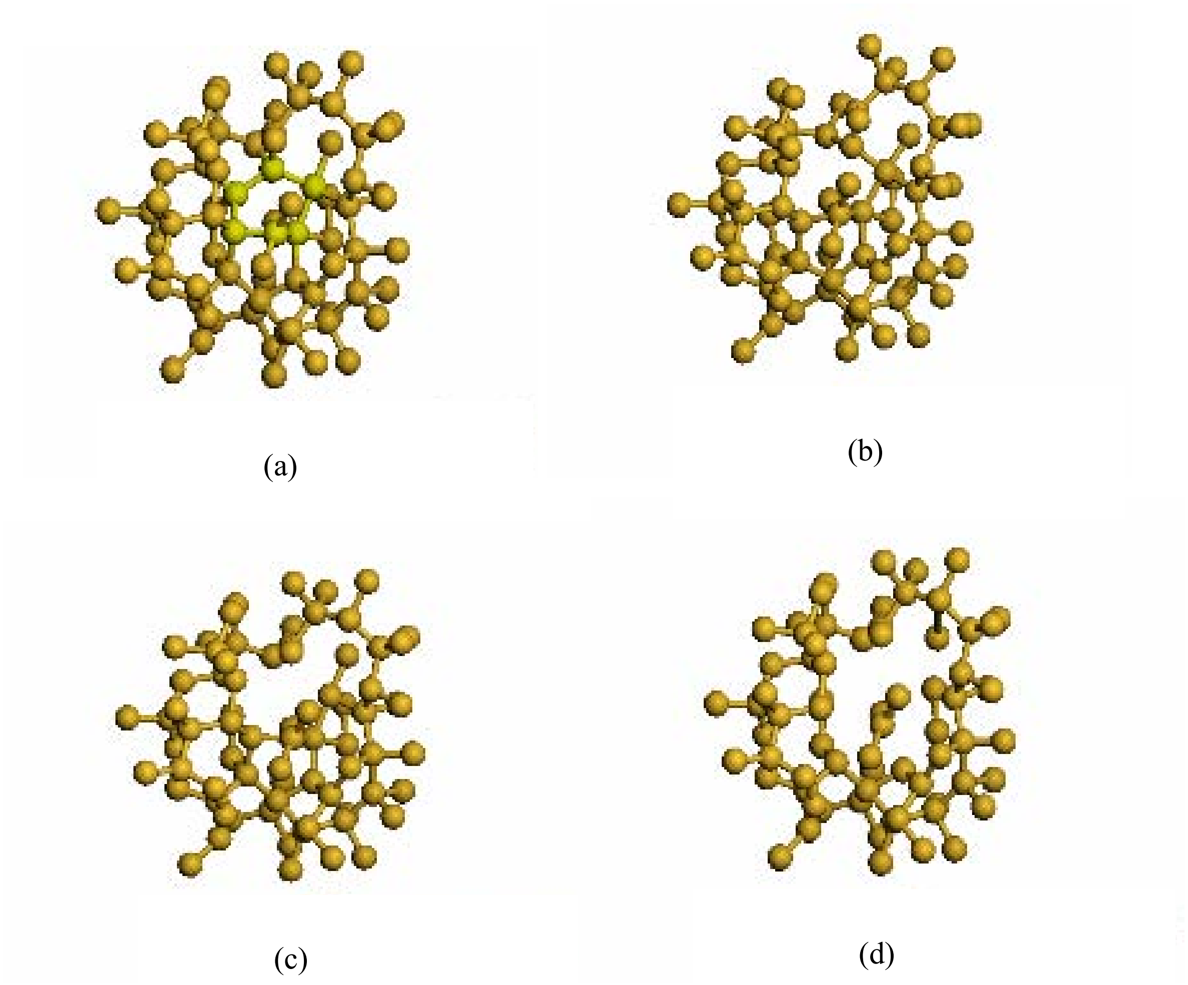

(a) (b) (c) (d)

Figure 3.2 Ball and stick models of open-volume defects showing: (a) hexagonal ring cluster (HRC) in hydrogen-free *a*-Si (highlighted in greenish-yellow); (b) Si monovacancy-like open volume defect in *a*-Si, obtained by deleting one Si atom from an HRC stack of Si-Si$_4$ tetrahedra within a Si$_{64}$ supercell; (c) divacancy-like open-volume defect, created by deleting two Si atoms from the HRC stack; and (d) a large open-volume defect, created by deleting five Si atoms from an HRC stack.

In Ref. [203] it is shown, that the formation mechanism of vacancy clusters in *c*-Si can be considered to be equivalent to either:

(i) the breaking of bonds; or

(ii) the forming of internal surfaces; or

(iii) the incorporation of a vacancy into the host structure.

It is also shown, that the coalescence of vacancies to form clusters is affected by:

(i) the variations in bond angle coordination;

(ii) the relaxations of the internal surface of the cluster; and

(iii) the interplay between the symmetry of the diamond lattice and the cluster topology.

As mentioned above, when one Si atom is removed from the centre of a cluster of Si atoms, a small void is obtained. Although, this structure is very unstable at 300 K, just as for the monovacancy in *c*-Si [204], the creation of larger voids is accompanied by considerable relaxation of the local structure. Fig 3.2(a) shows a two dimensional model of a hexagonal ring cluster (HRC) in a Si_{64} supercell. Open volume defects were created in hydrogen-free *a*-Si by deleting Si atoms from the Si_{64} cluster, and then relaxing the structure.

For a mono-vacancy-like defect, the dangling bonds collect around the site of the missing Si atom, to form a cavity-like open volume within the structure. Fig. 3.2(b) shows a monovacancy in hydrogen free *a*-Si, created by deleting one Si atom from the hexagonal ring of Fig 3.2(a), after static relaxation. During optimization of the geometry, the surrounding atoms re-arrange in a manner, that makes the vacancy volume shrink considerably. Larger size open volume defects are shown in Figs. 3.2(c) and 3.2(d). For reasons, similar to those enumerated for native dangling and floating bonds in the preceding section, charged vacancy-like defects will not be considered in this study. If it can be assumed, that the dynamics of monovacancy defects are strongly influenced by the presence of stress gradients (although the presence of impurity atoms, potential or thermal gradients could also be responsible) [205], then a large supercell must be chosen, to minimize the artificial gradient imposed by the periodic boundary condition. This is to ensure, that for sufficiently large distances between individual vacancies, the stress gradient does not change significantly with the size of the supercell.

Since the stability of the dangling bond cluster ($4T_3$ defect) in *a*-Si is very sensitive to the formation mechanism of the defect, stable vacancies are created by removing atoms from hexagonal ring clusters in *a*-Si following Ref. [203]. Just as observed in Ref. [206] for vacancy clusters in *c*-Si, the formation energy of isolated vacancy-like defects in *a*-Si depends on the number of dangling bonds created in the process. Using similar arguments in this work, a formation energy of 4.70 eV was required to create an isolated monovacancy in *a*-Si. This energy is higher, than the energy required to form a monovacancy in *c*-Si [207]. From self-consistent calculations, the estimated formation energy for a monovacancy-like open volume defect in *a*-Si is close to ~5.0 ± 0.5 eV [208]. This energy is equivalent to the cohesive energy, which is the energy required to create one free Si atom from a cluster of Si atoms. For comparison, the experimental cohesive energy for Si in the diamond lattice is 4.63 eV [209]. This energy is 0.7 eV higher than the formation energy of the equivalent defect in *c*-Si, see for comparison, Table 1 in Ref. [203].

After creating a large defect by deleting five Si atoms from the HRC stack, as shown in Fig 3.2(d), geometry optimizations show the formation of a void-like open volume as indicated in Fig 3.3, which has several unterminated dangling bonds. In this work, the defect size is restricted to a maximum of five missing Si atoms. In TBMD simulations, as the vacancy-size increases, it becomes increasingly difficult to optimize the geometry for the lowest total energy. In most cases, the resulting *a*-Si structure becomes unstable as the number of vacancies increases due to poor energy convergence.

The origin of this instability is attributable to several factors. Firstly, the high formation energy suggests, that the total entropy of the system of open-volume defects in *a*-Si, arises from the combined entropies of the defect formation, and the thermodynamically unstable *a*-Si matrix, is so high that the resulting defect structure becomes unstable. Secondly, the strong dependence of vacancy formation energy and binding energy on the number of dangling bonds created means that, the vacancy formation energy must increase with vacancy size. Also, the dependence of the stability, of a vacancy cluster on the energy associated with coalescence of another vacancy, on the sign of a second order energy difference allows a prediction that creation of larger clusters will involve higher number of dangling bonds. This will in turn involve a higher formation energy, except for cases where magic numbers [205] are permitted. Thirdly, monovacancy defects are generally believed to diffuse very rapidly in bulk Si [210].

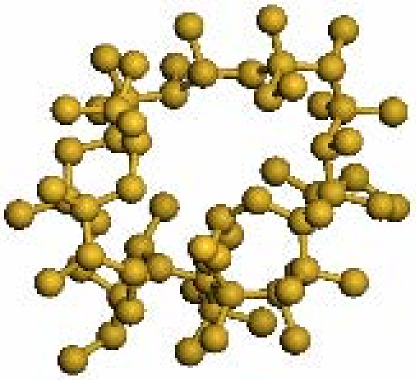

Figure 3.3 Optimized geometry of a large void in hydrogen-free *a*-Si showing a cavity-like open volume and several unterminated dangling bonds.

3.1.3 Hydrogen-decorated Vacancy-like Complexes

The introduction of hydrogen atoms into tetrahedral sites initiates the mechanism of hydrogen-mediated defect annealing [211-214]. The incorporation of hydrogen is therefore believed, to induce structural relaxations, that culminate in the formation of stable geometries of hydrogen-decorated vacancy complexes with low total energy. In this dissertation, these arguments are extended to discuss vacancy clusters in *a*-Si:H. However, it is worth noting, that the broken symmetry in *a*-Si:H implies, that the formation of vacancy clusters is sensitive to changes in bond angle and the incorporation of hydrogen into the internal surfaces of the vacancies.

It is difficult to locate the exact position of a vacancy cluster in *a*-Si:H because of the inherent structural relaxation and vacancy diffusion. However, the geometry of the vacancy cluster is preserved in an MD simulation, by simple counting of the near-neighbour bonds. This implies that additional parameters are required in a simulation to characterize the stability of the defect created. In the defect studies, these parameters are:

(i) the total energy for the formation of a particular type of defect;
(ii) the binding energy per vacancy; and
(iii) the number of dangling bonds, that must be created for a stable defect to form.

Although it is energetically favourable for a monovacancy to form at lower temperatures in *c*-Si, the divacancy has been reported to be much more stable at room temperature [206]. It is therefore important to explore the possibilities of mono-, di- and poly-vacancies in *a*-Si:H. Since total energy convergence in defect calculations is known to be dependent on supercell size [215-218], and in order to make the effects of inter-vacancy interactions negligible, to ensure a rapid convergence of the supercell energies to the bulk energies, a very large supercell of size $10l_0$, where $l_0 = 5.43Å$, is used in the defect computations.

A single hydrogen-terminated dangling bond defect (V_1H_3 site) was obtained, by creating a vacancy-like cluster of four dangling bonds, by randomly deleting one silicon atom from the H-free *a*-Si network. The structure was stabilized by inserting three hydrogen atoms at three T_3 sites, leaving one T_3 site unterminated. Structural relaxations were carried out, and the network was observed to relax after 27000 iterations. For this structure, the total energy converged to ±4.60 meV/atom. The introduction of H to the dangling bond sites stabilizes the vacancy structure, and gives rise to a formation energy of 1.175 eV for this defect complex. The situation of producing a hydrogen decorated complex, where only two T_3 sites are satisfied, is harder to accomplish. This is due to a higher energy of formation, characterized by very poor total energy convergence. Stable geometries of the V_1H_1 and V_1H_2 complexes are obtained with formation energies of 2.355 eV, and 3.513 eV, in each case.

A divacancy, V_2, was obtained by randomly removing two Si atoms from the equilibrated pure *a*-Si structure. As will be discussed later in chapter six, the resulting structure is very unstable in terms of total energy restrictions. In order to correct this thermodynamic instability, hydrogen was added selectively, to satisfy the dangling bond sites. This yields stable hydrogen-decorated divacancy complexes of various configurations. Stable configurations, such as

V_2H_5, V_2H_6, and V_2H_7, were obtained using the same algorithm as for hydrogen-decorated monovacancies. Numerically, the number of Si atoms N_{Si}, is decreased by randomly deleting Si atoms from the supercell, while the concentration of hydrogen C_H, is simultaneously increased in each case.

This procedure is equivalent to decorating the internal surface of the vacancy cluster with hydrogen atoms. The total number of hydrogen added, is directly determined by the size of the vacancy, and the number of dangling bonds to be terminated. It can be seen from the computational procedures, that the role of hydrogen in this mechanism is two-fold. Firstly, hydrogen saturates the dangling bonds, and mediates the structural relaxation by relieving strain [210]. Secondly, the introduction of hydrogen to the simulated structures leads to a considerable improvement in the total energy convergence. It should be noted though, that the procedures enumerated above are observed to be the only computationally effective method of obtaining large-sized hydrogen-decorated defect complexes, that are stable at 300 K by using TBMD.

3.2 Modelling Positron States in Defect Complexes

Positron annihilation spectroscopies (PALS) have developed into effective experimental techniques for probing the structure of defects, their spatial distribution, and the associated depth profile [219]. The method relies on the capability of the positron wave function to be strongly localized at open-volume regions in a solid. The information about the sites at which annihilation occurs is uniquely registered in the emitted gamma radiation. In crystalline materials, the thermalised positron state is a delocalized Bloch wave [220-222]. The positron can interact with a defect, and the interaction can culminate in the positron being trapped into a localized state. Eventually, the positron encounters an electron and annihilation occurs. This event leads to the emission of two gamma ray photons, of energy 511 keV, which bear a unique signature of the electron distribution at the site of the annihilation event. Due to momentum conservation requirements, the two gamma ray photons are emitted in directions roughly anti-parallel to each other. Any deviation of the emitted gamma ray photon from colinearity is caused by the momentum of the annihilating pair, and similarly the energies of the two photons are Doppler-shifted in opposite directions.

From an experimental viewpoint, there are numerous parameters that can be used to characterize open-volume defects in a solid. These include the positron lifetime, two-dimensional angular correlation of the annihilation radiation (2D-ACAR), and Doppler broadening of the annihilation line width [223,224]. The positron lifetime is a measure of the probability of annihilation, and therefore an indirect measure of the local electron density. Although the lifetime is suitable for defect studies, because defects act as trap sites, it cannot be used to provide direct information on the chemical variations at the defect sites, as there may be several similar defect configurations with similar characteristic positron lifetimes. On the other hand, even if the characteristic positron lifetimes are quite similar, the momentum distribution of annihilation photons (MDAP) can be very different. The MDAP for low values of momenta correspond mainly to positron annihilation with valence electrons, while annihilation of positron with electrons in deeper lying states gives rise to a broader momentum distribution.

In a defect-free region of any solid, positrons annihilate from delocalized states. When a positron encounters a negatively charged or neutral open-volume defect, it is trapped and its wave function becomes strongly localized. In the vicinity of positively charged defect, the positron density is depleted due to Coulomb repulsion, and the positron density (wave-function) may even be zero. In such cases, the probability of annihilation of trapped positrons with core electrons is significantly reduced. This arises because the overlap of the wave function of the core electrons and the trapped positron is severely reduced, and the positron is simply not available for the annihilation event [225]. The localization of the positron wave function at a defect site means, that the amplitude of its wave function must decrease very rapidly with the outward distance away from the trapping site. This causes the overlap of the wave function of the localized positrons and core electrons to be reduced.

Apart from Ref. [226], the use of positrons in earlier studies of Si relied mainly on Doppler broadening. The use of a combination of Doppler broadening and positron lifetime to study molecular beam epitaxy-grown *c*-Si films was first reported in Ref. [227]. Since the first application of positron lifetime to the study of *a*-Si was reported in Ref. [228], many other experimental positron lifetime and Doppler broadening measurements have been reported for *a*-Si and *a*-Si:H [229-237]. Although the thin film samples of *a*-Si, and *a*-Si:H used in all these experimental studies have been prepared using different deposition methods, the positron state is still not well-understood. This situation has been attributed to the lack of a suitable material for fundamental study [236]. As seen earlier, this situation can be attributed to the numerous possibilities of structural defects and bonding geometries in amorphous silicon.

It has been shown [238] that all the parameters discussed above can be directly computed based on the independent particle approximation (IPM) where the core and valence electrons are treated separately, although this scheme is not accurate. The partitioning of electrons states into core and valence contributions allows the computed positron annihilation characteristics to be directly compared to the high momentum and low momentum parts of the experimentally observed annihilation line shapes. It is therefore important to provide an accurate and reliable scheme for the calculation of positron properties in defects, in order to allow for direct comparison with experiment. As a result, the present study is one such effort aimed at providing a theoretical framework for the identification and characterization of a wide category of defect geometries in hydrogenated amorphous silicon. The present study utilizes accurate self-consistent first principles calculations based on the two-component density functional theory (TCDFT) to compute positron states and annihilation characteristics in different computational models of structural defects in hydrogenated amorphous silicon

3.2.1 Electron-Positron Potential

At open-volume defects, such as vacancy-related defects and impurity-decorated vacancy complexes, the potential experienced by positrons is lowered. This is due to the absence of the positively charged ion core, which leads to a reduction in the net repulsion at that site. This results in the localization of the positron wave function at the defect. Localized positron states therefore, have lower energies relative to delocalized states. This energy difference constitutes the positron binding energy at the given defect type. When the state of a thermalized positron undergoes a transition from the delocalized state to a localized state at any site in the bulk structure, it is said to be trapped. The trapping occurs in a manner, that during the transition, the energy difference between the initial and final positron states, known as the trapping energy, is transferred to the host solid.

The wave functions of the positrons, core, and valence electrons must be obtained in order to study positron annihilation characteristics in a given structure. In order to obtain the positron wave functions, the potential experienced by positrons at a given defect site has to be set up, and used in solving the Schrödinger equation for the ground state wave functions (and positron density), ground state energy, and binding energy. The resulting electron and positron wave functions are then used in evaluating the annihilation rate and positron lifetime. As a first approximation, the positron experiences a net potential, that arises as the sum of two parts. The first part is the Coulombic potential, arising from the charge distribution of the surrounding electrons and nuclei. The second part arises due to electron-positron correlation. The electron potential is assumed to be influenced by the presence of the positron, so that the positron potential described above is dependent on:

(i) the relative position of the positron and the charges of the nuclei and electrons; and on

(ii) the density of the electrons.

The positron potential can be expressed as a local potential $V_+(\boldsymbol{r})$, which represents the approximate potential, experienced by positrons in a given type of defect structure.

Within this approximation, the positron potential at a given defect site is expressed as the sum of the Hartree electrostatic potential, and the density dependent correlation potential as:

$$V_{+}(\boldsymbol{r}-\boldsymbol{R}) = V_{\mathrm{c}}(\boldsymbol{r}-\boldsymbol{R}) + V_{corr}(n(\boldsymbol{r}-\boldsymbol{R})). \tag{3.2}$$

In this equation, $V_{\mathrm{c}}(\boldsymbol{r}-\boldsymbol{R})$ represents the net Coulomb potential experienced by the positron due to all other charges in the system of interest. This is equivalent to the Coulomb potential for the electrons, but with the opposite sign. Due to the net positive charge carried by positrons, the Coulomb interaction is strongly repulsive in the vicinity of the nucleus due to the effective positive ionic charge. In the regions away from the atomic positions, this repulsive effect decays and the potential is slightly attractive. On the other hand, whenever an ion core is missing, as in the case of vacancies, the extra positive charge that would repel the positron is completely absent, which leaves a strongly negative potential. At a dangling bond site for instance, the extra electron of the sp^3 hybridized orbitals acts as a potent trap for positrons.

$V_{corr}(n(\boldsymbol{r}-\boldsymbol{R}))$ is the zero positron density limit of the electron-positron correlation potential defined in terms of the density of electrons responding to the presence of positrons. Physically, the electron-positron correlation potential acts as a function whose effect is to pile up electrons in the vicinity of the positron. $\boldsymbol{R}$ is used to denote the coordinate of the centre of symmetry of a given defect so that the positron density depletes where the electron density is enhanced [239]. The strength of this potential and the degree of response to the presence of positron depend on the character of electrons. It is largest for nearly-free electrons, and smallest for tightly bound core electrons. It is generally believed that the density of the core electrons is larger near the nuclei, and that in the vicinity of the nuclei, interplay of Coulomb repulsive interactions and electron-positron correlations contribute to the electron positron potential. This situation suggests that it matters very little how the electron-positron correlation potential $V_{corr}(n(\boldsymbol{r}-\boldsymbol{R}))$ is constructed near the nucleus.

In order to calculate the positron properties in the simulated bulk and isolated *ad hoc* defect structures of *a*-Si:H, the zero positron density limit of the TCDFT approach of Boroński and Nieminen [240] was adopted. The electron density needed for the calculation of the electron-positron correlation potential is based on the atomic superposition (ATSUP) method for atomic potentials and charge densities [241]. The ATSUP method utilizes electron densities, obtained from free atoms, to construct the charge density of the whole solid. An approximate charge density distribution in *a*-Si:H is calculated by building up charges in the simulated amorphous cell by superimposing atomic charge densities, so that the total electron density becomes

$$n_{-}(\boldsymbol{r}) = \sum_{\mathrm{i}} n_{at}(|\boldsymbol{r} - \boldsymbol{R}|), \tag{3.3}$$

and the Coulomb potential can be expressed in terms of the superimposed charge densities as

$$V_C(\boldsymbol{r}) = \sum_{\mathrm{i}} V_{at}(|\boldsymbol{r} - \boldsymbol{R}|). \tag{3.4}$$

Here, $\boldsymbol{R}$ specifies occupied atomic sites, and n_{at} and V_{at} denote the electron density and Coulomb potentials respectively.

3.2.2 Electron-Positron Band Structure Calculation

The foundation for electron-positron energy band structure calculations is the density functional theory [242], based on the work of Hohenberg and Kohn [52], with further developments by Kohn and Sham [243]. Over the years, this method has been developed to the extent that, most basic properties of solids can now be calculated accurately, without adjustments or fittings to experimental results [244,245]. In this thesis, interest is in the *ab initio* calculation of positron annihilation properties, such as positron lifetime, binding energy, and annihilation rate in *a*-Si:H. Quite fortunately, the two component generalization of the density functional theory [246-248] is well-suited for such calculations. The positron states and annihilation characteristics, such as wave function, binding energy, positron induced forces, annihilation rates of different atomic orbitals, momentum distribution of annihilating electron-positron pairs in solids were calculated using the code DOPPLER [249], developed at the Helsinki University of Technology, Finland.

To solve for the electron and positron densities, the total energy functional $E[n_-, n_+]$, for the electron-positron system in an external potential $V_{ext} = \sum_{\mathrm{i}} \frac{Z_{\mathrm{i}}}{|\boldsymbol{r} - \boldsymbol{R}_{\mathrm{i}}|}$, must be obtained in terms of the average electron and positron densities as

$$E[n_-, n_+] = F[n_-] + F[n_+] + \int dr \sum_{\mathrm{i}} \frac{Z_{\mathrm{i}}}{|\boldsymbol{r} - \boldsymbol{R}_i|}[n_-(\boldsymbol{r}) - n_+(\boldsymbol{r})] - \int dr \int dr' \frac{n_-(\boldsymbol{r}) n_+(\boldsymbol{r}')}{|\boldsymbol{r} - \boldsymbol{r}'|} + E_{\mathrm{c}}^{\mathrm{e-p}}[n_-, n_+]. \quad (3.5)$$

In this case, Z_{i} is the ionic charge and, $\boldsymbol{R}_i$ is the position vector of the ith ion, $E_c^{e-p}[n_-, n_+]$ is the electron-positron correlation energy functional, and F is the one-component functional of the density that minimizes the total energy of a positron, or an electron,

$$F[n] = T[n] + \frac{1}{2} \int dr \int dr' \frac{n(\boldsymbol{r}) n(\boldsymbol{r}')}{|\boldsymbol{r} - \boldsymbol{r}'|} + E_{xc}[n]. \quad (3.6)$$

$T[n]$ denotes the kinetic energy functional of non-interacting electrons or positrons, and $E_{xc}[n]$ denotes the exchange-correlation energy between the indistinguishable particles. The ground state electron and positron densities that minimize the energy $E[n_-, n_+]$, are then calculated using the generalized Kohn-Sham method. This requires, finding solutions to the one-particle Schrödinger equation for positron and electron states simultaneously

$$-\frac{1}{2} \nabla^2 \psi_i^+(r) + V_{eff}(r) \psi_i^+(r) = \varepsilon_i \psi_i^+(r), \quad (3.7)$$

and

$$-\frac{1}{2} \nabla^2 \psi_i^-(r) + V_{eff}(r) \psi_i^-(r) = \varepsilon_i \psi_i^-(r), \quad (3.8)$$

to determine the positron wave functions $\psi^+(r)$. The effective potential is expressed as

$$V_{eff} = V_c^T(r) + \frac{\delta E_{xc}[n_+]}{\delta n_+(r)} + \frac{\delta E_c^{e-p}[n_+, n_-]}{\delta n_+(r)}. \quad (3.9)$$

For the electron-positron system, $V_c^T(r)$ is the total Coulomb potential given by

$$V_C^T(r) = \int dr' \frac{n_+(r') + n_0(r') - n_-(r')}{|r - r'|}, \tag{3.10}$$

where, $n_0(r')$ is the positive charge density, which gives rise to the external potential V_{ext}. In order to determine the electron wave function for electron states, the effective potential V_{eff} in Eqns. (3.7), and (3.8) is the same as in Eqn. (3.9), with n_+ and n_- swapped, and the sign of the total Coulomb potential reversed. From the computed wave functions, the electron and positron densities can be obtained as

$$n_-(r) = \sum_{\varepsilon_i \le \varepsilon_f} |\psi_i(r)|^2, \quad n_+(r) = \sum_i^{N_+} |\psi_i^+(r)|^2 . \tag{3.11}$$

It is important to note that in Eqn. (3.11), the summation over electron states is up to the Fermi level, whereas only one positron state ($N_+ = 1$) needs to be considered.

The resulting eigenvalue problem is solved simultaneously for electron and positron states using the Rayleigh-Ritz method. This is based on an iterative procedure of minimizing the Rayleigh quotient using multigrids [250]. The charge densities obtained from neutral atoms are superposed to obtain the total electron density. Therefore, energy eigenvalues are obtained relative to the vacuum level. Since the positron energy is relative to the crystal zero, the positron binding energy in a given defect is obtained, as the energy difference between the positron energy eigenvalue in the system with a defect (positron localized) and in a system without it (positron delocalized). The resulting electron and positron wave functions are then used in evaluating the annihilation rate and positron lifetime at a given defect site.

3.2.3 Momentum Distribution Function

In order to compute the momentum distribution due to the core-state contributions, a parameterized form of the normalized positron wave function is used [251,252],

$$\psi_+(r) \approx a_0 + a_1\left(erf\left(\frac{r}{a_2}\right)\right)^{a_3} = a_0 + a_1\left(\frac{1}{\sqrt{2\pi}}\int_{-\infty}^{r} e^{-\left(\frac{r}{a_2\sqrt{2}}\right)^2} dr\right)^{a_3}, \qquad (3.12)$$

where r is the distance from the centre of the atomic sphere, and a_i are fitted parameters, with $i \in \{0,...,3\}$. The fitted parameters have been calculated for all the elements of the periodic table using the linear muffin-tin orbital method, within the atomic sphere approximation (LMTO-ASA) [253]. It is noteworthy, that for a particular atomic species, the only significant difference in these parameters is the first term a_0, which offsets the shift in positron wave function due to the overlapping atomic spheres. This ensures that the positions of maximum positron wave function coincide with the positions of minimum in the muffin tin potential, and vice versa. For bulk Si with diamond structure, the values of these fitted parameters are a_0 = 0.000534799, a_1 = 0.104654, a_2 = 2.53842, and a_3 = 1.6848. These values were used for positron calculations involving *a*-Si and *a*-Si:H. It is also important to note, that these values are very sensitive to the environment in which the Si atoms are placed. For example, in 2H-SiC, which crystallizes in the wurtzite structure, a_0 = 0.000674815, a_1 = 0.116239, a_2 = 2.34458, and a_3 = 1.67207. On the other hand, a_0 = 0.000933581, a_1 = 0.166725, a_2 = 2.3982, and a_3 = 1.67046 for Si in 3C-SiC, which crystallizes in the zincblende structure.

This is not wholly unexpected since the positron senses a different potential regime in a different local structure or at a defect. The associated positron wave function must therefore also change with the local environment through the parameters a_i. In Si-C systems, the delicate energetics of alloy disorder [254,255] and its relaxation effects, give rise to mild charge transfer. This makes the use of Si parameters in positron calculations of the wurtzite and zincblende structures inappropriate. In *a*-Si:H, only electrons from sp^3 hybridized orbitals are involved in annihilation events, unlike in Si-C alloys, where the annihilated electron could originate from sp^2, or other types of hybridized orbitals. This makes the use of *c*-Si parameters suitable for the present calculations, because it eliminates the uncertainties introduced by the influence of alloy disorder in Si-C systems.

The approach adopted for calculating the high momentum component (HMC) of the MDAP in *a*-Si:H is based on the concept of the state-dependent enhancement factor, originally introduced by Šob [256, 257] for valence electrons in *d* metals and intermetallic compounds. The motivation for using the state-dependent enhancement factor in this study, arises from its successful application in the analysis of positron annihilation spectra, in metallic systems containing *d* electrons [258-260], and in defect studies in bulk silicon [261]. The contribution $\rho^j(\boldsymbol{p})$ to the MDAP of an electron at quantum state *j* described by wave function $\psi_-^j(\boldsymbol{r})$ is given as

$$\rho^j(\boldsymbol{p}) = \pi r_e^2 c\gamma^j \left|\int exp(-i\boldsymbol{p}.\boldsymbol{r})\psi_-^j(\boldsymbol{r})\psi_+(\boldsymbol{r})d\boldsymbol{r}\right|^2, \qquad (3.13)$$

where $r_e = 2.82\times10^{-13}$ cm is the classical electron radius, and *c* is the speed of light. γ^j represents the enhancement factor for the quantum state *j*, and $\psi_+(\boldsymbol{r})$ represents the position-dependent positron wave function.

Equation (3.13) can be considerably simplified for cases of annihilation from core electrons, if it is assumed that all core states, from all the atoms in a system, contribute to the HMC of the MDAP. The core state contribution from the *i*th atom, and a shell characterized by principal quantum numbers *n* and angular momentum *l* quantum number is given by [262]

$$\rho^{i,nl}(\boldsymbol{p}) = 4\pi^2 r_e^2 cN^{i,nl}\gamma^{i,nl}\left|\int R_+(\boldsymbol{r})R_-^{i,nl}(\boldsymbol{r})j_l(\boldsymbol{p.r})r^2dr\right|^2 . \qquad (3.14)$$

Here, $N^{i,nl}$ denotes the number of electrons in the *nl* subshell, and j_l is the Bessel function. $R_+(\boldsymbol{r})$ and $R_-^{i,nl}(\boldsymbol{r})$ are the positron and electron radial wave functions respectively. This analysis assumes explicitly, that the positron wave function is predominantly of *s*-character. The constant $\gamma^{i,nl}$ denotes the state dependent enhancement factor, which is obtained as the ratio $\lambda_{enh}^{i,nl} / \lambda_{IPM}^{i,nl}$ of the partial annihilation rate $\lambda_{enh}^{i,nl}$ due to a core electron *i* at quantum state *nl*, relative to the IPM annihilation rate of a core electron belonging to the same quantum state.

The high momentum contributions (HMC) to the total momentum distribution of an annihilation event can also be computed [251], as the sum over all atomic sites of the corresponding core shells [252,262],

$$\rho(\boldsymbol{p}) = \sum_{i,nl} \int_{\mathrm{p}}^{\infty} \rho^{i,nl}(\rho')p'\,dp' . \tag{3.15}$$

Eqn. (3.15) applies only to the core electrons, and can be extended to study Doppler broadening of the annihilation line shapes due to core electrons in *a*-Si:H. Taking into consideration that the results of the valence and core electron contributions to the momentum distribution of annihilation photons (MDAP) in *a*-Si, can be reasonably compared to those of bulk *c*-Si [263], then in the context of the present study, any measured dependencies of the HMC will only be meaningful for momenta in the range $p_z \geq 10 \times 10^{-3}\, m_e c$.

The partial annihilation rate $\lambda^{i,nl}$ corresponding to the contributions of the *nl* core state of the *i*th atom to the total annihilation rate can be determined using the expression

$$\lambda^{i,nl} = \pi r_e^2 c \int \left|\psi_+(\boldsymbol{r})\right|^2 n_-^{i,nl}\left(\left|\boldsymbol{r} - \boldsymbol{r}_{\mathrm{i}}\right|\right)\gamma^{i,nl}\left[n_-(\boldsymbol{r})\right]dr . \tag{3.16}$$

In this case, $n_-^{i,nl}\left(\left|\boldsymbol{r} - \boldsymbol{r}_{\mathrm{i}}\right|\right)$ represents the radial core electron density per electron from the orbital *nl* of the *i*th atom, whose location is prescribed by position vector $\boldsymbol{r}_{\mathrm{i}}$. Here $\gamma^{i,nl}\left[n_-(\boldsymbol{r})\right]$ is the state dependent enhancement factor. It describes the piling up of electrons at positron site. The subscript IPM in the enhancement factor implies that the corresponding partial annihilation rate is calculated based on the independent particle model [263].

3.2.4 Positron Annihilation Rate and Lifetime

The total annihilation rate is proportional to the electron density at the position of the positron. It is evaluated in terms of the overlap integral of the electron and positron densities. When the electron and positron densities are known exactly, the conventional way of evaluating the positron annihilation rate is written as

$$\lambda = \pi r_e^2 c \int n_+(r)n_-(r)\Gamma(n_-(r))dr . \tag{3.17}$$

Unfortunately, in this case, the electron and positron densities are not known exactly. Hence, the electron-density enhancement $\Gamma(n_-(r))$ has to be calculated approximately. For a single positron in an electron gas, the contact density enhancement can be approximated by the Brandt-Reinheimer expression [264]

$$\Gamma(n_-) = 1 + \frac{\left(r_s^3(n_-) + 10\right)}{6}. \tag{3.18}$$

This equation is only valid for a single positron in an electron gas. In this case, $\Gamma(n_-(r))$ is the zero positron density ($n_+ \rightarrow 0$) limit of the electron-positron pair correlation function $g(0; n_+, n_-)$.

Within the two component density functional theory, Eqn. (3.17) must be replaced with the form [240,246]:

$$\lambda = \frac{1}{\tau} = \pi r_e^2 c \int n_+(r) n_-(r) g(0; n_+, n_-) dr . \tag{3.19}$$

The positron lifetime, τ is denoted by the inverse annihilation rate constant. This provides an estimate of the local electron density in a given structure. The zero-positron density limit of the pair correlation function $g(0; n_+, n_-)$, in Eqn. (3.19), is commonly denoted by γ, to represent the density of electrons in the vicinity of the positron. The most trivial form is simply when $\gamma = 1$. This approximation corresponds to the independent particle model, but its use in positron calculations does not yield good results. Whenever an approximation for $g(0; n_+, n_-)$ is required, a new formula for the contact density must be used, to correctly describe the enhancement effects in the electron-positron system.

It is very important to recall, that the electron-positron correlation energy, $E_c^{e-p}[n_-, n_+]$, and the exchange-correlation energy per particle in a one-component gas, $E_{xc}[n]$, which are terms that enter the expression for the effective positron potential V_{eff}(r) in Eqn. (3.9), are not known exactly. In fact these are treated as error terms in the total energy functional, and therefore require some form of approximation to estimate. In the case of the exchange-correlation energy, the usual procedure is to employ the local density approximation (LDA), in which the exchange-correlation energy is expressed approximately in terms of the exchange correlation energy of a homogeneous electron gas, with the replacement of the constant density n_0 by the local density $n(r)$. In this work, two

LDA based approximations for the contact density enhancement factor $g(0;n_+,n_-)$ are used.

The conventional scheme is based on the local density approximation (LDA), which uses the interpolation form suggested by Puska [265]. In this approximation, the attractive part of the positron potential due to electron-positron correlation effects is based on the Boronski and Nieminen many body calculations for a delocalized positron in a homogenous electron gas [240,246]. In this scheme, denoted as ATSUP-LDA-BN, the contact density becomes:

$$g(0;n_+,n_-) = 1 + 1.23r_s + 0.8295\,r_s^{\frac{3}{2}} - 1.26r_s^2 + 0.3286\,r_s^{\frac{5}{2}} + \left(1 - \tfrac{1}{\varepsilon_\infty}\right)\tfrac{r_s^3}{6}\,. \qquad (3.20)$$

The use of LDA for the computation of the annihilation rate also means, that the contact density, including the average density, and the density enhancement due to electron-positron correlation, depends, at a given point, on the total electron density at that point. The second approximation of the contact density is the form proposed by Arponen and Pajane [266]. In this case, the contact density has the form

$$g(0;n_+,n_-) = 1 + 1.23r_s - 0.0742r_s^2 + +\left(1 - \tfrac{1}{\varepsilon_\infty}\right)\tfrac{r_s^3}{6}\,. \qquad (3.21)$$

Results obtained within the LDA scheme, using the above parameterization, is denoted ATSUP-LDA-AP. For *a*-Si:H, the value for the high frequency dielectric constant of Si, ε = 11.7 [267] was used for the calculation of positron properties in both approximations.

The local density approximations (LDA) for $g(0;n_+,n_-)$ are calculated based on the homogenous electron gas model [268]. This simplified model suffices for metallic systems, where the screening of a positron by the conduction electrons can be described in terms of the free electron gas model. This model is quite good in predicting the positron annihilation rate and the positron lifetime at metallic densities, where 2 ≤ r_s ≤ 6. This is because in metals, the annihilation rate depends on the electron density at the site of the positron n_0, which makes contact with the positron. In the free electron gas model, n_0 is dependent on the ambient electron density, $n_v = \frac{3}{4\pi r_s^3}$, where r_s is the radius of the Wigner-Seitz cell, which for Si has a value of r_s = 1.68Å [269]. In most semiconductors and insulators the presence of an energy band gap prevents the valence electrons from responding effectively to external perturbations, unlike in metallic systems, hence the screening is not perfect. It is therefore not suitable to base the calculation of the annihilation rate on the free-electron gas model only. The screening for semiconductors proposed in Ref. [270], shows, that the dielectric constant ε must enter the contact density enhancement factor $g(0; n_+, n_-)$ explicitly.

Moreover, even in single-component electronic structure calculations, the LDA approximation has been shown to suffer from several shortcomings [271,272]. These include the prediction of:

(i) too diffuse electron densities, which lead to under-binding in free atoms [273,274];

(ii) over-binding in small molecules and extended solids [275,276]; and

(iii) too narrow band gaps in semiconductors and insulators [277-280].

In LDA-based positron calculations, these shortcomings result in an over estimation of positron properties. As a result, an alternative scheme based on the generalized gradient approximation has been proposed [281,282]. In this scheme, the effects of the non-uniform electron density are described in terms of the ratio between the local length scale $n_- / |\nabla n_-|$ of the density variations and the local Thomas-Fermi screening length $1/q_{TF}$. The zeroth-order correction to the LDA correlation hole density which describes the variation in electron density is given by

$$\varepsilon = \frac{|\nabla n_-|^2}{(n_- q_{TF})^2} = \frac{|\nabla \ln(n_-)|^2}{(q_{TF})^2}, \tag{3.22}$$

where,

$$q_{TF} = \left[\frac{4}{\pi}\left(3\pi^2 n_-\right)^{\frac{1}{3}}\right]^{\frac{1}{2}}. \tag{3.23}$$

The effective dielectric constant ε, is used to describe the reduction in the screening cloud in the vicinity of the positron. For an homogenous electron gas, $\varepsilon = 0$, whereas for an electron system with rapidly changing density $\varepsilon = \infty$. In the limiting cases where $\varepsilon = 0$, the LDA result for induced screening charge is valid, whereas, the limit $\varepsilon = \infty$ leads to the independent particle model, in which the contact density enhancement vanishes. In order to interpolate between these two limiting cases, a corrected enhancement factor of the form

$$g^{GGA}(0; n_+, n_-) = 1 + \left[g^{LDA}(0; n_+, n_-) - 1\right] exp(-\alpha\varepsilon), \tag{3.24}$$

is applied. Setting α = 0.22 in the expression above gives the GGA scheme [281,282]. This is to ensure that the calculated and experimental positron lifetimes agree as well as possible for a large number of different types of structures. Alternatively, setting α = 0 corresponds to the LDA scheme. The results obtained within the GGA scheme using the above parameterization are denoted by ATSUP-GGA.

Chapter Four

Modelling Stress and Strain

This chapter presents the classical and quantum mechanical descriptions of stress and strain. Emphasis is on residual stress, and three different types are described. The methods and algorithms used in the evaluation of residual stress in simulated structures are also presented.

4.1 Continuum Theory of Strain

The continuum model of describing the properties of a material is based on the mathematical concept in which the mass densities, linear and angular momenta, and total energy of a macroscopic body depend explicitly on the spatial degrees of freedom [283]. This idea can be used to describe the changes in the body in a manner that ignores the local structure of the material. In the continuum model, it is assumed that the average mass density ρ of the portion of the body δM, occupying a volume δV, which contains an arbitrary point O, as shown in Fig. 4.1 is mathematically defined as $\delta M/\delta V$.

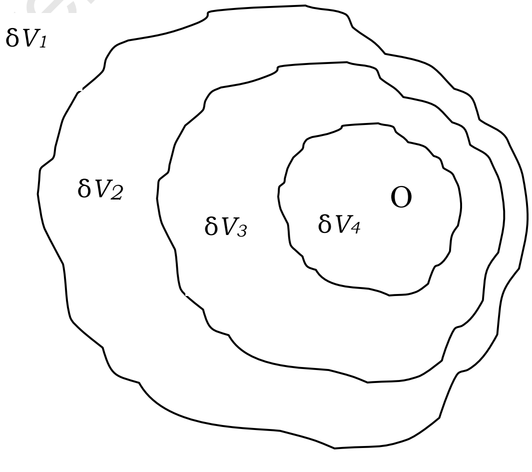

Figure 4.1 Spatial domain of volume δV containing an infinitesimal amount of matter δM, as the volume converges to point O in the structure.

Thus a limit exists for the average density as the volume δV shrinks through a sequence of smaller volumes δV_1, δV_2, δV_3, …, δV_n converging on *O*. This limiting value characterizes the mass distribution at point *O*, and is defined as

$$\rho = \lim_{\substack{i\to\infty \\ \delta V\to 0}} \frac{\delta M_i}{\delta V_i}\,, \tag{4.1}$$

where i denotes the sequence count of the shrinking volume element. In order to use the above concept to describe strain in the framework of the continuum theory in a deformable solid, a simplified case is considered, in which the body undergoes a deformation only, but no rigid body rotation or translation [284]. Such a deformation can manifest itself either as a change in shape or volume, so that the volume elements within the original volume are displaced from their initial positions. It is further assumed, that such a volume element of the unstrained, homogeneous body can be represented by a cube, and that three orthogonal unit vectors $\hat{\boldsymbol{x}}$, $\hat{\boldsymbol{y}}$ and $\hat{\boldsymbol{z}}$ located at a point in the material, as shown in Fig. 4.2, define the origin of a coordinate system.

After the solid has undergone a deformation, the volume element, and also the axes of the coordinate system are affected in orientation and length. The new axes $\boldsymbol{x}'$, $\boldsymbol{y}'$ and $\boldsymbol{z}'$ can be expressed in terms of the old axes according to [57]

$$\boldsymbol{x}' = (1+\varepsilon_{xx})\hat{\boldsymbol{x}} + \varepsilon_{xy}\hat{\boldsymbol{y}} + \varepsilon_{xz}\hat{\boldsymbol{z}}; \quad \boldsymbol{y}' = \varepsilon_{yx}\hat{\boldsymbol{x}} + (1+\varepsilon_{yy})\hat{\boldsymbol{y}} + \varepsilon_{yz}\hat{\boldsymbol{z}}; \text{ and } \boldsymbol{z}' = \varepsilon_{zx}\hat{\boldsymbol{x}} + \varepsilon_{zy}\hat{\boldsymbol{y}} + (1+\varepsilon_{zz})\hat{\boldsymbol{z}}. \tag{4.2}$$

The transformation tensor ε in Eqn. (4.2) will be shown below to be equivalent, for a small deformation, to the strain tensor. It is clear that after deformation, the vectors of the new axes are no longer of unit length, because the inner products, $\boldsymbol{x}'\cdot\boldsymbol{x}'$, $\boldsymbol{y}'\cdot\boldsymbol{y}'$, and $\boldsymbol{z}'\cdot\boldsymbol{z}'$ are each no longer equal to one. Assuming that the origin of the coordinate system is fixed at the centre of the volume element, and let the location of the volume element be uniquely specified by the position vector $\boldsymbol{r} = x\hat{\boldsymbol{x}} + y\hat{\boldsymbol{y}} + z\hat{\boldsymbol{z}}$, then, the obvious question arises: what is the effect of the deformation on the position of the volume element? For a uniform deformation, the point will be at position, $\boldsymbol{r}' = x'\hat{\boldsymbol{x}}' + y'\hat{\boldsymbol{y}}' + z'\hat{\boldsymbol{z}}'$, where the primed coordinate system is located at a different atom and $\hat{\boldsymbol{x}}'$, $\hat{\boldsymbol{y}}'$, and $\hat{\boldsymbol{z}}'$ are unit vectors in this system.

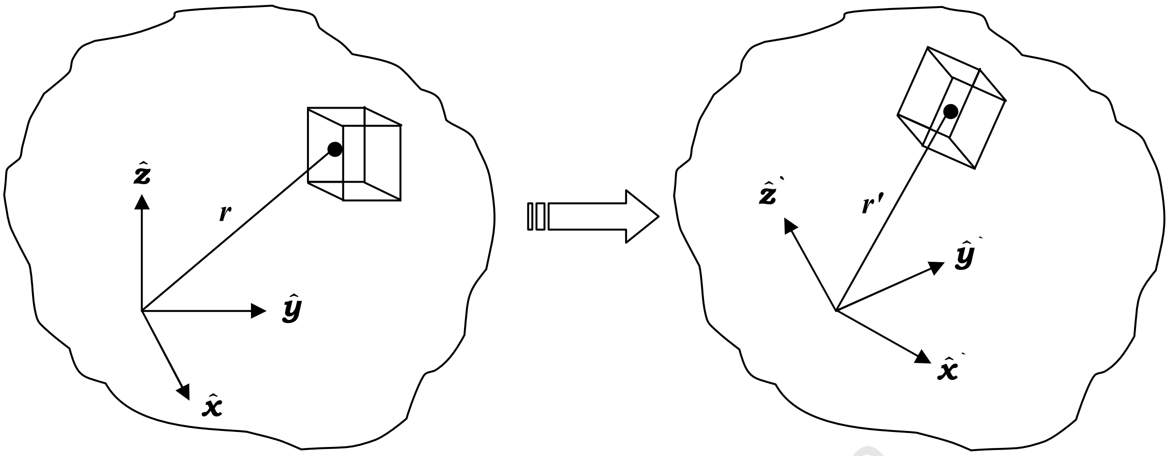

Figure 4.2 Sketch of the coordinate axes used to describe the state of strain, in terms of the orthogonal unit axes (x, y, z) fixed on a spatial domain in the unstrained state and (x', y', z') showing a uniform deformation of the strained state.

The displacement vector $\boldsymbol{R}$ can then be defined as

$$\boldsymbol{R}(\boldsymbol{r}) \equiv \boldsymbol{r}' - \boldsymbol{r} = (x' - x)(\hat{\boldsymbol{x}}' - \hat{\boldsymbol{x}}) + (y' - y)(\hat{\boldsymbol{y}}' - \hat{\boldsymbol{y}}) + (z' - z)(\hat{\boldsymbol{z}}' - \hat{\boldsymbol{z}}). \qquad (4.3)$$

For simplicity, for the magnitudes, and the corresponding unit vectors, the following identities x'-$x \equiv X$, y'-$y \equiv Y$ and z'-$z \equiv Z$ are introduced, so that the displacement vector becomes $\boldsymbol{R}(\boldsymbol{r}) \equiv \boldsymbol{r}' - \boldsymbol{r} = X\hat{\boldsymbol{X}} + Y\hat{\boldsymbol{Y}} + Z\hat{\boldsymbol{Z}}$. In terms of Eqn. (4.2) the deformation vector is

$$\boldsymbol{R}(\boldsymbol{r}) = \left(X\varepsilon_{xx} + Y\varepsilon_{yx} + Z\varepsilon_{zx}\right)\hat{\boldsymbol{X}} + \left(X\varepsilon_{xy} + Y\varepsilon_{yy} + Z\varepsilon_{zy}\right)\hat{\boldsymbol{Y}} + \left(X\varepsilon_{xZ} + Y\varepsilon_{yZ} + Z\varepsilon_{zZ}\right)\hat{\boldsymbol{Z}}. \qquad (4.4)$$

This expression is generalized by introducing local variables u, v and w [57], so deformation, the displacement vector in any direction will vary from point to point. This implies that the components of the displacement vector, u, v, and w must be related to the local strain. Equating Eqns. (4.3) and (4.4), and using this result in a Taylor series expansion of the displacement vector $\boldsymbol{R}$, where $\boldsymbol{R}(\boldsymbol{r} = 0) = 0$, gives nine components of a second rank tensor:

$$
\begin{aligned}
&X\varepsilon_{xx} = X\frac{\partial u}{\partial x}, \quad && Y\varepsilon_{yx} = Y\frac{\partial u}{\partial y}, \quad && Z\varepsilon_{zx} = Z\frac{\partial u}{\partial z}, \\
&X\varepsilon_{xy} = X\frac{\partial v}{\partial x}, \quad && Y\varepsilon_{yy} = Y\frac{\partial v}{\partial y}, \quad && Z\varepsilon_{zy} = Z\frac{\partial v}{\partial z}, \\
&X\varepsilon_{xz} = X\frac{\partial w}{\partial x}, \quad && Y\varepsilon_{yz} = Y\frac{\partial w}{\partial y}, \quad && Z\varepsilon_{zz} = Z\frac{\partial w}{\partial z}.
\end{aligned}
\tag{4.6}
$$

Physically, the tensor must be symmetrical [57], which leads to its final form

$$
\varepsilon = \begin{pmatrix} \varepsilon_{xx} & \varepsilon_{xy} & \varepsilon_{xz} \\ & \varepsilon_{yy} & \varepsilon_{yz} \\ & & \varepsilon_{zz} \end{pmatrix}.
\tag{4.7}
$$

The principal strain components are the diagonal terms of the 3×3 matrix:

$$
\varepsilon_{xx} = \frac{\partial u}{\partial x}; \; \varepsilon_{yy} = \frac{\partial v}{\partial y}; \text{ and } \varepsilon_{zz} = \frac{\partial w}{\partial z}.
\tag{4.8}
$$

The off-diagonal terms represent the shear strain components. Taking the symmetric part of Eqn. (4.6)

$$
\begin{aligned}
\varepsilon_{xy} &= \varepsilon_{yx} = \frac{1}{2}\left(\frac{\partial u}{\partial y} + \frac{\partial v}{\partial x}\right); \\
\varepsilon_{yz} &= \varepsilon_{zy} = \frac{1}{2}\left(\frac{\partial v}{\partial z} + \frac{\partial w}{\partial y}\right); \\
\varepsilon_{zx} &= \varepsilon_{xz} = \frac{1}{2}\left(\frac{\partial u}{\partial z} + \frac{\partial w}{\partial x}\right).
\end{aligned}
\tag{4.9}
$$

The six independent components $\varepsilon_{\alpha\beta}$ completely specify the strain, where the indices α and β represent any Cartesian component x, y, or z directions. This implies that a coordinate system can always be found, where the strain tensor has non-zero components only along its diagonal. This is the principal coordinate system.

4.2 Continuum Theory of Stress

Stress is a second rank tensor, which is defined to specify the interaction between adjacent parts of a body with each other [285]. In a body without a force acting on it, all parts of the material are in equilibrium with each other. This means that at any time, the resultant force on any portion of the material is zero. Whenever a force is applied, the macroscopic dimensions of the body change, and the body is no longer in its original state of equilibrium. As a consequence, within the elastic limit, forces arise within the material, which tend to return the body to its original state of equilibrium. These restoring forces, which act when the body is deformed, can be described in terms of a stress.

The tensor formulation of stress, based on the continuum approach, was first given by Cauchy in 1822 [286]. In a region of a continuum, bounded by a closed surface of area A, and volume *V,* the interaction between the material outside *A* and that inside can be divided into two kinds of interaction:

(i) surface forces due to the action across a boundary of surface area *A*, and

(ii) body forces due to "action-at-a-distance" type of forces, *e.g.* gravitational or electromagnetic forces, which can be expressed as the resultant force per unit volume.

In order to express the surface forces in a body, an infinitesimal surface element of area ΔA is considered on the imaginary closed surface which can be identified by its vector normal $\hat{\boldsymbol{n}}$, pointing out from the interior of *A*, as shown in Fig. 4.3. The material on either side of ΔA exerts a force $\Delta\boldsymbol{F}$ on the surface element. For a given distribution of forces, $\Delta\boldsymbol{F}$ depends on the location, size of the surface element, and the orientation of the normal vector $\hat{\boldsymbol{n}}$. As ΔA approaches zero, the ratio $\Delta\boldsymbol{F}/\Delta A$ tends to a definite limit $d\boldsymbol{F}/dA$, and the moment, due to the force $\Delta\boldsymbol{F}$ acting on the surface ΔA about any point within the surface of area *A*, vanishes in the limit. The limiting vector can be written as

$$\boldsymbol{T} = \lim_{\Delta A \to 0} \frac{\Delta F}{\Delta A}\hat{\boldsymbol{n}}, \tag{4.10}$$

where $\boldsymbol{T}$ is the traction or stress vector representing the force per unit area acting on the surface. Thus, the forces exerted on any given part of a body by its surroundings, acts only on the surface of that part of the body. The description of the interaction between the inside and outside of an imaginary closed surface in a material using the stress vector is called the Euler-Cauchy stress principle [287].

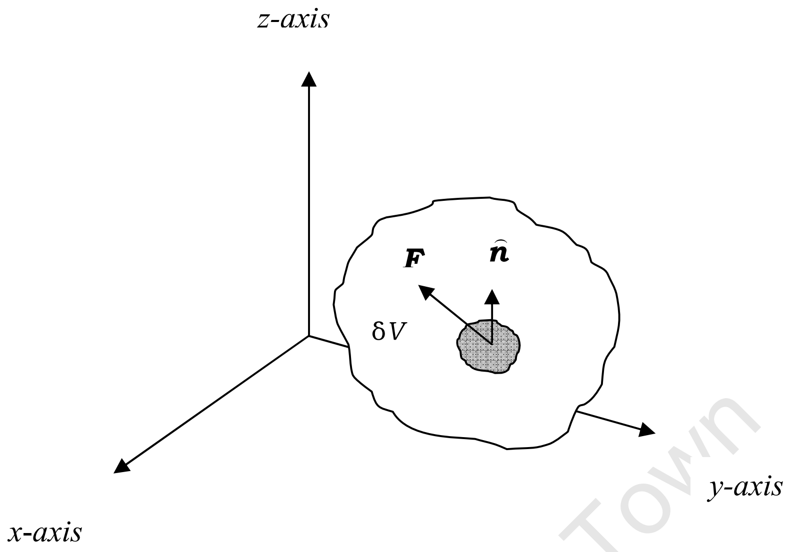

Figure 4.3 Stress principle showing the interaction between adjacent points in a continuum.

Assuming that an arbitrary surface ΔA_α, where $\alpha = x, y$, or z, is orientated perpendicular to any one of the axes of the Cartesian coordinates, so that the projection of the normal vector $\hat{\boldsymbol{n}}$ to the surface of area δA is in the positive direction of the axis, the traction vector T_α, must act along the direction of the coordinate axis. Thus the traction vector has three components: $\boldsymbol{T}_x$, $\boldsymbol{T}_y$ and $\boldsymbol{T}_z$. The components of the traction vector are used to introduce the stress tensor using Eqn. (4.10). $\boldsymbol{T}_x = \sigma_{xx}\hat{\boldsymbol{x}}$; $\boldsymbol{T}_y = \sigma_{yy}\hat{\boldsymbol{y}}$; and $\boldsymbol{T}_z = \sigma_{zz}\hat{\boldsymbol{z}}$, where $\hat{\boldsymbol{x}}$, $\hat{\boldsymbol{y}}$, and $\hat{\boldsymbol{z}}$ represent the unit vectors parallel to the x, y, and z directions respectively.

Assuming that the resultant forces acting on a macroscopic body can be represented in magnitude and direction as normal components of the forces acting on the faces of the cube, then the parallel components of the forces will act on the planes parallel to the area of the faces of a cubic volume element, as shown in Fig. 4.4. The shearing forces acting in the planes parallel to the faces x, y and z, give rise to shear stresses in these directions given by:

$$\sigma_{xy} = \frac{+F_x}{xy};\ \sigma_{yx} = \frac{-F_y}{yx};\ \sigma_{yz} = \frac{+F_x}{yz};\ \sigma_{zy} = \frac{-F_z}{zy};\ \text{and}\ \sigma_{xz} = \frac{+F_z}{xz};\sigma_{zx} = \frac{-F_z}{zx}. \quad (4.13)$$

The normal forces acting per unit area in the planes normal to the *x*-, *y*- and *z*-planes are given by

$$\sigma_x = \frac{+F_x}{x^2};\quad \sigma_y = \frac{+F_y}{y^2};\ \text{and}\quad \sigma_z = \frac{+F_z}{z^2}. \quad (4.14)$$

The stresses arising from the shearing forces that act in opposing directions are equal. Hence, $\sigma_{xy} = \sigma_{yx}$; $\sigma_{yz} = \sigma_{zy}$ and $\sigma_{xz} = \sigma_{zx}$.

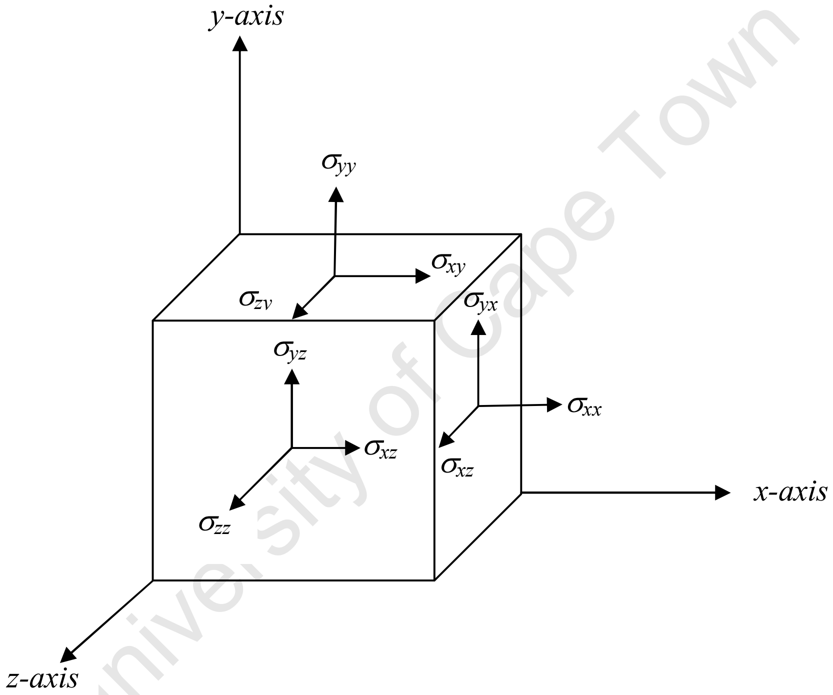

Figure 4.4 Orientations of the triaxial stress tensor components acting on the faces of a cube in static equilibrium showing the effects of normal and shearing forces.

There are three normal forces which give rise to normal stresses. The normal components of forces acting on each face of volume element will give rise to normal stresses $\sigma_{\alpha\beta}$ ($\alpha = \beta$). On the other hand, two equal and opposite shearing forces acting on each face will give rise to the shear stresses $\sigma_{\alpha\beta}$ ($\alpha \neq \beta$), which taken together gives nine components of the stress tensor. The stress tensor is symmetric since $\sigma_{\alpha\beta}$ = $\sigma_{\beta\alpha}$ as described above. Six independent components of $\sigma_{\alpha\beta}$ completely describes the stress state in a material. A triaxial stress state can therefore be expressed as

$$\sigma_{\alpha\beta} = \begin{pmatrix} \sigma_{xx} & \sigma_{xy} & \sigma_{xz} \\ & \sigma_{yy} & \sigma_{yz} \\ & & \sigma_{zz} \end{pmatrix}. \tag{4.15}$$

It is possible to perform a coordinate transformation so that the stress state is described only by normal stresses. In such a system, the normal stresses are known as the three principal stresses σ_x, σ_y and σ_z [287]. Besides the most general triaxial stress states, the stress can also occur in a uniaxial, biaxial and hydrostatic forms as shown in Fig. 4.5 [288]. In terms of the second rank tensor, the stress tensor for the uniaxial stress state is

$$\sigma_{\alpha\beta} = \begin{pmatrix} \sigma_x & 0 & 0 \\ 0 & 0 & 0 \\ 0 & 0 & 0 \end{pmatrix}. \tag{4.16}$$

A biaxial stress state can be represented by

$$\sigma_{\alpha\beta} = \begin{pmatrix} \sigma_x & \sigma_{xy} & 0 \\ \sigma_{yx} & \sigma_y & 0 \\ 0 & 0 & 0 \end{pmatrix}, \tag{4.17}$$

where the *x-y* plane represents the plane of the surface of the flat plate shown in Fig. 4.5 (b). The tensor given by Eqn. (4.17) characterizes a stress state that lies in the plane.

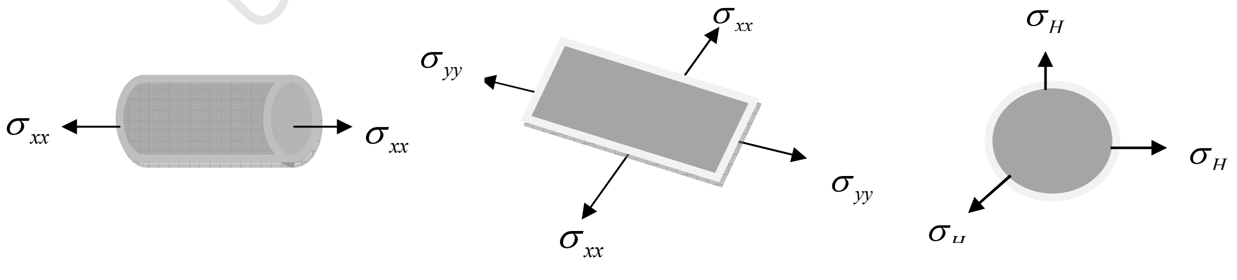

(a) (b) (c)

Figure 4.5: Representations of common stress states in materials: (a) uniaxial, (b) biaxial, and (c) triaxial (after Ref. [288]).

The hydrostatic stress state can be represented by

$$\sigma_{\alpha\beta} = \begin{pmatrix} \sigma_{\mathrm{H}} & 0 & 0 \\ & \sigma_{\mathrm{H}} & 0 \\ & & \sigma_{\mathrm{H}} \end{pmatrix}, \tag{4.18}$$

where $\sigma_x = \sigma_y = \sigma_z = \sigma_H$. In this case the stress is the same in all directions, and can be interpreted as a hydrostatic pressure. It is necessary to note, that for hydrostatic stress, the off-diagonal, or shear, components are always equal to zero in equilibrium.

4.3 Quantum Mechanical Theory of Stress

The quantum mechanical theory of stress originates from the quantum mechanical virial theorem [289-291], in which the total pressure in a many-body system is shown to depend on the kinetic energy, and the virial of the potential energy. It closely resembles the Hellman-Feynman force theorem [292,293], originally derived by Ehrenfest [294]. The stress tensor introduced into quantum mechanics by Schrödinger [295] and Pauli [296], can be derived for a many-body system by applying the variational principle, together with a scaling of the wave function. Nielsen and Martin [297,298] used the force theorem to derive an explicit, practical expression for the stress tensor of a solid.

In the derivation, it is assumed that total energy of a body can be obtained as the expectation value of the generalized many-body Hamiltonian of the form,

$$E_{tot} = \langle H_{int} + V_{ext} \rangle = \left\langle \sum_i \frac{p_i^2}{2m_i} + V_{int} + V_{ext} \right\rangle, \tag{4.19}$$

where p_i denotes the momentum of particle i, m_i is the mass of the i-th atom and V is the potential energy, which is a function of the positions r_i of all the particles. It is important to note, that i denotes both nuclei and electrons. The potential energy is divided into an internal part V_{int}, which is intrinsic to the system under consideration, and an external part V_{ext}, which describes all external influences. The solutions of the Schrödinger equation $H|\Psi\rangle = E|\Psi\rangle$

define the exact many body eigenstates $|\Psi\rangle$ and energies *E*. The variational arguments require, that the ground state energy of the many body Hamiltonian, in Eqn (4.19), is determined by the minimum of the expectation value of $\langle\Psi|\mathrm{H}|\Psi\rangle$ with respect to all allowed variations in $|\Psi\rangle$.

To derive the stress theorem [297,298], an infinitesimal homogeneous scaling is applied to the ground state wave function, $|\Psi\rangle$. It is equally relevant to note, that $|\Psi\rangle$ = $\Psi(\boldsymbol{r})$, where $\boldsymbol{r}$ denotes the position vector of all particles in the solid. The ground state wave function $\Psi(\boldsymbol{r})$ is stretched by applying the linear transformation to each particle cordinate $r_{i\alpha} \rightarrow r_{i\alpha} + \sum_{\beta}\varepsilon_{\alpha\beta} r_{i\beta}$, where $\varepsilon_{\alpha\beta}$ is the symmetric (*i.e.* rotation-free) strain tensor [284,299]. The quantum mechanical derivation of the macroscopic stress in a body follows from the variational property that, a stretching of the wave function of the ground state of the body does not change the total energy to first order [290]. The new, strained wave function is evaluated as a determinant

$$\Psi_{\varepsilon}(\boldsymbol{r}) = det\left|\frac{1}{\sqrt{1+\varepsilon}}\Psi\left(\frac{\boldsymbol{r}}{1+\varepsilon}\right)\right|, \tag{4.20}$$

where the prefactor preserves the normalization of the strained wave function $\Psi_{\varepsilon}(\boldsymbol{r})$. The expectation value of the Hamiltonian with respect to the strained state, $\Psi_{\varepsilon}(\boldsymbol{r})$ involves an integral over all particle coordinates $\boldsymbol{r}$, which by the new variable transformation $r \rightarrow (1+\varepsilon)r$ is given by

$$\langle\Psi_{\varepsilon}|H|\Psi_{\varepsilon}\rangle = \int \Psi^{*}(r)H\Psi(r)dr\,, \tag{4.21}$$

where the Hamiltonian of the strained state is given by

$$H = \sum_{i}\frac{1}{2m_i}\left[p_i^2 - 2\sum_{\alpha,\beta}\varepsilon_{\alpha\beta}p_{i\alpha}p_{i\beta} + \sum_{\alpha,\beta,\gamma}\varepsilon_{\alpha\beta}\varepsilon_{\alpha\gamma}p_{i\alpha}p_{i\gamma}\right] + V_{int}\left((1+\varepsilon)r\right) + V_{ext}\left((1+\varepsilon)r\right). \tag{4.22}$$

In Eqn. (4.21), $\Psi_{\varepsilon}(\boldsymbol{r})$ has been replaced by $\Psi(\boldsymbol{r})$ using Eqn. (4.20). The variational argument requires that $\langle\Psi_{\varepsilon}|\mathrm{H}|\Psi_{\varepsilon}\rangle$ differs from $\langle\Psi|\mathrm{H}|\Psi\rangle$ only to second order in strain $\varepsilon_{\alpha\beta}$. This stationarity condition on the total energy ensures, that

the first differential coefficient of the ground state energy of the strained state, with respect to the applied strain, must vanish.
Hence

$$\frac{\partial\left\langle \Psi_{\varepsilon}\middle|\mathrm{H}\middle|\Psi_{\varepsilon}\right\rangle}{\partial\varepsilon_{\alpha\beta}} = 0\,. \tag{4.23}$$

From Eqns. (4.21) and (4.22),

$$0 = \sum_{i}\left\langle \Psi\middle|\frac{p_{i\alpha}p_{i\beta}}{m_i} - r_{i\beta}\nabla_{i\alpha}\left(V_{int} + V_{ext}\right)\middle|\Psi\right\rangle. \tag{4.24}$$

Equation (4.22) is the fundamental expression of the stress theorem, used to derive the macroscopic stress in a solid. The term involving V_{ext} in Eqn. (4.24), is the total load stress $T_{\alpha\beta}$ exerted by external forces upon the solid given by

$$T_{\alpha\beta} = -\sum_{i}\left\langle \Psi\middle|r_{i\beta}\nabla_{i\alpha}\left(V_{ext}\right)\middle|\Psi\right\rangle. \tag{4.25}$$

If the solid is in equilibrium, the stress is represented by a symmetric tensor without any external torques. It follows therefore that the total stress intrinsic to the system is

$$T_{\alpha\beta} = -\sum_{i}\left\langle \Psi\middle|\frac{p_{i\alpha}p_{i\beta}}{m_i} - r_{i\beta}\nabla_{i\alpha}\left(V_{int}\right)\middle|\Psi\right\rangle. \tag{4.26}$$

The total internal stress integrated over the volume of the system, described by the tensor $T_{\alpha\beta}$ expressed in terms of the expectation values of internal operators intrinsic to the system, must be balanced by the stress due to external conditions for the body to be in equilibrium. The stress theorem therefore arises from the consequences of the quantum theory of stress that, the average macroscopic stress in a system $\sigma_{\alpha\beta}$ (where α and β are the Cartesian coordinates), is the expectation value of the linear term in the expansion of the Hamiltonian of the ground state wave function of a body with respect to an infinitesimal virtual strain $\varepsilon_{\alpha\beta}$. The average stress is then given by $\sigma_{\alpha\beta} = T_{\alpha\beta}/\Omega$, where Ω is volume of the solid. This is related to the hydrostatic pressure in the solid as $P = \frac{1}{3}\sum_{\alpha}\sigma_{\alpha\alpha}$, where the summation is over all principal stress components.

4.4 Applied and Residual Stress

The stresses that arise in a material as a result of the application of an external load are known as load stresses (LS). On the other hand, the self-equilibrating internal stresses that are present in any free body which has no external forces or constraints acting on its boundaries are known as residual stress (RS) [300]. In general, irregularities and misfits in the material give rise to residual stress fields. The causes of these are varied, and are a whole field of study in applied science and engineering. At the microscopic level, atomic scale voids or inclusions are examples of sources of residual stress. Residual stresses are, necessarily, in equilibrium over the whole body. Understanding of the origin, determination, and control of these stresses are essential because the mechanical performance of a component can be significantly altered by their presence. Residual stresses can be categorised in terms of [301]:

(i) the causative mechanism – for example thermal mismatch stress or elastic mismatch stress;

(ii) the length scale over which the self-equilibration mechanism occurs; and

(iii) the method used in determining the stress.

In this thesis, the length scale perspective is adopted. There are mainly three types of residual stresses: type I residual stress (or macrostress); and type II and type III residual stresses or microstresses [302].

4.4.1 Macroscopic Residual Stress

Long-range stresses are known as type 1 residual stresses, macroscopic stresses, or macrostresses. These are usually long-ranged relative to the scale of the dimensions of the local structure of the material on which they act. Such stresses can be estimated using continuum models, which ignore the polycrystalline or multiphase nature of a material, and are often calculated using finite element methods [303,304].

There are many ways in which macro residual stresses can develop in composite materials, *e.g.* through the interaction between misfitting components within an assembly [301,302]; or the generation of chemical, thermal, and plastically induced misfits between different regions [305]. In addition, thermal mismatch stresses are commonly found in multipart assemblies, which are made up of different materials that can experience varying temperatures. As an illustration, consider an amorphous silicon layer deposited on a glass substrate at an elevated temperature and cooled to room temperature. If the deposited thin film material has a lower coefficient of thermal expansion than the glass substrate, it will experience a compressive stress while the substrate will experience a tensile stress.

4.4.2 Microscopic Residual Stress

There are two types of micro residual stress: type II (or intergranular stresses) and type III (or intragranular stresses). Type II micro residual stresses vary over length scales that are comparable to the grain size in a polycrystalline material, while type III micro residual stresses vary over length scales within a single grain. Type II microstresses equilibrate over distances that are small enough to be comparable to the scale of the microstructure of the material, irrespective of the presence, or otherwise, of a phase-dependent residual stress over large distances [306,307]. Low level type II stresses nearly always exist in polycrystalline materials, simply from the fact that the elastic and thermal properties of differently oriented neighbouring grains are different. More significant grain scale stresses occur when the microstructure contains several phases, or when phase transformations take place. Type III residual stresses occur when atoms are placed in non-ideal environments. The misfitting regions span nanoscale dimensions. The type III category typically includes stresses due to lack of coherency in atomic positions at interfaces and local dislocation stress fields. The extreme case of a type III residual stress is the atomic level stress discussed below.

4.5 Atomic-level Stress

As seen in the discussions so far, continuum theory does not take the detailed local structure of a material into consideration when stress is evaluated. However, it has been recognized [308-311] that the arguments and definitions used in the continuum theory for describing the stress state in a body, give the same results as the thermodynamic definition of stress using the virial theorem of Clausius [312,313]. From Eqn. (4.26), a local stress field $\sigma_{\alpha\beta}(\boldsymbol{r})$ can be defined at any point within a system of atoms, such that the integral, $\int \sigma_{\alpha\beta}(\boldsymbol{r})d\boldsymbol{r}$ taken over the entire volume of the system, is equal to the total stress $\sigma_{\alpha\beta}$. It is worth noting that this stress field is defined at each point in space, and particularly at each atomic position, such that the integral of this stress over the surface of a vanishingly small volume enclosing a particular atom, will give the Hellman-Feynman force acting on that atom.

It follows therefore, that such definitions can be scaled down to describe the stress acting on atoms. The stress tensors describing the state of a body can then be expressed as a sum over all the atoms, and this approach has been used in the thermodynamic definition of hydrostatic pressure [314]. In order to extend the continuum definition of stress to the description of the forces that act on an atom in a solid, it is useful to consider the smallest volume that can enclose a single atom. In a crystalline material this can be represented by the Wigner-Seitz cell as shown schematically in Fig. 4.8. This volume is adequately represented by the equivalent Voronoi polyhedron in an amorphous solid, so that the above analysis can still apply. Hence, the continuum theory can be applied directly to obtain the components of the stress tensor.

The stress tensor associated with a given atom i at position $\boldsymbol{r}_i$ defines the atomic-level stress [315,316] as

$$\sigma^{i}_{\alpha\beta} = \frac{1}{\Omega_i}\int \sigma_{\alpha\beta}(\boldsymbol{r})d\boldsymbol{r} \,, \tag{4.27}$$

where the integral extends over the atomic volume Ω_i. The total stress is therefore the average of the local stress tensor over the volume of a system, given by

$$\sigma_{\alpha\beta} = \frac{1}{\Omega}\sum_{\mathrm{i}} \Omega_i \sigma^{i}_{\alpha\beta} \ . \tag{4.28}$$

In computational studies of stress, the evaluation of atomic-level stress tensors depends on the approach of calculating the total energy of the system, which can be based on the density functional theory, embedded atom method, or pair potentials, among many others.

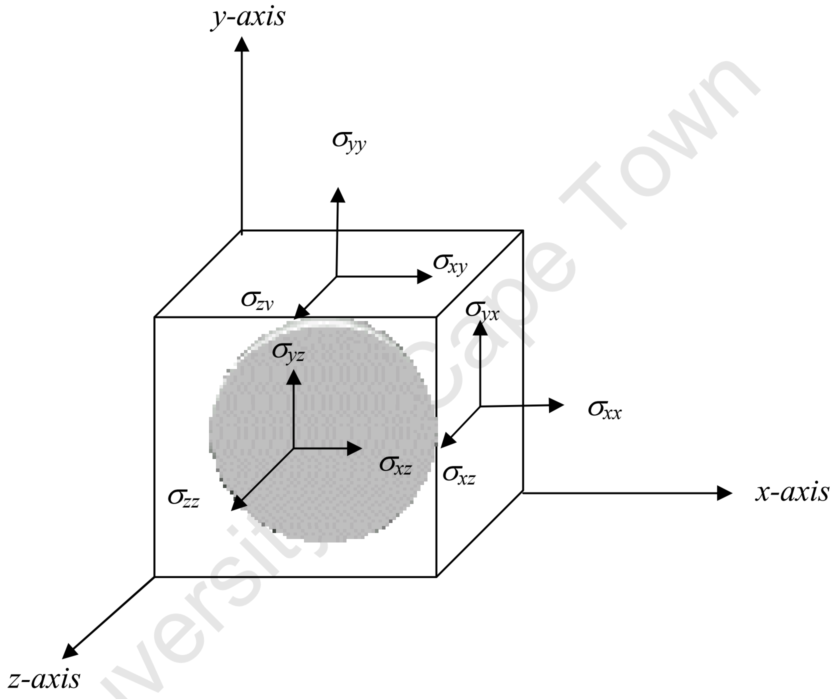

Figure 4.8 The triaxial stress state defined on the smallest volume enclosing an atom in a solid. This volume is equivalent to the volume of the Wigner-Seitz cell in crystalline solids, or the volume of the Voronoi polyhedron in amorphous solids.

In this study, the tight binding method is used to compute the total energy, forces, positions, and velocities in the simulated structures, as discussed earlier in chapter two. Hence, the expectation values of the position and momentum operators, which enter the stress theorem, are derived from the tight binding Hamiltonian. The atomic coordinates, forces and velocities were obtained from the MD simulations and used to compute atomic-level stresses in the simulated silicon networks. The Si-Si, and Si-H interatomic potentials used in modelling the local structure of hydrogenated amorphous silicon are smooth, short-ranged functions of inter-atomic separation r_{ij}. The atomic-level stresses are therefore treated as local responses of the atomic system to infinitesimal virtual strains $\varepsilon_{\alpha\beta}$ due to forces F^{a}_{ij} acting at individual atomic sites [317].

As a result, the stress tensor is re-written in a form that is suitable for implementation in a computer algorithm as follows:

$$\sigma^{i}_{\alpha\beta} = -\frac{1}{\Omega_i}\left[\frac{1}{2}\sum_{\mathrm{j}} F^{a}_{ij} r^{\beta}_{ij} + m_i v^{a}_{i} v^{\beta}_{i}\right], \tag{4.29}$$

where F_{ij} is the force on atom i due to atom j, m_i is the mass of atom i and v_i is the velocity of atom i. Therefore for any atom i, in the simulation cell, $\sigma_{\alpha\beta}(i)$ becomes a non-local property of the state of the material in the neighbourhood of that atom, since the interatomic potential has a finite range. In this thesis, the total stress was computed as

$$\sigma_{\alpha\beta} = \sqrt{\left(\sum_{i} \sigma^{i}_{\alpha\beta}\right)^{2}}\,. \tag{4.30}$$

4.5.1 Interpretation of the Atomic-level Stress Tensor

In terms of continuum theory, the atomic level stress tensor can be interpreted as the local contribution from a particular atom to the total stress tensor. The physical interpretation of the total stress is therefore straightforward, and consistent with the continuum definitions used in the continuum theory. Using statistical mechanics arguments, the total stress tensor can be treated as the flow of momentum through the surfaces of a volume element in the continuum [318]. An analogous interpretation also holds on the atomic scale. However, it is important to identify the terms contributing to the stress on the atomic scale.

In Eqn. (4.29), the first term is the static (or potential) contribution to the stress tensor, depending only on the interatomic potential between the interacting species of atoms. In the case where the interatomic potentials are short-ranged, this potential term is well-defined. Only the pairwise interactions between the atoms, on opposite sides of the surface separating them, need to be considered. The potential energy term therefore contains explicit information about the local structure of the material under investigation. In the first, static term, the principal components of the stress tensor ($\alpha = \beta$) give the elastic strain energy, while the cross-terms ($\alpha \neq \beta$) describe the torques acting on the volume element.

The second, kinetic energy term is equal in magnitude to the static contributions. However, the kinetic energy term is strongly dependent on temperature, and not on the local structure of the material. The second term can be interpreted as a measure of the transfer of linear momentum flux across the surface of cross-sectional area $\Omega_i / r_{ij}^{\beta}$, or the rate of transfer of angular momentum from one atom to another across the surface of the volume element bounding any two interacting atoms. Therefore it follows naturally that the sum of the principal components of the second term is a measure of the kinetic energy transfer across the surface of the volume element, while the sum of the cross-terms is a measure of the rate of transfer of angular momentum across the surface of the volume element.

For an isolated atom without external influences, the volume average of atomic level stress is zero. However, in a macroscopic body without external forces acting on it, intrinsic atomic-level stresses arise from local incompatibilities. These are present in a solid whenever an atom does not fit into its ideal equilibrium position such as in disordered networks, and in any network with non-equivalent atoms. Such examples also occur in crystalline materials, in the vicinity of inclusions or at surfaces.

On the atomic level, the combination of terms for which $\alpha = \beta$ in Eqn. (4.29), represents the net contribution of a given atom to the total pressure inside the system. The sum of all cross terms represents the net torque per unit volume on a given atom due to the combined effects of all other atoms. At any finite temperature, above absolute zero, the second term must be non-zero, as a direct consequence of the zero-point vibration in solids. Because of the principle of equipartition of energy, this term can be expected to be similar in magnitude to the potential energy term.

The superposition of all the atomic level stresses contributions in the supercell yields the macroscopic stress in the simulated structure. The magnitude of this stress is small, and the stress state is hydrostatic in nature because of the constraints of the MD simulation. In a real solid, *e.g.* deposited as a thin film, the situation is significantly different [319]. The true representation of the stress in the supercell, is therefore given by the fluctuations in the atomic level stress η and not on its absolute value. The fluctuations can be represented by a single scalar quantity, the rms stress, calculated as

$$\eta = \sqrt{\frac{1}{N}\sum_{i,\alpha,\beta}\left(\sigma_{\alpha\beta}\right)^2}\ . \tag{4.32}$$

The rms stress is studied with reference to the structural modification arising from the incorporation of hydrogen into *a*-Si.

4.5.2 Numerical Implementation

In order to evaluate the stress parameter η, a simple algorithm is developed for a fast computation of the atomic level stresses. The stress calculation is performed at the final time step of the equilibration procedure for a given structure, described in section 2.2. The block diagram of the numerical implementation scheme is presented in Fig. 4.9. When the logical condition *istep* = *nlast* is satisfied in the main TBMD simulation (where *istep* represents the current time-step of the simulation and *nlast* is the last step of the simulation), a set of nine floating point variables, denoting {*sumαβ*}, are automatically defined and initialized. For consistency with the continuum model of stress analysis, *αβ* is used to denote any combination of two coordinates chosen from the 3D Cartesian cordinates *x, y or z.* These are *sumxx, sumxy, sumxz, sumyx, sumyy, sumyz, sumzx, sumzy, sumzz.* These variables were used to store the intermediate results of the stress calculations. An atom *i* is arbitrarily chosen from an array of 1728 atoms, in increasing order, using a *do loop*. This allows for the evaluation of the local stress contributions due to each atom one by one until the contributions of all 1728 atoms are evaluated.

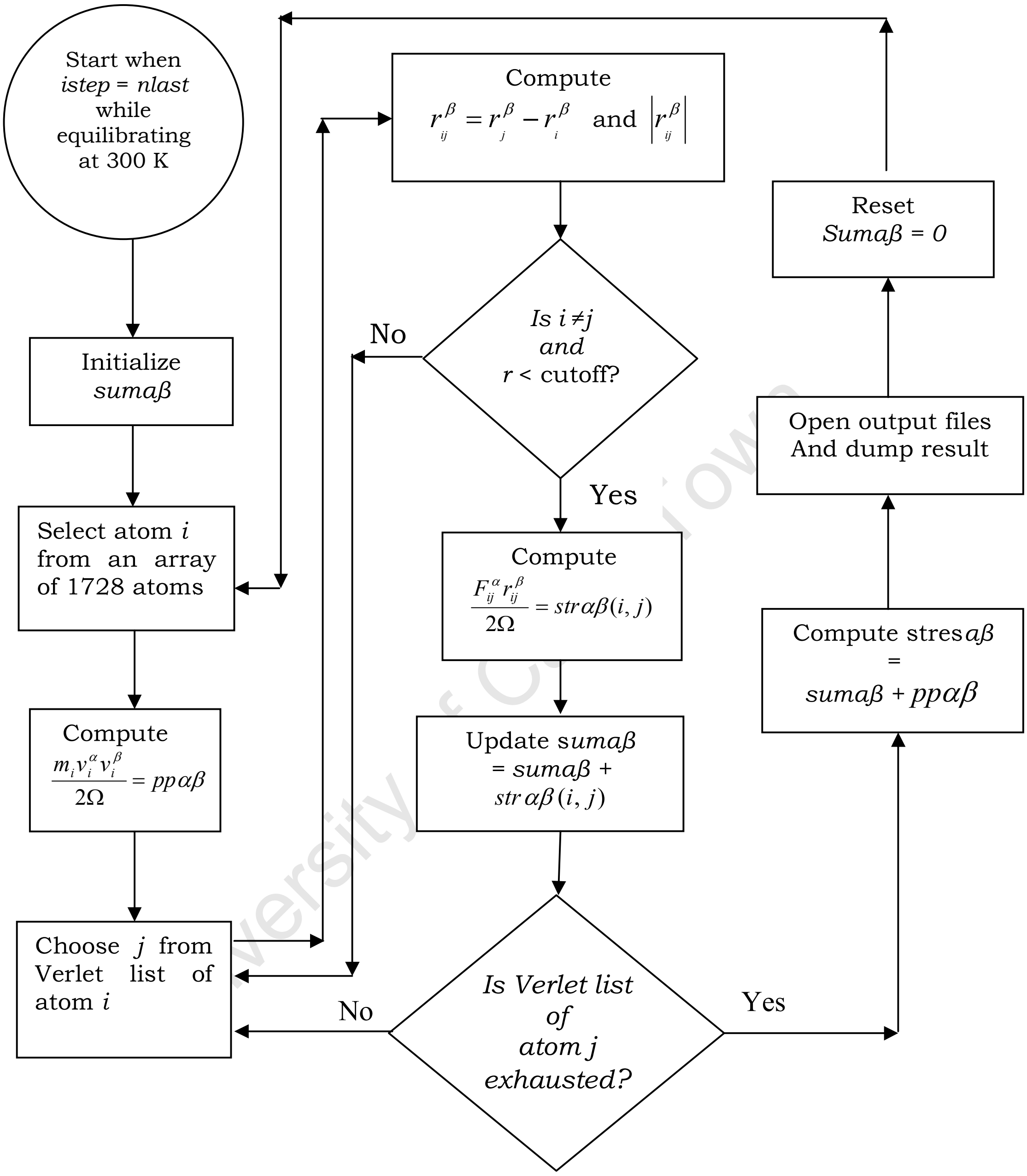

Figure 4.9 Flow chart of computer implementation algorithm used in computing the atomic level stress in a supercell model of *a*-Si:H.

The dynamic contribution to the stress tensor at atom *i* is then computed and stored in a new set of real variables {*ppαβ*} as

$$\frac{m_i v_i^{\alpha} v_i^{\beta}}{2\Omega} = pp\alpha\beta \, . \tag{4.33}$$

The exact variables used were *ppxx*(*i*), *ppxy*(*i*), *ppxz*(*i*), *ppyx*(*i*), *ppyy*(*i*), *ppyz*(*i*), *ppzx*(*i*), *ppzy*(*i*), and *ppzz*(*i*). Pair-wise contributions to the stress tensors are then computed by selecting atom *j* from the Verlet list of atom *i*, using a *do* statement. By selecting near-neighbour atoms *j* in this way, it is ensured that computational time was used efficiently. Next, the magnitude of the three components of relative separation vector $r_{ij}^{\beta} = r_j^{\beta} - r_i^{\beta}$ between atoms *i* and *j* are computed to yield three new real variables *xx*(*i,j*), *yy*(*i,j*) and *zz*(*i,j*). The effective distance r between atoms *i* and *j* are then evaluated, for use in Eqn (4.29).

In an effort to further save computational time, by avoiding useless computations of physically unrealistic separation vectors and separation distances, a logical statement is used to constrain the computer to perform the calculation of separation distances only when $i \neq j$ and $r <$ cutoff. Here the cutoff distance was 3.50 Å for Si-Si interaction and 2.00 Å for Si-H interaction. By implication, if these logical constraints are not satisfied simultaneously, then the next atom *j* is selected from the Verlet list of atom *i*. This process repeats iteratively until all nearest neighbours atom *i* are exhausted. Whenever this logical constraint is satisfied, the total force, exerted by atom *j* on atom *i*, is evaluated as the sum of the attractive and repulsive forces pair-wise forces.

The attractive component of the total force is adapted from the Hellman-Feynman force, while the repulsive forces are evaluated by numerical differentiation of the repulsive pair potentials described in chapter two. Using the pair wise forces F_{ij}^{α}, and the separations distances r_{ij}^{β}, the static contribution to the stress is evaluated as

$$\frac{1}{2\Omega} \sum_j F_{ij}^{\alpha} r_{ij}^{\beta} = str\,\alpha\beta(i,j) \ . \tag{4.34}$$

These are stored in a new set of nine real variables *strxx*(*i,j*), *strxy*(*i,j*), *strxz*(*i,j*), *stryx*(*i,j*), *stryy*(*i,j*), *stryz*(*i,j*), *strzx*(*i,j*), *strzx*(*i,j*), *strzz*(*i,j*). The sum *sumαβ* are then updated as

$$sum\,\alpha\beta = sum\,\alpha\beta + strr\,\alpha\beta(i, j)\,. \tag{4.35}$$

A logical *if statement* is then used to check if all members of the Verlet list of neighbours of atom *i* has been exhausted. If not, another atom *j* is selected from the Verlet list, and the process repeats. If the condition is satisfied, the difference between *sumαβ* and *ppαβ* is evaluated and stored in a new variable called, stres*αβ.* This gives a set of 3×3 real variables which completely specify the triaxial stress state in the supercell as prescribed in Eqn. (4.29). Then *sumαβ* is re-initialized, and the next atom is chosen from the array of 1728 using the *do statement*. This computational procedure is repeated iteratively for the next *i*th atom until all 1728 atoms are chosen.

Chapter Five

Configurational Landscapes

This chapter introduces a new perspective for the analysis of the local structure of a-Si:H in terms of a configurational landscape. The chapter starts with an introduction of concepts in landscape theory, in which the formal theory of fitness landscapes and methods of characterizing landscapes of arbitrary configurations are also presented. The notion of domains is introduced to allow for an unambiguous definition of one dimensional and two dimensional stress landscapes. This is followed by a detailed description of the construction of the stress landscape of a-Si:H. This is then used to investigate the mechanism of hydrogen-induced structure transitions, as well as to investigate the correlations between order and stress. The statistical model of the stress landscape is adopted, and used to characterise the stress landscape. This characterization allows for an interpretation of the transitions between neighbouring stress-configurations as a consequence of the random walk on the stress landscape. The possibilities and consequences of islands occurring within the domains are investigated, and the physical interpretations of such regions are presented.

5.1 Fitness Landscapes

In very fundamental terms, a landscape is a representation of a parameter or a set of parameters in a multivariate domain, or phase space. Such a representation, which allows for easy recognition of trends in data sets or relationships between data sets or both, has been used in areas of research as disparate as protein chemistry [320], theoretical biology [321], information technology [322] and combinational optimization problems in commerce [323]. The concept of a landscape is both clear and conceptually straightforward to understand, if the represented parameter is restricted to a single-valued function in a one or two dimensional domain.

Such a representation becomes comparable with a topographical landscape, where, for instance, the height is measured relative to the lateral position. The properties of the distribution of any specified feature of the objects in such a representation can be characterized using statistical functions, such as auto- and cross- correlation functions, and statistical parameters such as the standard deviation or variance. The presence of an explicit statistical relationship between the parameters, represented in a given domain, implies that an explicit mathematical relationship, or fitness function, can be used to describe the behaviour of the chosen parameter within that domain of the landscape.

The notion of fitness landscapes was originally introduced to describe the dynamical trends in evolutionary adaptation of biological systems [324]. Implicit in this notion is a collection of genotypes arranged in an abstract metric space, such that each genotype configuration can be accessible from a neighbour genotype by a single transition event such as mutation. As mentioned earlier, this conjecture is by no means restricted to theoretical biology, because over the years this idea has been developed into a powerful theoretical concept for describing a wide range of phenomena in complex systems. For instance, the Hamiltonian of disordered systems [325, 326] and the cost-function of numerous combinatorial optimization problems [327-331] have been shown to possess the same fundamental structure.

By formal definition [332-334], a landscape is a triple (X, x, f) consisting of:

(i) a finite, but very large set X of configurations x, such that $x \in X$, where any two configurations x_1 and x_2 are called neighbours;

(ii) a notion of neighbourhood, nearness, distance, or accessibility on X; and

(iii) a fitness function $f(x) \in \Re$.

The fitness function f, and its value for a particular configuration $x \in X$, is called the fitness of the configuration.

A landscape is therefore a representation of information in a multidimensional graph. Most quantitative and physical information about configurational landscapes is derived from statistical methods. This is usually obtained from considerations of the distribution of numerous configurational models of the parameter, instead of considering just a single configuration. For instance, the distribution of local optima and the statistical characteristics of a down-hill walk have been computed for the uncorrelated landscape of the random energy model [335-337], to provide detailed information on the features of the landscape.

The characteristics of a configurational landscape can be studied either from a *static* point of view or from a *dynamical* point of view. In the static point of view, emphasis is on the geometric features of the landscape. As observed earlier, the static point of view allows the properties of the distribution of specific features, in any such representation, to be characterized using appropriate statistical functions or statistical parameters, which can be interpreted and utilized to characterize the landscape. The geometrical properties include concepts such as the smoothness, roughness or ruggedness, and neutrality of the neighbourhood. Neutrality describes the degree to which neighbouring configurations x_i have the same fitness value f. In a topographical sense, ruggedness or roughness can be considered as the opposite of smoothness. A formal definition of ruggedness [334] has been given in terms of the correlation structure of the represented parameter and the statistical distribution of the local minima in the fitness function with a given domain.

On the other hand, the study of a configurational landscape from the dynamical point of view involves the study of time-dependent properties of the represented parameter. Although dynamical aspects of the parameter to be represented in this study are much more complicated to analyze in computer simulations, it is not impossible to investigate any time-dependence of the parameter. Time dependent physical properties such as diffusion [338] or time-dependent velocity gradients [339] have been studied from the dynamical point of view of some configurational landscape. The properties investigated in this work will however, only be studied from the static point of view. This is due to the fact that the mathematical analysis and interpretation of the results of such a computation is both straightforward and unambiguous in its physical meaning. Also, it is easy and straightforward to implement the calculation of the statistical functions such as auto-correlations, cross-correlations, and the fitness functions, for the investigation of the properties of a physical system, in a suitable computational algorithm.

5.2 Random-Walk Correlation Function

In the analysis of most complex systems, the number of configurations considered is usually very large. For example, for n molecular chains, there are 4^n configurations in the ribonucleic acid (RNA) analysis [340] and $n!$ configurations in protein folding [341]. Due to this large configuration, a robust characterization of the representation is necessary. A measure of the correlation in a landscape, which relates the fitness value of one neighbouring configuration x_i to another configuration x_j within a common domain, is one such approach. For a configurational landscape specified by the fitness function f, the mean of the landscape is defined as

$$\overline{f} = \frac{1}{|X|}\sum_{x\in X}|f(x)|, \tag{5.1}$$

and the variance of the landscape as

$$\sigma_f^2 = \frac{1}{|X|}\sum_{x\in X}\left|f(x)-\overline{f}\right|^2 = \overline{f^2} - \overline{f}^2. \tag{5.2}$$

The landscape is called flat if its variance, $\sigma_f^2 = 0$. The landscape can only be truly flat if $f(x)$ is constant. In using this statistical model to characterize the landscape, the parameters $\overline{f}$ and σ_f^2 are the mean and the variance of the representations respectively, and they carry the associated statistical interpretation. It is clear that the mean $\overline{f}$ and variance σ_f^2 of a given landscape are well-defined functionals of the fitness function $f(x)$, and independent of the neighbourhood structure [332-334].

The characterization of the ruggedness (roughness) or neutrality of a landscape by its autocorrelation function is believed to originate from the work of Weinberger [342]. The Weinberger model proposes the use of a random-walk $\{x_0, x_1, x_2, \ldots\}$, on the vertex set, to sample a time series $\{f(x_0), f(x_1), f(x_2), \ldots\}$, and the use of the autocorrelation, of this time series, as a characteristic of the landscape. In this case the fitnesses of the configurations are treated as random variables with a joint Gaussian distribution, so as to obtain an exponentially decaying random walk autocorrelation function. In order to characterize the structural features of a fitness landscape, Eigen *et al.* [343] introduced an alternative model. This involves the use of a correlation function that depends on the Hamming distance. The Hamming distance is a measure of the required number of substitutions, replacements or translations, that must be made on a given configuration, to change one configuration to another in a given sequence space within the chosen domain.

More recently, Stadler [333] derived a similar result in the wider context of elementary landscapes, and demonstrated that for a suitable statistical model of a configurational landscape, either the autocorrelation function of a time series generated by a random walk on the configuration space, or the correlation function, defined on suitable partitions of the set of all pairs of configurations, can be used to characterize the topological features of a landscape. It becomes clear that, for studies of representations from the static point of view, the correlation structure for the parameter representation is best described in terms of the scheme proposed in Ref. [343], while the Weinberger proposal [342] best suits the study of the dynamical features of the representation, due to the explicit time-dependence.

The idea of using correlation functions to characterize the neighbourhood of a representation can be interpreted in a straightforward manner to show regions that are either rugged or smooth. Mathematically, ruggedness or the rms roughness is the same as the standard deviation of an unweighted fit of a given model dependence to the trend line of the data. Therefore, if the extent to which the represented data deviates from the average distribution $\overline{f}$ is statistically insignificant, then the region is rugged. If on the other hand, the deviation of the parameter from the average is statistically significant, the region is smooth. Also, if independent determinations of the value of the parameter in any two neighbouring configurations x_i and x_j of the large set X should give values that vary by a factor that is less than the rms roughness, then the two configurations are statistically equivalent. Then, the landscape is neutral if independent determinations of the value of the represented parameter in any two neighbouring configurations x_i and x_j give the same numerical value. Neutrality in this case implies that the same constraints have an influence on both configurations.

Inherent in the use of a correlation function, within the statistical model of the landscape, is the concept of the correlation length. In a topographical landscape, the correlation length is loosely defined in terms of the distance over which there is a spatial correlation between similar topographical patterns. In the simple example of a topographical landscape, the correlation length is taken to represent the maximum distance that must be covered from a given reference point before a specified topographical pattern is repeated. In other cases, such as time series, and as will be shown in this work, in the stress landscape of *a*-Si:H, it is defined as the exponential distance over which relevant statistical information about the given structural configuration is lost.

5.3 Domains of the Stress Landscape

In chapter two it was demonstrated how the fluctuations in the local structure of a material can be described statistically in terms of the computed pair correlation function. Using the fact that atomic-level stress is an explicit characteristic of the internal state of the local structure of a material, it has been shown in chapter four how the true picture of the stress in the supercell models of *a*-Si:H, which result as a consequence of the non-equilibrium structure, are obtained in terms of a stress parameter, the rms stress η. As described in section 5.1, a landscape involves the representation of a parameter in a multivariate phase space or domain. A domain is an abstract mathematical space, which is spanned by the number of independent variables; x_1, x_2, x_3,…,x_n, where n is the dimension domain [344]. It is implicit in this representation that the domain, in which a given parameter is to be investigated, must preserve the characteristics of a vector space. In this sense, the basis set of the domain must span the entire phase space, so that the multivariate domain also has the properties of a vector space.

The stress parameter η is the central quantity extracted from atomic level stresses for representation in specified domains. These domains are necessary in order to study both, the correlation between structural order and stress, and the influence of hydrogen on stress in a-Si:H. On the other hand, the effects of hydrogen on local structure modifications in a-Si:H are studied by considering the distribution of statistical quantities obtained from the pair correlation function. For the a-Si:H networks investigated in this study, the possible parameters that could be used to construct the multidimensional domain include: the distributions of first and second nearest-neighbour distances ($f(r_1),f(r_2)$); the mean first and second nearest-neighbour distances (r_1,r_2); the mean number of first and second nearest neighbours (Z_1,Z_2); and the hydrogen concentration (C_H).

The representation of the stress parameter η in a multidimensional phase space, made up of all these parameters, would give rise to a very complicated stress landscape in which η is a function of all these parameters. However, such a representation is not helpful because it is mathematically cumbersome to handle, and physically meaningless to interpret. It is therefore necessary to restrict the phase space to physically meaningful parameter fields in order to allow for the extraction of useful physical information from a given representation.

It is also useful, although not mandatory, that for a two-dimensional domain, the parameters have the same dimensions, and preferably the same units. There are three pairs of such parameters that can be used:

(i) the mean first and second nearest-neighbour distances (r_1,r_2);

(ii) the mean number of first and second nearest neighbours (Z_1,Z_2); and

(iii) a pair of statistical parameters derived from the distribution of the first and second nearest-neighbour distances $f(r_1)$, $f(r_2)$, such as the standard deviations from the mean first, and second neighbour separations (δ_1,δ_2).

Any of these three pairs of parameters can be used to form a two-dimensional domain in which the stress parameter can be represented.

Therefore in a graphical sense, the representation of the rms stress η, within a given two-dimensional domain gives rise to a two-dimensional stress landscape. It is assumed that the stress landscape is an elementary landscape since η is single-valued within the domain. A more simplified case of a one-dimensional stress landscape can be investigated by studying the rms stress η in a one dimensional domain composed of any of the parameters δ_1, δ_2, r_1, r_2, Z_1, Z_2, C_H. In this way, it is possible to investigate the effects of hydrogen on stress by representing the rms stress η as a function of C_H, using an appropriate graph. Similarly, for the investigation of the effect of the hydrogen content on structural changes in *a*-Si:H, it is conceptually meaningful to plot η as a function of parameters, that characterize structural changes in *a*-Si:H using either a 1D or 2D domain.

To allow for the investigation of the correlations between stress and order in *a*-Si:H, it is important to utilize a domain constructed from variables that can explicitly characterize topological order. Although the mean first and second nearest neighbour distances (r_1,r_2) are good indicators of the quality of *a*-Si:H thin films [47], these parameters do not contain any information about the distribution of interatomic distances or the fluctuation of the interatomic distances from a known value. Hence, since there is no information about uncertainty in the absolute values of the parameters (r_1,r_2), these parameters cannot be used to estimate the disorder in the network. As shown earlier (see section 2.3.2), topological disorder in the *a*-Si:H network can be measured quantitatively in terms of statistical parameters, that can characterize the distribution of interatomic distances.

Moreover, Z_1 and Z_2 contain volume-averaged information about the coupling of topological disorder and the local bonding structure. The suitability of the domain constructed in the parameter space given by (Z_1,Z_2) would require a decoupling of the disorder from the local bonding structure. It is therefore proposed here that the standard deviation of the mean distribution of first and second nearest neighbour distances (δ_1,δ_2) constitutes a better structural parameter field which characterizes order. In this work, δ_1 and δ_2 are used to form the two-dimensional domain for the representation of the rms stress η.

In order to obtain δ_1,δ_2 and from the computed pair correlation functions $g(r)$, it is assumed that the distribution of interatomic distances, in each of the first two peaks in $g(r)$, can be approximately represented by a normal distribution of interatomic distances. This approximation allows the first two coordination peaks to be represented by Gaussian functions of the form

$$f(r_i) = \frac{1}{\delta_i \sqrt{2\pi}} \exp\left[-\frac{(r - r_{i0})^2}{2\delta_i^2} \right], \tag{5.3}$$

where, i indicates the coordination peak, r_{i0} represents the mean near-neighbour distances in coordination peak i, and r represents the near neighbour distances in peak i. Here, δ_i represents the standard deviation of the distribution of interatomic distances in a given coordination peak. The statistical package, Microcal Origin v. 7.0, was used to fit Gaussian functions to these peaks. For a given fit, statistical parameters were obtained which represent the area, centre, width, offset and height of a given peak. The centre of the Gaussian peak corresponds to the mean of the normal distribution of the interatomic distances. The standard deviation of the distribution σ is used as measure of the fluctuation in the distribution of interatomic distances.

5.4 The Stress Landscape of Hydrogenated Amorphous Silicon

In order to allow for a systematic characterization of the modifications of the local structure, it is also important to use the local stress fluctuations in these structures. As a result, we propose that the rms stress is a good measure of the standard deviation of the local atomic-level stress in these structures, because the mean stress is approximately zero, since the material is not experiencing any external force.

The stress landscape is constructed from the rms stress η, obtained from the superposition of a set of atomic level stress tensors, for 110 structural configurations obtained from TBMD simulations of bulk *a*-Si:H described in chapter two. These consist of eleven different structural configurations of *a*-Si:H, characterized by atomic hydrogen concentrations of zero, three, five, eight, 10, 13, 15, 18, 20, 23, and 25 percent respectively. The structural properties of each of these configurations are evaluated in terms of the pair correlation function, *g*(*r*). For each of these configurations, the atomic level stress tensor, and the rms stress are evaluated as described in chapter four. Molecular dynamics simulation is repeated ten times for each hydrogen concentration level. It is worth noting however, that for each stress configuration x_i, the parameter carrying the stress information could be any of: the total stress; the standard deviation of the stress; the variance of the stress *etc*.

For the set of 11 configurations, Table 5.1 shows a vanishingly small mean stress. The uncertainties quoted in the stress data, were obtained as the standard errors in the average values for a given configuration. Secondly, the disorder in the atomic positions implies that, the magnitude of the stresses must be non-vanishing at defect sites, and very small at fourfold coordinated sites, such that on average, the mean stress tends to vanish. The large set X is considered as a set of *stress* configurations in *a*-Si:H, that is characterized by unique and non-zero atomic-level stresses. It is assumed that there is a finite transition probability T_{x_1,x_2} for crossing over from a stress configuration x_1 to any another configuration $x_2 \neq x_1$ and so on, where $T_{x_1,x_2} \neq T_{x_2,x_1}$ for elementary landscapes [332-334]. This requires that transitions to any neighbour stress configuration, from an initial configuration x_1 is essentially irreversible. For any such transition, a single-valued correlation length l can be used to characterize the landscape in terms of an associated random walk on the domain of the landscape. This random walk implies an equal probability of transition between any neighbour configurations.

Table 5.1 Statistical analysis of stress parameters showing a decrease in mean stress with increasing hydrogen content.

C_H (%)	Stress range (KPa)	Mean stress (KPa)	Total stress (MPa)	Mean square stress (KPa)^2	RMS stress (KPa)
0	90.0	2.791(3)	4822(4)	268.987	16.4008
3	65.0	2.115(1)	3654(2)	155.066	12.4526
5	45.0	1.447(4)	2494(3)	73.683	8.5839
8	42.0	1.304(2)	2272(2)	61.123	7.8182
10	27.5	0.905(2)	1560(2)	28.834	5.3697
13	20.0	0.611(2)	1056(1)	13.593	3.6869
15	7.50	0.220(3)	378(2)	1.696	1.3023
18	1.10	0.033(1)	56(1)	0.03764	0.1940
20	0.90	0.0273(2)	43(1)	0.02617	0.1618
23	0.30	0.0085(1)	15(2)	0.00241	0.0491
25	0.25	0.0081(1)	14(1)	0.00209	0.0457

Any observed change of the network configuration, due to a structural transition, is conceptually consistent with the statistical interpretation of the correlation length as the distance in the domain over which there is a spatial correlation between similar patterns, or an exponential distance over which information is lost. The stress autocorrelation function S is therefore treated as the cross-correlation of stress in a given configuration with the shifted version of itself. This allows for a characterization of the stress landscape in terms of the stress autocorrelation function *S*, and an interpretation of structure transitions in simulated *a*-Si:H. In a statistical sense, the correlation length represents the average distance within a given domain, that must be covered before any neighbour configuration can be accessed on the landscape. Physically, accessibility of a neighbouring stress configuration could evolve by structural transitions, stress relaxations, or structural modifications, associated with native defect annealing. The microscopic mechanisms, that induce these structural changes, are associated with the inextricable presence of hydrogen in the network.

Chapter Six

Analysis of Local Structure Modifications

In order to provide the necessary and sufficient justification of the present methods of modelling *a*-Si:H, it is important for the modelling framework to produce not only the experimentally observable structural features of the material, but also, the computed electronic structure and phonon spectra of the simulated materials should show reasonable agreement with experimental observations. However, such agreement should only be considered in the context that, even when a good qualitative agreement is established with actual experimental results, the correspondence between the experimental film growth process and the computer-generation scheme is by no means established.

In order to avoid ambiguity in the results, it is essential to briefly summarize the four computational models of the equilibrated structures that have been considered. These are:

(a) the hydrogen-free *a*-Si network;

(b) the vacancy-like open-volume defect models of the hydrogen-free *a*-Si. Model b represents hydrogen-free *a*-Si containing *ad hoc* vacancy defects of size, V_n ($1 \leq n \leq 5$);

(c) the hydrogenated models of bulk *a*-Si. This represents a class of structural models of *a*-Si:H, which contain atomic hydrogen concentration ranging from 3% to 25%; and finally,

(d) the hydrogen-decorated vacancy-like defect model.

The vacancy-like defects in model *b* are treated as dangling bond clusters, so that the defect V_n (where $n = 1$), is considered to be equivalent to a cluster of four dangling bond defects ($4T_3$). The configurations of hydrogen-decorated vacancy-like defects (model *d*) considered in this work are restricted to models of hydrogen-decorated divacancy-like complexes. The specific configurations considered for model d are V_1H_1, V_1H_2, V_1H_3, V_2H_1, V_2H_2, V_2H_3, V_2H_4, and V_2H_5, respectively.

6.1 Thermodynamic Stability of Simulated Structures

6.1.1 Total Energy Fluctuations at 300 K

In order to investigate the thermodynamic stability of the simulated structures, it is important to study the potential energy distribution for the equilibrated state of the four models during the searches for the respective global energy minima. Fig. 6.1(a) shows a plot of the variations in total repulsive energy as a function of the MD equilibration time step for the divacancy defect model in hydrogen-free *a*-Si (model *b*). Within the first 100 MD time steps in the equilibration process, there is a visible increase in the total repulsive potential energy, of approximately 22 meV. At fixed supercell volume, this energy increase could only go towards increasing the internal energy of the atoms. Between 100 and 300 time steps, the total repulsive energy decreases steadily to a steady value of ~ 6.46 eV. It further decreases again to a global minimum of 6.42 eV, after about 520 time steps. For the remaining 480 time steps, the total repulsive energy increases steadily, reaching a value of 6.48 eV after 1000 time steps. At first sight, it appears that the equilibration procedure for obtaining defective hydrogen-free a-Si structures does not have to last as long as 1.0 ps, but, from the position of the global minimum, about 0.50 ps should suffice. However, an investigation of the band structure energy (Fig. 6.1(b)) during the same equilibration procedure shows a somewhat different behaviour.

Fig. 6.1(b) shows the dependence of the band structure energy on time during equilibration to obtain the same defect structure. Within the first 100 time steps, there is initially a very slow increase in band structure energy. After the first 100 time steps, the band structure energy then increases at an approximate rate of 0.289 meV/time step. This increase culminates in a global maximum in the band structure energy when there is a global minimum in the total repulsive energy. The physical meaning of this situation, in the numerical search for global energy minima, is only meaningful in the context of Eqn. (2.11). The total energy, evaluated as the sum of the repulsive and band structure energies, during the equilibration is plotted in Fig 6.2. It is clear that the band structure term predominates, such that the global minimum in total potential energy indicates a condition of metastability at about 520 time steps.

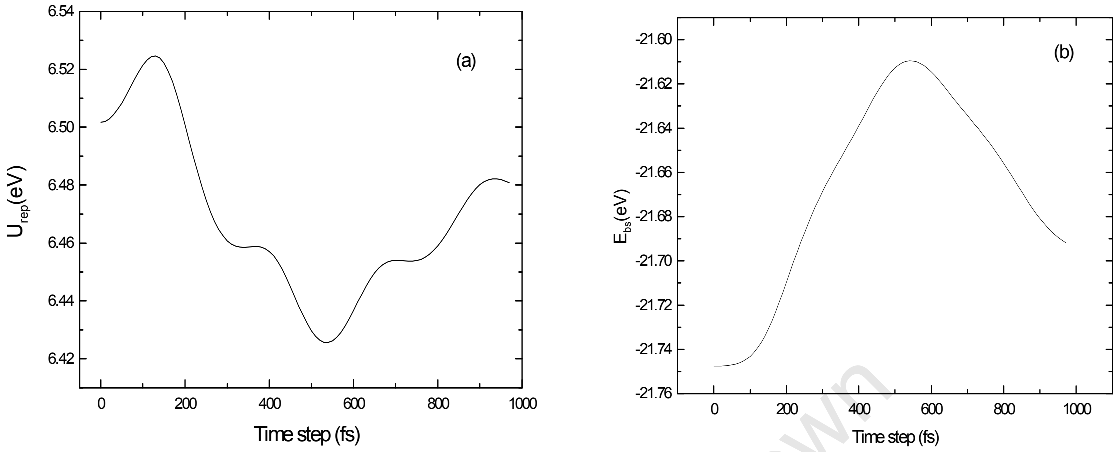

Figure 6.1 Plots of the evolution of the supercell energy with time step during equilibration to produce a divacancy-like open volume defect in hydrogen-free *a*-Si showing (a) only the total repulsive potential energy profile (b) only the band structure energy.

Apart from the initial structure, Fig. 6.2 shows that other positions of local energy minima occur, after 300 time steps and 800 time steps, respectively. Since the total energy difference after 1ps is only about 0.04 eV, relative to the total energy of the equilibrated H-free *a*-Si structure, it is suggested that this energy difference is probably due to network rearrangements. This is the only physically plausible explanation for this situation, because no thermal gradient has been applied within the NVE cycle. This prevailing situation has a profound effect on the total energy considerations of the simulated incorporation of hydrogen into simulated vacancy-like defects.

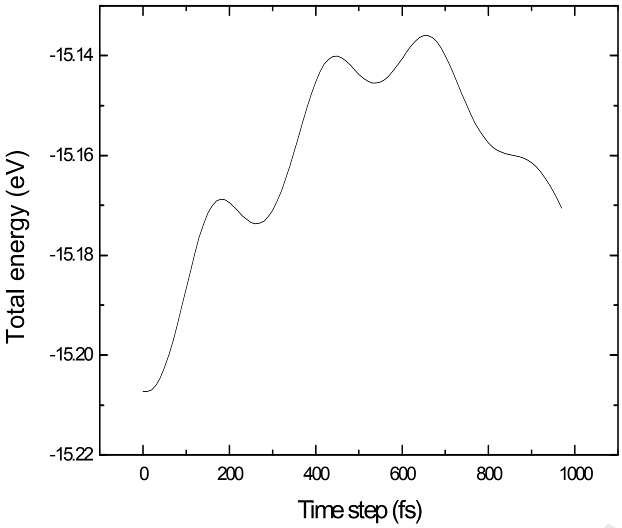

Figure 6.2 Variation of the total energy as a function of the simulation time steps showing the occurrence of global maxima after about 300, 520 and 800 time steps of the equilibration process.

Similarly, Figs. 6.3(a) and 6.3(b) show the distribution of total repulsive energy and band structure energy respectively, after hydrogen has been incorporated to produce a defect according to model *d*. As observed in the hydrogen-free structures, the band structure energy is the dominant component in the total energy of the hydrogenated structures. However, quite unlike the energy distributions of Fig. 6.1, the introduction of hydrogen to vacancy defects changes the energy distribution in a manner that:

(i) the observed local minimum in Fig 6.1(a) is completely lost, and

(ii) even after sufficiently long simulation times, the total energy does not converge to a global minimum.

In Fig. 6.3(a), the total repulsive energy of the hydrogen-decorated vacancy is observed to decrease slowly from about 6.90 eV to about 6.80 eV after 20000 time steps. Within this interval, the band structure energy increases steadily to a value of approximately -21.8 eV. Unlike the total energy of the vacancy defect models, the total energy of the hydrogenated structure shows a marked dependence on time. The total energy, at a constant temperature of 300 K, is observed to increase steadily for 20 ps, as shown in Fig. 6.4, with a net total energy increase of about 0.04 eV. The observed increase in energy with simulation time could not be attributed to any discrepancies between the analytic forces and the numerical forces obtained by differentiation of the energy expression. The numerical forces have been re-checked, and found to be equivalent to the analytic forces, and no evidence was found, of any inconsistencies was found, that could justify such discrepancies. In both the canonical and microcanonical ensembles, the principle of equipartition of energy should hold, and both potential and kinetic energy contribution should fluctuate around a constant value in an equilibrated system.

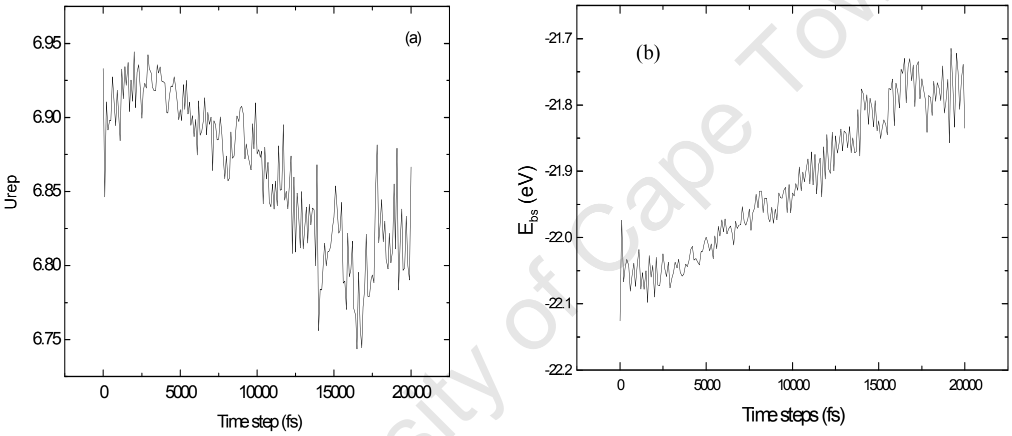

Figure 6.3 Variation of the total energy with MD simulation time steps during static relaxation to show the effect of hydrogen incorporation to the hydrogen-free divacancy on the evolution of: (a) total repulsive potential energy (b) band structure energy during the incorporation of hydrogen.

Overall, this situation is analogous to one in which the resulting structures would be physically unrealistic, since they are thermodynamically unstable. In order to obtain lower total energy configurations of these structures, the *c* - parameter of the LB functional for the interatomic potential must be varied slowly throughout the simulation, in steps of 0.01. For the hydrogen-free structures, lowest energy structures are obtained for $c = 0.12$. However, for the hydrogenated structures, setting $c = 0.12$ leads to the physically unreasonable situation depicted in Fig. 6.4(a), where the total energy continues to rise with equilibration time.

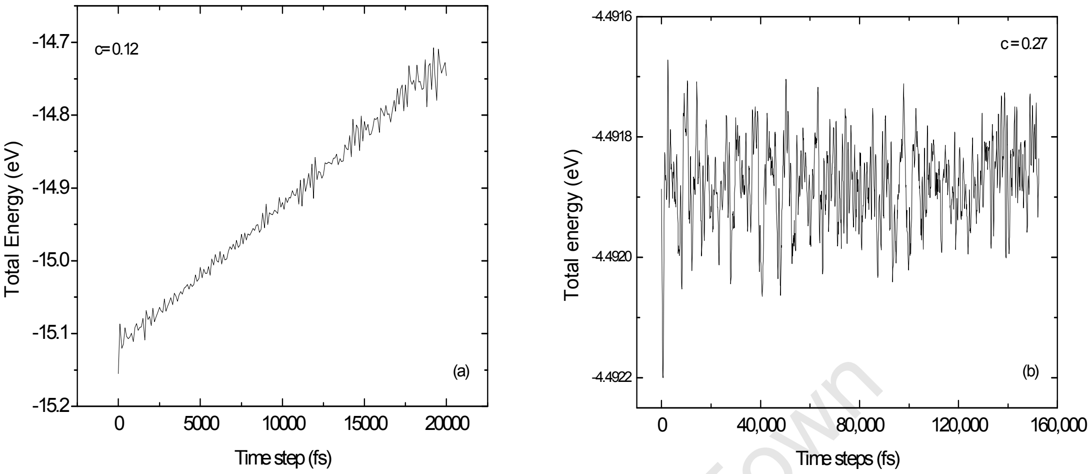

Figure 6.4 Variation of the total energy during equilibration of hydrogen decorated defect structures as a function of the simulation time steps (a) c = 0.12; showing a predominantly linear increase in total energy (b) global minimum in total energy with simulation time when c = 0.27.

Nevertheless, the lowest energy configurations were obtained for the hydrogenated structures when the c - parameter was set to 0.27. Fig. 6.4(b) illustrates the influence of this parameter on the total energy of the hydrogenated structures. First, the total energy is decreased significantly, by a factor of approximately 3, when c is set to 0.27 compared to the case for c = 0.12. Second, the total energy no longer rises continuously as observed when c was set to 0.12, but fluctuates around a mean value of -4.492 eV, with a scatter less than 5 meV. The c - parameter serves as a total energy switch, and provides a computationally convenient mechanism for achieving global minima in total energy [39], and therefore permits the characterization of local bonding environments in supercell models of *a*-Si. This computational scheme improves total energy convergence to a global minimum, and rectifies the observed anomaly in the equilibration procedures.

A distinct advantage of the TB method over empirical methods of materials modelling and simulation, is that it offers a direct access to the electronic structure of the materials studied. Although the use of GSP model in defect studies may yield results that are not as accurate as *ab initio* calculations [59], it nonetheless provides fairly accurate results for large systems. It is, however essential to examine the electronic structure of the simulated materials, to see the effects of hydrogen and native defects on the electronic structure of *a*-Si:H within the TB modelling scheme.

6.1.2 Total Electronic Density of States

Figs. 6.5 shows the computed electronic density of states, $g(E)$ for (a) the equilibrated hydrogen-free structure of *a*-Si; (b) the divacancy model of the hydrogen free *a*-Si structure; (c) the hydrogenated model of *a*-Si; and (d) hydrogen-decorated divacancy-like open-volume defect model. The $g(E)$ spectra show quantitatively how closely packed the energy levels are in the models of *a*-Si and *a*-Si:H. There are noticeable features in the computed $g(E)$ spectra that are worth noting immediately. Firstly, in all the structural models, the conduction and valence band states are clearly separated by a gap-like region. This leads to a partially filled band gap at about $E = 0$, and bears close resemblance with defect states that are generally observed in pure *a*-Si [63-66], due to its richness in dangling bonds. However, in Figs. 6.5(a) and (b) the band gap region is populated by more electron states than in Fig 6.5(d). Fig 6.5(c) shows the lowest population of energy gap states. Fig. 6.5(c) suggests that most of the mid-gap states in the hydrogen-free *a*-Si have been either completely removed or passivated after adding hydrogen. Fig. 6.5(d) shows the effects of hydrogen on the electronic structure.

It is equally important to investigate the effects of hydrogen incorporation on the energy gap of *a*-Si in each of these models. Figs 6.5(a) and (c) show clearly that incorporation of hydrogen into *a*-Si networks results in the opening up of the otherwise filled band gap energy levels, by eliminating the energy gap defect states, as seen in Fig. 6.5(c). If open-volume defects are present, the depletion of mid-gap states is not complete, and there is a finite number of mid-gap electronic states in the energy gap region of Fig. 6.5(d). These mid-gap states, which still appear even after hydrogen passivation, can be attributed to the electronic signature of the vacancy-like defects.

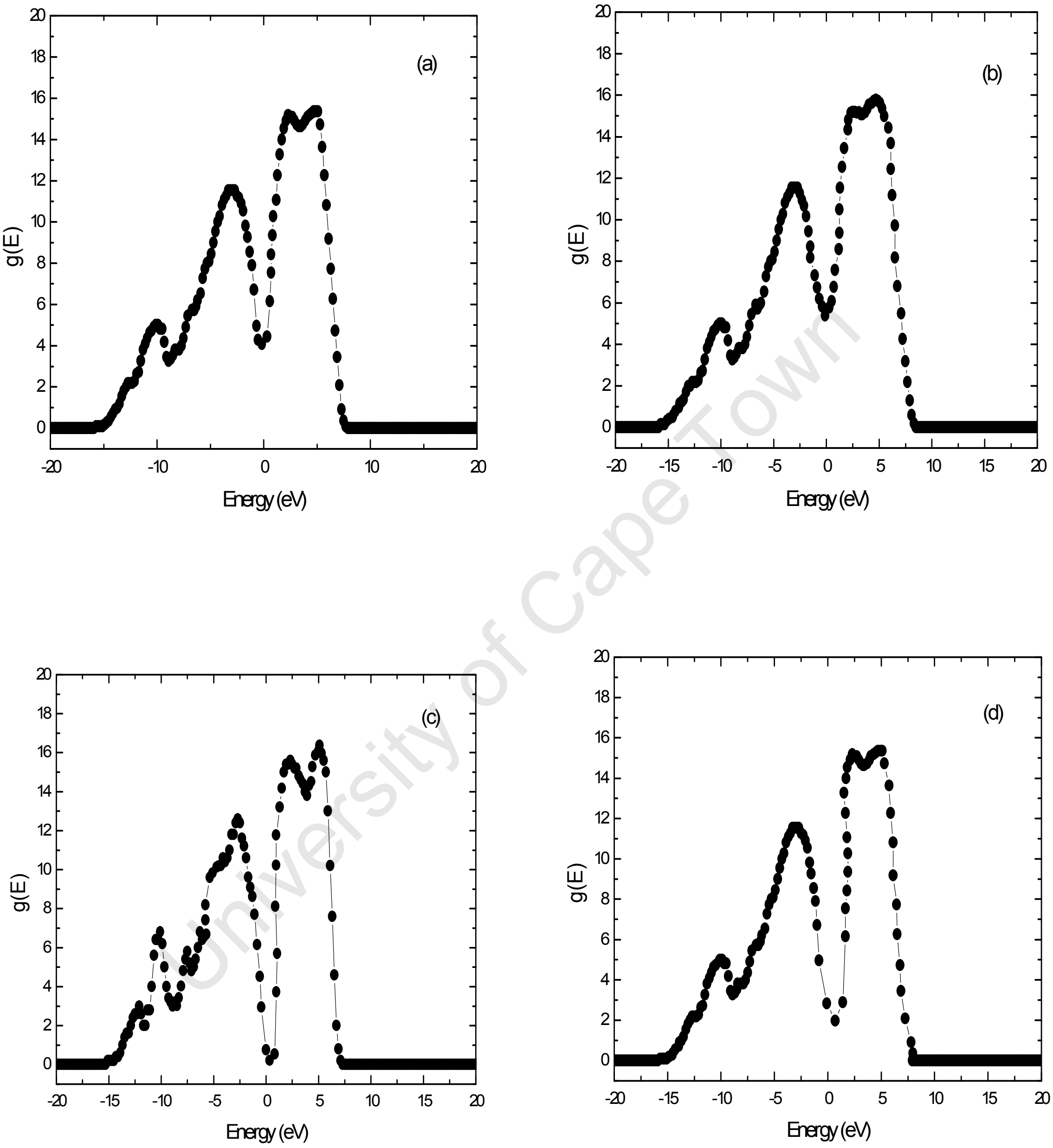

Figure 6.5 Total electronic density of states (eV/atom) for the equilibrated structures of: (a) hydrogen-free of *a*-Si model, (b) the open-volume defect model of the hydrogen free *a*-Si structure, (c) hydrogenated models of *a*-Si and (d) hydrogen-decorated open volume defect models of *a*-Si. These curves are smoothed using the 11-point adjacent averaging algorithm of Microcal Origin v. 7.0.

Fig. 6.6 shows the distribution of electronic states in the near-gap region, for energy -5.0 eV ≤ E ≤ 5.0 eV, in the structural models considered. The mid gap position appears to be centred around E = 0.5 eV in all cases. From Fig. 6.6, it is evident that the presence of dangling bond defects in hydrogen-free *a*-Si leads to the introduction of defect states with energy levels in the band gap. However, the incorporation of hydrogen to open-volume defects in *a*-Si (models *b* and *d*) causes a significant removal of the gap states.

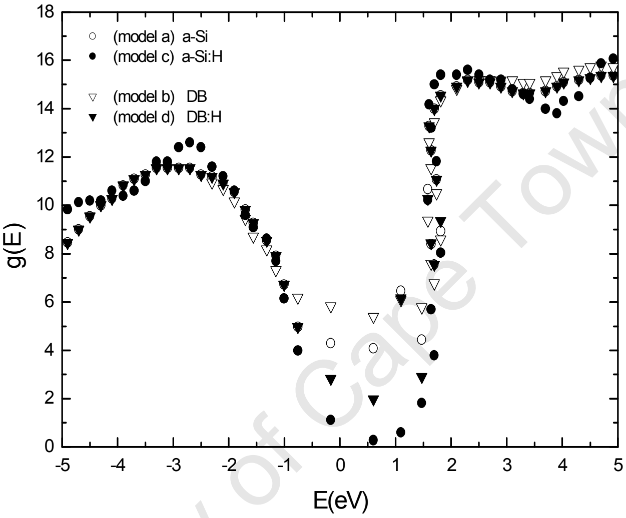

Figure 6.6 Partial electronic density of states (eV/atom) showing mid-gap electronic states of (a) hydrogen-free of *a*-Si model (b) the open-volume divacancy defect model of the hydrogen free *a*-Si structure (c) hydrogenated models of *a*-Si and (d) hydrogen-decorated divacancy open volume defect models of *a*-Si.

However, Fig. 6.6 also shows that the incorporation of hydrogen into *a*-Si structure to yield *a*-Si:H (model *c*) causes a depopulation of the conduction band states between the region of energy 3.8 eV and 4.5 eV. Most of these depopulated states appear to populate the valence band at -2.5 eV and -4.5 eV. At the moment, the origin and physical implication of this trend is not clear. However, these results show directly that H incorporation into *a*-Si evidently causes a passivation of native defect states. In model *a* and model *b*, Fig. 6.6 suggests that deep lying (mid-gap) states have been completely removed, whereas tail states are only slightly reduced when hydrogen is incorporated. On the other hand, the situation is considerably different for model *c* and model *d*. In model *d*, deep defect states are not completely removed, and the selective incorporation of hydrogen to vacancy-like defects does not influence the conduction and valence band states.

Moreover, a comparison of the profiles of $g(E)$ in Fig. 6.5 shows a slight distortion of the occupied energy bands as the network is hydrogenated. For example, the valence band states observed at E = -10.0 eV are more isolated after hydrogenation. It is equally worth noting that although most of the mid-gap states have been eliminated after adding hydrogen to the hydrogen-free structure (model *a*) the controversy over the exact origins of these mid-gap defect states is not yet explicitly resolved, because from Fig. 6.6, hydrogen-decorated vacancy-like defects also contribute to mid-gap states.

Experimental observations show that the density of mid-gap defect states is typically ~2.0×10^{20} cm^{-3} in H-free *a*-Si [180-182]. For *a*-Si:H containing ~20% H, the density of mid-gap defects lies between 10^{15} cm^{-3} and 10^{16} cm^{-3}. It has been shown [138] that this defect density corresponds to about 1 dangling bond defect in 500 - 700 Si atoms. On this basis, it could be concluded that, except for supercell models of *a*-Si:H where the total number of atoms are considerably larger than 1728 atoms, there should be no dangling bonds left in the simulated *a*-Si:H after hydrogenation to 25% using the present simulation scheme. This is based on the similarity of the computed electronic density of states for the hydrogenated samples (model *c*) with the results of the supercell calculation [138]. However, there are still some very low-lying mid-gap energy states in the density of states. These states occupy the regions of within 1.0 meV - 20.0 meV of the valence band edge. The exact origins of these residual shallow electronic states are not known at the moment, but it suffices to attribute these states to the inherent topological disorder [62].

For comparison, Fig. 6.7 shows the electronic density of states is *c*-Si at 300 K, calculated using the TB model proposed in this thesis. In all the simulations reported here, the crystal zero is fixed at 0 eV, which corresponds to the midgap level in *c*-Si. As would be expected the conduction and the valence bands, are well separated, by an energy gap. The projected band gap is 0.85 eV.

This is, however, considerably lower than the expected band gap 1.12 eV for *c*-Si. Nevertheless, the transferability of TB Hamiltonians, to properly model different phases of Si, is well-known to be sensitive to the fitting procedures used in obtaining the TB parameters. In spite of the discrepancy in the projected band gap, as seen in this case, the present TB Hamiltonian correctly describes the major features expected in the density of states spectrum for *c*-Si.

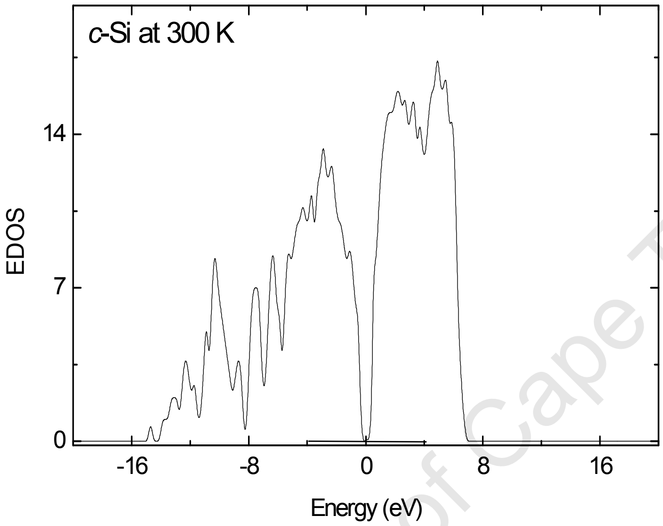

Figure 6.7 Total electronic density of states (eV/atom) showing an energy gap in the electronic states of the *c*-Si model.

6.1.3 Vibrational Density of States

It is equally important to clarify the dynamical features of the H-free bulk, and vacancy models, even before simulated hydrogenation is carried out. To this end, the vibrational density of states was computed, as the Fourier transform of the velocity autocorrelation function [136], for the equilibrated pure structure (model *a*), and for the vacancy defect model (model *b*). In H-free *a*-Si, the conservation of momentum for lattice vibrations is strongly relaxed by the presence of structural disorder. This causes all the normal modes of vibration to become Raman-active [345]. The first-order Raman scattering spectrum represents the spectrum of the density of states for lattice vibrations, or phonons, in crystals. Typically, the vibrational spectrum of *c*-Si has four energy bands. These are: the transverse optical band at 475 ± 5 cm^{-1} (58.90 ± 0.62 meV), a longitudinal optical band at 380 ± 10 cm^{-1} (47.11 ± 1.24 meV), a longitudinal acoustic band at 310 ± 5 cm^{-1} (38.44 ± 0.62 meV), and a transverse acoustic band at 150 ± 5 cm^{-1} (18.60 ± 0.62 meV) [4].

Figs. 6.8(a) and 6.8(b) show the computed vibrational density of states $D(\omega)$ for model a and model b as a function of vibrational energy. These show that the vibrational spectra of *a*-Si are qualitatively similar to the first-order Raman spectra for *c*-Si [346]. This implies that short range order plays a significant role in determining the vibrational properties. Although the effect of hydrogen concentration on the vibrational response of *a*-Si:H structures (model *c*) can equally be studied to investigate the effects of hydrogen on medium range order [347] using the above framework, it must be stated that, as a direct consequence of the discussions in section 2.3.3, the computation of $D(\omega)$ for this class of structures is completely unnecessary for the purpose of the present study. Figs. 6.8(a) and (b) show the computed vibrational spectrum for models *a* and b. These results show marked similarities with the results of the $O(N)$ computation of Biswas [348] for a 1000-atom model of *a*-Si. Two distinct peaks are clearly seen, in very good agreement with experimental measurements [349,350], which have been attributed to a low energy transverse acoustic mode and a high energy transverse optical mode. However, a low intensity peak is also observed at ~ 40 meV.

A direct comparison of the computed phonon spectra with experimental results shows significant high energy modes beyond 65 meV in *a*-Si. In both cases, the phonon density of states $D(\omega)$ becomes zero at $\omega = 0$. This shows that micro-diffusion, and local atomic rearrangements do not occur in the unhydrogenated structures after equilibration. A well-defined transverse acoustic (TA) peak appears at a low energy of 20 meV. However, when the result of Fig. 6.8(a) is compared with the computed vibrational density of states of a four-fold coordinated structure of the WWW model [351,352], two major observations become immediately apparent. Firstly, a significant fraction low energy vibrational modes are found below 10 meV. Secondly, very high energy vibrational modes predominate in *model a*, with energy greater than 65 meV. The VDOS spectrum $D(\omega)$ of the WWW model shows lowest energy vibrational modes at ~8 meV unlike in experimental observations [353], where the lowest energy modes occur near zero.

In Fig 6.8(a), the low energy vibrational modes can only be attributed to the native floating bond defects, while the high energy vibrational modes are due to dangling bond defects. This is physically justifiable because of the significantly lower concentration of floating bonds relative to the number of dangling bonds. Apart from the presence of the TA and TO peaks in both spectra, Fig 6.8(b) is significantly different. Firstly, the small peak at about 40 meV, which corresponds to the LA peak, is somewhat more broadened in Fig 6.8(b) than in Fig 6.8(a). Secondly, the LO band is absent. Fig. 6.8(b) also shows a low intensity, high energy TO peak at ~95 meV. When compared to the vibrational spectrum of model *a*, this high energy vibrational mode can only be interpreted as the vibrational signature of the open-volume vacancy-like defects. In both cases, the $D(\omega)$ spectra show that the dynamical response of the H-free structures are consistent with known computational models of *a*-Si, and therefore validates the present computational framework.

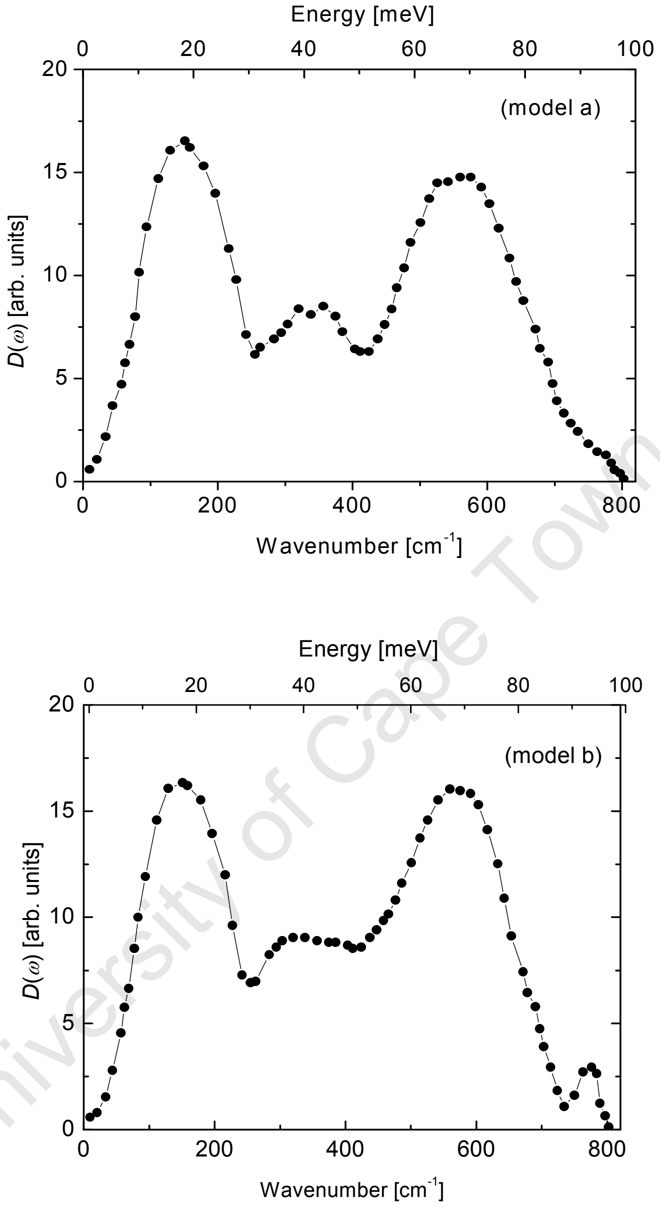

Figure 6.8 The phonon density of states for; (a) the equilibrated structure of the 1728-atom supercell model of hydrogen free *a*-Si (model *a*), and (b) a 1728-atom supercell model of *a*-Si containing open-volume defect (model *b*) computed as the Fourier transform of the velocity autocorrelation function, showing a zero diffusion constant at ω = 0 at 300 K.

6.2 Analysis of the Local Structure

6.2.1 Pair Correlation Function

The results of the bulk structures presented here are for structures selected from two different regions of the stress landscape (see chapter 7). Fig. 6.9 shows the ball and stick models of the simulated H-free and hydrogenated *a*-Si structures at 300 K. In Fig. 6.9(b), the hydrogenated structure contains 3% H. Similarly, Fig. 6.9(c) and (d) show the ball and stick representation of bulk structures containing 18% and 23% hydrogen respectively. The figures were obtained by converting the atomic coordinates obtained from TBMD simulations to a binary (*.XYZ) format using the open-source file conversion utility of gOpenMol-3.00 software [354]. Using the re-formatted positions as inputs, the 3D graphics were rendered using the graphic user interface. A visual inspection of the ball and stick model of Fig 6.9(a) confirms the presence of several defects in the H-free structure.

The dominant types of defect in the hydrogen free structure are dangling and floating bonds, although the structure is dominated by four-fold coordinated Si atoms. As would be expected, most of the incorporated hydrogen atoms in Fig. 6.9(b) go towards terminating the dangling bonds. The network topology lacks translational periodicity in both cases. As more hydrogen is progressively incorporated, the structural network relaxes until tetrahedral coordination is restored as shown in Fig. 6.9(d). Relative to the structural configurations for low hydrogen concentrations, Fig. 6.9(c) and Fig. 6.9(d) show a more ordered topology. However, when compared to the network configuration of *c*-Si, the network configurations are still considerably disordered.

This prevalent disorder at high C_H could be attributable to the large activation barrier of about 3.7 eV between the amorphous and crystalline phases [355]. Although the first nearest neighbour coordination peak of *c*-Si is still present in the simulated *a*-Si, with its centre at about 2.35 Å, it is significantly broadened. In Fig. 6.10(a), it can be observed that the third nearest neighbour coordination peak, which normally appears at 4.50 Å in *c*-Si, as shown earlier in Fig. 2.7, is absent. Moreover, the distribution of triplet correlation angles (Fig. 6.10(b)) shows a mean correlation angle of about 109.48 degrees with a variation of ±10°. In addition, the second and the third nearest neighbour coordination peaks of *c*-Si are observed to merge together to form a very broad second peak in *a*-Si with its centre at ~3.90 Å. These observations are consistent with the situations observed for experimental samples formed by physical vapour phase deposition [356], radio frequency sputtering [357], and hot wire chemical vapour deposition [358] methods.

One striking feature of hydrogen-free *a*-Si is the presence of several unterminated dangling bonds as seen in Fig. 6.9(a). This structure also contains many weak Si-Si bonds compared to the results of Ref. [15]. These weak bonds are indicated by the presence of a non-zero pair correlation at an interatomic distance of about 3.00 Å. This difference is attributed to our choice of 3.50 Å as the cut-off distance for Si-Si interaction. Unlike in [15] the resulting structure is not forced into equilibrium, because the extra 0.50 Å allowed for near neighbour interactions is sufficient to allow a complete structural evolution, since the typical Si-Si bond length is 2.35 Å. The evolution of the network structures of *a*-Si:H (model *c*) is shown in Fig. 6.11, as a combined plot of the different Si-Si pair correlation functions, $g(r)$. The minimum Si-Si first near-neighbour correlation distance in *a*-Si is 2.14 Å and remains the same for all levels of hydrogen concentration.

At low C_H, the position of the centre of the first coordination peak deviates significantly from 2.35 Å. Within a 5.0 Å correlation distance, only the first and second neighbour coordination peaks are observed for H concentrations below 8%. A shoulder starts to appear at 4.50 Å on the second coordination peak as the hydrogen level increases to 10%. This shoulder gradually evolves into the third coordination peak as C_H is increased from 10% to 18%. This evolution is complete at 20% H, when the third peak is centred at 4.45 Å. A further increase in C_H from 20% to 25% does not change the characteristics of the distribution function. At intermediate concentrations (10% - 15%), four distinct peaks evolve, with centres at 4.44 Å, 5.84 Å, 6.72 Å and 7.91 Å, respectively. Similarly, as C_H

increases further from 18% to 20%, two additional peaks appear as a result of the splitting of the 5.9 Å and 6.8 Å peaks. Neither the number of coordination peaks appearing in this long range correlation distance, nor their mean positions is changed when C_H is further increased from 20% to 25%, although the relative intensity of these peaks constantly increase as C_H increases to the upper limit of 25%.

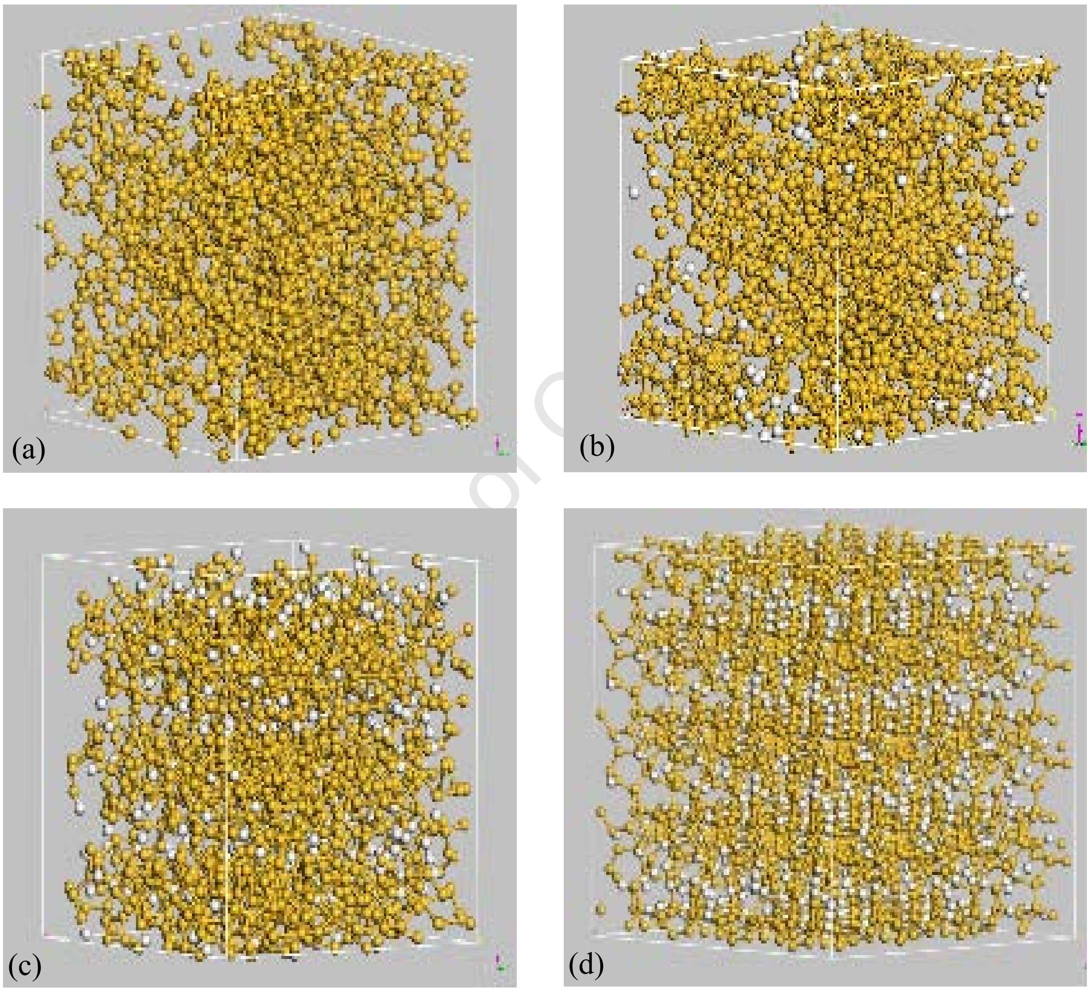

Figure 6.9 Ball and stick model of: (a) hydrogen-free amorphous silicon; (b) hydrogenated amorphous silicon containing 3% H; (c) hydrogenated amorphous silicon containing 18% H; and, (d) hydrogenated amorphous silicon containing 23% H.

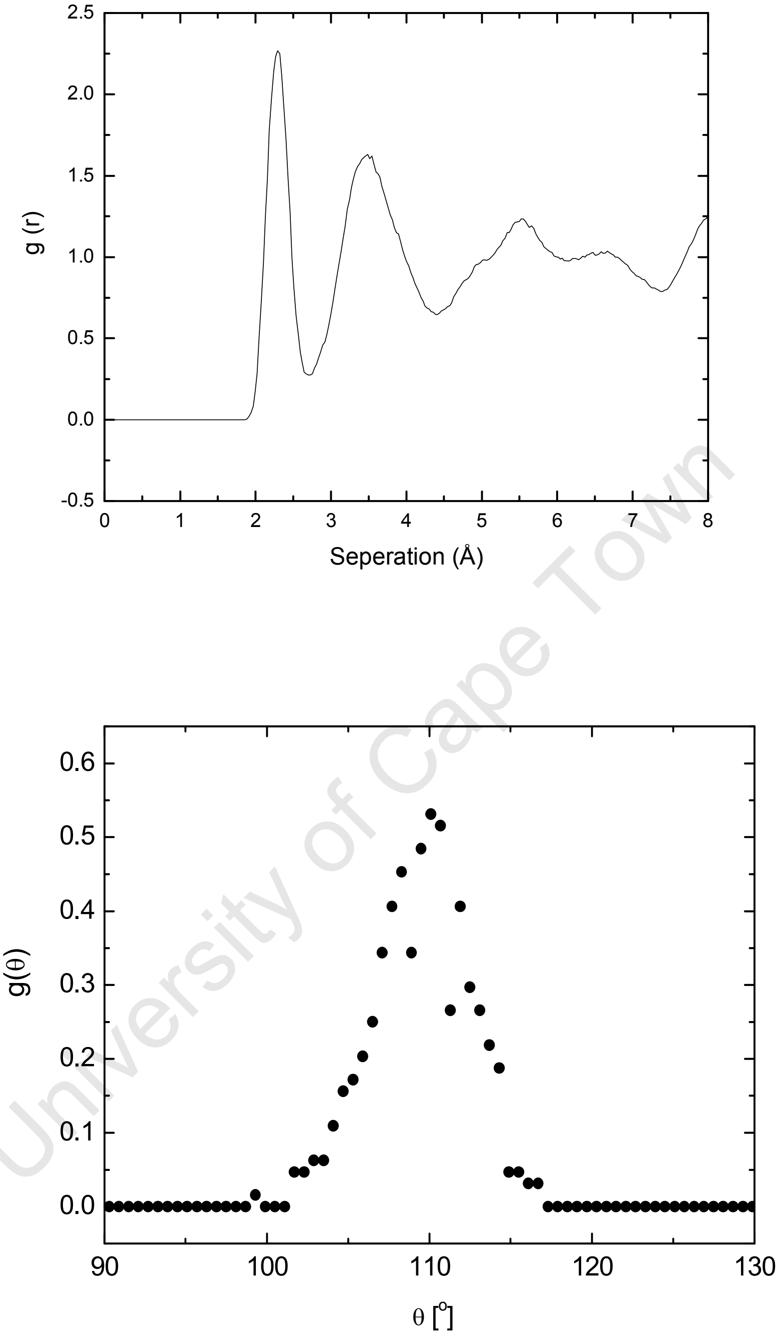

Figure 6.10 (a) Si-Si pair correlation function for a 1728 atom supercell model of H-free *a*-Si (model *a*) averaged over 1000 configuration in 1ps; (b) Distribution function for triplet correlation angle in *a*-Si:H (23%) averaged over 1000 configurations in 1ps showing a bond angle fluctuation of Δθ = ±10° from the tetrahedral bond angle of 109.47°.

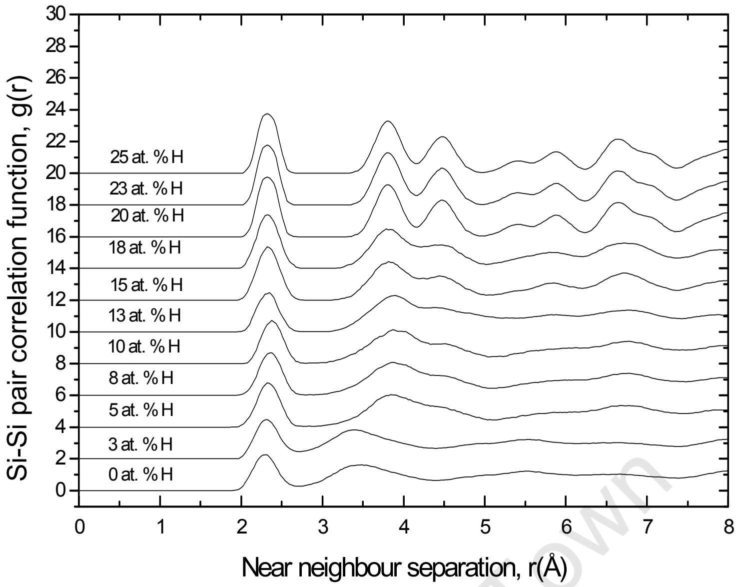

Figure 6.11 Combined plot of the Si-Si pair correlation function *g*(*r*) showing the structural evolution of hydrogenated *a*-Si at 300 K (model c) containing variable hydrogen concentration ranging from 0 - 25 %.

This suggests that a more structurally ordered form of *a*-Si:H is obtained at high hydrogen concentrations. It is worth recalling that during H incorporation, no H-H interaction was permitted, within distances less than 1.0 Å, at low hydrogen concentrations. This condition was imposed to avoid the formation of molecular hydrogen when most of the T_3 sites had not yet been passivated. As a result, hydrogen must therefore be distributed randomly in the structure, especially at low C_H, thus going mainly to terminate the dangling bonds. Moreover, the structural evolution observed in Fig 6.10 shows that hydrogen plays a non-trivial role in *a*-Si:H. It is therefore essential to study the structural evolution, especially at high C_H, to identify the hydrogen configurations in the model structure.

Fig 6.12 shows the Si-H pair correlation function, for model *c*, at high C_H. Although not shown in the figure for lower C_H, the first near neighbour Si-H correlation peak is always well-defined. This peak is centred at approximately 1.48 Å, which corresponds to the approximate Si-H distance in the silane molecule. This sharp, well-defined first near neighbour peak reflects the fact that there is no bond-centred hydrogen (Si-H-Si), even at sufficiently high C_H. Between 13% and 18% hydrogen concentration, two peaks can be observed at 2.90 Å and 3.50 Å. The first coordination peak reduces with increasing hydrogen, and the whole structure moves to smaller interatomic separations, as the two peaks merge to form a single broad peak. This splitting of the second Si-H correlation peak for hydrogen concentrations below 18% in *a*-Si:H, is consistent with similar observations for *a*-Si:H structures, which contain both monohydride and dihydride species [359]. The first feature of this split peak was attributed to Si-Si-H bonding configurations. The second feature is thought to occur [39] from Si-H pairs, where silicon is not a bonded second neighbour of the hydrogen but in a nearby position, as shown in the inset in Fig. 6.12.

The position of this peak is observed to shift to 3.0 Å when C_H is increased beyond 20%. Although the above situation does not suggest the formation of molecular hydrogen, it strongly supports a situation where more silicon atoms act as second (or third) near neighbours to the monohydride configurations. Therefore, at 25% H, the computed Si-H pair correlation does not necessarily suggest the presence of the dihydride and trihydride configurations. Indeed, if it did the intensity of the first correlation peak would increase, as discussed in section 6.2.2 below. However, the presence of the dihydride configuration in structural configurations, which contain hydrogen concentrations between 13% and 18% cannot be ruled out, because of the removal of the restrictions on H-H interaction at high C_H.

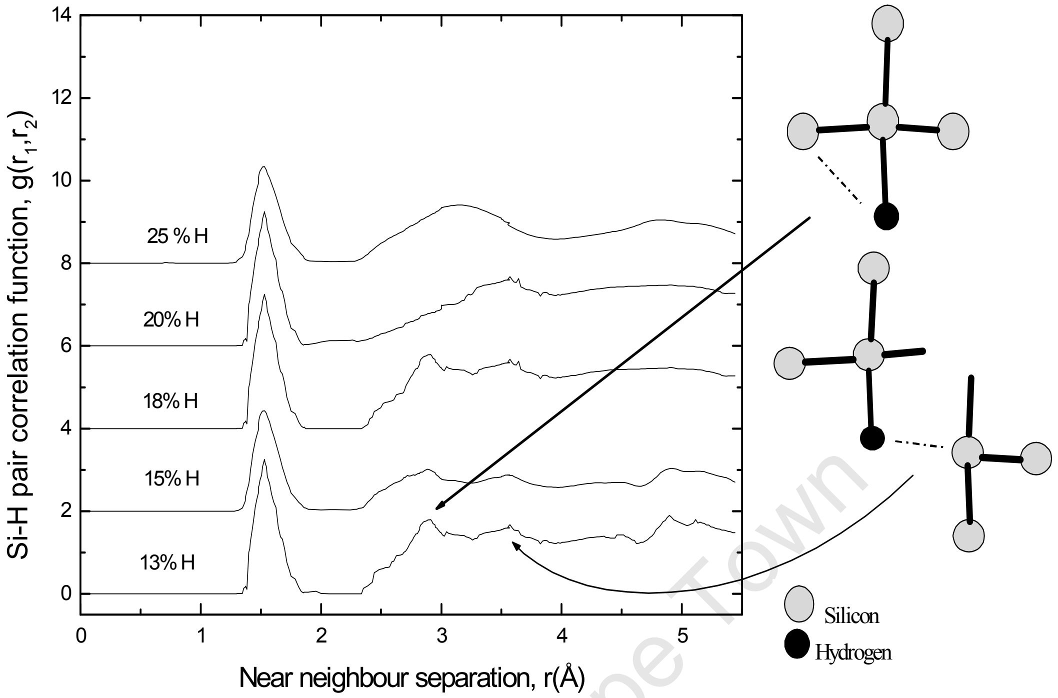

Figure 6.12: Combined plot of the Si-H pair correlation function *g*(r) showing the bonding configurations of hydrogen in *a*-Si:H at 300K (model c) at high hydrogen concentration (13 – 25 at. %).

6.2.2 Distribution of Nearest Neighbours

Table 6.1 shows the average values of the Gaussian fitting parameters of pronounced peaks in the pair correlation function *g*(*r*), with changing hydrogen concentration C_H. In particular, the intensities of the first two coordination peaks are observed to change due to progressive hydrogen incorporation, relative to the H-free structure. It is found that as C_H is increased, the position of the centres of the first two coordination peaks decrease towards the equivalent values in *c*-Si. In addition, the average intensities of the first and second peaks increase steadily, while the widths decrease steadily with increasing C_H.

In order to further illustrate the above structural changes, it is necessary to evaluate the coordination number using the computed Si-Si and Si-H pair correlation functions. This provides an accurate numerical procedure, for determining the number of atoms of a particular kind, which surrounds a given Si atom in a given structure, as the structure relaxes towards a more ordered state. The coordination number, Z_i can be obtained by integrating over a specified interval (r_i - δr, r_i + δr) around any pronounced cordination peak as [360]

$$Z_i = \int_{r_i - \delta r}^{r_i + \delta r} 4\pi r^2 g(r) dr \ , \qquad (6.1)$$

where i denotes the particular coordination peak in the pair correlation function.

Table 6.2 shows the mean Si-H coordination number for structures Z_H, which contain high hydrogen concentration. For all structures concentration, the mean coordination number is approximately one. This strongly suggests that, most of the hydrogen in the structures exist, as monohydride configurations. Although this observation does not support the presence of the dihydride configuration, the presence of the dihydride configuration cannot be excluded. Between 13% and 20% H, the average coordination number is varies non-uniformly, with an average value of approximately one.

Fig. 6.13 shows the dependence of the mean number of Si-Si first, and second nearest neighbours in the structures, on the hydrogen concentration C_H. The error bars were obtained as standard errors in the mean coordination numbers, obtained from ten configurations at each level of hydrogen concentration, C_H. It is immediately clear that the mean number of first (Z_1) and second (Z_2) nearest neighbours appears to decrease continuously as the hydrogen concentration increases steadily to 25%. At very high C_H, the mean coordination number is significantly lower than the mean coordination number in *c*-Si, and its dependence on hydrogen concentration, as shown in Fig. 6.13, agrees very well with a similar estimate for the *a*-Si:H system [361].

Table 6.1. Mean values of the Gaussian fit parameters for the first and second coordination peaks in Si-Si $g(r)$ to show the effects of hydrogen concentration, C_H.

C_H (%)	*First coordination peak*			*Second coordination peak*		
	Area (Å^2)	Centre (Å)	Width (Å)	Area (Å^2)	Centre (Å)	Width (Å)
0	1.04(2)	2.30(3)	0.61(1)	1.50(4)	3.50(1)	0.87(3)
3	1.17(3)	2.33(2)	0.50(1)	1.73(4)	4.14(2)	0.85(1)
5	1.21(1)	2.33(3)	0.45(1)	1.93(1)	4.10(1)	0.83(1)
8	1.51(1)	2.33(1)	0.43(2)	1.95(2)	4.03(1)	0.77(3)
10	1. 64(2)	2.33(1)	0.42(2)	2.01(3)	4.02(1)	0.76(3)
13	1.60(1)	2.34(2)	0.31(1)	2.21(1)	3.89(1)	0.73(1)
15	2.41(1)	2.35(2)	0.26(2)	2.20(2)	3.86(2)	0.68(2)
18	2.70(1)	2.35(1)	0.21(2)	2.31(2)	3.85(1)	0.62(1)
20	2.75(1)	2.35(2)	0.19(2)	2.73(1)	3.81(1)	0.46(2)
23	2.75(1)	2.35(2)	0.19(2)	2.73(1)	3.83(1)	0.46(2)
25	2.75(1)	2.35(2)	0.19(2)	2.73(1)	3.81(1)	0.46(2)

Table 6.2. Mean values of the first Si-H coordination number for various hydrogen concentrations, C_H.

C_H (%)	13	15	18	20	25
Z_H	1.06(1)	1.06(2)	1.16(3)	1.16(1)	0.87(1)

Fig. 6.13 also agrees well with an empirical form [362] for the dependence of the number of first nearest neighbours on hydrogen concentration, C_H. A similar trend was also found for the dependence of the number of first neighbours on hydrogen concentration in a Ge-H system studied experimentally using extended X-ray absorption fine structure [363]. In this model, the average first nearest neighbour coordination Z_1 in *a*-Si:H was modelled as a function of hydrogen concentration C_H as,

$$Z_1 = 4 - \frac{C_H}{100 - C_H}, \tag{6.2}$$

where C_H is in %. This estimate assumes that the number of dangling bonds is negligible in the network, compared with the number of Si-H bonds.

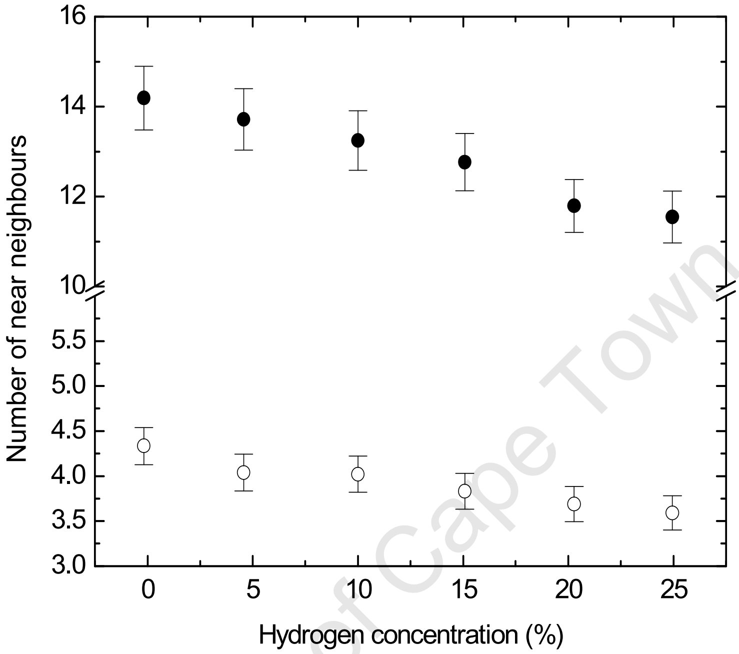

Figure 6.13: Combined plot of the mean number of Si-Si first nearest neighbours (Z_1) (open symbols) and second nearest neighbours (Z_2) (closed symbols) as a function of hydrogen concentration, C_H.

It could therefore be expected that as more hydrogen is incorporated in the network, more of the Si atoms are displaced, so that this leads to an increased number of the dihydride configurations. These observations support the earlier assertion, that apart from the monohydride configuration, other bonding configurations are quite likely in *a*-Si:H, especially at high C_H. In particular, this situation tends to support the existence of bonding configurations where one central Si atom is bonded to two H atoms, especially between 13% - 20% H, when Z_H is slightly above one. Fig. 6.13 clearly shows that, hydrogen incorporation has a more profound effect on the number of second neighbours, than on the number of first nearest neighbours, for Si-Si interactions. This situation can be considered to support the earlier conclusion, that the Si-H pairs are formed in a manner that does not allow Si to be a bonded second neighbour to the H at low C_H, but occupies another network position in the proximity of the monohydride.

6.2.3 The Role of Hydrogen in Amorphous Silicon

The effects of disorder on the electronic properties of amorphous materials have been discussed quite extensively in the literature [364,365]. In *a*-Si:H in particular, it is important to investigate the obvious issue of the role of hydrogen and influence of hydrogen on structural disorder. Recently, hydrogen has been shown to have a more substantial effect on medium range order than short range order. From the present results so far, apart from influencing structural order in *a*-Si:H, hydrogen has also has also been observed to induce significant relaxation of the network strain, even without being exposed to band gap photons.

Fig. 6.14 shows the variations in the Gaussian widths of ten different structural configurations of the first and second coordination peaks in $g(r)$ as a function of C_H. It is immediately obvious that the widths of both coordination peaks decrease with increasing hydrogen concentration. The addition of 5% hydrogen causes a decrease of the width from 0.60 Å to 0.45 Å. Similar increases in hydrogen concentration from 10% to 20% also causes a corresponding decrease in the Gaussian width from about 0.42 Å to 0.20 Å. Further increases in C_H beyond 20% yield no appreciable changes in the width of the peaks. However in Fig. 6.14 there is a stepwise dependence of the decrease in width with C_H. This stepwise character suggests the existence of two different structural configurations for hydrogen concentrations below 10% and above 18% respectively.

In order to explain the physical origin of this stepwise character, it is necessary to recall that the local structure of hydrogen free *a*-Si (model *a*) and hydrogenated *a*-Si (model *c*) either can be described in terms of the continuous random packing of distorted Si-Si_4 tetrahedra, or interpreted in terms of the CRN model [8]. At low and intermediate concentrations of hydrogen, existing dangling bonds in *a*-Si become terminated with hydrogen. After an initial reconfiguration of highly distorted tetrahedra, this has less effect on the structure, and leads to the plateau in Fig. 6.14. As more hydrogen is incorporated into the structure, the extra hydrogen atoms tend to act as substitutional impurities in *a*-Si:H. By displacing Si atoms from tetrahedral sites, more Si-H bonds are formed. At sufficiently high C_H, this situation favours the formation of Si-H pairs in close proximity to one another. It could be supposed that the structure now consists of, essentially disconnected ordered regions, as in this regime the peak widths are constant with very little scatter.

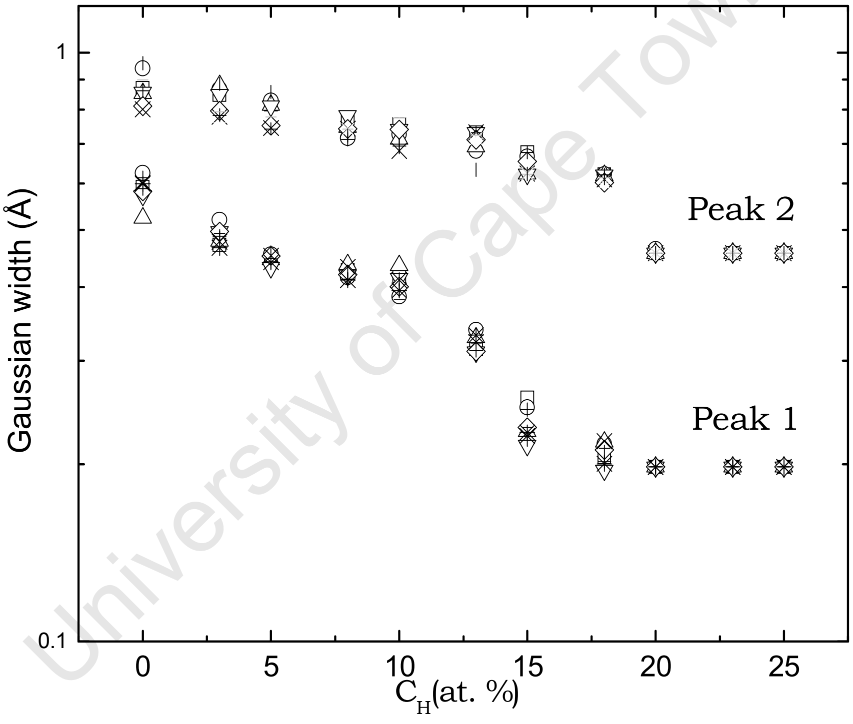

Figure 6.14 Combined log-linear plot of the width of the first coordination peak of ten structural configurations of *a*-Si:H (model *c*).

Chapter Seven

Analysis of Local Stress Fluctuations

7.1 Influence of Hydrogen on Atomic-level Stress

As seen earlier in chapter four, the overall atomic-level stress in the supercell models of a-Si:H is best described by its rms stress fluctuations. For the structural configurations simulated, the corresponding rms stress η, has been studied with respect to the hydrogen concentration level. Fig 7.1 shows the dependence of η with 11 different hydrogen concentrations C_H. For each of the eleven hydrogen concentrations, ten simulations were performed, leading to 110 different structural configurations.

Generally, as C_H increases from 0 to 18%, η shows a corresponding decrease. As for the Gaussian widths of the coordination peaks (Fig. 6.14) there is a noticeable step-like dependence of the rms stress with changing hydrogen concentration. It is important to note that above 10% H, there is no appreciable statistical fluctuation in the value of η unlike the observed trends for corresponding values of η below C_H of 10%. Above 18%, the rms stress drops to zero, and a further increase in C_H up to 25% does not cause any changes in the stress level. Assuming a linear decrease in the rms stress with increasing hydrogen concentration below a concentration of 18%, then at a hydrogen concentration of about 8%, a definite change in slope is observed. This allows the identification of three independent regions in the rms stress/hydrogen concentration curve, which can be used to classify the response of the a-Si:H structure to the incorporation of hydrogen, which, in turn, suggests that there are three types of structural response to changes in hydrogenation level. The first region, at low concentrations of hydrogen, is marked by rapidly changing stress levels. It is believed that most of the existing dangling bond defects are passivated by hydrogen. The second region, at intermediate concentrations of hydrogen, is marked by a significantly different slope. This is most probably an indication of the onset of saturation. The third region marks the development of a relaxed structure characterized by complete relaxation of the stress.

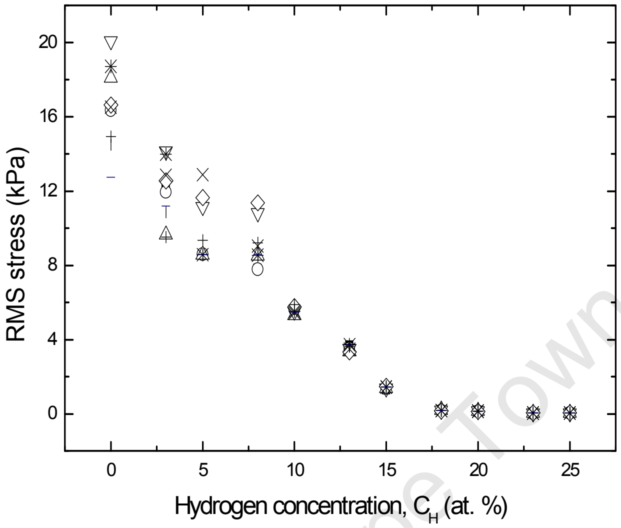

Figure 7.1: Plot of the rms stress η in *a*-Si:H (model *c*) showing a decreasing stress with increasing hydrogen concentration, C_H.

In several experimental studies [366-370], it has been found that there are compressive stresses in *a*-Si:H due to the invasive incorporation of hydrogen during film growth. Although not directly comparable, as no experimental studies have focused on stress fluctuations, and because the simulations are insensitive to macrostresses (see chapter four), these experimental observations are compatible with the behaviour seen in Fig. 7.1. Since the simulated hydrogen-free structure contains a high concentration of unterminated dangling bond defects, when hydrogen is first incorporated into the network structure, these native dangling bonds must be satisfied first. At sufficiently high hydrogen concentrations however, the excess hydrogen atoms must, according to the constraints of the simulation, break weak Si-Si bonds, thus displacing the silicon atoms by pushing them from their tetrahedral sites, so that the neighbouring tetrahedron becomes compressed.

If it is assumed that the stress is determined by the amount of hydrogen incorporated into the Si network, then the structural properties of the resulting *a*-Si:H network should be correlated, to a great extent, with the stress [371]. When there is a large number of strained, and therefore weak Si-Si bonds in the *a*-Si network at low H concentrations, the surrounding bonded atoms in the network must cause such bonds to break and reform, causing the Si atoms to be easily displaced from their initial position. The consequence of the associated network rearrangements due to the hydrogen insertion, leads to a reduction in the total stress fluctuations. This interpretation is consistent with the observed reduction in rms stress with increasing hydrogen concentration in Fig. 7.1.

7.2 Stress Density of States

Further insight into the distribution of stress is provided by investigating the distribution over all atoms in the system. The density of states for stress was computed for *a*-Si:H using model *c*, as described in section 4.5 at different values of hydrogen concentrations. The mean values of the principal components of the stress tensor were computed at 300 K, so that there are contributions to atomic stresses from thermal broadening (see Eqn. 4.29), and there is no directional information. The normalized probability $P(\sigma)$, of finding an atom under a stress state σ is shown in Figs. 7.2 to 7.4 for low, moderate and high C_H respectively. From these distributions, some important features of the stress distribution can be helpful in drawing preliminary conclusions concerning the stress within the supercell. Firstly, the total distribution of the magnitude of the local stress, which is obtained as a superposition of the contributions from all atoms in the supercell, is very broad at low C_H. This is an indication of the presence of large local internal stresses. The figures show also that, apart from the stress distributions at 23% and 25% H concentration (Fig 7.4), all other stress distributions exhibit significant tails for both compressive and tensile stress states. The tails are more pronounced at low C_H. This can be considered to originate from atoms with severely strained bonds and twisted bond angles, as it is the case in H-free structures and the structures with low C_H.

Secondly, the stress distributions in Fig. 7.4 show distinctive differences from the distributions in Fig. 7.2 and Fig. 7.3. In Figs. 7.2 and 7.3, the width of the distribution changes, more or less uniformly with C_H whereas in Fig. 7.4 a significant narrowing in the profile of the stress distribution as C_H changes from 20% to 23% can be seen. In contrast, minimal changes are observed in the profiles beyond 23% H. The distribution at the high hydrogen concentration limit is marked by a symmetrical normal distribution, with a high probability of stress states around zero. Evidently, this transition marks saturation in the stress relaxation, caused by the addition of hydrogen. Thirdly, and perhaps more importantly, there is no preferred stress state in all the supercell models of *a*-Si:H. Both tensile and compressive stresses are observed for each structural configuration at almost equal intensities. This symmetry is a direct consequence of the quasi-equilibrium of the modelled structure. As a result, the average or total intrinsic stress in any given structural configuration is almost relaxed.

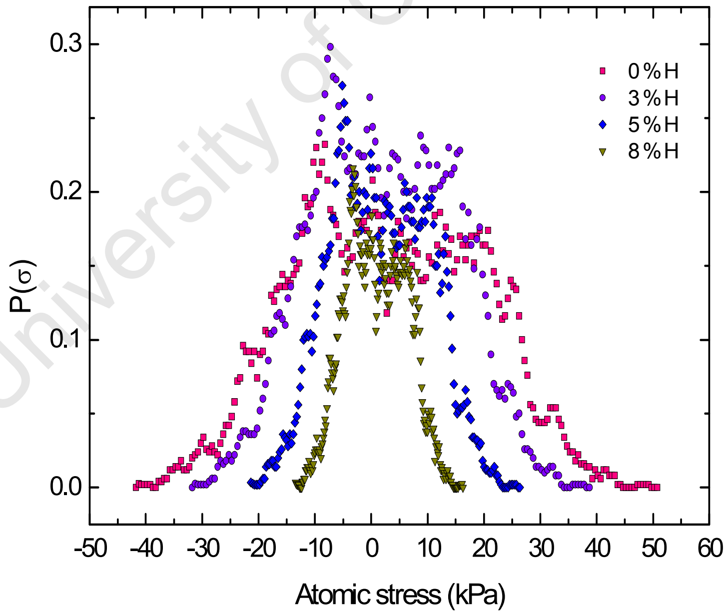

Figure 7.2 Normalized probability distributions of atomic stresses in supercell models of *a*-Si:H at 300 K at low hydrogen concentrations.

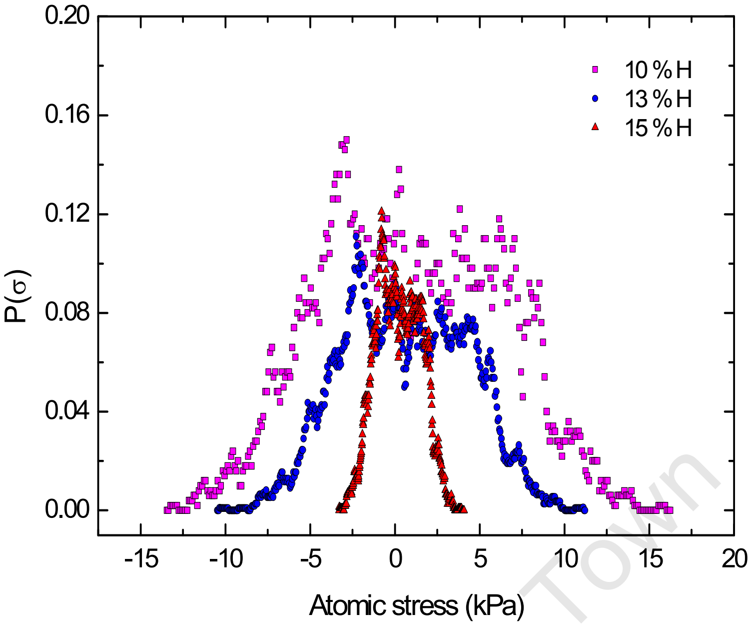

Figure 7.3 Normalized probability distributions of atomic stresses in supercell models of *a*-Si:H at 300 K at moderate hydrogen concentrations.

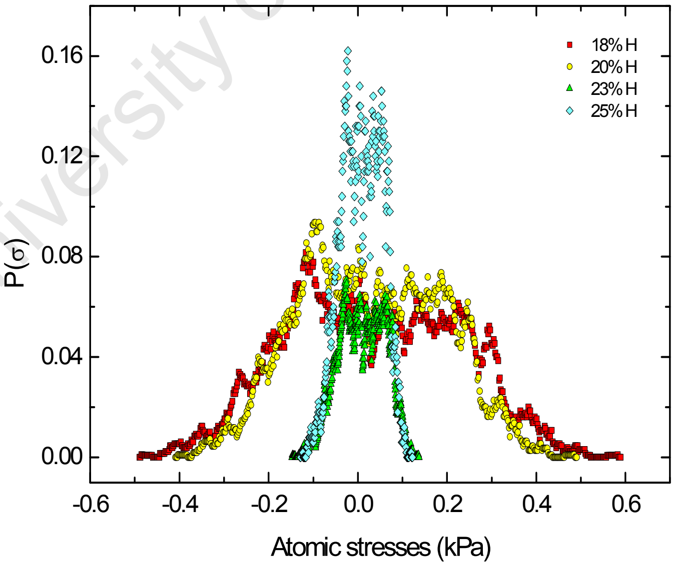

Figure 7.4 Normalized probability distributions of atomic stresses in supercell models of *a*-Si:H at 300 K at high hydrogen concentrations.

7.3 Islands of the Stress Landscape

In case of a 2D domain defined by the pair of parameters such as the peak widths (δ_1, δ_2), it is clear that not all points in the domain can be accessible. This situation is however, non-trivial, and directly relates to the geometry of the local structure and its response to external perturbations. To illustrate what is mentioned above, δ_2 is plotted as a function of δ_1 in Fig. 7.5 for the 110 structural configurations. The data tend to form an island in this domain, with no data points existing far away from the origin, and close to either of the axes. Although not marked on the plot, it is worthwhile to note, that *a*-Si:H network configurations represented by the data points closest to the origin of the coordinate system contain the highest hydrogen concentration, and has the smallest spread in interatomic distances. Points farther away from the origin denote *a*-Si:H networks which contain decreasing hydrogen concentrations.

The scatter plot of Fig. 7.5 shows that, in this domain, data are clustered along a linear trend line at a preferred orientation, relative to the horizontal axis. This preferred orientation is approximately 36 degrees, and its similarity to Plato's golden ratio is noted without comment. However, this orientational dependence has also been tested for tetrahedral amorphous carbon (*ta*-C) networks simulated in the same computational framework. For the *t*a-C structures, Fig. 7.6 shows the scatter plot on a similar domain. Although the response of the *ta*-C system to H incorporation is not as pronounced as *a*-Si, the linear trend line shows the same preferred orientation. This suggests that this angle is likely to be related to the local tetrahedral symmetry of the tetrahedrally-bonded covalent networks. In a perfect tetrahedron, the dihedral angle is 71.53°, and 35.77° is the angle between the axis and the edge, defined by r_1 and r_2 in Fig. 2.5.

The preferred orientation of the island of data does not violate the implicit requirement that the basis must span the entire domain. However, it is instructive to refer to Fig. 2.5 again in order to explain the physics of this situation. For the *a*-Si:H networks under study, it is simply unphysical, to have a near neighbour atom with a very small deviation in its first neighbour distance and a very large deviation in the second neighbour distance. This observation is a direct consequence of the local structure of tetrahedrally-bonded materials, because every first nearest neighbour atom is also a second nearest neighbour of another atom. It becomes clear, that any induced change in the first nearest neighbour distance r_1 simultaneously causes a change in the second nearest neighbour distance r_2. The fluctuations in interatomic distances are therefore always coupled throughout the structure.

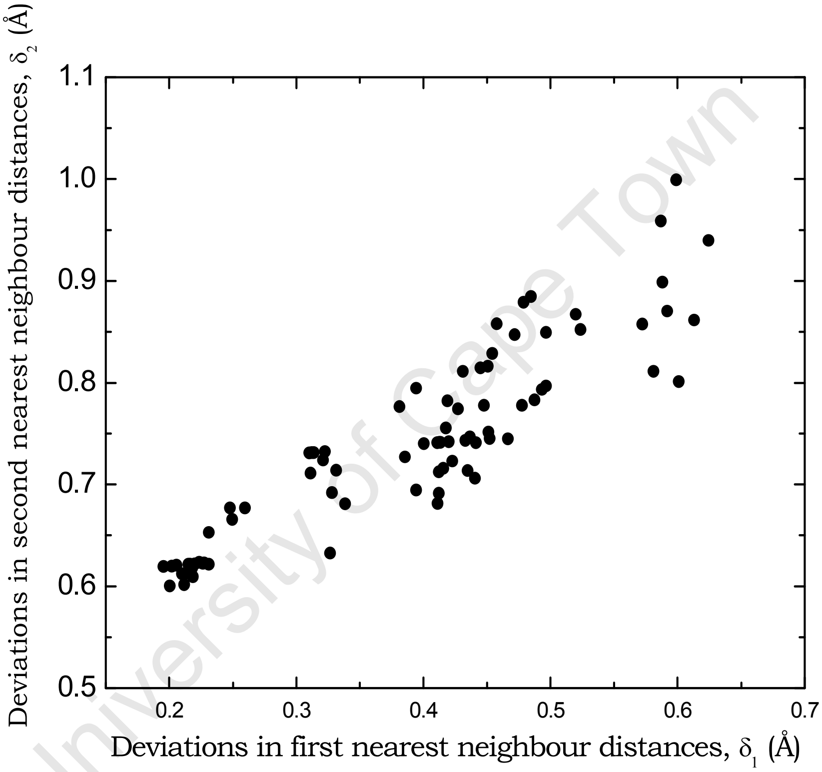

Figure 7.5 Dependence of the standard deviation in the mean second nearest neighbour distances in 110 structural configurations of hydrogenated amorphous silicon as a function of standard deviation in first nearest neighbour distances.

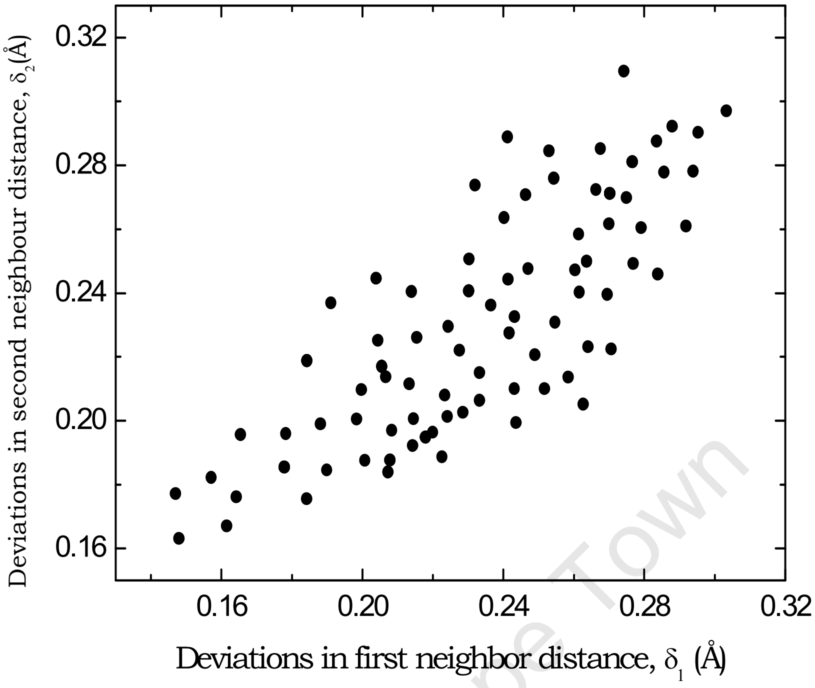

Figure 7.6 Dependence of the standard deviation in the mean second nearest neighbour distances in 110 structural configurations as a function of standard deviation in the first nearest neighbour distances showing a preferred orientation of data points at an angle of 36 (± 2) degrees relative to the horizontal axis for (hydrogenated amorphous carbon.

This coupling significantly restricts the accessible points in the domain for which stress information could be obtained to those points accessible on the island of Fig. 7.5. It is therefore obvious that stress information can only be available for points in the domain where the coordinates are well defined. The coupling of the changes in interatomic distances and the preferred orientation within this domain suggest that it is possible to use a single parameter to characterize order in the structure. In order to test this hypothesis, the coordinates of the domain are re-defined, in terms of rotated axes as

$$\delta_1' = \delta_1 \cos \frac{\pi}{5} + \delta_2 \sin \frac{\pi}{5}, \tag{7.1}$$

and

$$\delta_2' = -\delta_1 \sin \frac{\pi}{5} + \delta_2 \cos \frac{\pi}{5}, \qquad (7.2)$$

where δ_1' is directed parallel to the island, and δ_2' is perpendicular to it. Fig. 7.7 shows the rms stress η, plotted as a function of each of these new parameters. There is a clear trend for the dependence of the rms atomic stress on the distance along the island δ_1'. This dependence is observed in two well-defined regions: region 1, which is characterized by high hydrogen concentration showing little scatter; and region 2, which is characterized by low hydrogen concentration marked by more scatter.

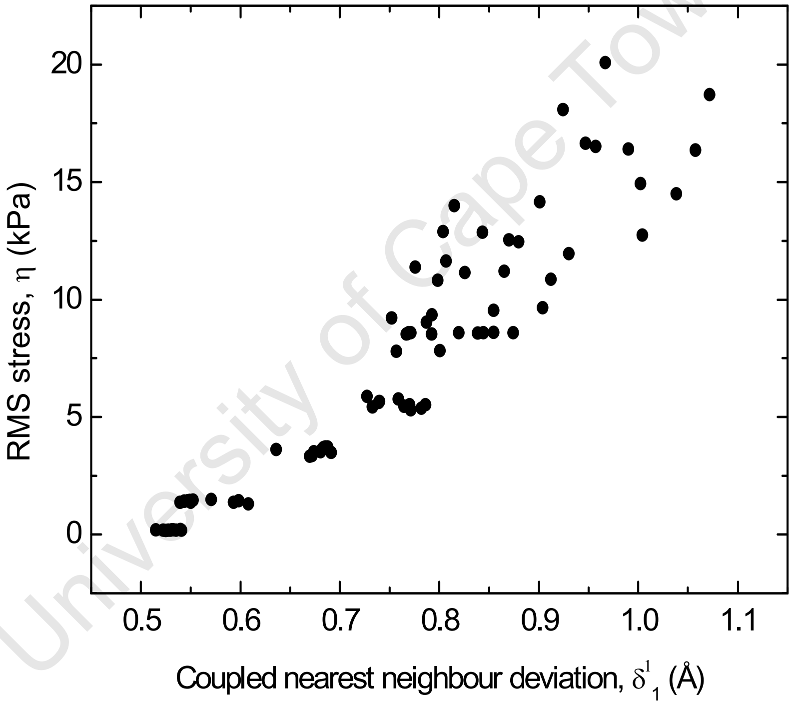

Figure 7.7 Dependence of the rms stress on coupled nearest-neighbour deviations, with distance parallel to the island of data.

However, Fig. 7.8 shows that there is no correlation between the local stress fluctuations and the normal distance δ_2', because the scatter points do not follow any discernible trend. It can therefore be concluded, that in order to establish a relationship between local atomic stress fluctuations and local structural fluctuations in *a*-Si:H, the order in the *a*-Si:H network can be quantified by a single parameter δ_1'. Subsequent analyses of results will only consider the variations of the rms stress with the structural order parameter δ_1'.

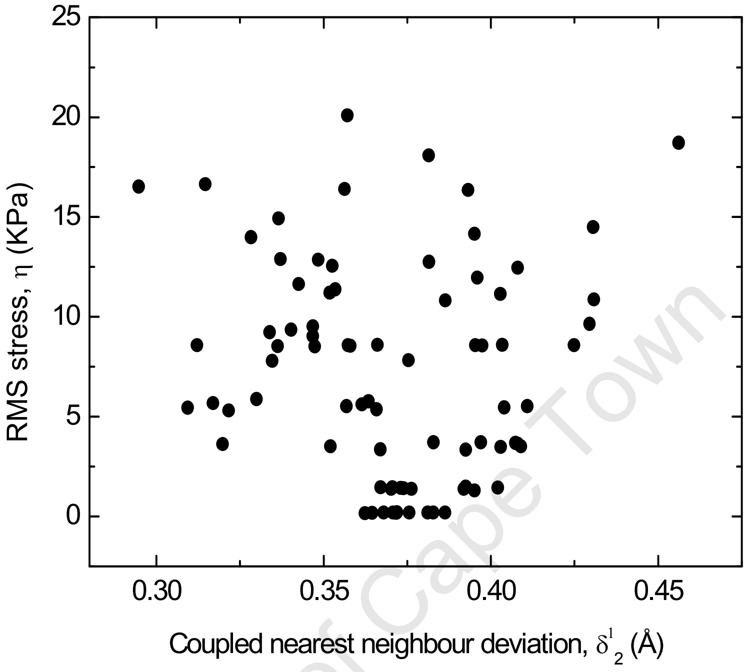

Figure 7.8 The dependence of the rms atomic level stress on coupled nearest neighbour deviations, with distance normal to the island of data.

In order to characterize the stress landscape, it is instructive to note, that Fig 7.7 shows two clear regions corresponding to hydrogen concentration values above and below 15%. Region 1 is smooth, while region 2 is rugged. In the smooth region there is a definite linear correlation between the rms stress and the disorder parameter, marked by a correlation coefficient of 0.92. At lower hydrogen concentrations, there is more scatter in the data, but there is also a clear increase in stress with disorder. Between the two regions there is also a noticeable change in slope, suggesting a transition between two types of structures. To investigate this further, this one dimensional landscape can be analyzed in a more detailed manner using the same statistical tools as for analysing a topographical profile, for which notions of roughness and correlation length are well established [372].

7.4 Correlation of Structural Order with Atomic Stress

The ruggedness or smoothness of a configurational landscape can be described in the statistical representation, in terms of its correlation structure. From a static viewpoint, for a topographical landscape for instance, the correlation length is defined to explain the spatial correlation between similar features. The correlation length is therefore considered to represent either the distance within which a certain pattern repeats itself, or an exponential distance over which information is lost. In the appropriate domain, these two types of correlation length can be observed in a plot of the autocorrelation function of the parameter under investigation. In the case described here, the first appears as distinct peaks or steps, in the stress autocorrelation function, and the second as an exponential decay length within the prescribed domain.

For the rms stress η, the autocorrelation S, as a function of the lag δ in the order parameter δ_1', is given by

$$S(\delta)=\frac{\int_0^{\infty}\eta(\delta_1'+\delta)\eta(\delta_1')d\delta_1'}{\int_0^{\infty}\eta(\delta_1')\eta(\delta_1')d\delta_1'}. \tag{7.3}$$

Fig. 7.9 shows the rms stress autocorrelation function at 300 K, obtained from Eqn. (7.3) as a function of the lag in the order parameter for the entire stress landscape. It is immediately clear that the stress autocorrelation exhibits a significant decrease, as the lag in order parameter increases from zero to 0.05 Å, where there is an onset of a step-like trend. Further increases in the lag, from 0.05 Å to 0.15 Å, results in very small changes in the stress autocorrelation function. Beyond a lag of 0.15 Å but below 0.18 Å, a sharp decrease in autocorrelation is obtained for small increases in lag. Above a 2.0 Å lag in the order parameter, the stress autocorrelation decreases steadily and reaches a minimum at a lag of 0.35 Å. Beyond a lag of 0.35 Å, the stress autocorrelation drops to zero.

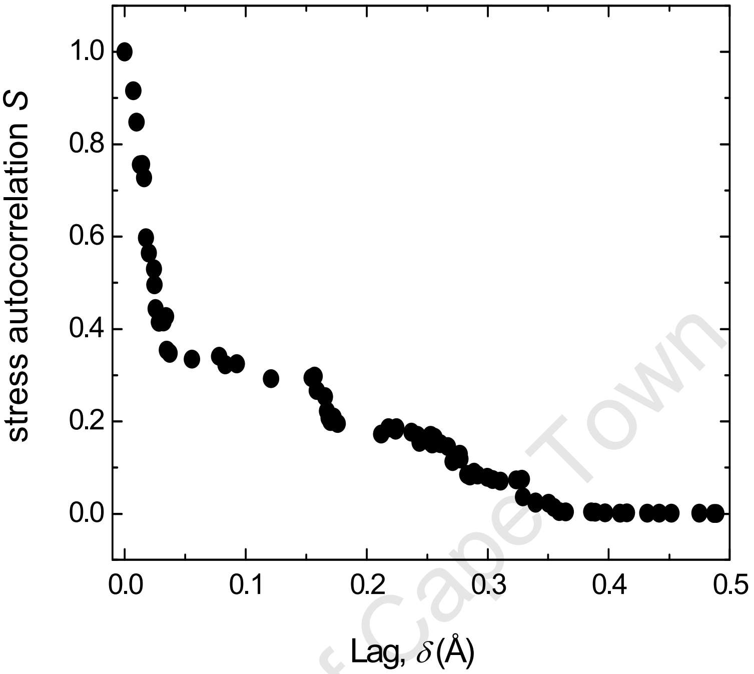

Figure 7.9 RMS stress autocorrelation function at 300 K as a function of the lag in order parameter for the entire stress landscape of *a*-Si:H (model *c*).

It is also important to investigate the origin of the step-like correlation structure, and its possible implications on the stress landscape of *a*-Si:H. To address this, the stress autocorrelation function is evaluated independently, as a function of the lag in the order parameter, for the smooth and the rugged regions of Fig. 7.7. In the smooth region, Fig. 7.10 shows the dependence of the stress autocorrelation on the lag in order parameter. Similar step-like features are observed in the correlation structure at 0.04 Å, 0.08 Å, and 0.16 Å respectively. Beyond 0.16 Å, the stress auto correlation drops off to zero. This implies that within the smooth region, there is no correlation between any two structures separated by 0.16 Å within the domain.

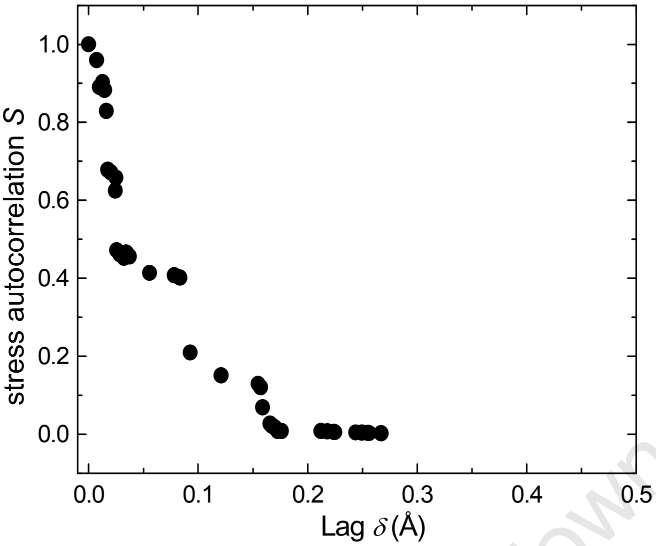

Figure 7.10 RMS stress autocorrelation function at 300 K as a function of lag in order parameter for the smooth region of the stress landscape, showing the correlation structure in the high C_H limit of model *c*.

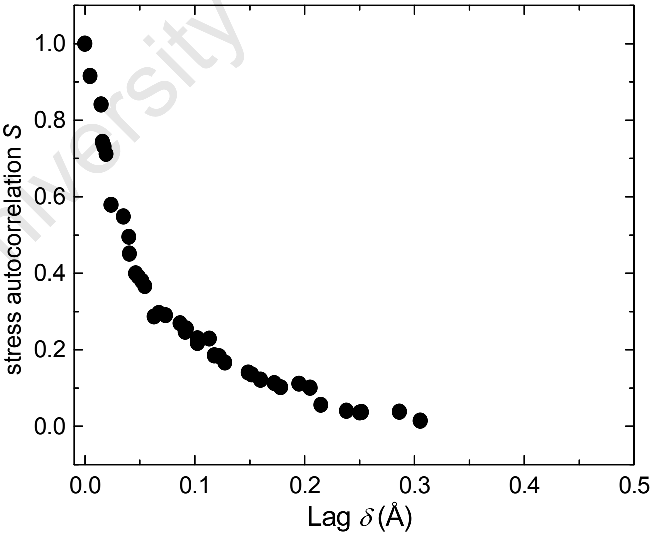

Figure 7.11 RMS stress autocorrelation function at 300 K as a function of lag in order parameter for the rugged region of the stress landscape, showing the correlation structure in the low C_H limit of model *c*.

In contrast, the stress autocorrelation for the rugged region, which denotes configurations with low hydrogen concentration (Fig. 7.11), shows a monotonic decrease with lag in structural order, with little or no visible correlation structure. If the stress autocorrelation function in the rugged region is modelled in terms of a first order exponential decay in the order parameter within the domain, then a single exponential distance is obtained, over which no correlation exists between any two stress configurations. This gives a correlation length of approximately 0.070 (± 0.003) Å for amorphous silicon networks in the low C_H limit. For any two structures with low hydrogen concentration, whose order parameters differ by significantly more than this value, there is no significant correlation between the levels of their atomic level stress.

Summarizing above results, it is clear that most of the structures seen in Fig. 7.9 are due to correlations in the smooth region of the landscape, whose stress autocorrelation shows discrete steps at lags of approximately 0.04, 0.08, and 0.16 Å. A comparative analysis of the correlation structure shows, that any two stress configurations separated by 0.35 Å fall into different regions of the domain. The separation by a distance of 0.35 Å, of any structural configuration belonging to either the smooth or the rugged regions, within the domain, leads to a structural change, from the rugged region to smooth region and vice versa. This suggests that there is a phase transition from a disordered to a more ordered structure as the hydrogen concentration is increased above a certain level.

The interpretation of the observed stepwise correlation length is non-trivial with respect to understand the H-induced structural changes. In order to obtain insights into its physical meaning, it is important to recall, that the domain represents the structural order parameter field, and not a physical distance in the amorphous network. The implication therefore is, that there are discrete reductions in the degree of the dependence of the stress on the structural order, as the variation in neighbour separations increases by multiples of a fixed amount. This is almost certainly related to the repeated reconfiguration of the a-Si network, probably by hydrogen termination, as the strain on individual bonds exceeds a certain limit. However, the development of a complete and realistic physical model for this situation is well beyond the scope of this thesis.

7.5 Mechanical Response of the Local Structure to Stress

So far, it has been observed that a more ordered structural network is obtained for high hydrogen concentration in *a*-Si:H. It is worth recalling, that the distribution of first and second nearest neighbours in a perfectly ordered network of *c*-Si is singular, such that the number of first and second nearest neighbours, Z_1 and Z_2, are always constrained to be 4 and 12, respectively. This is a unique characteristic of the ordered tetrahedral network. To investigate the distribution of nearest neighbours as the structure undergoes the transition from the disordered state to the ordered state, Fig 7.12 shows the dependence of the rms stress η with the number of (a) first (Z_1) and (b) second (Z_2). These results show an increase in the number of first and second neighbours at high levels of stress. The eleven data points in Fig. 7.12 (a) and (b) are an average of 10 individual simulations at each hydrogen concentration. Similarly, the error bars were obtained as the standard deviations in the mean value of the number of near neighbours, calculated from the ten repeated calculations.

In Fig. 7.12, data points with the lowest hydrogen concentration are furthest away from the origin, and have the highest scatter indicated by the large error bars. On the other hand, data points obtained from highest hydrogen concentrations are nearest to the origin, and have least scatter. At the higher hydrogen concentrations, there is neither a scatter in the rms stress nor any defined pattern for the dependence of rms stress on the number of near neighbours. In Fig. 7.12 and Fig. 7.13, two regions can clearly be identified.

(i) a region of well-defined linear decrease in stress with decreasing number of near neighbours; and

(ii) a region where there is no apparent relationship between the two, marked by a vanishingly small rms stress.

For low and intermediate hydrogen concentrations C_H, an extrapolation of the linear dependence shows limiting values of approximately 3.92 and 12.4 for the numbers of first and second nearest neighbours respectively. These limiting values are in qualitative agreement with the results obtained in section 6.2.2 for the distribution of first and second nearest neighbours as a function of hydrogen concentration.

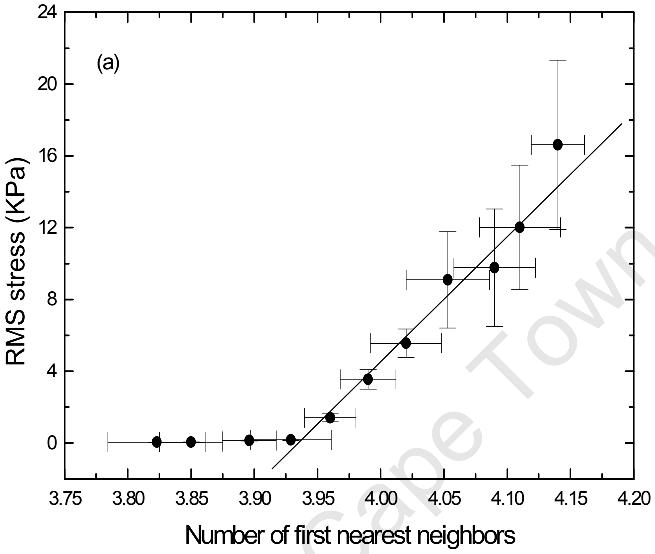

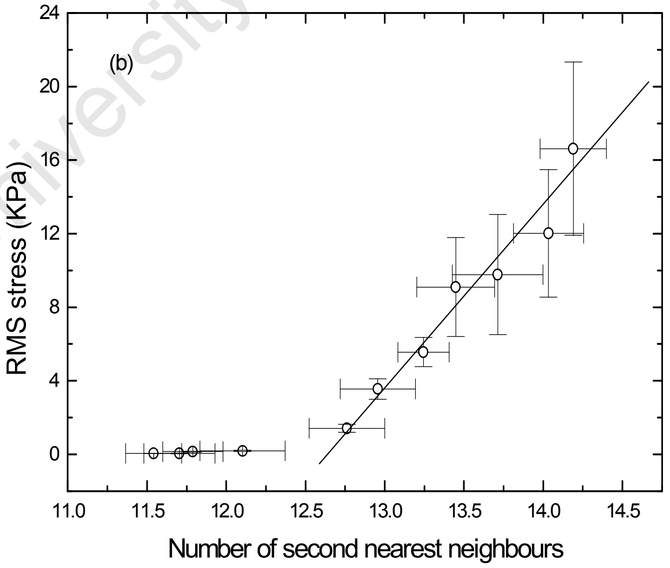

Figure 7.12 Variation of rms atomic stress with the number of first (Z_1) (a), and second (Z_2) (b) nearest neighbours in bulk hydrogenated amorphous silicon.

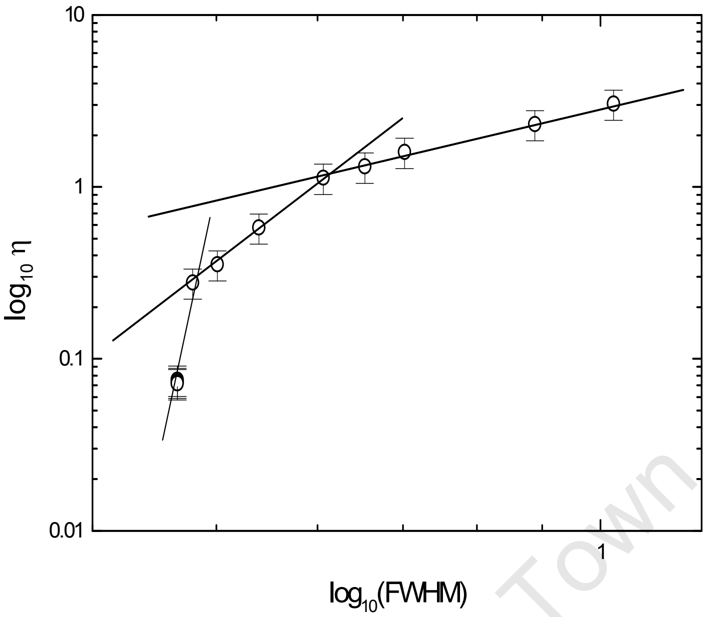

Figure 7.13 Log-scale dependence of the root mean square stress on the full width at half maximum, showing a three-stage structure transition from disorder-to-order.

From established correlations between structural order and atomic stress, it is possible to investigate the mechanical properties of the evolving network structures. Fig. 7.13 shows a log-scale plot of the dependence of the local contributions to stress on the full width at half maximum (FWHM) of the first coordination peak. This clearly reveals three regions, similar to those seen in Fig. 7.9. For the low C_H, a linear dependence exists suggesting a linear elastic response of the structure to stress, in line with Hooke's law. The slope of the two linear regions can be interpreted as an effective elastic modulus. The modulus obtained for the linear region is 73 ± 15 GPa. Within the error, this calculated value agrees very well with the expected value of 80 ± 20 GPa for H-free *a*-Si [373]. The decrease in stress from region 1 to region 2, with increasing hydrogen content is also a clear evidence of some local structural rearrangements in the *a*-Si network, which as noted before, is highly influenced by hydrogen termination of dangling bonds. These rearrangements are characterized by a decrease in stress, and the onset of local structure ordering.

Chapter Eight

Analysis of Positron Properties

Hitherto, insights into the local network structure of all physical (hand-built) or computer-generated models of *a*-Si and *a*-Si:H have been obtained only in terms of the pair correlation function [374-376], the atomic-level stress [315,316], and the associated strain fields [377,378]. This arises mainly because the pair correlation function can be determined experimentally, for direct comparison with results of computer simulations and theoretical predictions. However, it has been demonstrated [379-381] that, depending on the computational model of the amorphous material under investigation, the local structure of the material can also be characterised, in terms of parameters that can be defined on the atomic scale.

Since the positron can sense a uniquely different potential that is only dependent on the vicinity of the annihilation site within a material [239,240], its associated wave function, which is measured in terms of the positron density [382] can be used to characterize the local bonding environment of the simulated structures [241]. To test this hypothesis, basic positron properties are investigated in the simulated structures. The positron density profiles presented here are results obtained for structural configurations chosen from the two regions identified in the stress landscape of a-Si:H. For the rugged region, which is characterized mainly by low hydrogen concentration, results are presented for bulk structures containing 0%, 3% and 5% hydrogen concentrations. For the smooth region, characterized mainly by high hydrogen concentrations, positron density profiles are presented for structures containing 18%, 20% and 25% hydrogen concentrations. In addition, to help in the identification of defects in positron annihilation studies of *a*-Si:H, results obtained for a wide class of *ad hoc* defects are also presented.

8.1 Normalized Positron Density

The profiles of the positron density reported here represent an approximate estimate of the character of the general solution of the time-independent solution of the Schrödinger equation for the positron potential, which corresponds to a given defect or bulk structure. Two different representations are used to visualize these solutions. Firstly, a general overview is given by a superposition of the 3D isosurface on a ball and stick model of the structure. Secondly, more detailed information of specific sites is given by contour maps projected onto particular planes in the simulation box. For the 3D isosurface plots, the volume of the box is divided into a uniform cubic grid of dimension $96 \times 96 \times 96$. For a box containing 1728 atoms, the length of simulation box is 61.598 Bohr (32.58Å) per axis, with each grid corresponding to a spacing of thickness 0.64165 Bohr. For the 2D contour plots, the positron density is plotted on planes normal to the z-axis of the simulation box.

To illustrate the superposition of the contour plot on the structure, consider the simulation box shown in Fig. 8.1, which is divided into a uniform grid as described above. The time independent positron density could then be calculated on a median plane corresponding to the middle of the simulation box. Any other median plane could be chosen, provided it is not located near the surfaces or edges of the simulation box, since to avoid edge effects contour plots along the surfaces of the simulation box are not considered. As depicted in Fig. 8.1, atoms which intersect the chosen plane are described as *in-plane*, while those lying above or below the median plane are described as *above-plane* or *below-plane* atoms respectively. These three sets of atoms are differentiated by plotting different colours on the contour maps. Atoms whose spatial cordinates deviate from a given median plane by distances within ± 1.0 Bohr are considered to be in the median plane. This is physically justifiable because the distance (0.529 Å) is far less than the mean first near neighbour separation for either Si-Si or Si-H bonds. The maximum distance from the median plane for an atom to be counted as either above-plane or below-plane is set to 4.442 Bohr. This distance is the mean Si-Si bond length and corresponds to twice the radius of Si atoms when in tetrahedrally-bonded covalent bonds [57].

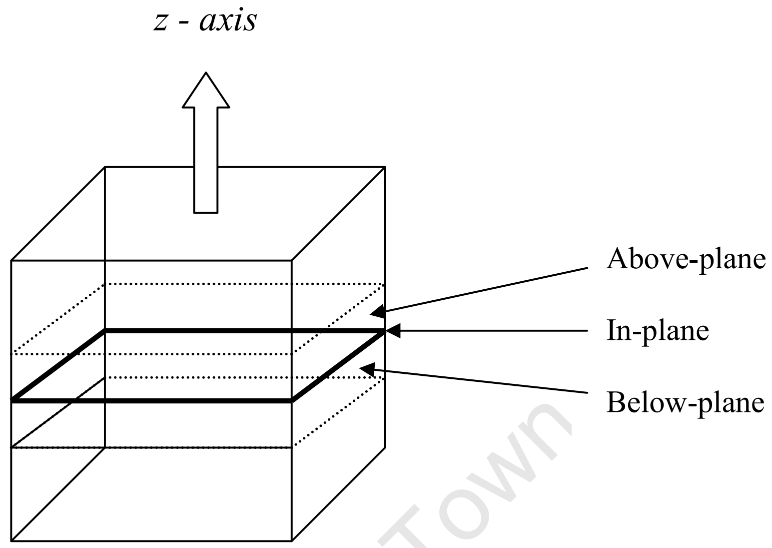

Figure 8.1 Illustration of the simulation box, to show positions of atoms lying (i) in-plane, (ii) above-plane and (iii) below-plane relative to the contour plot of positron density.

Fig. 8.2 shows a 3D isosurface map of the positron density superimposed on the ball and stick model of the structural configuration of the hydrogen-free model of *a*-Si. The direction of view is parallel to the *z*-axis of the simulation box. It is immediately clear that the positron wave function is strongly localized in an empty space within the simulation box, which corresponds to a region of open volume in the structure visible in the right hand panel. The extent of this localization is a very strong. The positron density is restricted to a well-defined region in the bulk structure. Apart from this point of strong localization, the positron density is observed to vanish everywhere else in the bulk structure.

A close inspection of Fig. 8.2 shows that:

(i) most of the Si atoms observed in the vicinity of the localized positron density are not four-fold coordinated

(ii) most of these unterminated dangling bond defects appear to cluster together;

(iii) the clustering of these dangling bond defects sets up an empty space, which corresponds to a larger defect complex; and

(iv) in the ball and stick model, this large defect complex appears as a region of low ionic density relative to other parts of the network.

This low ionic density sets up a local minimum in the positron potential, which acts as a positron trap. From Fig. 8.2, the strength of the positron density localization at open-volume region of the hydrogen-free structure allows an intuitive assumption that the long positron lifetime observed in bulk hydrogen free a-Si [232] is most likely to be due to positrons trapped at regions of low ionic densities. Such a region is more likely to be created by clusters of unterminated dangling bonds than by isolated unterminated dangling bond defects.

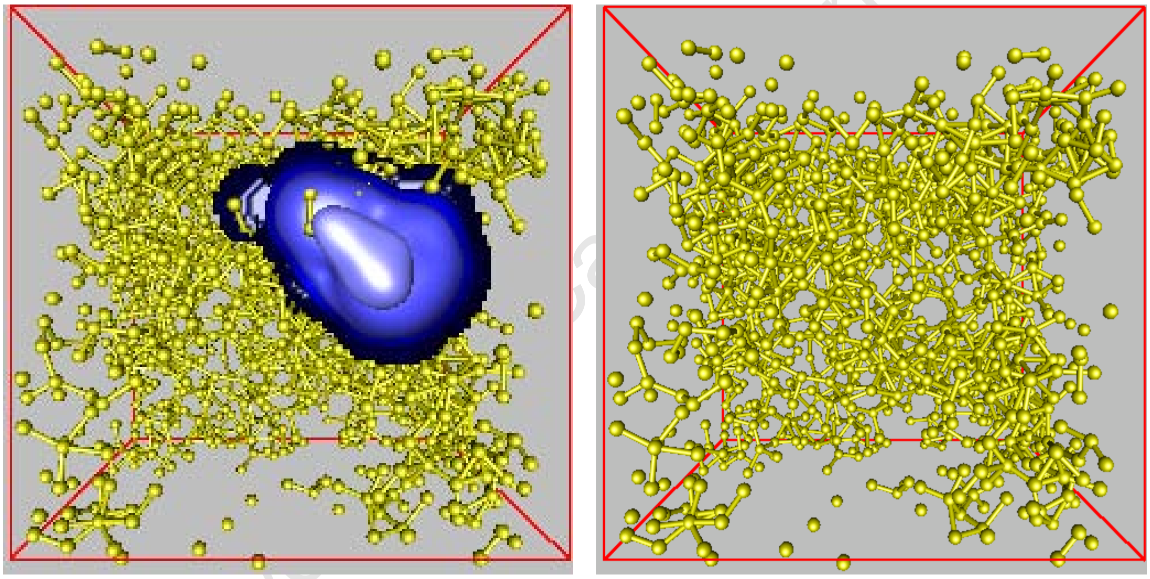

Figure 8.2 3D isosurface map of the positron density superimposed on the ball and stick model of the hydrogen-free model of amorphous silicon to show a strongly localized positron density at an open-volume region of the structure.

Fig. 8.3 shows the 3D isosurface plot of the normalized positron density in hydrogenated amorphous silicon containing 3% atomic hydrogen, which has a significant effect on the positron density. Two clearly different regions of positron density are identifiable. First, an extensive region of lower positron density, shown in blue, is identified. This region, in which the positron density is effectively delocalised, is predominantly associated with Si atoms. The second region, shown in white, is marked by a comparatively high positron density. The region of higher positron density is primarily associated with the vicinity of hydrogen atoms. The high positron density regions are found to be more localized and cover a less extensive spatial location within the structure. The defect associated with the localized positron density could be attributable to a trap arising from the clustering of hydrogen terminated dangling bonds.

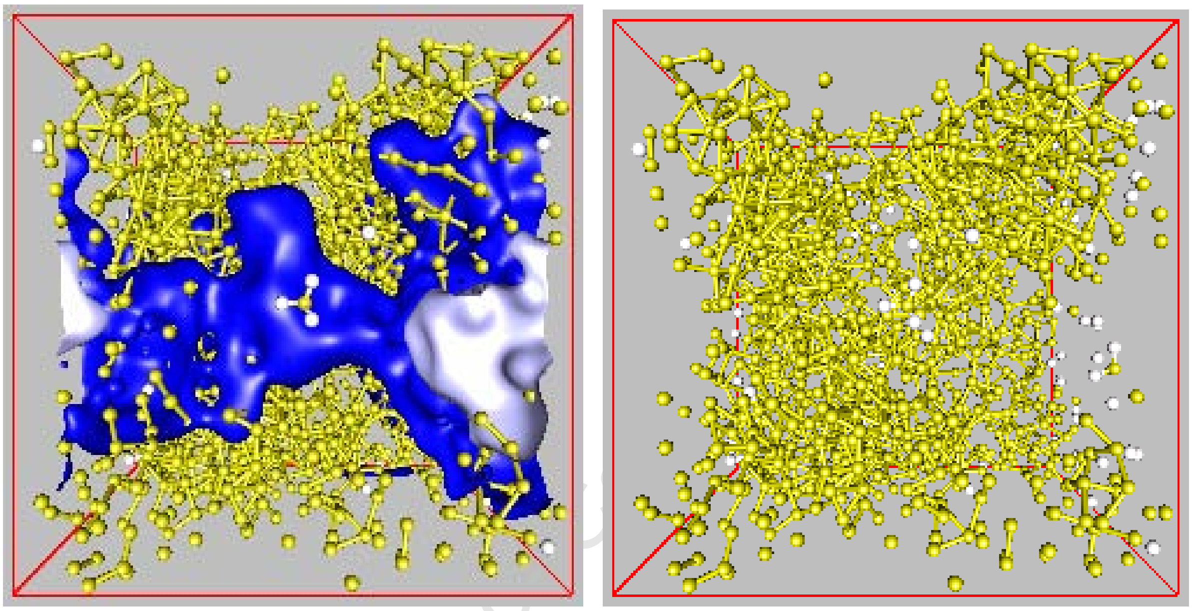

Figure 8.3 The delocalized positron density in bulk hydrogenated amorphous silicon showing evidence of enhanced positron density in the vicinity of hydrogen atoms.

In order to explore the extent of the localization in the two regions, it is necessary to plot the positron density as 2D contour maps along selected median planes along the z axes of the structure. It is equally important to correlate the ball and stick representations of points corresponding to the positron densities around these planes. Figs. 8.4 to Fig. 8.7 show the normalized positron density viewed along median planes, cut at z = 15.485, 30.3248, 45.1646 and 54.8427 Bohr respectively, in the hydrogenated model of amorphous silicon, which contains 3% hydrogen. The ball and stick models, which are shown alongside figures, correspond to the local bonding geometry in each case. These are plotted for points within a 22.31 Bohr radius from the point of maximum positron density on the corresponding plane. The extent of the positron localization in Figs. 8.4 and Fig. 8.6 are not as high as those observed for the hydrogen-free model.

The strongest localisation is at the defect shown in Fig. 8.4. The positron density drops by seven orders of magnitude in a distance of about 10 Bohr from its centre. The ball and stick model, shows that the open volume region is made up of mono and poly-hydrides. The presence of the polyhydride configurations suggest that larger vacancies must have been created spontaneously in the structure. Such a spontaneous defect creation, which must be followed, by their decoration with hydrogen, can be expected to occur during structural relaxation. The second strongest positron density localisation is observed in Fig. 8.7. In this case, the positron density is observed to drop by four orders of magnitude over a distance of 10 Bohr. In the ball and stick model, this defect appears to be an unterminated dangling bond, or a pair of dangling bonds. In Fig. 8.7, there is no appreciable localisation of the positron density at a single hydrogen terminated dangling bonds. Figs. 8.5 and 8.6 show similar weak localisation at dangling bond clusters and at H-terminated dangling bond clusters respectively. The total intensity of the positron density in these defects may be lower because of competition by the stronger traps seen in Figs. 8.4 and 8.7.

Figs. 8.8 to Fig. 8.11 show the positron density as contour plots on median planes cut along the same planes in the simulation box for the hydrogenated structure containing 5% hydrogen concentration. Fig. 8.8 shows the positron density viewed from the plane z = 15.485 Bohr. From this positron density profile, it could be said that the positron wave function is weakly localized. This suggests that this positron trap is a shallow trap. An inspection of Fig. 8.8 shows that an *in-plane* atom is located directly at the point of highest positron density.

Using the spatial coordinates of this atom, an estimate of number of Si or H atoms lying within a spherical surface of radius 4.54 Bohr (2.40 Å) suggests that this atom is a single unterminated dangling bond defect. Physically, the choice of 2.40 Å corresponds to the maximum Si-Si near neighbour separation obtainable from the simulations. Similarly, Fig. 8.9 shows the positron density viewed from the plane z = 30.3248 Bohr. Fig. 8.9 shows no *in-plane* atoms in the vicinity of the localized positron density. It should also be noted that, for this

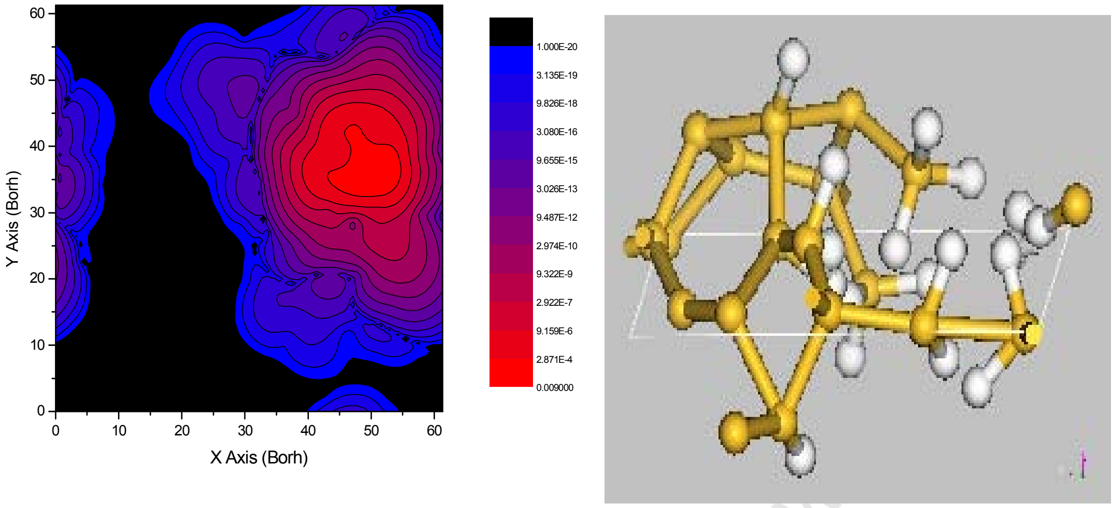

(a) (b)

Figure 8.4 (a) 2D contour map of the normalized positron density in hydrogenated amorphous silicon showing a weakly localized positron density when viewed along the plane z = 15.458 Bohr.

(b) Ball and stick model of the region shown in (a) indicating the plane used.

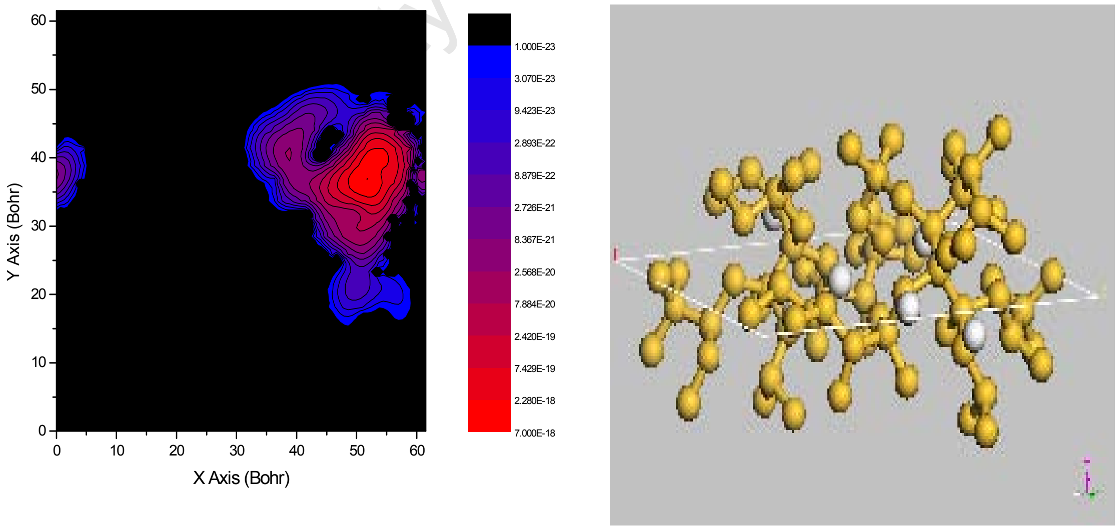

(a) (b)

Figure 8.5 (a) 2D contour map of the normalized positron density in hydrogenated amorphous silicon showing a more strongly localized positron density when viewed along the plane z = 30.3248 Bohr.

(b) Ball and stick model of the region shown in (a) indicating the plane used.

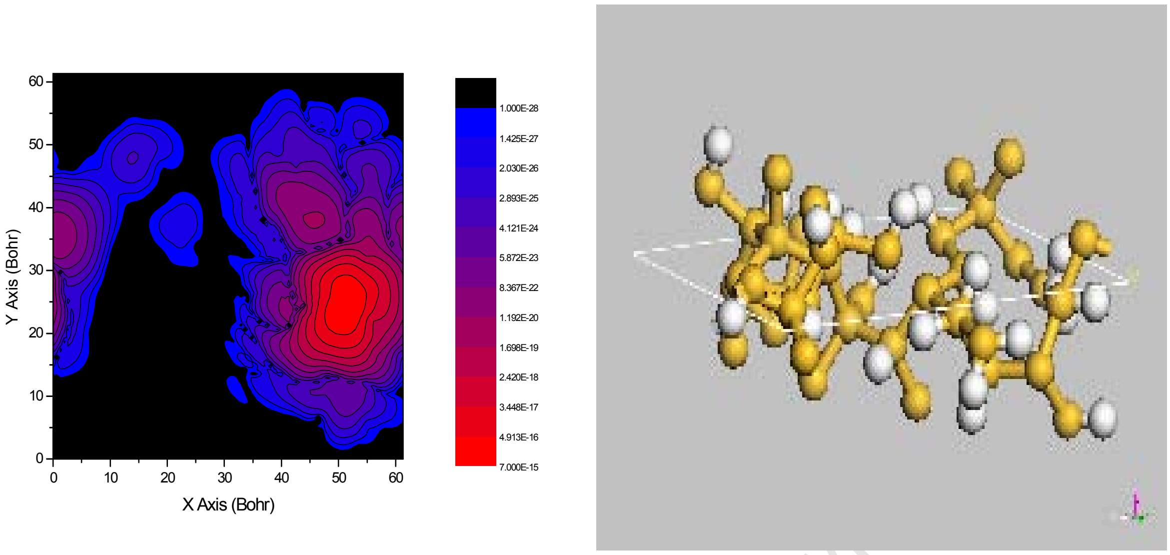

(a) (b)

Figure 8.6 (a) 2D contour map of the normalized positron density in hydrogenated amorphous silicon showing a weakly localized positron density when viewed along the plane z = 45.1646 Bohr.

(b) Ball and stick model of the region shown in (a) indicating the plane used.

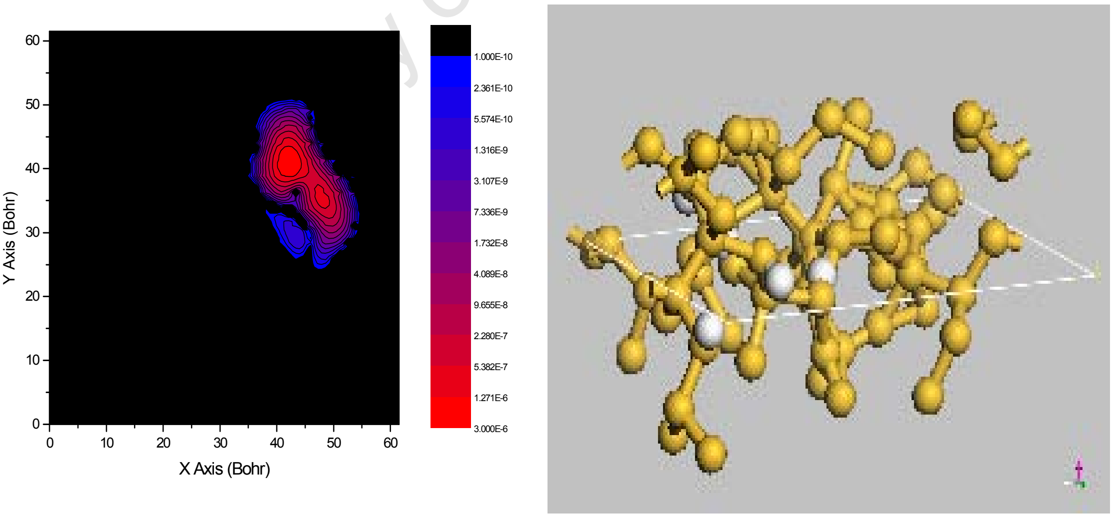

(a) (b)

Figure 8.7 (a) 2D contour map of the normalized positron density in hydrogenated amorphous silicon showing a more strongly localized positron density when viewed along the plane z = 54.8427 Bohr.

(b) Ball and stick model of the region shown in (a) indicating the plane used.

plane, the maximum positron density is two orders of magnitude smaller than that shown in Fig. 8.8. Assuming that similar arguments also hold for this median plane, then the observed positron density localization can only be attributable to a localized high electron density source that can be attributed to atoms lying above and below the plane.

The situation is very different in Fig. 8.9 and Fig. 8.11, when compared to Fig. 8.5 and Fig. 8.7 because the extent of positron density localization is weaker due to the marginal increase in C_H from 3% to 5%. The extent of the delocalization of the positron density suggests that the dominant defect types are shallow traps. In Fig. 8.10 and Fig. 8.11, the positron density is clearly split into two well-defined high-density regions. In the first region, the positrons are localized in the vicinity of an *in-plane* atom. However, in the second region, the highest positron density corresponds to an *empty space* within the supercell.

No *in-plane* atoms are found close to the regions of maximum positron density in Fig. 8.9 and Fig. 8.10, which could suggest that the trap site is not due to a localized high electron region. The observed weak positron localization can only be attributable to empty spaces corresponding to regions of low ionic density within the network structure. In addition, the nearest atom to the contour line, which represents the trough of the localized positron density, is located on *Z*-planes below 45.1646 Bohr and 54.8427 Bohr in each case. These results clearly show that the incorporation of more hydrogen atoms into the hydrogen-free network causes the otherwise strongly localized positron density to become effectively delocalized throughout the bulk structure.

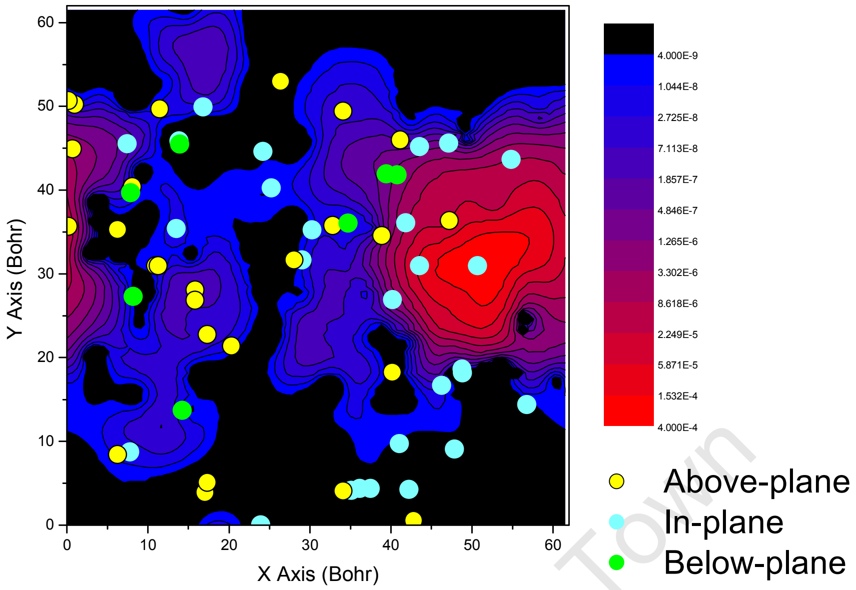

Figure 8.8 Contour plot of positron density in *a*-Si:H containing 5% H, with atomic positions superimposed, viewed from the plane *z* = 15.485 Bohr.

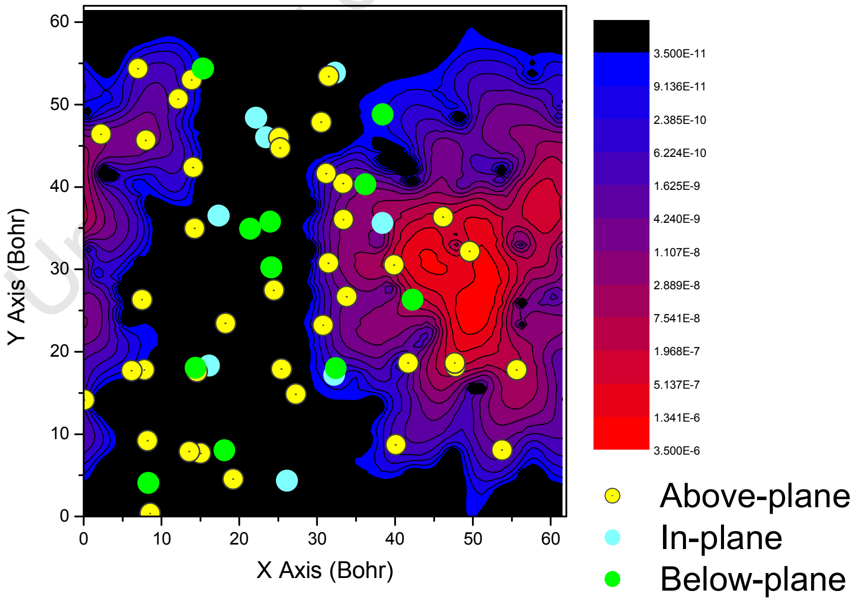

Figure 8.9 Contour plot of positron density in containing 5% H, with atomic positions superimposed, viewed from the plane *z* = 30.3248 Bohr.

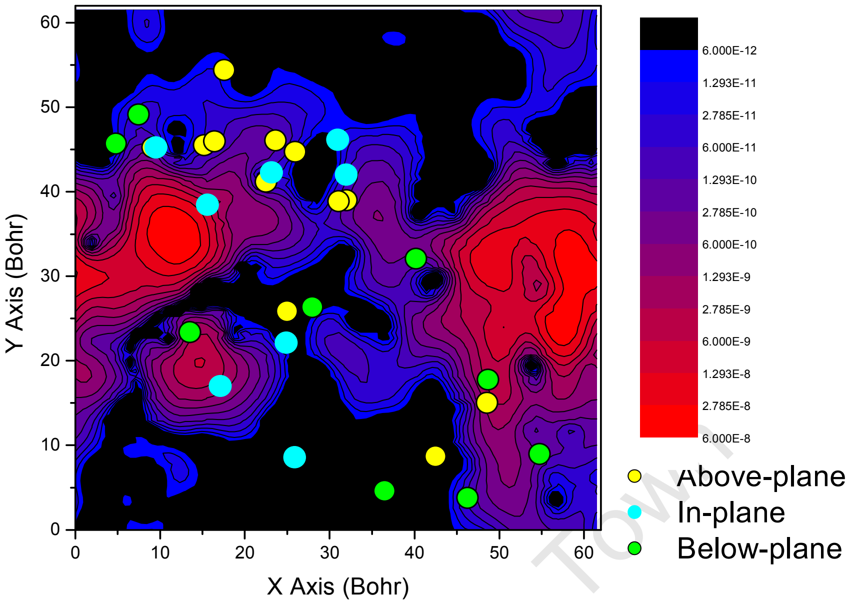

Figure 8.10 Contour plot of positron density in *a*-Si:H containing 5% H, with atomic positions superimposed, viewed from the plane $z = 45.1646$ Bohr.

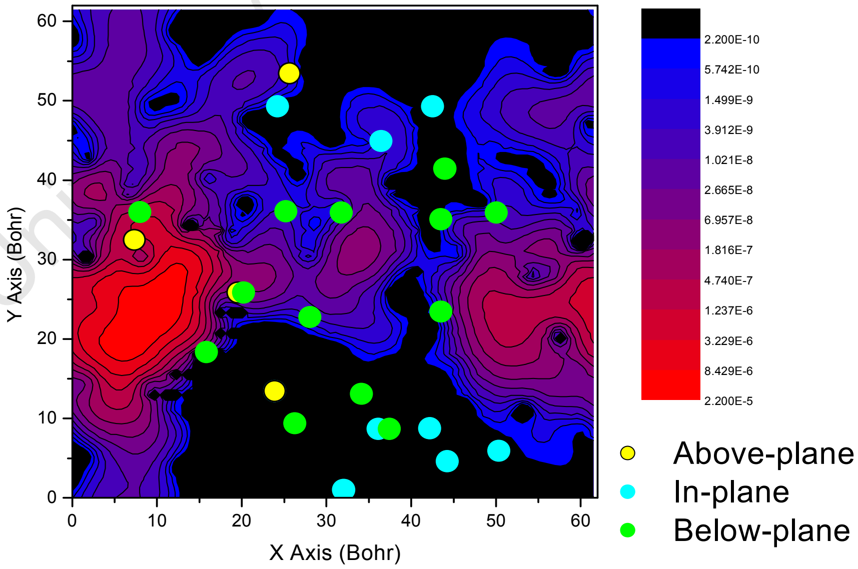

Figure 8.11 Contour plot of positron density in *a*-Si:H containing 5% H, with atomic positions superimposed, viewed from the plane $z = 54.8427$ Bohr.

As discussed in chapter three, the thermalized positron state is not well understood in amorphous silicon because of the complexity of the local structure of the material. In regular defect-free periodic solids, like *c*-Si for instance, the thermalized positron state is a delocalized Bloch wave. Fig. 8.12 shows a 3D isosurface map of the delocalized positron density superimposed on the ball and stick model of a *c*-Si superlattice. This shows that the normalized positron density is delocalized throughout the bulk structure. The magnitude of the positron density is highest in the interstitial regions, and vanishes in the vicinity of the Si atoms due to Coulomb repulsion. The distribution of the delocalized positron density within the entire volume of the bulk structure is uniform and symmetric. In such a structure, the presence of a vacancy defect introduces a local minimum in the effective positron potential. This potential energy minimum leads to a low energy positron state. At thermal equilibrium, this low-energy positron state is trapped at the vacancy. The trapping of a positron at a defect leads to a strongly localized positron density, with a local maximum at the centre of the vacancy.

The positron densities obtained for hydrogenated amorphous silicon structures classified in the rugged region of the stress landscape in chapter seven, are different in terms of shape, extent of localization and amplitude to those for the smooth region. As seen previously, these features depend mainly on the local structure of the defect, or on the local bonding structure. Fig. 8.13 and Fig. 8.14 show 3D isosurface maps of the normalized positron density superimposed on the ball and stick model of hydrogenated amorphous silicon containing 18% and 20% atomic hydrogen respectively. The plane of view is normal to the *z*-axes of the bulk structure in each case. A comparison of Fig. 8.2 with Fig. 8.13 and Fig. 8.14 shows the complete delocalization of positron density when the concentration of hydrogen, C_H is very high. It is therefore concluded, that hydrogen has the non-trivial effect of inducing the delocalization of positron densities. The strongly localized positron density observed at lower hydrogen concentrations is seen to be completely delocalized in the structure when hydrogen concentration is higher than 18%.

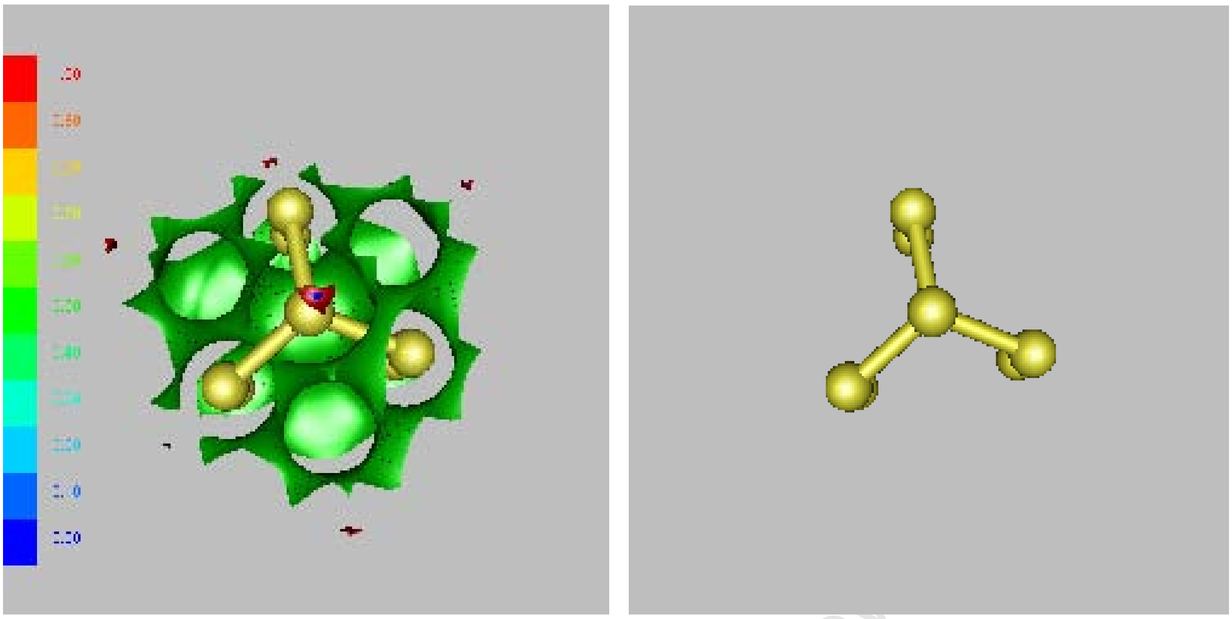

Figure 8.12 3D isosurface plot of the delocalized positron density superimposed on a ball and stick model of a *c*-Si superlattice showing the positron wave function restricted to the interstitial region between successive Si-Si near neighbours.

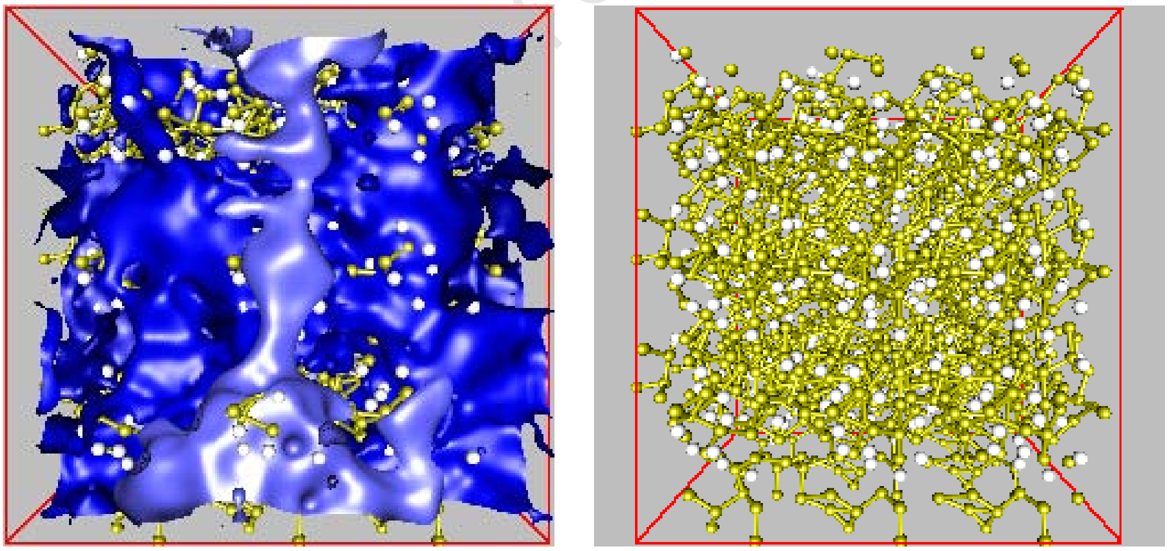

Figure 8.13 3D isosurface map of the positron density superimposed on the ball and stick model of the hydrogenated model of amorphous silicon containing 18% atomic hydrogen to show the delocalization of the positron density throughout the bulk structure. The plane of view is parallel to the *Z*- axis of the bulk structure.

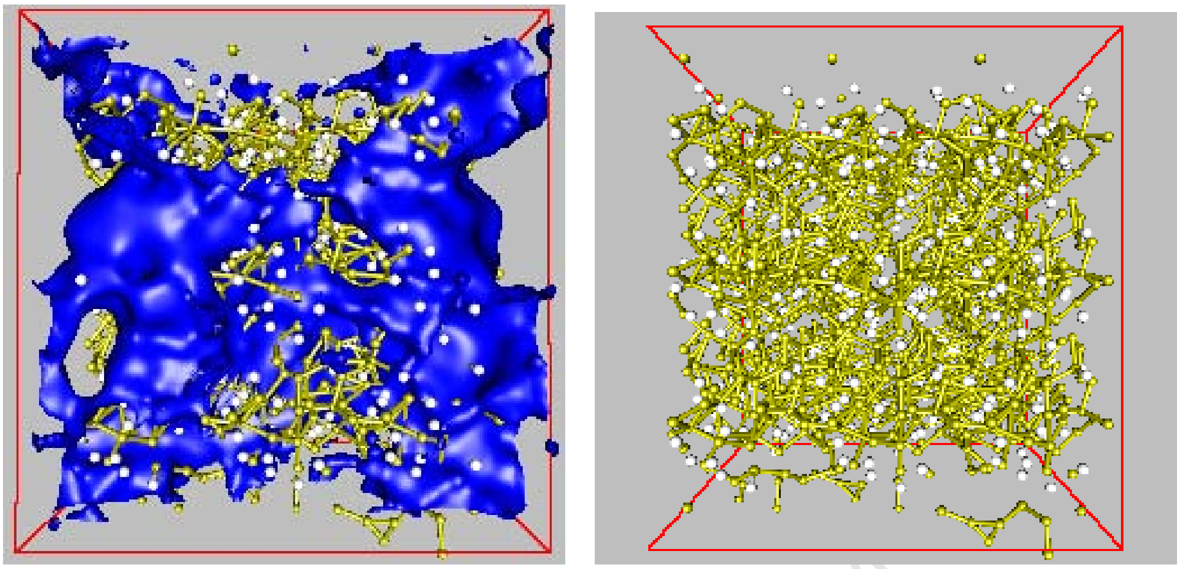

Figure 8.14 3D isosurface map of the positron density superimposed on the ball and stick model of the hydrogenated model of amorphous silicon containing 20% atomic hydrogen to show the delocalization of the positron density throughout the bulk structure. The plane of view is parallel to the z- axis of the bulk structure.

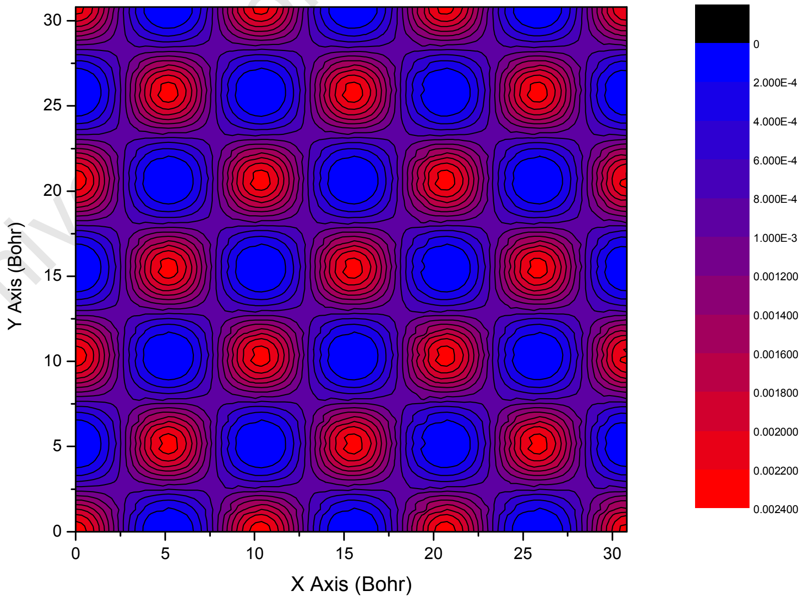

Figure 8.15 2D contour map of the positron density in crystalline silicon showing the effect of long-range order and translational periodicity.

In terms of the configurational landscapes, at higher hydrogen concentrations, the structures were found to become comparatively more ordered when compared to structures with lower hydrogen concentration. In terms of the positron properties, as more hydrogen is incorporated, there is evidence of progressive delocalization of the positron density. Contrary to the situation observed in the case of *c*-Si, the delocalized positron density is non-symmetric and irregular even for the comparatively more ordered structures of the smooth region of the landscape. This delocalized positron state is not a Bloch wave. In terms of Fig. 8.15, this situation could be attributed to the prevalent disorder in atomic positions. The effect of the residual disorder is to cause the overlap of the positron wave function at spatial positions between near neighbour pairs thereby causing the positron density to be delocalized in the bulk structure. Experimentally, the predominant positron lifetime component associated with such structures could therefore not be associated with a specific type of defect since there are no localized regions of high positron density.

8.2 Positron Annihilation Characteristics

The positron lifetime, total annihilation rate, and the positron binding energy in the hydrogen-free, and defect structures have been computed within the zero positron density limit of the electron-positron correlation function $g(0;n+,n-)$ [240,246]. The positron calculations were first carried out based on the two parameterizations of the contact density enhancement factor, within the local density approximation (LDA) [240,246,266], and then repeated based on the generalized gradient approximation (GGA) to the contact density enhancement factor [281-282]. The polarizability a, was set to either 0.22 or 0 in each case, to correspond to calculations based on the generalized gradient approximation (GGA) or the local density approximation (LDA), respectively. Results obtained using the LDA parameterizations of Boronski and Nieminen [240] are denoted ATSUP-LDA-BN, while those obtained using the LDA parameterizations of Arponen and Pajane [266] are denoted ATSUP-LDA-AP for comparison.

Table 8.1 shows the results of positron properties in different bulk structures of amorphous silicon in the two identified regions of the stress landscape using the LDA scheme. Each of these results is obtained as an average over ten configurations of the respective structural geometry, and all the errors quoted (in brackets) were obtained as the standard errors in the mean of ten equivalent calculations of the same data. Also included are the positron properties, calculated within the same LDA schemes, for similar structures in crystalline silicon. For comparison, Table 8.2 shows similar results for positron properties obtained in different simulated bulk structures of amorphous silicon, using the GGA scheme for the enhancement factor.

Although there is no correlation between the modelling methods used in simulating the bulk *a*-Si structures used in this study with any known experimental method of film growth method, it is nonetheless helpful to compare the results of actual experimental positron lifetime spectroscopy (PLS) for thin *a*-Si films grown using a wide range of methods since the local structures and topologies are more or less similar in both cases. This is to see, qualitatively, if hydrogen has any influence or not on the positron properties. Table 8.3 shows a summary of the experimental PLS results collated from various sources on amorphous silicon thin films obtained from different growth techniques. The GGA scheme is observed to give values that are generally lower than those obtained with either of the LDA-based parameterizations.

More importantly, The ATSUP-LDA-AP scheme is observed to give higher values for the positron lifetime and binding energy when compared with the ATSUP-LDA-BN scheme. The positron lifetimes shown in Tables 8.1 and 8.2 are found to be in agreement within the limits of the experimental lifetime obtained for HWCVD thin films in Table 8.3. In thin films grown from the PECVD method [393,231], long positron lifetimes are observed due to the presence of very large voids in *as-grown* samples. There is also evidence of a second positron lifetime component attributed to the bulk of the sample. For instance, a positron lifetime of 402 ps in the bulk region [393] is in qualitative agreement with the observed trend in the results of the calculations.

Table 8.1 Positron properties in bulk *c*-Si and *a*-Si:H for varying concentrations of hydrogen showing the mean value of positron lifetime (τ), positron binding energy E_b, and total annihilation rate obtained using the ATSUP-LDA-BN and ATSUP-LDA-AP schemes for the contact-density enhancement factor.

Bulk		ATSUP-LDA-BN			ATSUP-LDA-AP		
Structure	C_H(%)	τ(ps)	E_b(eV)	λ(ns^{-1})	τ(ps)	E_b(eV)	λ(ns^{-1})
c-Si	0	224(1)	0.92(1)	4.46(1)	227(2)	1.07(1)	4.41(1)
a-Si	0	391(3)	3.27(4)	2.55(3)	395(4)	3.57(3)	2.53(3)
a-Si:H	*3*	348(2)	2.85(3)	2.87(4)	362(3)	2.93(2)	2.76(2)
a-Si:H	*5*	328(2)	2.52(2)	3.04(6)	351(2)	2.83(2)	2.85(3)
a-Si:H	*8*	322(2)	2.47(3)	3.10(2)	347(2)	2.64(1)	2.88(2)
a-Si:H	*10*	317(2)	2.23(1)	3.15(5)	342(1)	2.33(1)	2.92(4)
a-Si:H	*13*	311(3)	2.13(2)	3.21(5)	336(4)	2.20(3)	2.97(2)
a-Si:H	*15*	308(2)	2.02(1)	3.24(4)	332(3)	2.14(1)	3.01(2)
a-Si:H	*18*	303(3)	1.82(1)	3.30(1)	324(2)	2.03(2)	3.09(1)
a-Si:H	*20*	288(2)	1.57(1)	3.47(2)	292(2)	1.83(3)	3.43(1)
a-Si:H	*23*	218(1)	1.33(1)	4.58(1)	232(1)	1.73(2)	4.31(1)
a-Si:H	*25*	217(1)	1.32(1)	4.60(1)	221(2)	1.63(1)	4.53(3)

Table 8.2 Positron properties in bulk *c*-Si and *a*-Si:H for varying concentrations of hydrogen showing the mean value of positron lifetime (τ), positron binding energy E_b, and total annihilation rate obtained using the ATSUP-GGA scheme for contact-density enhancement factor.

Structure		ATSUP-GGA		
	C_H(%)	τ(ps)	E(eV)	λ(ns^{-1})
c-Si	0	219(2)	0.54(1)	4.57(1)
a-Si	0	384(6)	3.54(2)	2.60(4)
a-Si:H	*3*	334(3)	2.70(1)	2.91(2)
a-Si:H	*5*	325(1)	2.43(2)	3.08(2)
a-Si:H	*8*	318(3)	2.11(2)	3.15(2)
a-Si:H	*10*	312(2)	2.03(2)	3.21(1)
a-Si:H	*13*	308(1)	1.87(4)	3.25(2)
a-Si:H	*15*	302(2)	1.72(1)	3.31(1)
a-Si:H	*18*	293(1)	1.52(2)	3.41(3)
a-Si:H	*20*	285(1)	1.37(1)	3.51(1)
a-Si:H	*23*	213(1)	1.13(2)	4.70(2)
a-Si:H	*25*	209(1)	0.99(2)	4.82(1)

Table 8.3 Summary of positron lifetime spectroscopy results for *as-grown* amorphous silicon thin films showing percentage hydrogen content, C_H, positron lifetime (τ) and the corresponding film growth method.

Structure	C_H(%)	τ(ps)	Growth Method	References
a-Si	0	303-352	MBE	[232]
a-Si:H	1-5	322-350	HWCVD	[10,48,48,220,236]
a-Si:H	10-20	> 3000	PECVD	[231]
		402 (1800)	PECVD	[382]
a-Si:H	10-20	400-500	Sputtering	[230]

For the bulk structures there was no requirement for an explicit consideration of the contributions of core-states to the total annihilation rate. It is useful to consider the positron properties in the *ad hoc* defects created (model *c* and model *d*) in terms of the effects of core-state contributions to the annihilation events. Table 8.4 shows the computed positron properties in different models of vacancy-like open-volume defects (model *c*) in hydrogen-free a-Si obtained using the two parameterizations of contact density within the LDA scheme. Similar results obtained within the GGA scheme are presented in Table 8.5 for comparison. As would probably be expected, the positron binding energy and the corresponding positron lifetimes at these defects show a systematic increase with increasing number of dangling bonds, N_{db}. Using the GGA scheme, the positron properties in different vacancies in *c*-Si are investigated to provide a benchmark for these positron lifetimes in *a*-Si structures. For instance, a mean lifetime of 234 (± 2) ps is obtained for a monovacancy in *c*-Si, as shown in Table 8.6. Generally, there is a in continuous increase in the positron lifetime as the vacancy size increases.

Table 8.7 shows the results of positron properties obtained within the two LDA schemes for hydrogen-decorated vacancy complexes in *a*-Si. Similar results obtained from the GGA scheme are shown in Table 8.8. Even when the core state contributions to the annihilation rate are explicitly included in the calculations for the vacancy-like defects, the core contributions are not expected to significantly affect the positron lifetimes and binding energy, because the annihilation of positrons from core-electrons is generally a low-probability event. This is clearly demonstrated in Tables 8.4 and 8.5, where the explicit inclusion of core state contributions does not change the general trend of dependence of the binding energy and positron lifetimes with number of dangling bonds N_{db}. However, in terms of the high momentum component of annihilation line, the relative strengths of the core contribution can be quite useful in the determination of vacancy-type defects [383].

Table 8.4 Number of dangling bonds N_{ab}, mean value of positron lifetime (τ), positron binding energy B_e, relative core-state contribution to the total annihilation rate (λ_c/λ), and total annihilation rate in bulk hydrogen-free *a*-Si (model *a*) and in different sizes of vacancy-like open volume defects in *a*-Si (model *c*) obtained using the ATSUP-LDA-BN and ATSUP-LDA-AP schemes for the enhancement factor.

Defect Geometry	N_{db}	ATSUP-LDA-BN				ATSUP-LDA-AP			
		τ (ps)	E_b (eV)	λ_c/λ (%)	λ(ns^{-1})	τ (ps)	E_b(eV)	λ_c/λ(%)	λ(ns^{-1})
T_4	0	211(3)	0.03(4)	1.33(3)	4.74(1)	207(2)	0.98(3)	0.9(1)	4.82(6)
V_1	4	253(3)	1.31(2)	1.65(3)	3.95(2)	247(7)	1.00(4)	0.8(1)	4.04(2)
V_2	6	267(2)	1.32(2)	1.67(2)	3.74(3)	266(4)	1.02(2)	0.8(2)	3.76(1)
V_3	8	279(2)	1.64(1)	1.68(5)	3.58(2)	276(5)	1.70(4)	0.8(3)	3.61(2)
V_4	10	334(4)	1.81(1)	1.67(2)	2.99(2)	318(2)	2.28(6)	0.7(1)	3.13(1)
V_5	12	347(3)	1.92(1)	1.68(4)	2.88(2)	326(2)	2.43(6)	0.8(1)	3.06(1)

Table 8.5 Number of dangling bonds N_{db}, mean value of positron lifetime (τ), positron binding energy E_b, relative core-state contribution to the total annihilation rate (λ_c/λ), and total annihilation rate in bulk hydrogen-free *a*-Si (model *a*) and in different sizes of vacancy-like open volume defects in *a*-Si (model *c*) obtained using the ATSUP-GGA scheme for the enhancement factor.

Defect Geometry	N_{db}	ATSUP-GGA			
		τ (ps)	E_b(eV)	λ_c/λ (%)	λ(ns^{-1})
T_4	0	207(1)	0.10(2)	0.90(1)	4.83(3)
V_1	4	247(1)	1.04(2)	0.80(1)	4.04(2)
V_2	6	266(1)	1.03(1)	0.83(2)	3.76(1)
V_3	8	276(1)	1.70(1)	0.80(3)	3.62(1)
V_4	10	318(1)	2.28(2)	0.67(3)	3.13(7)
V_5	12	326(1)	2.43(1)	0.78(1)	3.06(3)

Table 8.6 Mean value of positron lifetime (τ), positron binding energy (E_b), relative core-state contribution to the total annihilation rate (λ_c/λ), in different sizes of vacancy defects in *c*-Si obtained using the ATSUP-GGA scheme for the enhancement factor.

Defect Geometry	N_{db}	ATSUP-GGA τ(ps)	 E_b(eV)	 λ_c/λ (%)	 λ(ns^{-1})
Bulk	0	219(2)	0.78	1.93	4.57
V_1	4	234(2)	1.14	1.47	4.27
V_2	6	252(2)	1.28	1.36	3.97
V_3	8	261(4)	1.57	1.46	3.83
V_4	10	278(3)	1.63	1.45	3.60
V_5	12	286(2)	1.96	1.47	3.49

Table 8.7 Number of dangling bonds N_{db}, mean values of positron lifetime (τ), positron binding energy E_b, total annihilation rate (λ) obtained for hydrogen-decorated monovancies and divacancies complexes (model d) using the ATSUP-LDA-BN and ATSUP-GGA-AP schemes for the enhancement factor in a-Si.

Geometry		ATSUP-LDA-BN			ATSUP-GGA-AP		
	N_{db}	τ (ps)	E_b (eV)	λ(ns^{-1})	τ(ps)	E_b (eV)	λ (ns^{-1})
V_1H_1	3	331(2)	1.51(1)	3.02(1)	322(2)	1.41(2)	3.11(3)
V_1H_2	2	323(4)	1.24(4)	3.10(1)	312(3)	1.20(2)	3.20(3)
V_1H_3	1	305(2)	1.18(3)	3.30(2)	298(1)	1.10(1)	3.35(2)
V_2H_1	5	374(1)	1.97(4)	2.74(1)	365(2)	1.94(1)	2.74(2)
V_2H_2	4	368(3)	1.71(1)	2.72(3)	361(1)	1.78(1)	2.77(1)
V_2H_3	3	352(3)	1.71(2)	2.84(1)	344(2)	1.63(2)	2.90(4)
V_2H_4	2	322(2)	1.32(1)	3.10(6)	318(3)	1.30(1)	3.14(2)
V_2H_5	1	292(1)	1.20(4)	3.42(5)	291(1)	1.11(2)	3.43(1)

In hydrogen-decorated defect complexes (model *d*) in *a*-Si:H, there appears to be an additional contribution to the total annihilation rate due to the 1s orbital of the incorporated hydrogen atoms. Physically, this situation arises from the hydrogen-decoration of the vacancy-like open-volume defects. Practically, the hydrogen 1*s* orbital contribution to the total annihilation rate is not a core-state contribution. Hence the decoration of the vacancy-like defects with hydrogen does not change the core state contributions. In model *c* and model *d*, only two Si core-states contribute to the HMC of MDAP. These are the (1*s*) and (2*s*, 2*p*) core states in Si denoted by principal quantum number n = 1 and 2. These give rise to three core-level dependent contributions to the total annihilation rate, λ.

Table 8.8 Number of dangling bonds N_{db}, mean values of positron lifetime (τ), positron binding energy E_b, total annihilation rate (λ) obtained from the ATSUP-GGA scheme in hydrogen-decorated for monovancy and divacancies in *a*-Si (model *d*).

Geometry		ATSUP-GGA		
	N_{db}	τ (ps)	E_b (eV)	λ(ns^{-1})
V_1H_1	3	313(2)	0.25(1)	3.20(3)
V_1H_2	2	318(3)	0.02(2)	3.15(5)
V_1H_3	1	326(3)	0.02(2)	3.07(1)
V_2H_1	5	344(4)	0.51(3)	2.91(3)
V_2H_2	4	336(1)	0.44(1)	2.98(1)
V_2H_3	3	313(2)	0.27(1)	3.20(6)
V_2H_4	2	320(1)	0.04(1)	3.13(4)
V_2H_5	1	328(2)	0.02(1)	3.05(4)

Table 8.9 shows the contributions of the decoupled core states in model *c*. The corresponding 3*s* and 3*p* valence-level contributions to the total annihilation rate λ show that the contribution from the unfilled 3*s* and 3*p* valence-levels dominates the annihilation properties as expected. The 2*p* core state has the highest contribution to the HMC with the least contributions coming from innermost 1*s* core-electrons. Table 8.10 shows the results of the core (valence)-state dependent contributions to the enhancement factor calculated within the GGA, the contributions from the 1*s* orbital of H atoms, and the decomposed core-state dependent annihilation rate λ_c in models of hydrogen-decorated divacancy complexes in *a*-Si:H calculated from the GGA scheme.

It is immediately clear from Table 8.10 that as more hydrogen atoms decorate the vacancy-like defects, the contribution from the 1*s* orbital from hydrogen to the total annihilation rate becomes increasingly significant even though it is not, strictly speaking, a core state. A comparison of Table 8.9 with Table 8.7 shows that the situation depicted by an increased H-decoration of vacancies to create H-decorated complexes leads to progressive increase in annihilation rate. It also, correspondingly, leads to a progressive lowering of positron lifetime. For the bulk structure, Table 8.1 and Table 8.2 show that at very high C_H, the positron lifetime in *a*-Si:H approaches the limiting value measured for bulk *c*-Si. This further supports the earlier observed phenomenon of improved structural order in *a*-Si:H at the high C_H limit.

Table 8.9 Core and valence state contributions to the enhancement factor, and the decoupled core and valence electron-state dependent annihilation rate in vacancy defect models of hydrogen-free *a*-Si obtained from the GGA scheme (α = 0.22).

Electron state-dependent annihilation rate [ns^{-1}]							
Defect	γ_c	γ_v	*1s*	*2s*	*2p*	*3s*	*3p*
T_3	2.2(3)	4.4(4)	0.0001(2)	0.019(2)	0.11(4)	1.61(2)	2.92(3)
T_4	1.6(4)	5.1(3)	0.0006(1)	0.008(4)	0.32(3)	1.23(2)	2.58(2)
$4T_3$	1.6(1)	5.0(1)	0.0005(1)	0.007(3)	0.36(4)	1.32(4)	2.66(3)
V_2	1.7(6)	5.7(1)	0.0004(7)	0.007(1)	0.22(4)	1.30(1)	2.51(1)
V_3	1.6(4)	5.3(4)	0.0004(1)	0.006(2)	0.27(2)	1.20(2)	2.42(1)
V_4	1.6(2)	5.9(3)	0.0004(3)	0.005(2)	0.42(4)	0.95(2)	2.16(2)
V_5	1.6(3)	6.1(2)	0.0004(1)	0.005(2)	0.51(3)	0.95(3)	2.10(1)

Table 8.10 Electron-state dependent contributions to the total annihilation rate λ in models of hydrogen-decorated monovacancy and divacancy complexes in *a*-Si:H obtained from the GGA scheme showing contributions from the 1*s* orbital of H atoms.

Electron state-dependent annihilation rate [ns^{-1}]						
	Hydrogen	Silicon				
Defect	1*s*	1*s*	2*s*	2*p*	3*s*	3*p*
V_1H_1	0.02(2)	0.1(2)e-04	0.2(6)e-02	0.15(2)e-01	0.7(3)	2.32(3)
V_1H_2	0.05(1)	0.1(8)e-04	0.2(1)e-02	0.15(3)e-01	0.7(1)	2.41(3)
V_1H_3	0.07(2)	0.1(6)e-04	0.4(1)e-02	0.15(1)e-01	0.7(1)	2.55(1)
V_2H_1	0.10(3)	0.2(4)e-04	0.4(1)e-02	0.15(2)e-01	0.8(3)	1.77(5)
V_2H_2	0.13(2)	0.2(8)e-04	0.4(1)e-02	0.14(3)e-01	0.8(3)	1.92(2)
V_2H_3	0.15(1)	0.2(9)e-04	0.4(1)e-02	0.14(2)e-01	0.8(2)	1.92(1)
V_2H_4	0.18(2)	0.3(1)e-04	0.4(1)e-02	0.13(1)e-01	0.8(2)	2.11(3)
V_2H_5	0.21(2)	0.3(3)e-04	0.4(1)e-02	0.13(1)e-01	0.8(2)	2.38(1)

8.3 Momentum Distribution

As discussed in the previous section, the annihilation due to core electrons is due primarily to the 2*p* electrons of silicon in all defect types. In addition, the effect of hydrogen decoration does not affect the domination of the core state contribution to the annihilation line by the 2*p* core state in these defects (see Table 8.9 and Table 8.10). However, the total annihilation rate and positron lifetime is significantly affected by hydrogen decoration. The trend in Table 8.10 suggests that as more hydrogen decorates the vacancies, the contribution of the 1*s* orbital of H tends to dominate the core-state contributions in hydrogen decorated complexes. Nevertheless, it is quite clear that the overall core state contributions are quite small compared to the annihilation from valence states. For instance, the contributions from the 3*p* valence state dominates the contributions from the 3*s* valence sate. Taken together, the total core-state contributions are typically less than 2% for vacancy-like defects in hydrogen free *a*-Si (model *c*) and for hydrogen decorated complexes (model *d*).

Fig. 8.16 shows the high momentum component (HMC) of the momentum distribution of annihilation photons (MDAP) calculated within the ATSUP-GGA scheme, for hydrogen-free (model *a*), and for different sizes of vacancy defects V_n ($1 \leq n \leq 5$) (model *c*), constructed from the sum of the partial annihilation rates for all core states (Table 8.9), as described in section 3.2.3. Fig. 8.16 shows that the HMC curves for the various vacancy-like defects in hydrogen free *a*-Si lie well below the HMC curve for bulk (NSB) geometry just as observed in Refs. [253,254] for monovacancy and divacancy defects in *c*-Si.

Fig. 8.17 demonstrates how the characteristic core-electron wave functions influence the MDAP spectra for the monovacancy defect in hdrogen-free *a*-Si. The decomposition of the HMC of the MDAP into state-dependent contributions (Fig. 8.17) also shows that 2*p* core states dominate the annihilation rate just as seen in Table 8.9 and Table 8.10. Consequently, the momentum distributions of the 2*p* states in any defect complex will have the same fundamental shape with Fig. 8.17 at high energies and momenta, irrespective of the structural geometry. Besides, not all positrons will annihilate after being trapped at a defect. Some may annihilate from delocalised or weakly localised bulk states. Therefore in order to understand the positron momentum spectra of *a*-Si:H, it is important to show the plots of the corrected HMC as ratios of positron annihilation rates at the localized states in defects to the delocalized states in the bulk [225].

Figs. 8.18 - 8.20 show the normalized HMC of the MDAP, in various complexes in *a*-Si:H (model *c* and model *d*) as ratios of the type

$$HMC = \frac{\rho^{defect}(\mathbf{p})}{\rho^{bulk}(\mathbf{p})}. \tag{8.1}$$

This form has been shown in Ref. [253] to correctly visualize the differences among shapes, and magnitudes of the HMC curves. In Fig 8.18, the ratio HMC curves normalized to the bulk NSB geometry is shown for vacancy defects, V_n ($1 \le n \le 5$) only. Generally, the linear dependences in Fig. 8.18 show that the profiles of ratios of the HMC to bulk for vacancy-like defects in *a*-Si are similar in shape to the HMC plots for mono- and divacancies in *c*-Si (see Ref. [254]).

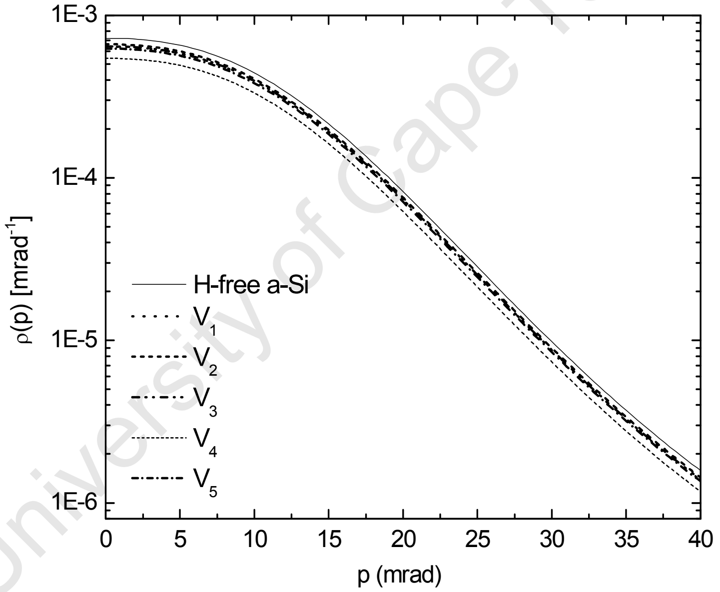

Figure 8.16 High momentum component (HMC) of the momentum distribution of annihilation photons (MDAP) for bulk region and for different sizes of ideal vacancy-like defects V_n ($1 \le n \le 5$).

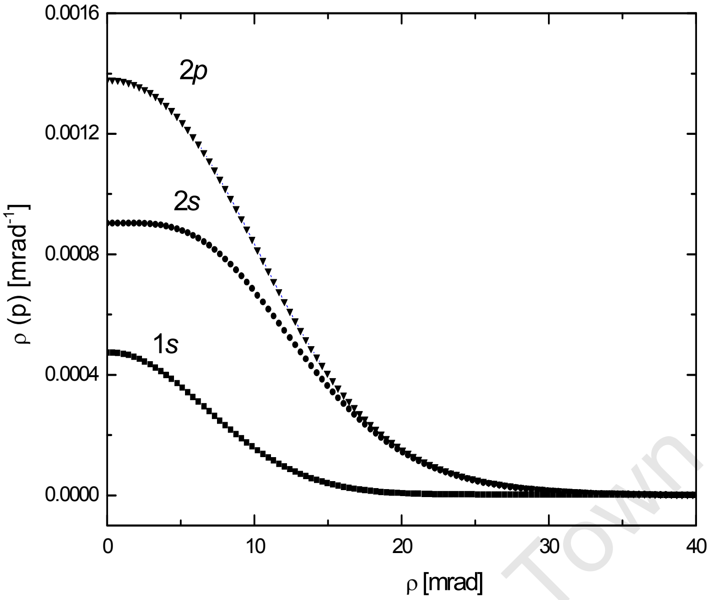

Figure 8.17 Decoupled core-state contributions to the momentum distribution of annihilation photons in the monovacancy defect in H-free *a*-Si.

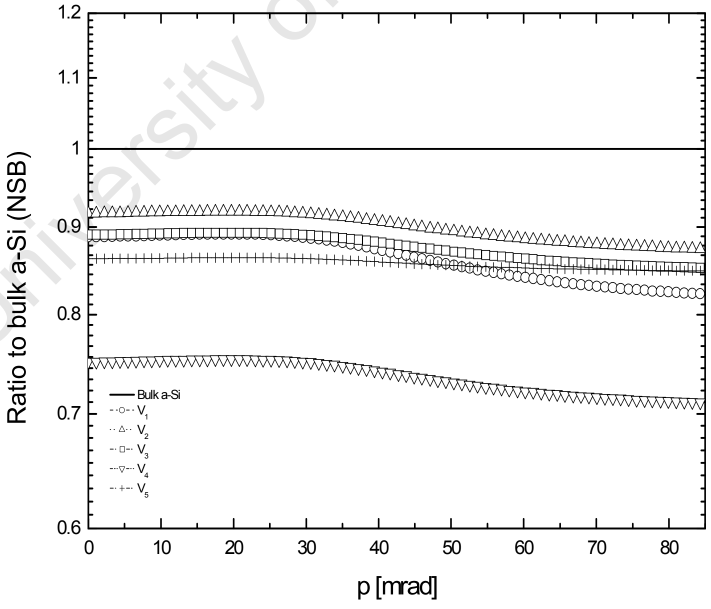

Figure 8.18 Ratio HMC curves normalized to bulk NSB for vacancy-like defect in hydrogen-free *a*-Si calculated within ATSUP-GGA scheme to show the effect of the vacancy size on momentum distribution.

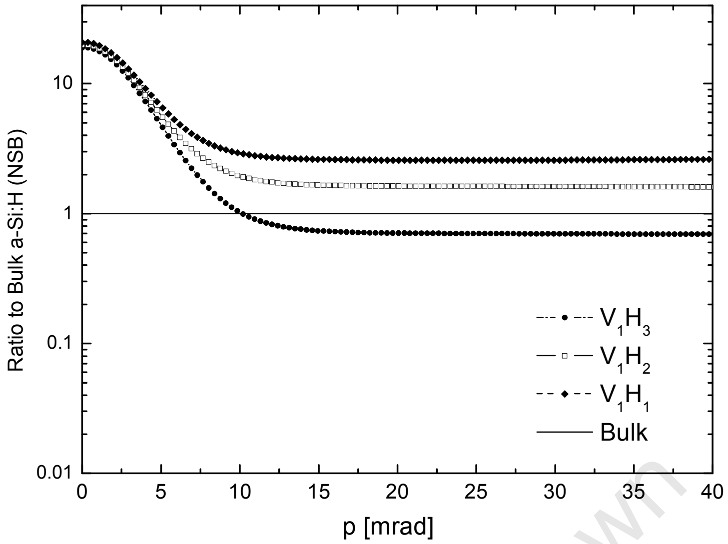

Figure 8.19 Ratio HMC curves normalized to bulk NSB for hydrogen-decorated monovacancy-like defect in hydrogenated a-Si calculated within ATSUP-GGA scheme.

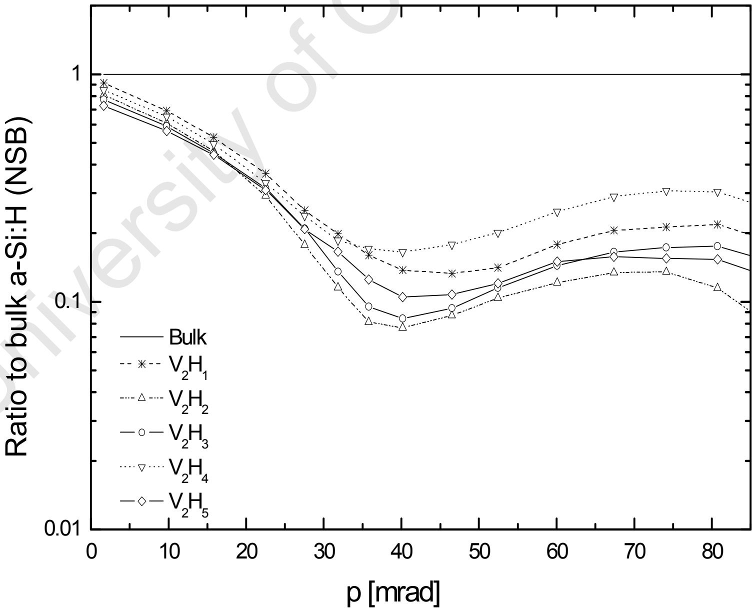

Figure 8.20 Ratio HMC curves normalized to bulk NSB for hydrogen-decorated divacancy-like defect in a-Si:H calculated within ATSUP-GGA scheme.

However, some basic difference can still be observed in the momentum distribution for these defects as the vacancy size changes. Firstly, the divacancy-like defect is closest to the bulk at all values of energy and momentum. Secondly, the monovacancy and trivacancy-like defects have the same momentum distribution below 40 mrad. At a momentum of 50 mrad, the pentavacancy (V_5) and the monovacancy (V_1) defects have the same high momentum distribution. Finally, the tetravacancy (V_4) lies furthest from the bulk curve. The shape of these curves may contain information on the relative structural stability of these isolated defects in hydrogen-free *a*-Si. Within the region of momentum ≤ 30 mrad, there is basically no difference in the high momentum contribution of the mono- and trivacancy defects (model *c*) to the momentum distribution of annihilation photons. Similarly, the ratio HMC curves for hydrogen-decorated monovacancy (Fig 8.19) and divacancy (Fig. 8.20) related defect complexes show fundamental differences in the distribution of the high momentum component of MDAP.

Relative to the bulk structure, the decoration of monovacancy-like defects with hydrogen changes the distribution of the high momentum components of MDAP significantly from the linear dependence observed in Fig 8.18 to the exponential decay dependences seen in Fig. 8.19. For hydrogen-decorated divacancy complexes, the distribution of the high momentum components shows even more appreciable differences as more hydrogen atoms decorate the divacancy. Moreover, ratio HMC curves corresponding to hydrogen-decorated monovacancy-like defects have a fundamentally different shape from those associated with hydrogen-decorated divacancy-like defects. The ratio HMC curves for hydrogen-free vacancy-like defects approach the line with ratio of unity. The decoration of monovacancy-like defects with hydrogen in this work yields very high ratio HMC results (see Fig. 8.19), relative to the decoration of divacancies with hydrogen as shown in Fig. 8.20.

Chapter Nine

Discussion

Although the reliability of the quantum-mechanical description of bonding in *a*-Si:H is undisputed, it is still useful to provide an approximate scheme for identifying, and characterizing the local bonding environment in *a*-Si:H. To this end, TBMD simulations have been performed to study the formation of typical *a*-Si:H networks, and to study the local contributions to the total stress, and the corresponding network rearrangements, induced by progressive incorporation of hydrogen. At a cut-off distance of 3.50 Å for Si-Si interactions, and 2.00 Å for Si-H interactions, the simulated networks structures are assumed to evolve freely under the simulation conditions. Four computational models of *a*-Si:H have been studied. Model *a* denotes the hydrogen-free *a*-Si network. Model *b* denotes the vacancy-like defect models of the hydrogen-free network, which contain *ad hoc* open-volume defects of size V_n ($1 \leq n \leq 5$). Model *c* denotes the hydrogenated networks, and contains no *ad hoc* defects. This represents a class of structural models of *a*-Si:H, which contains atomic hydrogen concentrations ranging from 3% to 25%. Finally, model *d*, which contains hydrogen-decorated vacancies.

The disordered structure of *a*-Si:H has been shown to be characterized by broad peaks, with a varying non-zero background. The computed pair correlation function confined, to a radial distance of 8.0 Å, showed three coordination peaks at low hydrogen concentrations. This was found to comprise of two well-defined coordination peaks, and broad third peak. The number of coordination peaks was found to increase steadily from three to nine as C_H increased from 0 to 25%, showing clearly that the structure changed as hydrogen was incorporated. From the structural evolution seen in the computed pair correlation functions, the amorphous silicon networks are found to become more ordered as hydrogen is progressively incorporated.

The relative position, width and intensity of the Gaussian peaks, fitted to nearest neighbour coordination peaks, when considered for varying concentrations of hydrogen C_H, also shows significant changes, that indicate an improvement in structural order, especially at high C_H. It was found that as C_H is increased, the average position of the centre of the first two coordination peaks decreases towards the equivalent values in *c*-Si. When the more ordered *a*-Si:H network, which arises from the incorporation of high concentrations of hydrogen is compared with *c*-Si, it is clear that there is still some disorder in bond lengths and bond angles, although the structural order has improved. The local structure, as typified by the pair correlation function is characterized by an incomplete development of higher-order coordination peaks.

Using the new perspective of configurational landscapes, the stress landscape of *a*-Si:H has been defined, from the distribution of local stress fluctuations, in 110 configurations of model *a* and model *c*. The stress landscape has been investigated using identifiable domains. More importantly, for the domain that allows for a systematic characterization of structural order, the fluctuation within the order parameter field (δ_1, δ_2), shows that the region of data on the domain forms an island with a preferred orientation of 36 ± 2°, relative to the horizontal axis. Apart from hydrogenated amorphous silicon networks, this preferred orientation has also been found for hydrogenated tetrahedral amorphous carbon networks. Consequently, this orientational dependence has to be an attribute of the geometrical property of the intersecting dihedral planes of the randomly-packed distorted Si-Si_4 tetrahedra (see Fig. 2.7). This shows the possibility of using a single parameter, that is, the “distance” along this trend line to describe the structural order in the structure.

This hypothesis has been tested by redefining the order parameter in terms of a new set of rotated axes to give two parameters δ_1' and δ_2' which couple the standard deviations in the first and second nearest neighbour distances. The former is directed along the island, and the latter is normal to it. Results of plots of the rms stress fluctuations against these two parameters show clear trends for the dependence of the rms stress on the coupled parameter δ_1', whereas no discernable correlation exists between the rms stress and δ_2'. As far as stress fluctuations are concerned, the structural order in the *a*-Si:H network can be quantified by a single parameter δ_1'.

Two clearly different regions have been identified in the stress landscape. These two regions, marked by clear differences in slope, and ruggedness correspond to *a*-Si:H networks containing hydrogen concentrations less than, or greater than 15%, respectively. The correlation between stress and order in these two regions has been observed to behave differently. In the rugged region, characterized by low concentration of hydrogen, results show that the stress autocorrelation exhibits an almost exponential decrease with increase in the lag in the order parameter. In the smooth region, where hydrogen concentration is very high, the correlation structure reveals a dominant, discrete, step-like character in the correlation profile at lags of ~ 0.04, 0.08, and 0.16 Å.

The physical structures in rugged region of the domain are characterised by significant fluctuations in stress, and a higher degree of structural disorder. Fig. 9.1 shows the ball and stick model of an *a*-Si:H structure in this rugged region, which contains 3% H, alongside the corresponding pair correlation function. Similarly, Fig. 9.2 shows similar plots for a structure in the smooth region of the stress landscape, which contain 15%. Fig. 9.1 and 9.2 show clearly that the structures corresponding to the rugged region of the stress landscape are less ordered than those in the smooth region. Furthermore, the observed stress fluctuations increase with disorder. The changes in stress in the structures within the smooth region, in addition to the exponential-decay correlation structure for the dependence of stress on the lag in order parameter, show that there is a continuous relaxation of the Si network, due to the passivation of dangling bonds, as more hydrogen is incorporated. For the structures in the smooth region, which are characterized by lesser disorder, the stress fluctuations are small, and the step-like correlation structure between the stress and the lag in order parameter, clearly alludes to a discrete set of repeated Si network reconfigurations, as bonds break and re-form.

The pair correlation function of structures in the rugged region is characterized mainly by significant changes in the second coordination peak. The changes in the first coordination peak are less than 0.05 Å. Using the positions of the first two peaks in the Si-Si pair correlation function, the average bond angle in the H-free network is estimated to be 98.9°. This is noticeably smaller than the tetrahedral angle of 109.47° of the sp^3 hybridised covalent bond in *c*-Si, but still in broad agreement with acceptable structures for hydrogen-free *a*-Si and hydrogenated amorphous silicon [13,384-390]. The smaller bond angle leads to a substantially reduced second nearest neighbour distance of approximately 3.49 Å, and has been interpreted as the presence of 4 member square rings in the medium range order [391]. Close examination of the second nearest neighbour peak for 3% H shows the continued presence of this correlation, as a shoulder in the main peak centred at 3.94 Å.

However, as shown in Fig. 8.10, introduction of as little as 3% hydrogen relaxes the first and second nearest neighbour distances, and hence bond angle, towards the values expected for tetrahedrally bonded Si. The addition of 5% hydrogen shows an increase in the projected bond angle to 113.6°, which is slightly larger than the ideal case. However, this value decreases steadily and stabilizes at 109.9° when the hydrogen concentration exceeds 20%.

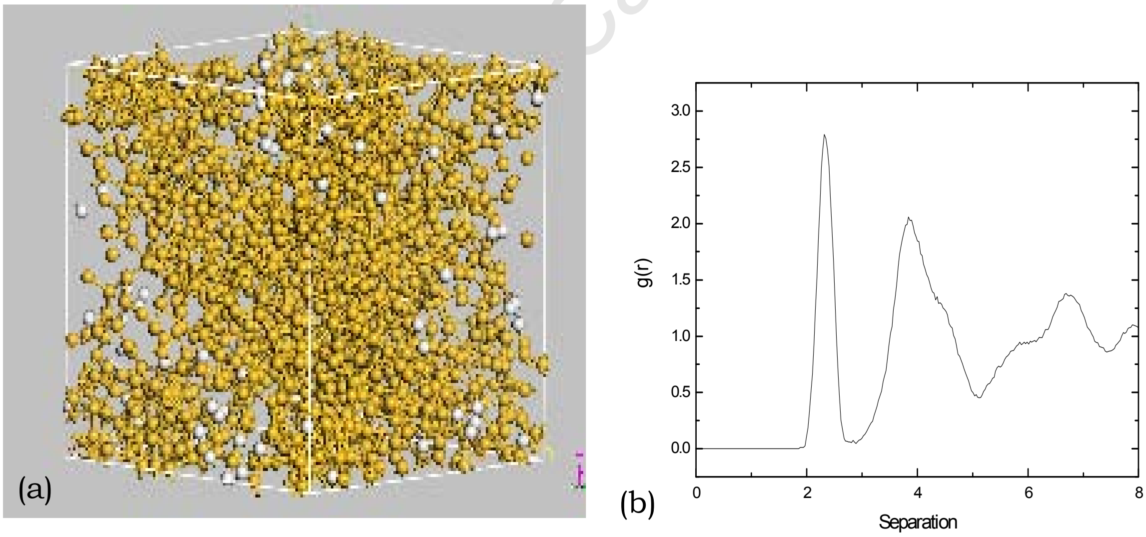

Figure 9.1 Ball and stick model of an *a*-Si:H structure in this rugged region which contains 3% H (a), and the corresponding pair correlation function (b).

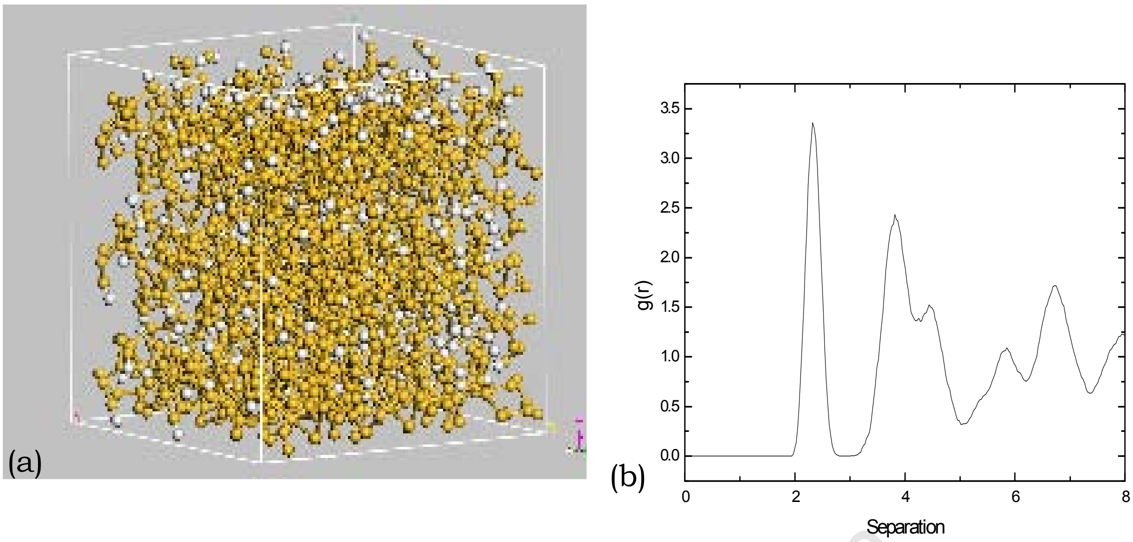

Figure 9.2 Ball and stick model of an a-Si:H structure in this smooth region which contains 15% H (a), and the corresponding pair correlation function (b).

Fig. 8.10 clearly shows that increasing the concentration of hydrogen in the simulation leads to a more ordered structure. For the structures in the smooth region of the stress landscape, the changes in the second coordination peak leads to the formation of the third, and higher coordination peaks, although perfect crystallinity is never achieved. In both smooth and rugged regions, when the lag in order parameter increases beyond 0.35 Å, the magnitude of the stress autocorrelation falls to zero. This result shows that any two network configurations in the stress landscape that are separated by this distance in the domain will fall into different halves of the order parameter field. This leads to the conclusion that, there is no statistical correlation between the atomic level stresses in the corresponding structures of the two regions, and suggests strongly that, there is a phase transition from a disordered to a more ordered structure as the hydrogen concentration increases above a certain level.

Two structural models have been considered, to study positron interactions in a-Si:H. The characteristics of positrons trapped at these defects have also been modelled. The positron wave function was seen to be highly sensitive to the local geometry of the structure. The two LDA schemes used in the positron calculations yield results that agree with *a priori* expectations for the positron interaction with neutral defects in silicon [392,393]. The results support the general observation that the positron lifetime and binding energy increases as the free-volume, and number of dangling bonds (N_{db}) in a given vacancy increases. One important observation which is at variance with the above observation is that positron binding energy to open volume, and H-decorated complexes, is less than 2.0 eV. The positron binding energy is observed to change significantly from 1.313 eV, in an undecorated monovacancy to 1.50 eV, after decorating with one H atom, even though the effective free volume of the V_1H_1 defect is less than that of the V_1 defect. A similar comparison shows that the binding energy of positrons to the divacancy defect in *a*-Si (V_2) changes from 1.322 eV to 1.974 eV, when the divacancy is decorated with one atom of hydrogen to give the V_2H_1 complex.

The above observations are not consistent with the expected decrease in binding energy with decreasing number of unterminated dangling bonds and decreasing free-volume. It is therefore instructive to investigate more deeply, the influences of hydrogen-decoration on these defects. In hydrogen-decorated defect complexes (model *d*), there is an additional contribution to the total annihilation rate due to the 1*s* orbital of the incorporated hydrogen atoms. Results show that the contributions from the 1*s* orbital of H atoms increases as more hydrogen atoms decorate the vacancy-like defects. As seen earlier, the situation of increased H-decoration of defect complexes leads to progressive increase in annihilation rate, and correspondingly leads to a lowering of positron lifetime, as free volume decreases.

As observed in model *a* and model *c*, when more hydrogen is incorporated into the *a*-Si network, a significant network reconfiguration occurs, which leads to stress relaxations, culminating in a more ordered topological network structure. The properties of the thermalized positron state provide clear evidence to support the phenomenon of hydrogen-induced delocalization of the positron density within the bulk structure. The high stress fluctuations, observed in the structures in the rugged region of the stress landscape, also imply that a high strain fluctuation occurs for these structures. This leads to a considerable density fluctuation, and the existence of vacancy-sized open volume. The progressive incorporation of hydrogen leads to the decoration of the internal surfaces of these vacancies with hydrogen, as seen in Fig. 8.4. The weak localisation of the positron density, in such hydrogen-rich open-volume regions of structures in the rugged region, shows clearly that, hydrogen causes the delocalisation of the positron density in the smooth region of the stress landscape. For structures in the smooth region, the passivation of dangling bond defects at high C_H implies a complete elimination of localized high electron density, or low ionic density regions.

Chapter Ten

Conclusions

In this thesis, the tight binding molecular dynamics approach has been used, to study the physical properties of different configurations of bulk, and defect structures in hydrogenated amorphous silicon. The changes in the local structure, which arise from the incorporation of hydrogen into the amorphous silicon network, have also been investigated. The local structure of tetrahedrally bonded solids has been described, at a fundamental level, in a manner that allows the structural order to be characterized. The variations in the atomic-level stresses have also been determined, and used, to characterize the modifications of the structural networks, due to the incorporation of hydrogen.

In this thesis, the concept of configurational landscapes has been introduced, as a new framework, for the analysis of the modifications in the local structure, and the corresponding fluctuations in atomic-level stress in hydrogenated amorphous silicon networks. A single order parameter, which is a linear combination of the standard deviations of the first and second nearest neighbour separations, has been identified. This parameter can be derived directly from either theoretical or experimental pair correlation functions. It is proposed that this parameter uniquely characterises structural disorder in all tetrahedrally bonded solids.

A clear statistical correlation has been observed in the domain, between the stress in the structures and the order in the networks. Using this order parameter, in the stress landscape of amorphous silicon, two distinctly different regions have been identified. These two regions correspond to different structural network configurations, one containing less than 15% hydrogen, and one containing more than 15% hydrogen. The correlation structure in the stress landscape shows clearly that there is no statistical correlation of the stress in the structures between the two regions. This suggests a phase transition, between two fundamentally different structural configurations, when higher amounts of hydrogen are incorporated, or when the order parameter exceeds a critical value.

Two different correlation structures are observed, in the two regions. In the first, the rugged region, there is an exponential decay dependence of the stress autocorrelation on the lag in the order parameter. For the second, the smooth region, a step-like structure has been observed, for the correlation between order and stress. The step-like correlation structure of the stress within the domain, suggests a repeated reconfigurations of the network structure as the order increases.

The observed hydrogen-induced improvement of structural order is similar to the experimental observation of hydrogen induced crystallization of amorphous silicon under dynamic hydrogenation, which suggests that the phenomenon of network relaxation in the silicon networks could be a universal phenomenon, and therefore that the phase transition does not depend on the method, in which the amorphous silicon networks is prepared.

The positron annihilation characteristics have also been computed for the structural networks in each of the two regions of the stress landscape, in addition to *ad hoc* defects. The properties of the thermalized positron state provide clear evidence to support the phenomenon of hydrogen-induced delocalization of the positron density. The high stress fluctuations observed in the rugged region also imply that a high strain fluctuation occurs for these structures. This leads to a considerable density fluctuation, and the existence of vacancy-sized open volume. The progressive incorporation of hydrogen leads to the decoration of the internal surfaces of these vacancies with hydrogen. The weak localisation of the positron density, in such hydrogen-rich open-volume regions, shows clearly that, hydrogen causes the delocalisation of the positron density. For structures in the smooth region, the passivation of dangling bond defects at high C_H implies a complete elimination of localized high electron density, or low ionic density regions.

References

[1] R. M. Schaffert and C. D. Oughton, J. Opt. Soc. Am., **38**, 991 (1948).

[2] A. Madun and M. P. Shaw, *The Physics and Applications of Amorphous Semiconductors*, Academic Press, Boston, (1988).

[3] R. A. Street, *Hydrogenated Amorphous Silicon,* Cambridge University Press, Cambridge, (1991).

[4] K. Tanaka, E. Maruyama, T. Shimada, H. Okamoto, *Amorphous Silicon*, John Wiley and Sons Ltd. West Sussex, England, (1999).

[5] S. Nakhmanson, *Theoretical Studies of Amorphous and Paracrystalline Solids*, Ohio University, USA, PHD Thesis. (2001).

[6] J. D. Bernal, Nature **183**, 141 (1959).

[7] W. H. Zachariesen, J. Am. Chem. Soc. **54**, 3841 (1932).

[8] D. E. Polk and D. S. Boudreaux, Phys. Rev. Lett. **31**, 92 (1973).

[9] D. E. Polk, J. Non. Cryst. Solids **5,** 365 (1971).

[10] D. T. Britton, E. Minani, D. Knoesen, H. Schut, S. W. H. Eijt, F. Furlan, C. Giles and M. Härting, Appl. Surf. Sci. **252**, 3194 (2006).

[11] P. F. Stadler, Europhys. Lett. **20**, 479 (1992).

[12] J. D. Bernal, Proc. Roy. Soc. A **280**, 299 (1964) ; Nature **188**, 910 (1960).

[13] F. Wooten, K. Winer and D. Weaire, Phys. Rev. Lett. **54**, 1392 (1985).

[14] R. Car and M. Parrinello, Phys. Rev. Lett. **55**, 2471 (1985).

[15] I. Štich, R. Car and M. Parrinello, Phys. Rev. B **44**, 11092 (1991).

[16] I. Lee and K. J. Chang, Phys. Rev. B **50**, 18083 (1994).

[17] R. Biswas, G. S. Grest, and C. M. Soukoulis, Phys. Rev. B **36**, 7437 (1987).

[18] R. Biswas and D. R. Hamann, Phys. Rev. B **36**, 6434 (1987).

[19] R. Biswas and D. R. Hamann, Phys. Rev. Lett. **55**, 2001 (1985).

[20] F. Stillinger and T. Weber, Phys. Rev. B **31**, 5262 (1985).

[21] E. Pearson, T. Takai, T. Halicioglu and W. A. Tiller, J. Cryst. Growth **70**, 33 (1984).

[22] B. C. Bolding and H. C. Anderson, Phys. Rev. B **41**, 10568 (1990).

[23] M. I. Baskes, Phys. Rev. Lett. **59**, 2666 (1987).

[24] B. R. Djordjević, M. F. Thorpe, and F. Wooten, Phys. Rev. B **52**, 5685 (1995).

[25] G. T. Barkema and N. Mousseau, Phys. Rev. B **62**, 4985 (2000).

[26] P. N. Keating, Phys. Rev. **145**, 637 (1966)

[27] D. W. Brenner and B. J. Garrison, Phys. Rev. B **34**, 1304 (1986).

[28] J. Tersoff, Phys. Rev. B **37**, 6991 (1988).

[29] J. Tersoff, Phys. Rev. Lett. **56**, 632 (1986).

[30] B. W. Dodson, Phys. Rev. B **35**, 2795 (1987).

[31] M. Z. Bazant and E. Kaxiras, Phys. Rev. Lett. **77**, 4370 (1996).

[32] M. Z. Bazant, E. Kaxiras and J. F. Justo, Phys. Rev. B **56**, 8542 (1997).

[33] J. F. Justo, M. Z. Bazant, E. Kaxiras , V. V. Bulatov and S. Yip, Phys. Rev. B **58**, 2539 (1998).

[34] D. G. Pettifor, I. I. Olenik, Progress in Materials Science, **49**, 285 (2004).

[35] D. G. Pettifor, I. I. Olenik, Phys. Rev. B **59**, 8487 (1999).

[36] R. Drautz, X. W. Zhou, D. A. Murdick, B. Gillespie, H. N. G. Wadley, and D. G. Pettifor, Progress in Materials Science. **52**, 196 (2007).

[37] L. Colombo, in *Annual Reviews in Computational Physics,* Vol. IV, D. Stauffer (Editor), World Scientific, Singapore, (1996) p. 164.

[38] L. Goodwin, A. J. Skinner and D. G. Pettifor, Europhys. Lett. **9**, 701 (1989).

[39] Q. Li and R. Biswas, Phys. Rev. B **50**, 18090 (1994).

[40] R. Car and M. Parrinello, Phys. Rev. Lett. **55**, 2471 (1985).

[41] R. Car and M. Parrinello, Phys. Rev. Lett. **60**, 204 (1988).

[42] D. A. Drabold, P. A. Fedders, O.F. Sankey, and J.D. Dow, Phys. Rev. B **42**, 5135 (1990).

[43] G. Servalli and L. Colombo, Europhys. Lett. **22**, 107 (1993).

[44] D. Maric and L. Colombo, Europhys. Lett. **29**, 623 (1995).

[45] G. Panzarini and L. Colombo, Phys. Rev. Lett. **73**, 1636 (1994).

[46] S. Lanzavecchia and L. Colombo, Europhys. Lett. **36**, 295 (1996).

[47] A. H. Mahan, J. Wang, S. Guha, and D. L. Williamson, Phys. Rev. B **61**, 1677 (2000).

[48] M. Härting, D. T. Britton, E. Minani, T. P. Ntsoane, M. Topic, T. Thovhogi, O. M. Osiele, D. Knoesen, S. Halindintwari, F. Furlan, and C. Giles, Thin Solid Films, **501**, 75 (2006).

[49] D. T. Britton, A. Hempel, and M. Härting, G. Kögel, P. Sperr, and W. Triftshäuser, C. Arendse and D. Knoesen, Phys. Rev. B **64**, 075403 (2001).

[50] S. Polezzo and P. Fantucci, Theor. Chem. Acc. **73**, 393 (1988).

[51] M. Born and J. R. Oppenheimer, Ann. Physik, **84**, 457 (1927).

[52] P. Hohenberg and W. Kohn, Phys. Rev. **136**, B864 (1964).

[53] D. A. Mirabella, C. M. Aldao, and R. R. Deza, Phys. Rev. B **50**, 12152 (1994).

[54] B. A. McKinnon and T. C. Choy, Phys. Rev. B **52**, 14 531 (1995).

[55] M. Menon and K. R. Subbaswamy, Phys. Rev. Lett. **67**, 3487 (1991).

[56] M. van Schilfgaarde and W. A. Harrison, Phys. Rev. B **33**, 2653 (1985).

[57] C. Kittel, *Introduction to Solid State Physics*, 8th Edition, John Wiley and Sons, USA, (2005).

[58] W. A. Harrison, *Electronic Structure and the Properties of Solids,* Dover, New York, (1989) p. 479.

[59] C. M. Goringe, D. R. Bowler and E. Hernandez, Rep. Prog. Phys. **60**, 1447 (1997).

[60] L. J. Lewis and N. Mousseau, Comput. Mater. Sci. **12**, 210 (1998).

[61] W. A. Harrison, Pure and Appl. Chem. **61**, 2161 (1989).

[62] D. Weaire and M.F. Thorpe, Phys. Rev. B **4**, 2508 (1971).

[63] D. Weaire and M. F. Thorpe, Phys. Rev. Lett. **27**, 1581 (1971).

[64] J. L. Mercer, Jr. and M. Y. Chou, Phys. Rev. B **43**, 6768 (1991).

[65] D. Weaire, Phys. Rev. Lett. **26**, 1541 (1971).

[66] J. Dong and D. A. Drabold, Phys. Rev. B **54**, 10284 (1996).

[67] S. K. Bose, K. Winer and O. K. Anderson, Phys. Rev. B **37**, 6262 (1988).

[68] C. S. Nicholas and K. Winer, Phys. Rev. B **38**, 9850 (1988).

[69] D. C. Allan and J. D. Joannopoulos, Phys. Rev. Lett. **44,** 43 (1980).

[70] F. Herman and S. Skillman, *Atomic-Structure Calculations*, 2nd Edition, Prentice-Hall Inc., Englewood Cliffs, New Jersey (1963).

[71] J. L. Fry, N. E. Brener, F. C. Case, and N. L. Desai, Phys. Rev. B **15**, 5811 (1977).

[72] J. C. Slater and G. F. Koster, Phys. Rev. **94**, 1498 (1954).

[73] W. A. Harrison, Pure and Appl. Chem. **61**, 2161 (1989).

[74] W. A. Harrison, Phys. Rev. B **24**, 5835 (1981).

[75] S. Froyen and W. A. Harrison, Phys. Rev. B **20**, 2420 (1979).

[76] W. A. Harrison, in *Festkorperprobleme,* J. Treusch (Editor), Vieweg, Braunschweig, (1977), Vol. XVII, p. 135.

[77] D. J. Chadi and R. M. Martin, Solid State Commun. **19**, 643 (1976).

[78] D. J. Chadi, Phys. Rev. Lett. **41**, 1062 (1978); Phys. Rev. Lett. **43**, 43 (1979).

[79] D. J. Chadi, Phys. Rev. B **29**, 785 (1984); Phys. Rev. Lett. **59**, 1691 (1987).

[80] D. J. Chadi, J. Vac. Sci. Technol. **16**, 1290 (1979).

[81] G. X. Qian and D. J. Chadi, Rev. B **35**, 1288 (1987).

[82] A. K. McMahan and J. E. Klepeis, Phys. Rev. B **56**, 12250 (1986).

[83] M. Kohyama, J. Phys. Condens. Matter **3**, 2193 (1991).

[84] J. L. Mercer, Jr. and M.Y. Chou, Phys. Rev. B **47**, 9366 (1993).

[85] M. J. Mehl and D. A. Papaconstantopoulos, Phys. Rev. B **54**, 4519 (1996).

[86] T. J. Lenosky, J. D. Kress, I. Kwon, A. F. Voter, B. Edwards, D. F. Richards, S. Yang and J. B. Adams, Phys. Rev. B **55**, 1528 (1997).

[87] M. S. Tang, C. Z. Wang, C. T. Chan, and K. M. Ho, Phys. Rev. B **53**, 979 (1996).

[88] D. J. Chadi, in *Atomic Simulation of Materials Beyond Pair Potentials*, V. Vitek and D. J. Srolovitz (Editors), Plenum, New York (1988) p. 309.

[89] J. L. Mercer, Jr. and M. Y. Chou, Phys. Rev. B **49**, 8506 (1994).

[90] R. E. Cohen, M. J. Mehl, and D. A. Papaconstantopoulos, Phys. Rev. B **50**, 14694 (1994).

[91] M. J. Mehl, D. A. Papaconstantopoulos, R. E. Cohen, and M. M. Sigalas, in *Alloy Modelling and Design*, G. Malcolm Stocks (Editor), Minerals, Metals and Materials in Society, Warrendale, PA, (1994) p. 25.

[92] M. J. Mehl, D. A. Papaconstantopoulos and R. E. Cohen, Int. J. Thermophys. **16**, 503 (1995).

[93] C. Z. Wang, C. T. Chan and K. M. Ho, Phys. Rev. B **40**, 3390 (1989).

[94] C. Z. Wang, C. T. Chan, and K. M. Ho, Phys. Rev. B **42**, 11276 (1990).

[95] C. H. Xu, C. Z. Wang, C. T. Chan, and K.M. Ho, Phys. Rev. B **43**, 5024 (1991).

[96] B. J. Min, Y. H. Lee, C. Z. Wang, C. T. Chan and K. M. Ho, Phys. Rev. B **45**, 6839 (1992).

[97] S. Goedecker and L. Colombo, Phys. Rev. Lett. **73**, 122 (1994).

[98] S. Goedecker and L. Colombo, Proc. Int. Conf. on Supercomputing, IEEE Computer Society Press, California. **73**, 670 (1994).

[99] B. A. Gillespie, X. W. Zhou, D. A. Murdick, H. N. G. Wadley, R. Drautz and D. G. Pettifor, Phys. Rev. B **75**, 155207 (2007).

[100] I. Kwon, R. Biswas, C. Z. Wang, K. M. Ho and C. M. Soukoulis, Phys. Rev. B **49**, 7242 (1994).

[101] M. T. Yin and M. L. Cohen, Phys. Rev. B **26**, 5668 (1982).

[102] X. J. Huang and X. Y. Zhu, Semicond. Sci. Technol. **20**, 847 (2005).

[103] E. Kim and Y. H. Lee, Phys. Rev. B **49**, 1743 (1994).

[104] D. E. Boucher and G. G. DeLeo, Phys. Rev. B **50**, 5247 (1994).

[105] C. Z. Wang, C.T. Chan, and K. M. Ho, Phys. Rev. Lett. **66**, 189 (1991).

[106] E. G. Song, E. Kim, Y. H. Lee, and Y. G. Hwang, Phys. Rev. B **48**, 1486 (1993).

[107] P. B. Rasband, A. P. Horsfield, and P. Clancy, Phil. Mag. B **73**, 71 (1996).

[108] P. B. Rasband, P. Clancy, and M. O. Thompson, J. Appl. Phys. **79**, 8998 (1996).

[109] E. Kim, Y. H. Lee and J. M. Lee, J. Phys. Condens. Matter, **6**, 9561 (1994).

[110] E. A. Davis, J. Non-Cryst. Solids, **198-200**, 1 (1996).

[111] M. Cardona, Phys. Status Solidi B, **118,** 436 (1983).

[112] K. C. Pandey, T. Sakurai, and H. D. Hagstrum, Phys. Rev. Lett. **35,** 1728 (1975).

[113] E. Kim, K.H. Lee, H. J. Lee and Y.H. Lee, J. Phys. Condens. Matter, **4**, 6443 (1992).

[114] C. G. Van de Walle, Phys. Rev. Lett. **80**, 2177 (1998).

[115] G. Herzberg, *Molecular Spectra and Molecular Structure*, Vol. 1, Van Nostrand Reinhold, New York, (1966) p.532.

[116] C. H. Xu, C. Z. Wang, C. T. Chan, and K. M. Ho J. Phys. Condens. Matter, **4**, 6047 (1992).

[117] B. N. Davidson, and W. E. Pickett, Phys. Rev. B **49**, 11253 (1994).

[118] A. P. Horsfield, P. D. Godwin, D. G. Pettifor, and A. P. Sutton, Phys. Rev. B **56**, 15773 (1996).

[119] D. W. Brenner, Phys. Rev. B **42**, 9458 (1990).

[120] D. L. Gray and A. G. Robiette, Mol. Phys. **37,** 1901 (1979).

[121] D. W. Van Krevelen, *Properties of polymers, their estimation and correlation with chemical structure*, 3rd Edition Elsevier, New York (1990).

[122] V. I. Gavrilenko, Phys. Rev. B **47**, 9556 (1993).

[123] G. Kopidakis, C.Z. Wang, C. M. Soukoulis, and K. M. Ho, Phys. Rev. B **58**, 14106 (1998).

[124] J. Li, *Basic Molecular Dynamics*, in S. Yip (Editor) *Handbook of Materials Modelling: Methods and Models*, Vol. 1, Springer, Berlin, Germany (2005) pp. 565-588.

[125] D. Frenkel and B. Smit, *Understanding Molecular Simulation, From Algorithms to Applications*, Second Edition, Academic Press, San Diego. (2002) p. 28.

[126] M. P. Allen and D. J. Tidesley, *Computer Simulation of Liquids*, Clarendon, Oxford (1987).

[127] L. Colombo, Comp. Mat. Sci. **12**, 278 (1998).

[128] P. Deák, Phys. Stat. Sol. B **217**, 9 (2000).

[129] J. H. Harding and A. M. Stoneham, Phil. Mag. B **43,** 705 (1981).

[130] M. Leslie and M. J. Gillan, J. Phys. C: Solid State Phys. **18,** 973 (1985).

[131] M. J. Gillan, J. H. Harding, and M. Leslie, Phys. C, Solid State Phys. **21,** 5465 (1988).

[132] N. Martensson, J. Phys. F: Metal Phys. **8,** 27 (1978).

[133] M. E. Barone and D. Maroudas, J. Comput.-Aided Mater. Des. **4**, 63 (1997).

[134] R. C. Weast (Editor) *Handbook of Physics and Chemistry,* 55th Edition, CRC Press, Cleveland, USA (1974).

[135] P. A. Deymier, V. Kapila and K. Muralidharan, *Atomistic Simulation Methods,* in A. Lakhtakia (Editor), *Nanometre Structures: Theory, Modelling and Simulation,* SPIE Press*, Washington,* (2004) p. 211.

[136] R. Virkkunen, K. Laasonen and R. M. Nieminen, J. Phys. Condens. Matter, **3**, 7455 (1991).

[137] I. Štich, and R. Car and M. Parrinello, Phys. Rev. Lett. **63**, 2240 (1989).

[138] J. M. Holender, G. J. Morgan and R. Jones, Phys. Rev. B **47**, 3991 (1993).

[139] B. Turtle and J. B. Adams, Phys. Rev. B **53**, 16265 (1996).

[140] C. G. Van de Walle and R. A. Street, Phys. Rev. B **51**, 10615 (1995).

[141] Y. S. Su and S. T. Pantelides, Phys. Rev. Lett. **88**, 165503(1) (2002).

[142] T. L. Hill, *Statistical Mechanics*, McGraw-Hill Book Company, New York (1956) pp. 179-285.

[143] D. Chandler, *Introduction to Modern Statistical Mechanics*, Oxford University Press, New York (1987) pp. 195-201.

[144] D. Henderson and M. Plischke, Proc. Royal Soc. A **410**, 409 (1987).

[145] N. Jakse and I. Charpentier, Phys. Rev. E **67**, 061203 (2003).

[146] P. H. Gaskell, J. Phys. C: Solid State Phys. **12**, 4337 (1979).

[147] M. C. Wilding, M. Wilson, and P. F. McMillan, Chem. Soc. Rev. **35**, 964 (2006).

[148] O. U. Uche, F. H. Stillinger, S. Torquato, Physica A, **360**, 21 (2006).

[149] F. H. Stillinger, S. Torquato, J. M. Eroles, and T. M. Truskett, J. Phys. Chem. B , **105**, 6592 (2001).

[150] Y. Okada, *Diamond cubic Si: structure, lattice parameter and density*, in R. Hull (Editor) *Properties of Crystalline Silicon*, EMIS Data Review Series, No. 20, INSPEC Publication, (1999) pp. 91.

[151] M. A. Popescu, Journal of Ovonic Research, **1**, 7 (2005).

[152] T. Proffen, K. L. Page, S. E. McLain, B. Clausen, T. W. Darling, J. A. TenCate, S. Lee and E. Ustundag, Zeitschrift für Kristallographie, **220**, 1002 (2005).

[153] T. Proffen and K. L. Page, Zeitschrift für Kristallographie, **219**, 130 (2004).

[154] T. Proffen, S. J. L. Billinge, T. Egami and D. Louca, Zeitschrift für Kristallographie, **218**, 132 (2003).

[155] P. J. Steinhardt, D. R. Nelson, and M. Ronchetti Phys. Rev. B, **28**, 784 (1983).

[156] L. D. Landau Phys. Z. Soviet **11**, 26 (1937).

[157] T. M. Truskett, S. Torquato, and P. G. Debenedetti, Phys. Rev. E **62**, 993 (2000).

[158] S. Torquato, T. M. Truskett, and P. G. Debenedetti, Phys. Rev. Lett. **84**, 2064 (2000).

[159] J. R. Errington and P. G. Debenedetti, Nature, **409**, 318 (2001).

[160] P. L. Chau and A. J. Hardwick, Mol. Phys. **93**, 511 (1998).

[161] A. Haymet, Complex Systems, **107**, 77 (1984).

[162] N. Quirke and P. Shenge, Chem. Phys. Lett. **110**, 63 (1984).

[163] M. J. Uttormark, M. O. Thompson, and P. Clancy, Phys. Rev. B **47**, 15717 (1993).

[164] P. M. Voyles and A.R. Abelson, *Medium range order in amorphous silicon measured by fluctuation electron microscopy*, Technical Report: NREL/SR 520-34826, Contract No. DE-AC36-99 GO10337, National Renewable Energy Laboratory, USA (2003) pp 1-36.

[165] M. Popescu, and H. Bradaczek, Journal of Optoelectronics and Advanced Materials, **3**, 249 (2001).

[166] D. S. Franzblau, Phys. Rev. B. **44**, 4925 (1991).

[167] M M. J. Treacy and J. M. Gibson, Acta Cryst. A **52**, 212 (1996).

[168] P. M. Voyles, M. M. J. Treacy and J. M. Gibson, J. Elec. Microscopy, **49**, 259 (2000).

[169] R. Radhakrishnan and B. L. Trout, *Order Parameter Approach to Understanding and Quantifying the Physico-Chemical Behaviours of Complex Systems*, in S. Yip (Editor), Handbook of Materials Modelling: Methods and Models, Vol. 1, Springer, The Netherlands, (2005), pp 1-15.

[170] J. P. Sethna, *Order Parameters, Broken Symmetry, and Topology*, in L. Nagel and D. Stein (Editors), Proceedings of the Santa Fe Institute Studies in the Science of Complexity, Vol. XV, Addison-Wesley, New York (1992), pp 1-10.

[171] A. M. Ukpong, Turk. J. Phys. **31**, 317 (2007).

[172] K. Ding and H.C. Anderson, Phys. Rev. B **34**, 6987(1986).

[173] M.D. Kluge, J. R. Ray and A. Rahman, Phys. Rev. B **36**, 7437 (1987).

[174] M.D. Kluge and J. R. Ray, Phys. Rev. B **37**, 4132 (1988).

[175] W. D. Luedtke and U. Landman, Phys. Rev. B **37**, 4656 (1988); Phys. Rev. B **40**, 1164 (1989).

[176] D. Adler, Phys. Rev. Lett. **41**, 1755 (1978).

[177] M. Kastener, D. Adler and H. Fritzsche, Phys. Rev. Lett. **37**, 1504 (1976).

[178] J. J. Boland, Phys. Rev. Lett. **67**, 1539 (1991).

[179] A. Bongiorno, L. Colombo and T. Diaz De la Rubia, Europhys. Lett. **43**, 695 (1998).

[180] A. Bienenstock, in *Amorphous and Liquid Semiconductors*, J. Stuke and W. Brenig (Editors), Taylor and Francis, London (1973) p. 49.

[181] T. Umeda, S. Yamasaki, J. Isoya, K. Tanaka, Phys. Rev. B **59**, 4849 (1999).

[182] M. Stutzmann and D. K. Biegelsen, Phys. Rev. B **40**, 9834 (1989).

[183] M. H. Brodsky and R. S. Title, Phys. Rev. Lett. **23**, 581 (1969).

[184] G. K. Walters and T. L. Estle, J. Appl. Phys. **32**, 1854 (1961).

[185] A. L. B. Neto, T. Dylla, S. Klein, T. Repmann, A. Lambertz, R. Carius, and F. Finger, J. Non-Cryst. Solids, **338-340**, 168 (2004).

[186] Y. Yamazaki, K. Ishikawa, S. Samukawa and S. Yamazaki, Physica B, **376-377**, 327 (2006).

[187] Y. Kuo, Vacuum, **59**, 484 (2000).

[188] K. Winer, Annu. Rev. Mater. Sci. **21**, 1 (1991).

[189] J. I. Pankove and N. M. Johnson (Editors) *Semiconductors and semimetals*, Vol. 34, *Hydrogen in Semiconductors*, Academic, Boston, (1991).

[190] R. Tsu, D. Martin, J. Gonzalez-Hernandez, and S. R. Ovshinsky, Phys. Rev. B. **35**, 2385 (1987).

[191] S. T. Pantelides, Phys. Rev. Lett. **57**, 2979 (1986).

[192] S. T. Pantelides, Phys. Rev. Lett. **58**, 1344 (1987).

[193] S. T. Pantelides, Phys. Rev. B. **36**, 3479 (1987).

[194] P. A. Fedders and A. E. Carlson, Phys. Rev. B **39**, 1134 (1989).

[195] P. A. Fedders and A. E. Carlsson, Phys. Rev. Lett. **58**, 1156 (1987).

[196] R. Biswas, C. Z. Wang, C. T. Chan, K. M. Ho, and C. M. Soukoulis, Phys. Rev. Lett. **63**, 1491 (1989).

[197] J. H. Stathis, Phys. Rev. B **40**, 1232 (1989).

[198] S. Knief and W. von Niessen, Phys. Rev. B **60**, 5412 (1999).

[199] P. A. Fedders, D. A. Drabold, P. Ordejón, G. Fabricius, D. Sanchez-Portal, E. Artacho and J. M. Soler, Phys. Rev. B **60**, 10594 (1999).

[200] M. Ishimaru, S. Munetoh, and T. Motooka, Phys. Rev. B **56**, (1997) 15133.

[201] M. Ishimaru, J. Appl. Phys. **91**, 686. (2002)

[202] M. Fornari, M. Peressi, S. de Gironcoli and A. Baldereschi, Europhys. Lett. **47**, 481 (1999).

[203] A. Bongiorno, L. Colombo and T. Díaz de la Rubiai, Europhys. Lett. **43**, 695 (1998).

[204] M. Tang, L. Colombo, J. Zhu, and T. Diaz de La Rubia, Phys. Rev. B **55**, 14 279 (1997)

[205] M. Härting, M. Yaman, R. Bucher, and D. T. Britton, Adv. Eng. Mater., **4**, 592 (2002).

[206] D. J. Chadi and K. J. Chang, Phys. Rev. B **38**, 1523 (1988).

[207] R. M. Nieminen and M. J. Puska, *Vacancy defects in c-Si, electronic and ionic structures*, in R. Hull (Editor) *Properties of Crystalline Silicon*, EMIS Data Review Series, No. 20, INSPEC Publication, (1999) pp. 309.

[208] R. Car, P. J. Kelly, A. Oshiyama and S.T. Pantelides, Phys. Rev. Lett. **52**, 1814 (1984).

[209] D. Tománek and M. A. Schlüter, Phys. Rev. Lett. **56**, 1055 (1986).

[210] G. D. Watkins, in *Deep centres in semiconductors. A state of the art approach*, S. T. Pantelides (Editor), Gordon and Breach Publication, New York (1992) p. 177.

[211] I. Kaiser, N. H. Nickel, W. Fuhs, and W. Pilz, Phys. Rev. B **58**, R1718 (1998).

[212] N. H. Nickel and W. B. Jackson, Phys. Rev. B **51**, 4872 (1995).

[213] J. J. Boland and G. N. Parsons, Science, **256**, 1304 (1992).

[214] H. Shirai, J. Hanna, and I. Shimizu, Japan J. Appl. Phys. **30**, L679 (1991).

[215] J. Shim, E. Lee, Y. J. Lee, and R. M. Nieminen, Phys. Rev. B **71**, 245204 (2005).

[216] A. M. Ukpong and I. A. Fuwape, Nigeria J. Pure and Appl. Phys. **2**, 36 (2003).

[217] G. Makov, R. Shah and M. C. Payne, Phys. Rev. B **53**, 15513 (1996).

[218] M. J. Puska, S. Pöykkö, M. Pesola and R. M. Nieminen, Phys. Rev. B **58**, 1318 (1998).

[219] A. Dupasquier and A. P. Mills, Jr. (Editors), *Positron Spectroscopy of Solids,* IOS Press, Amsterdam, (1995).

[220] D. T. Britton, A. Hempel and W. Triftshäuser, Phys. Rev. Lett. **87**, 217401 (2001).

[221] N. Bouarissa, J. Phys. Chem. Solids, **61**, 109 (2000).

[222] G. Trumpy and K. Petersen, J. Phys.: Condens. Matter **6**, 7483 (1994).

[223] P. Asoka-Kumar, K. G. Lynn and D. O. Welch, J. Appl. Phys. **76**, 4935 (1994).

[224] R. Krause-Rehberg and H. S. Leipner, *Positron Annihilation in Semiconductors - Defect Studies*, Springer-Verlag, Berlin, (1999) pp 16-37.

[225] S. Szpala, P. Asoka-Kumar, B. Nielsen, J. P. Peng, S. Hayakawa, K. G. Lynn and H. J. Gossmann, Phys. Rev. B 54, 4722 (1996).

[226] R. Suzuki, Y. Kobayashi, T. Mikado, A. Matsuda, P. J. McElheny, S. Mashima, H. Ohoaki, M. Chiwaki, T. Yamazaki, and T. Tomimasu, Japan J. Appl. Phys. **30**, 2438 (1991).

[227] D. T. Britton, P. Willutzki, T. E. Jackman, and P. Mascher, J. Phys. Condens. Matter, **4**, 8511 (1992).

[228] S. Dannefaer, D. Kerr and B. G. Hogg, J. Appl. Phys. **54**, 155 (1983).

[229] A. L. Jung, Y. H. Wang, G. Liu, J. J. Xiong, B. S. Cao, W. Z. Yu and D. Adler, J. Non. Cryst. Solids **74**, 19 (1985).

[230] Y. J. He, M. Hasegawa, R. Lee, S. Berko, D. Adler and A. L. Jung Phys. Rev. B **33**, 5924 (1986).

[231] V. G. Bhide, R. O. Dusane, S. V. Rajarshi, A. D. Shaligram and S. K. David, J. Appl. Phys. **62**,108 (1987).

[232] R. Haakvoort, A. van Veen, H. Schut, M.J. van den Boogaard, A.J.M. Berntsen, S. Roorda, P. A. Stolk and A. H. Reader, *AIP Conf. Proc.* **303**, 48 (1994).

[233] J. Störmer, P. Willutzki, D.T. Britton, G. Kögel, W. Triftshäuser, W. Kiunke, F. Wittman and I. Eisele, Appl. Phys. A **61**, 61 (1995).

[234] X. Zou, Y. C. Chan, D. P. Webb, Y. W. Lam, Y. F. Hu, C. D. Beling, S. Fung and H. M. Weng, Phys. Rev. Lett. **84**, 769 (2000).

[235] D. T. Britton, A. Hempel, D. Knoesen, W. Bauer-Kugelmann and W. Triftshäuser, Nucl. Instrum. Meth. B **164-165**, 1010 (2000).

[236] D. T. Britton, M. Härting, A. Hempel, G. Kögel, P. Sperr, W. Triftshäuser, M. Hempel and D. Knoesen, J. Non-Cryst. Solids, **299-302**, 249 (2002).

[237] M. Härting, D. T. Britton and W. Egger, Appl. Surf. Sci., **252**, 3188 (2006).

[238] K. G. Lynn, J. E. Dickman, W. L. Brown, M. F. Robbins and E. Bonderup, Phys. Rev. B **20**, 3566 (1979).

[239] M. J. Puska and R. M. Nieminen, Rev. Mod. Phys. **66**, 841 (1994).

[240] E. Boroński and R. M. Nieminen, Phys. Rev. B **34**, 3820 (1986).

[241] M. J. Puska and R. M. Nieminen, J. Phys. F: Met. Phys. **13**, 333 (1983).

[242] R. G. Parr and W. Yang, *Density-functional Theory of Atoms and Molecules*, Oxford Science Publications, OUP (1989) p. 47.

[243] W. Kohn and L. J. Sham, Phys. Rev. **140**, A1133 (1965).

[244] M. C. Payne, M. P. Teter, D. C. Allan, T. A. Arias and J. D. Joannopoulos, Rev. Mod. Phys. **64**, 1045 (1992).

[245] R. O. Jones and O. Gunnarsson, Rev. Mod. Phys. **61**, 689 (1989).

[246] R. M. Nieminen, E. Boroński, and L. J. Lantto, Phys. Rev. B **32**, 1377 (1985).

[247] R. M. Nieminen, in *Positron Solid State Physics*, W. Brandt and

A. Dupasquier, (Editors), North Holland, Amsterdam, (1983).

[248] B. Chakraborty and R. W. Siegel, Phys. Rev. B **27**, 4535 (1983).

[249] T. Torsti, V. Lindberg, I. Makkonen, E. Ogando, E. Räsänen, H. Saarikoski, M. J. Puska and R. M. Nieminen, *Ψ_k Newsletter, Highlight of the Month*, No. **65** (October 2004), pp. 105–131.
The code DOPPLER is available, under license, as an open-source code within the Multigrids Instead of K-space Algorithms (MIKA) package at: http://www.csc.fi/physics/mika/doppler/index.html

[250] M. Heiskanen, T. Torsti, M. J. Puska, and R. M. Nieminen, Phys. Rev. B **63**, 245106 (2001).

[251] I. Makkonen, M. Hakala, and M. J. Puska, Phys. Rev. B **73**, 035103 (2006).

[252] M. Alatalo, B. Barbiellini, M. Hakala, H. Kauppinen, T. Korhonen, M. J. Puska, K. Saarinen, P. Hautojärvi and R.M. Nieminen, Phys. Rev. B **54**, 2397 (1996).

[253] M. J. Puska, O. Jepson, O. Gunnarson and R. M. Nieminen, Phys. Rev. B **34**, 2695 (1986).

[254] T. A. Abtew and D. A Drabold, Phys. Rev. B **75**, 045201 (2007).

[255] P. C. Kelires, Phys. Rev. B **46**, 10048 (1992).

[256] M. Šob, in *Proceedings of the 10th Annual International Symposium on Electronic Structure of Metals and Alloys*, Gaussig, Germany, P. Ziesche (Editor), Dresden, Germany p. 106.

[257] M. Šob J. Phys. F. Metal Phys. **12**, 571 (1982).

[258] J. Svoboda and M. Šob, Phil. Mag. B **48**, 523 (1983).

[259] P. Genoud, A. K. Sing, A. A. Manuel, T. Jarlborg, E. Walker, M. Peter, and M. Weller, J. Phys. F. Metal Phys. **18**, 1933 (1988).

[260] M. Matsumoto and S. Wakoh, Physica B **149**, 57 (1988).

[261] R. N. West, Adv. Phys. **22**, 263 (1973).

[262] J. Kuriplach, A. L. Morales, C. Dauwe, D. Seegers and M. Šob, Phys. Rev. B **58**, 10475 (1998).

[263] M. Hakala, M. J. Puska, and R. M. Nieminen, Phys. Rev. B **57**, 7621 (1998).

[264] W. Brandt and J. Reinheimer, Phys. Lett. **35A**, 109 (1971).

[265] M. J. Puska, J. Phys.: Condens. Matter, **3**, 3455 (1991).

[266] J. Arponen and E. Pajanne, Ann. Phys. **121**, 343 (1979).

[267] W. C. Dunlap, Jr., and R. L. Watters, Phys. Rev. **92**, 1396 (1953).

[268] D. M. Cerpeley and B. J. Alder, Phys. Rev. Lett. **45**, 566 (1980).

[269] M. R. Zachariah and M. J. Carrier, J. Phys. Chem. **100**, 14856 (1996).

[270] M. J. Puska, S. Mäkinen, M. Maninen, and R. M. Nieminen, Phys. Rev. B **39**, 7666 (1989).

[271] U. Yxklinten, J. Hartford and T. Holmquist, Physica Scripta, **55**, 499 (1997).

[272] J. P. Perdew, J. A. Chevary, S. H. Vosko, K. A. Jackson, D. J. Singh, and C. Fiolhais, Phys. Rev. B **46**, 6671 (1992).

[273] G. Santoro, S. Sorrele, F. Becca, S. Scandolo, and E. Tossati, Surface Science **402**-**404**, 802 (1998).

[274] J. Garza, R. Vargas, J. A. Nichols, and D. A. Dixon, J. Chem. Phys. **114**, 639 (2001).

[275] A. J. Bridgeman and G. Cavigliasso, Chem. Phys., **279**, 143 (2002).

[276] A. van de Walle and G. Ceder, Phys. Rev. B **59**, 14992 (1999).

[277] E. D. Jones, N. A. Modine, A. A. Allerman, S. R. Kurtz, A. F. Wright, S. T. Tozer and X. Wei, Phys. Rev. B **60**, 4430 (1999).

[278] R. J. Turton, *Calculational Methods for Determining the Band Structure of Bulk c-Si*, in R. Hull (Editor) *Properties of Crystalline Silicon*, EMIS Data Review Series, No. 20, INSPEC Publication, (1999) pp. 387.

[279] P. Schröer, P. Kruger, and J. Pollman, Phys. Rev. B. **47**, 6971 (1993); Phys. Rev. B. **48**, 18264 (1993).

[280] G. B. Bachelet and N. E. Christensen, Phys. Rev. B **31**, 879 (1985).

[281] B. Barbielini, J. Puska, T. Torsti and R. M. Nieminen, Phys. Rev. B **51**, 7341 (1995).

[282] B. Barbielini, M.J. Puska, T. Korhonen, A. Harju, T. Torsti and R. M.

Nieminen, Phys. Rev. B **53**, 16201 (1996).

[283] D. Frederick, T. S. Chang, *Continuum Mechanics*, Scientific Publishers Inc., Cambridge, (1972).

[284] J. F. Nye, *Physical Properties of Crystals*, Oxford University Press, Oxford, (1957).

[285] A. S. Saada, *Elasticity: Theory and Applications*, Pergamon Press Inc., New York, 1974.

[286] A. Cauchy, "*Abstracts,*" Bulletin des Sciences ã la Sociétè philo-mathique, 1823, and A. Cauchy, "*Exercises de Mathêmatique, De la pression ou tension dans un coprs solide,*" Bulletin des Sciences ã la Sociétè philo-mathique, 1828. Cited in A. E. H. Love, *A Treatise on the Mathematical Theory of Elasticity*, Fourth Edition, Cambridge University Press, London, (1930).

[287] Y.C. Fung, *A first Course in Continuum Mechanics*, Prentice-Hall, Englewood Cliffs, New Jersey, (1969).

[288] I. C. Noyan and J. B. Cohen, *Residual Stress Measurement by Diffraction and Interpretation*. Springer, New York (1987).

[289] M. Born, W. Heisenberg, and P. Jordan, Z. Phys. **35** 557 (1926).

[290] J. C. Slater, *Quantum theory of molecules and solids*, Vols. 1 & 3, McGraw-Hill New York, (1963).

[291] V. Fock, Z. Phys. **63** 855 (1930).

[292] H. Hellmann, *Einfürung in die Quantenchemie*, Deuticke, Leipzig, (1937). pp. 61 and 285.

[293] R. P. Feynman, Phys. Rev. **56**, 340 (1939).

[294] P. Ehrenfest, Z. Phys. **45** 455 (1927).

[295] E. Schrödinger, Ann. Phys. **82** 265 (1927).

[296] W. Pauli, *Handbuch der Physik*, Band XXIV, 1 Teil, Springer, Berlin (1933), pp. 83-272.

[297] O. H. Nielsen and R. M. Martin, Phys. Rev. B **32**, 3780 (1985).

[298] O. H. Nielsen and R. M. Martin, Phys. Rev. Lett. **50**, 697 (1983).

[299] A. Sommerfeld, *Mechanics of Deformable Bodies*, Lectures on Theoretical

Physics, Vol. II, Academic Press, New York, (1950).

[300] V. Hauk, *Structural and Residual Stress Analysis by Non Destructive Methods*, Elsevier, Amsterdam (1997) pp 139-152.

[301] P. J. Withers and H. K. D. H. Bhadeshia, Mater. Sci. Technol. **17**, 355 (2001).

[302] P. J. Withers and H. K. D. H. Bhadeshia, Mater. Sci. Technol. **17**, 366 (2001).

[303] A. N. Arkhipov, and Yu. M. Temis, Strength of Materials, **12**, 892 (1980).

[304] V. Vignal, J. Favergeon and R. Oltra, Phil. Mag. Lett. **82**, 503 (2002).

[305] A. D. Krawitz, *Introduction to diffraction in Materials Science*, John Wiley, New York (2001) p. 278.

[306] P. J. Withers, W. M. Stobbs, and O. B. Pedersen: Acta Metall., **37**, 3061 (1989).

[307] K. Ohno, H. Harada, T. Yamagata, M. Yamazaki, and K. Ohsumi, Adv. X-Ray Anal., **32**, 363 (1989).

[308] E. Kröner, International Journal of Solids and Structures, **3**, 731 (1967).

[309] E. Kröner, in *Mechanics of Generalized Continua,* E. Kröner (Editor), Springer-Verlag, Berlin (1967) pp 330.

[310] A. Kunin, *The Theory of Elastic Media with Microstructures*, Springer-Verlag, Berlin (1986).

[311] M. Born and K. Huang, *Dynamical Theory of Crystal Lattice*, Clarendon Press, Oxford (1954).

[312] R. Clausius, Phil. Mag. **40**, 122 (1870).

[313] J. H. Jean, *The Dynamical Theory of Gases,* Dover Publications, New York, (1960) p. 160.

[314] J. S. Rowlinson and B. Widom, *Molecular Theory of Capillarity*, Clarendon Press, Oxford (1982) p. 85.

[315] V. Vitek and T. Egami, Phys. Stat. Sol. B **144**, 145 (1987).

[316] P. C. Kelires, Int. J. Mod. Phys. B, **14**, 256 (2000).

[317] A. M. Ukpong, M. Härting and D. T. Britton, Phil. Mag. Lett. **88**, 293 (2008).

[318] J. F. Lusto, J. Appl. Phys. **64**, 1152 (1988).

[319] Y. C. Tsui and T. W. Clyne, Thin Solid Film **306**, 23 (1997).

[320] L. L. Chavez, J. N. Onucic, and C. Clementi, J. Am. Chem. Soc. **126**, 8427 (2004).

[321] A. Sasaki, and M. A. Nowak, J. Theor. Biol. **224**, 241 (2003).

[322] P. F. Stadler, *Towards a theory of landscapes*, in *Complex Systems and Binary Networks*, R. Lopez-Pena, R. Capovilla, R. Garcia-Pelayo, H. Waelbroeck, and F. Zertuche (Editors), Springer, Berlin (1995) pp 73-163.

[323] E. L. Lawler, J. K. Lenstra, A.H.G.R. Kan, and D.B. Shmoys. *The Travelling Salesman Problem. A Guided Tour of Combinatorial Optimization*, John Wiley & Sons, 1985.

[324] S. Wright, *The Role of Mutation, Inbreeding, Crossbreeding and Selection in Evolution.* In D. F. Jones (Editor) *International Proceedings of the Sixth International Congress on Genetics*, Vol. 1 (1932) pp 356-366.

[325] K. Binder and A. P. Young, Rev. Mod. Phys. **58**, 801 (1986).

[326] M. Mézard, G. Parisi, and M. Virasoro, *Spin Glass Theory and Beyond,* World Scientific, Singapore (1987).

[327] Y. Fu and P. W. Anderson, J. Phys. A: Math. Gen. **19**, 1605 (1986).

[328] P. F. Stadler and W. Schnabl, Phys. Letters A, **161**, 337 (1992).

[329] P. F. Stadler and R. Happel, J. Phys. A. Math. Gen. **25**, 3103 (1992).

[330] P. F. Stadler, Europhys. Lett. **20**, 479 (1992).

[331] G. B. Sorkin, Algorithmica, **6**, 367 (1991).

[332] C. M. Reidys and P. F. Stadler, SIAM Review **44**, 3 (2002).

[333] P. F. Stadler, J. Math. Chem. **20**, 1 (1996).

[334] C. M. Reidys and P. F. Stadler, Appl. Math. and Computation, **117,** 321 (2001).

[335] C. Macken, P. Hagan and A. Perelson, SIAM J. Appl. Math. **51**, 799 (1991).

[336] H. Flyvbjerg and B. Lautrup, Phys. Rev. A **46**, 6714 (1992).

[337] P. Bak, H. Flyvbjerg and B. Lautrup, Phys. Rev. A **46**, 6724 (1992).

[338] M. R. H. Javaheri and R. V. Chamberlin, J. Chem. Phys. **125**, 154503 (2006).

[339] J. Chave and E. Guitter, J. Phys. A. Math. Gen. **32**, 445 (1999).

[340] W. Fontana, P. F. Stadler, E. G. Bornberg-Bauer, T. Griesmacher, I. L. Hofacker, M. Tacker, P. Tarazona, E. D. Weinberger and P. Schuster, Phys. Rev. E **47**, 2083 (1993).

[341] S. C. Kou, J. Oh and W. H. Wong, J. Chem. Phys. **124**, 244903(1) (2006).

[342] E. D. Weinberger, Biological Cybernetics, **63**, 325 (1990).

[343] M. Eigen, J. McCaskill, and P. Schuster, Adv. Chem. Phys. **75**, 149 (1989).

[344] M. Yaman, *Scientific Visualization of Stress Tensor Information with Applications to Stress Determination by X-ray and Neutron Diffraction*, University of Cape Town, South Africa, PhD Thesis (2007), p. 42.

[345] R. Shuker and R. W. Gammon, Phys. Rev. Lett. **25**, 222 (1970).

[346] J. S. Lannin, *Physics Today*, July 1988, p 28.

[347] S. Gupta, R. S. Katiyar, G. Morrell, S. Z. Weisz and I. Balberg, Appl. Phys. Lett. **75**, 2803 (1999).

[348] P. Biswas, Phys. Rev. B **65**, 125208 (2002).

[349] W. A. Kamitakahara, C. M. Soukoulis and H. R. Shanks, U. Buchenau, and G. S. Grest, Phys. Rev. B **36**, 6539 (1987).

[350] T. Ishidate, K. Inoue, K. Tsuji, and S. Minomura, Solid State Commun., **42**, 197 (1982).

[351] R. Biswas, A. M. Bouchard, W. A. Kamitakahara, G. S. Grest, C. M. Soukolis, Phys. Rev. Lett. **60**, 2280 (1988).

[352] M. Marinov and N. Zotov, Phys. Rev. B **55**, 2938 (1997).

[353] W. A. Kamitakahara, H. R. Shanks, J. F. McClelland, U. Buchenau, F. Gompf and L. Pintschovius, Phys. Rev. Lett. **52**, 644 (1984).

[354] L. Laaksonen, J. Mol. Graphics, **10**, 33 (1992).

[355] S. Roorda, W. C. Sinke, J. M. Poate, D. C. Jacobson, S. Dierker, B. S. Dennis, D. J. Eaglesham, F. Spaepen, and P. Fuoss, Phys. Rev. B **44**, 3702 (1991).

[356] S. Kugler, G. Molnár, G. Petö, E. Zsoldos, and L. Rosta, A. Menelle and R. Bellissent, Phys. Rev. B **40**, 8030 (1989).

[357] J. Fortner and J. S. Lannin, Phys. Rev. B **39**, 5527 (1989).

[358] O. Imagawa and T. Akiyama and K. Shimakawa, Appl. Phys. Lett. **45**, 438 (1984).

[359] I. Kwon, R. Biswas, and C. M. Soukoulis, Phys. Rev. B **45**, 3332 (1992).

[360] B. Rauschenbach, G. Otto, K. Hohmuth, and V. Heera, J. Phys. F: Met. Phys. **17**, 2207 (1987).

[361] S. Minomura, *Semiconductors and semimetals*, J. I. Pankove (Editor), Vol. **21A**, Academic Press, London, (1984) p.18.

[362] E. Spanakis, E. Stratakis, P. Tzanetakis and Q. Wang, J. Appl. Phys., **89**, 4294 (2001).

[363] G. Dalba, P. Fornasini, R. Grisenti, F. Rocca, I. Chambouleyron and C. F. O. Graeff, J. Phys.: Condens. Matter **9**, 5875 (1997).

[364] N. E. Cusack, *Physics of Structurally Disordered Matter*, IOP Publishing Ltd., Bristol, (1987).

[365] S. R. Elliot, *Physics of Amorphous materials*, Longman, Essex, (1990).

[366] B. Pantchev, P. Danesh, and B Schmidt, Appl. Phys. Lett. **87**, 023104 (2005).

[367] U. Kroll, J. Meier, A. Shah, S. Mikhailov and J. Weber J. Appl. Phys. **80**, 4971 (1996).

[368] K. S. Stevens, N. M. Johnson, J. Appl. Phys. **71**, 2628 (1992).

[369] W. B. Jackson and C. C. Tsai, Phys. Rev. B **45**, 6564 (1992).

[370] Y. Hishikawa, J. Appl. Phys. **62**, 3159 (1987).

[371] B. Pantchev, P. Danesh, I. Savatinova, E. Liarokapis, B Schmidt and D. Grambole, J. Phys. D: Appl. Phys. **34,** 2589 (2001).

[372] A. T. Nguyen and D.L. Butler, Meas. Sci. Technol. **16**, 1813 (2005).

[373] L. B. Freund and S. Suresh, *Thin film materials,* Cambridge University Press, Cambridge, (2003) p. 96.

[374] N. Lümmen and T. Kraska, Modelling Simul. Mater. Sci. Eng. **15**, 319 (2007).

[375] D. M. C. Nicholson, R. I. Barabash, G. E. Ice, C. J. Sparks, J. L. Robertson and C. Wolverton, J. Phys.: Condens. Matter **18,** 11585 (2006).

[376] D. Srolovitz, T. Egami and V. Vitek, Phys. Rev. B **24**, 6936 (1981).

[377] T. Egami and D. Srolovitz, J. Phys. F.: Met. Phys. **12**, 2141 (1982).

[378] D. Srolovitz, K. Maeda, S. Takeuchi, T. Egami and V. Vitek, J. Phys. F.: Met. Phys. **11**, 2209 (1981).

[379] T. Egami, K. Maeda, D. Srolovitz and V. Vitek, Journal de Physique **41**, C8-272 (1980).

[380] D. Srolovitz, K. Maeda, V. Vitek and T. Egami, Phil. Mag. A **44**, 847 (1981).

[381] K. Maeda and S. Takeuchi, J. Phys. F.: Met. Phys. **12**, 2767 (1982).

[382] H. E. Schaefer, R. Würschum, R. Schwarz, D. Slobodin and S. Wagner, Appl. Phys. A **40**, 145 (1986).

[383] I. Makkonen, M. Hakala, M.J. Puska, Physica B, **376-377**, 1 (2006).

[384] A. A. Valladares, F. Alvarez, Z. Liu, J. Sticht, and J. Harris, Eur. Phys. J. B **22**, 443 (2001).

[385] M. Durandurdu, D. A. Drabold, and N. Mousseau, Phys. Rev. B **62**, 15307 (2000).

[386] J. M. Holender and G. J. Morgan, Modelling Simul. Mater. Sci. Eng. B **2***,* 1 (1994).

[387] P. A. Fedders and D. A. Drabold, Phys. Rev. B **47**, 13277 (1993).

[388] N. Mousseau and M. F. Thorpe, Phys. Rev. B **48**, 5172 (1992).

[389] D. A. Drabold, P. A. Fedders, O. F. Sankey, and J. D. Dow, Phys. Rev. B **42**, 5135 (1990).

[390] P. C. Kelires and J. Tersoff, Phys. Rev. Lett. **61**, 562 (1988).

[391] S. Kugler, K. Kohary, K. Kádas, and L. Pusztai, Sol. Stat. Comm. **127**, 305 (2003).

[392] K. Saarinen, J. Nissilä, H. Kauppinen, M. Hakala, M. J. Puska, P. Hautojarvi, and C. Corbel, Phys. Rev. Lett. **82**, 1883 (1999).

[393] Z. Wang, H. S. Leipner, R. Krause-Rehberg, V. Bodarenko and H. Gu, Microelectronic Engineering, **66**, 358 (2003).